Multiphysics characterization of GaN materials and devices for power applications

Atse Julien Eric N'dohi

▶ **To cite this version:**

Atse Julien Eric N'dohi. Multiphysics characterization of GaN materials and devices for power applications. Electronics. INSA de Lyon, 2023. English. NNT : 2023ISAL0011 . tel-04220296

HAL Id: tel-04220296
https://theses.hal.science/tel-04220296

Submitted on 27 Sep 2023

HAL is a multi-disciplinary open access archive for the deposit and dissemination of scientific research documents, whether they are published or not. The documents may come from teaching and research institutions in France or abroad, or from public or private research centers.

L'archive ouverte pluridisciplinaire **HAL**, est destinée au dépôt et à la diffusion de documents scientifiques de niveau recherche, publiés ou non, émanant des établissements d'enseignement et de recherche français ou étrangers, des laboratoires publics ou privés.

N°d'ordre NNT : 2023ISAL0011

THESE de DOCTORAT DE L'INSA LYON, membre de l'Université de Lyon

Ecole Doctorale N° ED610
(Electronique Electrotechnique Automatique)

Spécialité/ discipline de doctorat :
Electronique, micro et nano-électronique, optique et laser
Soutenue publiquement le 03/03/2023, par :
Atse Julien Eric N'DOHI

MULTIPHYSICS CHARACTERIZATION OF GAN MATERIALS AND DEVICES FOR POWER APPLICATIONS

Devant le jury composé de :

MALBERT, Nathalie	Professeure des Universités	IMS / Université de Bordeaux Présidente
BOUDART, Bertrand	Professeur des Universités	GREYC / Université de Caen Normandie Rapporteur
KUBALL, Martin	Professeur des Universités	Université de Bristol – UK Rapporteur
JUILLAGUET, Sandrine	Maitre de Conférence HDR	L2C / Université de Montpellier II Examinatrice
SONNEVILLE, Camille	Maitre de Conférence	AMPERE / INSA de Lyon Co-Directrice de thèse
PLANSON, Dominique	Professeur des Universités	AMPERE / INSA de Lyon Directeur de thèse

Cette thèse est accessible à l'adresse : https://theses.insa-lyon.fr/publication/2023ISAL0011/these.pdf
© [A.J.E. N'Dohi], [2023], INSA Lyon, tous droits réservés

Département FEDORA – INSA Lyon - Ecoles Doctorales

SIGLE	ECOLE DOCTORALE	NOM ET COORDONNEES DU RESPONSABLE
CHIMIE	**CHIMIE DE LYON** **https://www.edchimie-lyon.fr** Sec. : Renée EL MELHEM Bât. Blaise PASCAL, 3e étage secretariat@edchimie-lyon.fr	**M. Stéphane DANIELE** C2P2-CPE LYON-UMR 5265 Bâtiment F308, BP 2077 43 Boulevard du 11 novembre 1918 69616 Villeurbanne **directeur@edchimie-lyon.fr**
E.E.A.	**ÉLECTRONIQUE, ÉLECTROTECHNIQUE, AUTOMATIQUE** **https://edeea.universite-lyon.fr** Sec. : Stéphanie CAUVIN Bâtiment Direction INSA Lyon Tél : 04.72.43.71.70 secretariat.edeea@insa-lyon.fr	**M. Philippe DELACHARTRE** INSA LYON Laboratoire CREATIS Bâtiment Blaise Pascal, 7 avenue Jean Capelle 69621 Villeurbanne CEDEX Tél : 04.72.43.88.63 **philippe.delachartre@insa-lyon.fr**
E2M2	**ÉVOLUTION, ÉCOSYSTÈME, MICROBIOLOGIE, MODÉLISATION** **http://e2m2.universite-lyon.fr** Sec. : Bénédicte LANZA Bât. Atrium, UCB Lyon 1 Tél : 04.72.44.83.62 secretariat.e2m2@univ-lyon1.fr	**Mme Sandrine CHARLES** Université Claude Bernard Lyon 1 UFR Biosciences Bâtiment Mendel 43, boulevard du 11 Novembre 1918 69622 Villeurbanne CEDEX **sandrine.charles@univ-lyon1.fr**
EDISS	**INTERDISCIPLINAIRE SCIENCES-SANTÉ** **http://ediss.universite-lyon.fr** Sec. : Bénédicte LANZA Bât. Atrium, UCB Lyon 1 Tél : 04.72.44.83.62 secretariat.ediss@univ-lyon1.fr	**Mme Sylvie RICARD-BLUM** Institut de Chimie et Biochimie Moléculaires et Supramoléculaires (ICBMS) - UMR 5246 CNRS - Université Lyon 1 Bâtiment Raulin - 2ème étage Nord 43 Boulevard du 11 novembre 1918 69622 Villeurbanne Cedex Tél : +33(0)4 72 44 82 32 **sylvie.ricard-blum@univ-lyon1.fr**
INFOMATHS	**INFORMATIQUE ET MATHÉMATIQUES** **http://edinfomaths.universite-lyon.fr** Sec. : Renée EL MELHEM Bât. Blaise PASCAL, 3e étage Tél : 04.72.43.80.46 infomaths@univ-lyon1.fr	**M. Hamamache KHEDDOUCI** Université Claude Bernard Lyon 1 Bât. Nautibus 43, Boulevard du 11 novembre 1918 69 622 Villeurbanne Cedex France Tél : 04.72.44.83.69 **hamamache.kheddouci@univ-lyon1.fr**
Matériaux	**MATÉRIAUX DE LYON** **http://ed34.universite-lyon.fr** Sec. : Yann DE ORDENANA Tél : 04.72.18.62.44 yann.de-ordenana@ec-lyon.fr	**M. Stéphane BENAYOUN** Ecole Centrale de Lyon Laboratoire LTDS 36 avenue Guy de Collongue 69134 Ecully CEDEX Tél : 04.72.18.64.37 **stephane.benayoun@ec-lyon.fr**
MEGA	**MÉCANIQUE, ÉNERGÉTIQUE, GÉNIE CIVIL, ACOUSTIQUE** **http://edmega.universite-lyon.fr** Sec. : Stéphanie CAUVIN Tél : 04.72.43.71.70 Bâtiment Direction INSA Lyon mega@insa-lyon.fr	**M. Jocelyn BONJOUR** INSA Lyon Laboratoire CETHIL Bâtiment Sadi-Carnot 9, rue de la Physique 69621 Villeurbanne CEDEX **jocelyn.bonjour@insa-lyon.fr**

Cette thèse est accessible à l'adresse : https://theses.insa-lyon.fr/publication/2023ISAL0011/these.pdf
© [A.J.E. N'Dohi], [2023], INSA Lyon, tous droits réservés

ScSo	**ScSo*** **https://edsciencessociales.universite-lyon.fr** Sec. : Mélina FAVETON INSA : J.Y. TOUSSAINT Tél : 04.78.69.77.79 melina.faveton@univ-lyon2.fr	**M. Bruno MILLY** Université Lumière Lyon 2 86 Rue Pasteur 69365 Lyon CEDEX 07 **bruno.milly@univ-lyon2.fr**

*ScSo : Histoire, Géographie, Aménagement, Urbanisme, Archéologie, Science politique, Sociologie, Anthropologie

Cette thèse est accessible à l'adresse : https://theses.insa-lyon.fr/publication/2023ISAL0011/these.pdf
© [A.J.E. N'Dohi], [2023], INSA Lyon, tous droits réservés

ABSTRACT

Silicon power electronics has shown its limits due to its incapacity to sustain high voltage, high temperature and high frequency applications. Therefore, the need to resort to materials with larger band gap and solve silicon (Si) technological issues for high voltage operations has been getting more and more intense. Wide band gap materials such as Silicon Carbide (SiC), Gallium Nitride (GaN), and Diamond are very promising for power electronics because of their interesting physical properties such like high carrier mobility, high critical electric field and good thermal conductivity than Si that enable them to perform at high voltage and temperature domains. Semiconductors manufacturing companies indeed, consider them as potentials power or current converters, inverters and rectifers for improving home and industrial energy distribution and consumption in a better way. However, the road to get them into a larger mass production technology is still long because recent researches have shown that their performance is pinned by some physical phenomena such as structural defects appearance, strain and stress effects, doping and dopant control and effectivess and so on. Thus, ruling out these problems by a deep understanding of the physical mechanisms behind them is a key option in optimizing their performance. In this thesis, we confronted the physical and electrical properties of GaN material and devices through multiphysics and electrical characterizations approach such as micro Raman, cathodoluminescence and classical current-voltage I (V) measurements. The objective is to get an insight into the physical performance of these power electronic materials (SiC, GaN), especially of GaN based power devices due to their higher carrier mobility compared to SiC and their growing technology maturity for mass production and distribution; and suggest if possible, ways of optimizing their operating abilities at a micro level. The coupling of these characterization methods allow us to have a deep view of the physical mechanisms that support the high voltage or temperature operation of these GaN based materials and as well as help us to grab the discrepancy existing between physical theoretical parameters established through finite elements simulations and true experimental value.

Cette thèse est accessible à l'adresse : https://theses.insa-lyon.fr/publication/2023ISAL0011/these.pdf
© [A.J.E. N'Dohi], [2023], INSA Lyon, tous droits réservés

Cette thèse est accessible à l'adresse : https://theses.insa-lyon.fr/publication/2023ISAL0011/these.pdf
© [A.J.E. N'Dohi], [2023], INSA Lyon, tous droits réservés

TABLE OF CONTENT

Cette thèse est accessible à l'adresse : https://theses.insa-lyon.fr/publication/2023ISAL0011/these.pdf
© [A.J.E. N'Dohi], [2023], INSA Lyon, tous droits réservés

Cette thèse est accessible à l'adresse : https://theses.insa-lyon.fr/publication/2023ISAL0011/these.pdf
© [A.J.E. N'Dohi], [2023], INSA Lyon, tous droits réservés

Cette thèse est accessible à l'adresse : https://theses.insa-lyon.fr/publication/2023ISAL0011/these.pdf
© [A.J.E. N'Dohi], [2023], INSA Lyon, tous droits réservés

Cette thèse est accessible à l'adresse : https://theses.insa-lyon.fr/publication/2023ISAL0011/these.pdf
© [A.J.E. N'Dohi], [2023], INSA Lyon, tous droits réservés

LIST OF FIGURES

Cette thèse est accessible à l'adresse : https://theses.insa-lyon.fr/publication/2023ISAL0011/these.pdf
© [A.J.E. N'Dohi], [2023], INSA Lyon, tous droits réservés

Cette thèse est accessible à l'adresse : https://theses.insa-lyon.fr/publication/2023ISAL0011/these.pdf
© [A.J.E. N'Dohi], [2023], INSA Lyon, tous droits réservés

Cette thèse est accessible à l'adresse : https://theses.insa-lyon.fr/publication/2023ISAL0011/these.pdf
© [A.J.E. N'Dohi], [2023], INSA Lyon, tous droits réservés

Cette thèse est accessible à l'adresse : https://theses.insa-lyon.fr/publication/2023ISAL0011/these.pdf
© [A.J.E. N'Dohi], [2023], INSA Lyon, tous droits réservés

LIST OF TABLES

Cette thèse est accessible à l'adresse : https://theses.insa-lyon.fr/publication/2023ISAL0011/these.pdf
© [A.J.E. N'Dohi], [2023], INSA Lyon, tous droits réservés

Cette thèse est accessible à l'adresse : https://theses.insa-lyon.fr/publication/2023ISAL0011/these.pdf
© [A.J.E. N'Dohi], [2023], INSA Lyon, tous droits réservés

AKNOWLEDGEMENTS

It has been a long run to complete this thesis project for three years. During these three years, I have developed technical, managerial and pedagogical skills. I have successfully managed to work autonomously under close and efficient supervision. This helped me to value any steps of the research work in national and international conferences. In addition, as fruits from the supervised work done through the thesis project, we published at least three articles in some international journals. Therefore, I want to express my deep gratitude to everyone who has been involved in the project directly or indirectly.

Firstly, I am grateful to Ampere laboratory to have given me the opportunity to work practically on the PHD project. I used very good and efficient lab facilities that helped me to run my experiments without any technical difficulties. I am also sincerely grateful to Dominique Planson, Camille Sonneville and Lung Viet for their supervision in the different aspects of the thesis project during these three years. I have great and fruitful experiences with them. I also thank Pascal for his help in some technical aspects during experimental section of the project. A part from that, I met good people, friends, PHD students, Internship students, research engineers, professors. I have had some good moments with them. Secondly, as the thesis was a collaborative project, I want to take time to thank Saint-gobain Lumilog for the provision of GaN freestanding substrates. I also give thanks to CHREA for providing GaN Schottky diodes. In particular, I thank Yvon from CHREA who really helped with the whole GaN device technical aspects and some preliminary analyses as well. Furthermore, the project involved also experienced researchers such as Hassan Mayer, Frédéric Morancho from LN2 laboratory in Sherbrook and LAAS in Toulouse. I want to thank them all for their technical contribution in the success of the project.

Finally, I am very grateful to the French government, the Aura region, INSAVALOR for funding the project and giving additional financial aid in order to complete successfully the thesis project

Cette thèse est accessible à l'adresse : https://theses.insa-lyon.fr/publication/2023ISAL0011/these.pdf
© [A.J.E. N'Dohi], [2023], INSA Lyon, tous droits réservés

Cette thèse est accessible à l'adresse : https://theses.insa-lyon.fr/publication/2023ISAL0011/these.pdf
© [A.J.E. N'Dohi], [2023], INSA Lyon, tous droits réservés

INTRODUCTION

For years, semiconductors technology has been mainly dominated by the massive use of silicon (Si) due to its physical properties and beneficial advantages for electronic systems. However, when operating at high power systems, Si-based power device exhibits some important limitations regarding its voltage blocking capability, operation temperature and switching frequency [1]. Nowadays, power electronic systems designers and manufacturers are more focused on new and innovating power devices based on Wide Bandgap Semiconductor material especially GaN. It appears to overcome the Si limitations and facilitates power electronics development, due to its physical properties that help to increase the overall power efficiency at high frequency, high voltage and high temperature applications. This helps to reduce power losses effects in many power-based devices like data center power supplies, motors and pumps, and UPS systems leading to substantial energy and cost savings [2]. In addition, the industrial interest for GaN power devices has therefore been increasing recently because GaN in its competition with SiC can offer better high-frequency and high-voltage performances and allow a good utilization in the field of radio frequency and power conversion system. As GaN power devices, vertical and lateral structure are the two main configurations that are being developed for power electronic applications. Vertical GaN device mostly includes structures being homoepitaxially grown on GaN bulk substrate or freestanding substrate while the lateral one is mainly heteroepitaxially formed on foreign substrates such as SiC, Si, GaAs, and Sapphire. Until recently, a variety of GaN power devices including GaN power diodes and transistors in both lateral and vertical form has been manufactured and made available on the semiconductors market. However, all these GaN based power devices still suffer from intense leakage current during operation, insufficient breakdown voltage reached so far [3,4]. This has been reported to stem from the activity of some structural defects, residual stress in the device, some doping inhomogeneities and even poor edge terminations realizations during fabrication process. These physical problems do not enable a better trade-off between theoretical characteristics (high-voltage blocking capability, high-temperature operation and high switching frequencies) and real commercial availability of GaN power devices.

Up to now, tentative explanations to circumvent these situations are now going on but fundamental aspects of these problems that hamper the reliability, the mass production and commercialization of GaN power electronics are still lacking clear investigations and effective treatments. Therefore, the deep understanding of physical mechanisms underlying the occurrence of these problems are of huge interest for improving the performance of GaN power devices.

Cette thèse est accessible à l'adresse : https://theses.insa-lyon.fr/publication/2023ISAL0011/these.pdf
© [A.J.E. N'Dohi], [2023], INSA Lyon, tous droits réservés

Here, we propose to investigate these phenomena through multiphysics characterizations approach based on innovating and non-invasive physical characterization tools such as micro-Raman spectroscopy and cathodoluminescence for the physical part coupled with standard current-voltage (I-V) measurements for the electrical part. The choice of these characterization methods as the core part of this thesis stems from the fact that in materials engineering, characterization refers to the broad and general way by which materials'structure and properties are tuned and accurately measured. It is a fundamental process in the field of materials sciences, without which no scientific meaning or understanding of materials, engineering could be probed. Every single characterization tool has its own specific advantage and orientation concerning the properties of the materials under test. Therefore, to get a very deep view of the link between fundamental properties and the performance of GaN based materials and power devices, a couple or more characterization tools is requested. Hence, the objective of this work is to get an insight into the physical performance of the GaN power devices and possibly suggest some solutions for optimizing their operating abilities at a micro level. The coupling of these characterization tools would allow us to establish a correlative study between optical and electrical properties of GaN based materials and devices in order to have an effective explanation of the physical mechanisms that support their electrical performance at high voltage operations.

In order to conduct this work better, the thesis has been split in seven chapters starting from bibliography aspects of GaN materials and devices to the results that we have obtained during the project. The **chapter 1** presents a general overview of GaN material, its physical properties, introduces the state of the art on GaN power devices and finally exposes the interest of this thesis for GaN vertical devices. The **chapter 2** gives details about the physical and non-destructive characterization tools such as Micro Raman spectroscopy and Cathodo-Luminescence used in this project. **In chapter 3,** the generality of the electrical characterization method by current–voltage (I-V) measurements, especially on GaN Schottky devices is shown. **In chapter 4,** the first result of our work is presented. This chapter is a study of GaN substrates using micro-Raman spectroscopy for the purpose of vertical device technology. The objective was to investigate the residual stress in these n-doped GaN substrates by investigating some Raman modes. In **Chapter 5,** micro Raman characterizations of homoepitaxial n-doped GaN layers with different Si concentration have been performed. The objective is to probe the doping concentration level and its influence on the GaN material and devices crystalline quality. **In chapter 6**, physical characterizations using a correlation approach between micro-Raman and Cathodo-Luminescence spectroscopy has been performed on some vertical GaN Schottky diodes. Finally, **in chapter 7**, we present the electrical properties of the same diodes used in chapter 6 and we establish a correlative study between their physical properties and their electrical behaviors.

Cette thèse est accessible à l'adresse : https://theses.insa-lyon.fr/publication/2023ISAL0011/these.pdf
© [A.J.E. N'Dohi], [2023], INSA Lyon, tous droits réservés

REFERENCES

[1] Flack, T.J.; Pushpakaran, B.N.; Bayne, S.B.; Ga, N. Technology for power electronic applications: A review. J. Electron. Mater., (2016).

[2] Frost & Sullivan, Gallium Nitride Power Semiconductors, New Product Innovation Award, Europe, (2019) consulted on October (2022).

[3] Dang G T, Zhang A P, Mshewa M, et al. “High breakdown voltage Au/Pt/GaN Schottky diodes” Journal of Vacuum Science and Technology, (2000).

[4] http://www.microsemi.com/.

Cette thèse est accessible à l'adresse : https://theses.insa-lyon.fr/publication/2023ISAL0011/these.pdf
© [A.J.E. N’Dohi], [2023], INSA Lyon, tous droits réservés

Cette thèse est accessible à l'adresse : https://theses.insa-lyon.fr/publication/2023ISAL0011/these.pdf
© [A.J.E. N'Dohi], [2023], INSA Lyon, tous droits réservés

CHAPTER 1: GaN BASED MATERIALS AND POWER DEVICES

This section will discuss a general view of GaN material properties, its main growth techniques and eventually, its potential applications in power electronics.

1.1. GENERALATIES OF GaN MATERIAL

Gallium Nitride (GaN) has a large band gap energy of 3.4 eV. It is the most mature wide bang material among the groupe III-Nitrides compounds due to the recent progress in GaN technology production. During the last decades, it has been successfully used to produce short wavelength optoelectronic devices such like blue light emitting diodes (LEDs) [1]. GaN has a strong critical electric field (E_c) of about 10 times that of silicon (Si) which enables electrical performance for high voltage applications. The saturation velocity (v_{sat}) is 2 times higher than in Si and its carrier mobility (μ_n) is good enough to allow device operations at high frequency. Its physical properties are materialized through the physical parameters listed in table1.1 [2] and in figure 1.1 as well. These parameters are essential factors that give GaN material the ability to work at high voltage, high temperature and high frequency range for power switching applications.

However, the lack of good quality bulk GaN substrates is a disadvantage for high quality power devices [3]. Despite the fact of having superior physical functions better than Si, GaN material is still subject to some problems like mechanical stress, lattice matching substrate, and structural defects, doping inhomogeneity, which hinder their perfect quality during device manufacturing.

Materials	E_g **(eV) at 300 K**	μ_n **(cm^2/V.S)**	μ_p **(cm^2/V.S)**	v_{sat} **(cm/.S)**	E_c **(V/cm)**	ε_r
Si	1,1	1450	450	10^7	3.10^5	11.7
SiC (4H, 6H, 3C)	3.2-2.9-2.3	450-1000	45-115	2.10^7	2.10^6	10
GaN(wurtzite)	3.4	1000	35	2.10^7	5.10^6	8.9
Diamond	5.6	2200	1800	3.10^7	$5{,}6.10^6$	5.7

Table 1. 1: Physical properties of Wide band gaps semiconductors [2].

Cette thèse est accessible à l'adresse : https://theses.insa-lyon.fr/publication/2023ISAL0011/these.pdf
© [A.J.E. N'Dohi], [2023], INSA Lyon, tous droits réservés

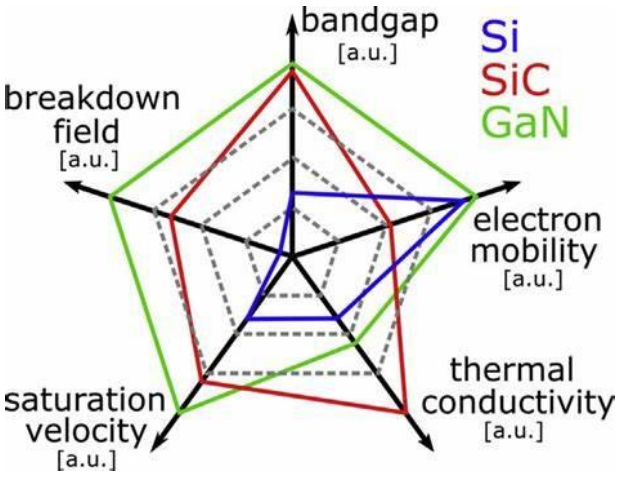

Figure 1. 1: Comparison of the relevant material properties for Si, SiC and GaN power electronics [4].

The growth technique of the GaN materials can be split into two categories: the bulk crystal growth, which is more related to substrate growth and the epitaxial growth that is more oriented on epilayers growth. Bulk GaN crystal growth can be done by **Halide Vapor Phase Epitaxy (HVPE) [5], sublimation, high-pressure liquid solution, ammonothermal methods [6]**. Among them, **HVPE and ammonothermal methods** have been recently proved as the most efficient techniques to deliver high quality GaN substrates.

As for **epitaxial growth of high-quality GaN**, two kinds of epitaxial growth can be synthesized: homo-epitaxial growth that requires the substrate and the grown layer to be of the same type and the hetero-epitaxy that requires the substrate and the layer over it to be of different type such as Silicon (Si), Sapphire (Al_2O_3), SiC, Gallium Arsenide (GaAs) for the substrate. A variety of growth synthesis methods exist to obtain epitaxial GaN layers, among which Molecular Beam Epitaxy (MBE), Metal Organic Chemical Vapor Deposition (MOCVD) and HVPE are the main processing techniques.

Hydride Vapor Phase Epitaxy (HVPE): HVPE is one of the most commonly used epitaxial growth process, in which HCl reacts with liquid Gallium to form GaCl. Subsequently GaCl along with NH_3 are carried to process chamber (typically a quartz furnace) using H_2 or N_2 or argon gas to form GaN. Figure 2 illustrates the HVPE growth steps. This technique results in higher growth rate compared to any other methods approximately 200 - 300 $\mu m.h^{-1}$, on relatively large (2-in.) substrate. However, films grown using HVPE technique suffer from higher threading dislocation density (TDD) about 10^9 cm^{-2} when grown on hetero-substrates [7]. For instance, the lattice mismatch between GaN and substrates such as Si, SiC, and sapphire are reported to be 17%, 3.3%, and 13% respectively [8].

Additionally, HVPE layers are rough and suffer from high strain that result in bowing and cracking at the GaN/Substrate interface [9].

Cette thèse est accessible à l'adresse : https://theses.insa-lyon.fr/publication/2023ISAL0011/these.pdf
© [A.J.E. N'Dohi], [2023], INSA Lyon, tous droits réservés

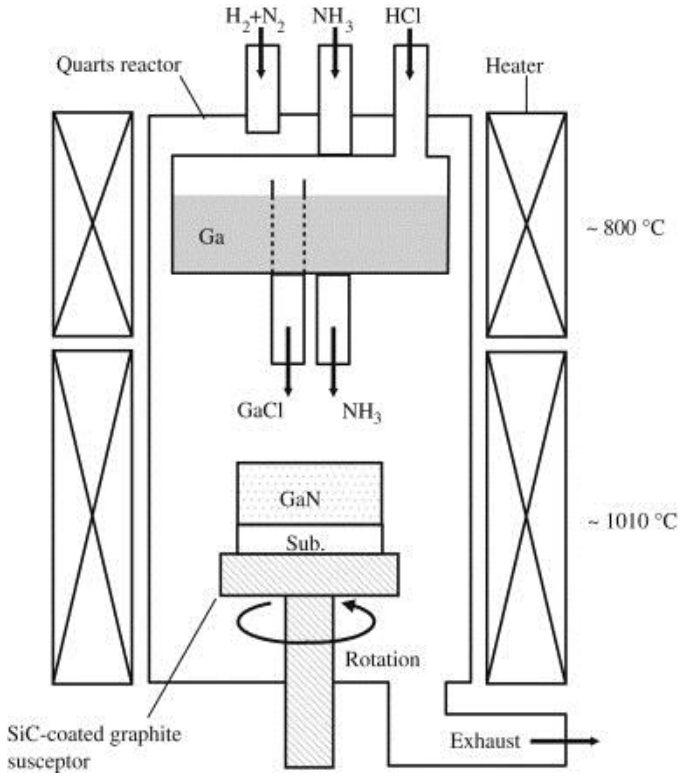

Figure 1. 2: HVPE growth of GaN [8].

HVPE Bulk GaN substrates: in order to reduce the threading dislocations, thicker GaN films need to be grown on sapphire, as the threading dislocation density (TDD) is higher at the interface and the defects propagate along the direction of the growth for several microns (µm). For the layers thickness between 350 - 500 µm thick, the number of defect lines that extend to the surface tends to decrease. Further, GaN layers are removed from the seed substrates resulting in a bulk substrate with lower TDD values of 10^6 cm^{-2} [10]. Despite, the separation of the freestanding GaN layer from hetero-substrate, the obtained GaN wafers remain typically bowed.

Metal organic chemical vapor deposition (MOCVD): MOCVD is the most widely implemented method to grow high-quality GaN films. In fact, MOCVD is a two-step process, involving (1) transportation of metalorganic and nitrogen precursors to the process chamber and then (2) reaction on the surface of the heated substrate. Trimethylgallium (TMGa) and NH_3 are typically used chemical sources for Ga, and N. TMGa is initially vaporized by flowing hydrogen gas through the bubbler and is then mixed with NH_3 in the main channel. The two precursors are then flowed in parallel into the chamber, to decompose and form GaN layers on the heated substrate. Then, a secondary gas is flowed perpendicular to the substrate to maintain the reactants closer to the substrate (shown in figure 2). Further, using a low temperature grown buffer layer [11], the GaN films produced by MOCVD result have substantially lower TDD about 10^5 cm^{-2} when grown on hetero-substrates.

Cette thèse est accessible à l'adresse : https://theses.insa-lyon.fr/publication/2023ISAL0011/these.pdf
© [A.J.E. N'Dohi], [2023], INSA Lyon, tous droits réservés

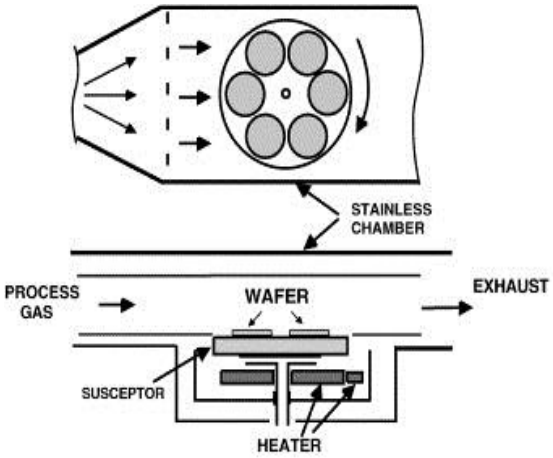

Figure 1. 3: MOCVD reactor set up for GaN growth [12].

Although the MOCVD technique can produce high-quality films [13], the growth rate of this method is very low in the order of 1-2 μm/h only.

Ammono thermal: The two growth techniques discussed above mostly rely on hetero-substrates such as SiC and sapphire due to the lack of freestanding and high-quality GaN substrates. With the thermodynamic limitation of GaN, e.g., decomposition at 8770°C under atmospheric conditions [14], it cannot be grown from the stoichiometric melt without extreme pressure and temperature of > 6 GPa at 2220°C [15]. Hence, only vapor phase and solution techniques are appropriate to produce group-III nitride crystals in an economic way. More recently, however, the ammonothermal growth of GaN has emerged as a powerful technique for the mass-production of large size GaN crystals [16].

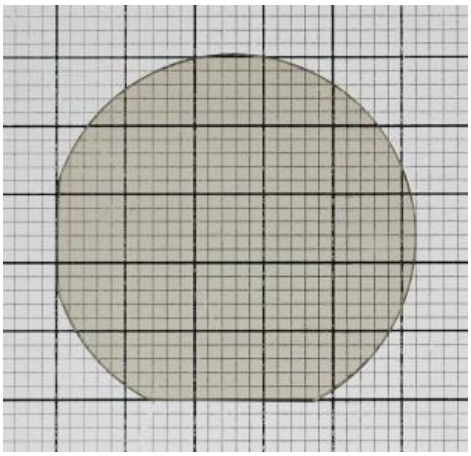

Figure 1. 4: GaN bulk crystals obtained by Ammono thermal method [16].

The ammonothermal technique belongs to the wide family of solvothermal techniques, employing a polar solvent of inorganic or organic nature under subcritical or even supercritical conditions to dissolve and re-crystallize a polar material. The process to grow GaN crystals uses a solvent comprised of supercritical ammonia with added mineralizers to grow GaN via recrystallization at seed

Cette thèse est accessible à l'adresse : https://theses.insa-lyon.fr/publication/2023ISAL0011/these.pdf
© [A.J.E. N'Dohi], [2023], INSA Lyon, tous droits réservés

crystals [17]. Ammonothermal growth is a bulk process that does not use non-native starting substrates. This method has yielded the lowest defect density of 5×10^3 cm^{-2} in a 1-in. wafer. Table 1.2 summarizes all the growth techniques.

Molecular beam epitaxy (MBE): Molecular beam epitaxy is an ultra-high vacuum (UHV) growth technique with a number of features for the fabrication of semiconductor devices. MBE systems are based on UHV chambers that are typically evacuated to less than 10 Torr. The UHV medium provide MBE with the great advantage of being a very clean process, for the semiconductor growth. During MBE process, thermal precursors sources produce beams of atoms or molecules that are directed to the heated substrate where thin film grows. The beams of atoms and molecules are in the molecular flow regime and can thus be considered as non-interacting and unidirectional sources. This allows the control of the reacting species during growth. In addition, MBE is also a low-temperature growth processes and for GaN the temperatures are usually in the range of 700-800°C. Growth rates are typically about 1/3 μm/hr (approximately one-third monolayer per second) allowing thickness control on the atomic level [18].

Growth Technique	**Advantages**	**Disadvantages**
Hydride Vapor Phase epitaxy (HVPE)	High growth rate ($200 – 300$ $\mu m.h^{-1}$)	High defect density (10^9 cm^{-2})
Metal organic chemical vapor deposition (MOCVD)	Low defect densities (10^5 cm^{-2})	Low growth rate ($1\text{-}2$ $\mu m.h^{-1}$)
Bulk Hydride Vapor Phase epitaxy	High growth rate ($200 – 300$ $\mu m.h^{-1}$)	Cracking at the interface and bowing of the wafer
Ammono thermal	Low defect density (5×10^3 cm^{-2})	Long growth time
Molecular beam epitaxy (MBE)	Good thicknes control at the atomic level	Very low growth rate

Table 1. 2: Summary of GaN growth techniques.

Cette thèse est accessible à l'adresse : https://theses.insa-lyon.fr/publication/2023ISAL0011/these.pdf
© [A.J.E. N'Dohi], [2023], INSA Lyon, tous droits réservés

1.2. PROPERTY OF GALLIUM NITRIDE

This section will describe the crystal structure of GaN, its vibrational properties and its doping types that is useful to probe its electrical behavior. A broad understanding about these fundamental physical properties is vital to grab any other idea about its potential applications as power devices and its integration in power electronic systems.

1.2.1. CRYSTAL STRUCTURE OF GALLIUM NITRIDE

GaN and its alloys can crystallize in both wurtzite (WZ) phase known as $(\alpha - phase)$ and in zinc blende (ZB) structure $called\ (\beta\ phase)$. Due to some thermodynamic conditions, the wurtzite structure appears to be the most stable and useful form for bulk materials. The metastable zinc blende structure is more often obtained by tuning the growth conditions during epitaxial technique on quasi-perfectly matched cubic substrates such as β-SiC. In both phases, GaN mostly behaves as a direct band gap material. Figure 1.5 shows the crystalline appearance of both Wurtzite and Zinc blende polytype.

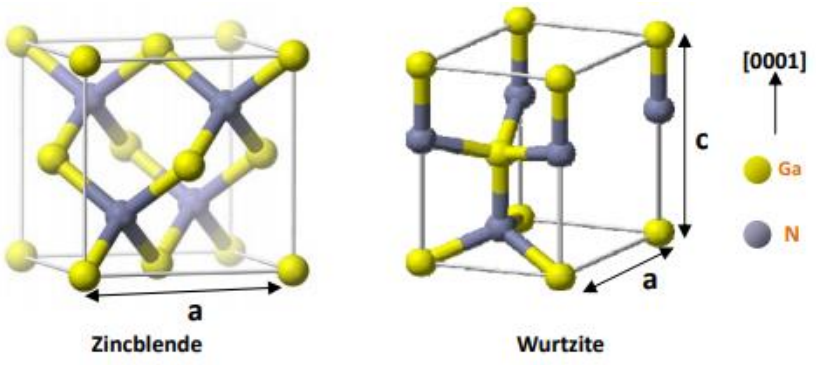

Figure 1. 5: Zinc blende and Wurtzite GaN polytypes [19].

As seen in the picture, the symmetry of the WZ and ZB crystal structures can be divided into C_{6v}^4 and T_d^2 space groups respectively in the Schoenflies notation [19]. These space groups symmetry are indicative elements of vibration modes that occur when each polytype is experiencing any lattice dynamics. The atomic bonding in both polytype rearrange in a tetrahedral form, meaning that each atom has four possible nearest neighbors in terms of coordination property. In clear terms, one Ga atom of the two GaN pairs is tetrahedrally coordinated by four N atoms, and vice versa. This bonding is partially divided in covalent and ionic bonds. The basal plane lattice parameter is depicted by a and the axial lattice parameter, perpendicular to the basal plane, is usually described by c and adopted as

Cette thèse est accessible à l'adresse : https://theses.insa-lyon.fr/publication/2023ISAL0011/these.pdf
© [A.J.E. N'Dohi], [2023], INSA Lyon, tous droits réservés

the crystal growth direction in many litteratures. The Wurtzite (ZW) [0001] (c-axis) and Zincblende (ZB) [111] axes are the equivalent axes, and differences in the electronegativities between the group III and group V elements create polarization along these axes. The hexagonal and cubic structures differ only in the stacking sequence of the Ga–N bilayers along the cubic [111] direction, which actually coincides with the hexagonal [0001] direction. The stacking order is in ABCABC... sequence in the cubic structure and ABAB... arrangement in the hexagonal structure with A, B, and C denoting the allowed sites of the Ga–N pair during the stacking sequence. In cubic crystals, the {100} planes are non-polarized, and are usually employed as crystal growth surfaces. In Wurtzite form, the growth conditions generally depend on the polarization (+c, –c) of the c surfaces [20].

1.2.2. POLARITY AND POLARIZATION

Wurtzite crystal structure of group III-nitrides has a lack of inversion symmetry. In general, the growth direction of III-nitrides is along the c-axis (the polar axis), that is normal to the basal plane. On this plane, atoms placed in bilayers consist of two closely spaced hexagonal close-packed layers. One has the cations, and the other one has the anions. The polarity orientation is given by these bilayers, and it is reported that the film has III-polarity (+c III-nitride), if the basal surface is III-N bond oriented along the c-direction (from III atom to nitrogen atoms). The film has N-polarity (-c III-nitride), if the basal surface is N-faced oriented along c-direction (from nitrogen atom to III atom). The termination refers to the surface property. If the III-faced surface is covered with N-atoms, it can be N-terminated. However, if it is to be N-faced, the crystal needs to be flipped [21]. Figure 1.6 presents the two polarities of III-nitrides. The polarity of the film depends on the growth modes.

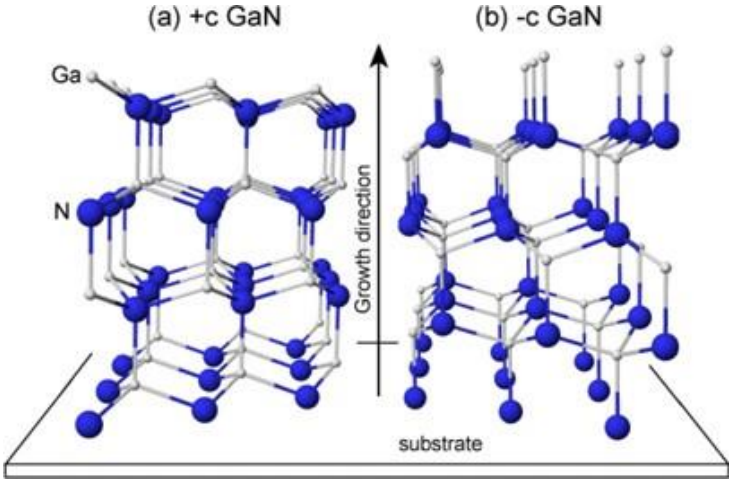

Figure 1. 6: Schematic illustration of GaN wurtzite crystal structure exhibiting the polarity along the c axis. The small and large spheres indicate Ga and N, respectively. GaN with Ga-face (+c) polarity on left side and GaN with N-face (−c) polarity on right side. When the direction of the three bonds of the III element is towards the substrate, the polar structure

Cette thèse est accessible à l'adresse : https://theses.insa-lyon.fr/publication/2023ISAL0011/these.pdf
© [A.J.E. N'Dohi], [2023], INSA Lyon, tous droits réservés

is defined as +c polarity. On the other hand, when the bonds are upward against the substrate, it is defined as having –c polarity [22].

Typically, the wurtzite structure of group III-nitride materials is grown in [0001] direction. In the strained materials, there exists a piezoelectric polarization field that is associated with electrostatic charge densities [23]. The direction of the piezoelectric polarization (PPZ) depends on the polarity of the materials [24]. Mechanical stress whether compressive or tensile also results in the piezoelectric polarization. Classically, PPZ is negative for tensile stress and positive for compressive stress. In addition, group III-nitride materials also have a large spontaneous polarization (PSP). The crystalline cell size in the epitaxial films can be different from the ideal crystalline size and cause the positive and negative charges of the centers to locate at different places. The cell itself creates an electric dipole [25]. The phenomenon is called spontaneous polarization (which is independent of strain), and it is along c-axis and depends on the polarity of the materials, lattice constants a, c, c/a ratio and the internal parameter u [26, 27]. The spontaneous polarization has a negative sign, and it increases from GaN over InN to AlN [28] due to the increasing non-ideality of the crystal structure. The piezoelectric polarization also increases with the strain in the same order under the same strain. When defining the orientation of the two polarizations, it is assumed that positive direction is the direction from the metal to the nearest nitrogen atom on the c-axis. Thus, in general, if the strain is tensile, the orientation of both polarizations is parallel, and it is antiparallel in the case of compressive strain. When both polarizations are in the same direction, the total polarization (P) will be P = PSP + PPZ [29]. Spontaneous and piezoelectric polarization can influence the optical and electrical properties of the group III-nitride layers.

1.3. DEFECTS IN GALLIUM NITRIDE

Defects are found in nitrides materials whatever the growth technology (MBE, MOCVD or VPE) used to grow them. A deep analysis of topological GaN and its related alloys has been driven so far in order to gauge the performance of GaN based devices and technology. Defects usually disturb the continuous lattice form during crystal nucleation and create unwanted energy states inside the forbidden band gap. They are usually formed during the growth, and they can be classified as point defects (zero-dimensional defects), line defects (one-dimensional defects), planar defects (two-dimensional defects), and volume defects (three-dimensional defects).

- **Point defects** can be identified as intrinsic defects, which come from the crystal itself, and extrinsic defects, that are caused by foreign atoms (impurity or solute). Interstitials, vacancies, and substitutional atoms are the main three types of point defects, and there are few other

Cette thèse est accessible à l'adresse : https://theses.insa-lyon.fr/publication/2023ISAL0011/these.pdf
© [A.J.E. N'Dohi], [2023], INSA Lyon, tous droits réservés

types as well. Vacancies and interstitials, and anti-site represent intrinsic defects, while interstitial impurity and substitutional are ascribed to extrinsic defects. When an atom is missing from the place where it has to be, it leaves an empty place that it is called a vacancy. Migration of atoms in the crystal lattice (diffusion phenomenon) can only happen because of vacancies. As the temperature increases, the number of vacancies increases as well and can be seen through the following equation:

$$N_v = N_A \exp\left(\frac{E_v}{k_B T}\right) \quad (1)$$

Where, N_A, E_v, k_B, and T are the total number of atoms in the solid, the energy required to form a vacancy, Boltzmann constant, and the temperature in Kelvin, respectively [30].

If an additional atom is inserted between the atomic sites (interstitial sites, a small void space), a self-interstitial is formed. To develop the self-interstitial defects in a crystal, it must have enough space between the host atoms. When a foreign atom occupies a site between regular atoms, instead of a regular crystal site, it is an interstitial impurity defect. The impurity atom must have enough low energy to stay at the interstitial site. If a different atom replaces one atom in the crystal, a substitutional defect occurs. If a foreign atom occupies a crystal site, it is called substitutional impurity. Substitutional impurity can be produced in the crystal intentionally by doping (n- or p-type) of the semiconductor, or it can be present in the crystal unintentionally as a contaminant.

In binary systems (group III-nitride semiconductors), the first atom can occupy a regular site of the second atom and the second atom can occupy the first atom site [31]. This kind of defects does not fall into either a vacancy, impurity, or an interstitial and it is called an antisite defect. Furthermore, the lattice is under tension when the substitutional atom is smaller than the original atom; it is in compression when the substitutional atom is larger than the original atom.

Cette thèse est accessible à l'adresse : https://theses.insa-lyon.fr/publication/2023ISAL0011/these.pdf
© [A.J.E. N'Dohi], [2023], INSA Lyon, tous droits réservés

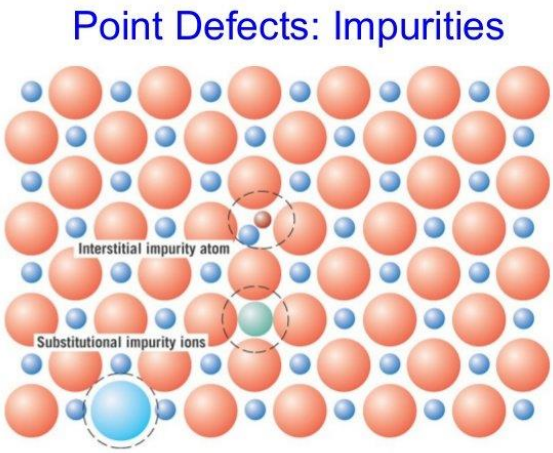

Figure 1. 7: Illustration of common type of point defects [32].

In GaN material, oxygen was the main residual impurity detected in the crystals by SIMS [32] at an estimated concentration of 10^{19} cm^3. It is reported that oxygen is the most active single donor in GaN. From the references [33, 34], the most probable n-type native defects in GaN crystals are Ga-vacancies (V_{Ga}) because of their low formation energy even at strongly Ga-rich conditions of crystallization. The presence of the negatively charged Ga-vacancies, at concentration of $10^{18}cm^{-3}$, in the n-type pressure-grown GaN crystals, was detected by positron annihilation experiments [35]. In addition, the incorporation of Mg (p type) into the growth solution extremely influences the electrical properties of GaN crystals by increasing their resistivity by orders of magnitude. This increase of the electrical resistance in GaN: Mg crystals is linked to an important decrease of free electron concentration.

.

- **Line defects or dislocations** are sudden changes in the regular ordering of atoms (generally, due to misalignment of atoms or existence of vacancies) along a line (dislocation line). In GaN, there are three main types of dislocations known as **edge dislocations**, **screw dislocations**, and **mixed dislocations** that is a mixed of both edge and the screw dislocations. Dislocations are materialized by the Burgers vector, **b**. The Burgers vector defines the magnitude and direction of the lattice distortion [36]. **Edge dislocations** take place when an extra plane of atoms inserted into a part of the crystal lattice results in one part of the lattice containing extra atoms while the other part contains the correct number of atoms. Due to this, the lattice part with the extra atoms may be under compressive stresses, while the other part may be under tensile stresses [37]. The Burgers vector, **b** is perpendicular to the dislocation line that is at the end of the plane, in the edge dislocation. The second type of dislocations are **screw dislocations** that occur when planes are displaced relative to each other through shear

Cette thèse est accessible à l'adresse : https://theses.insa-lyon.fr/publication/2023ISAL0011/these.pdf
© [A.J.E. N'Dohi], [2023], INSA Lyon, tous droits réservés

stress, and the Burger vector is parallel to the dislocation line. It is difficult to visualize the screw dislocations in a crystal. Due to the shear stress, the right region of the crystal is shifted/slipped one atomic distance to the down relative about the left region.

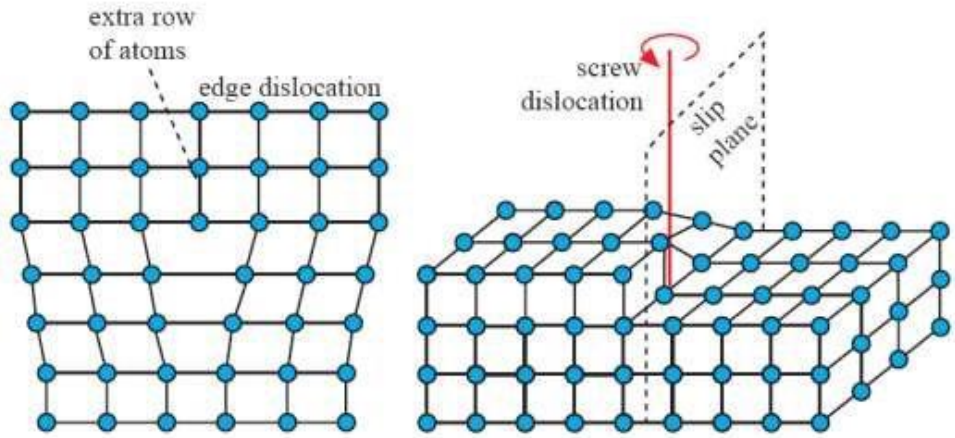

Figure 1. 8: Schematic diagrams of an edge and screw dislocation in an atomic lattice [38].

In real crystals, most dislocations are neither purely edge nor purely screw, and they usually exhibit a combination of the two that is named as mixed dislocations. Figure 1.8 illustrates the schematic representation of mixed dislocations in a crystal. The Burgers vector is nor perpendicular or parallel to the dislocation line, in this case, however, there is a fixed orientation in space. The dislocations presence, their density and their role in GaN crystals can be investigated using optical spectroscopy and microscopes. For instance, the edge (a –type) TD causes biaxial component of stress, σB and uniaxial stress, σzz [39,40] along with non-zero shear stress in c-plane, and σxy [41,42], if neglected or not. Importantly, low Poisson's ratio, $\nu = 0.1830(3)$ for α-GaN [42] ensures that σB is significantly larger than σzz [43,44]. The screw (c –type) TDs behave differently and generate only two kinds of shear stress, σxz and σyz , but its shear stress in c-plane, σxy is still zero [45,46]. It is important to recognize that $\sigma xx = \sigma zz = \sigma yy = 0$ (and $= \sigma xy$) for the screw character, all of which could have been detected non-zero by Raman peak shift (and split) for example [47,48]. This implies that the screw (c –type) TDs are not detectable by means of Raman peak shift, at least theoretically, in case of the E_2(high) phonon experimentally verified by a recent Raman study by N. Kokubo et al. (2018) [49].

Cette thèse est accessible à l'adresse : https://theses.insa-lyon.fr/publication/2023ISAL0011/these.pdf
© [A.J.E. N'Dohi], [2023], INSA Lyon, tous droits réservés

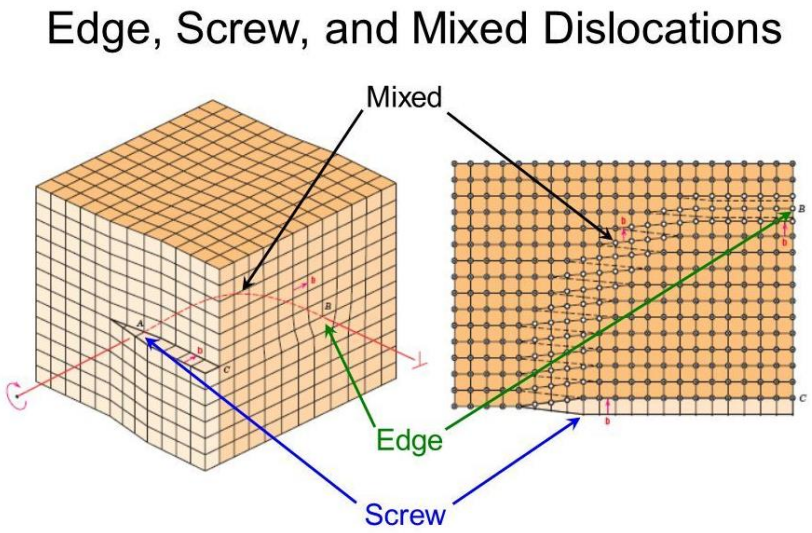

Figure 1. 9: Image of mixed dislocations in an atomic lattice [50].

- **Planar defects** are the discontinuity of the ideal crystal structure across a 2D plane. The stacking fault, grain boundaries, and twin boundaries can be seen as planar defects. Irregular sequence in the stacking of lattice planes, over a few atomic spacing produces a stacking fault. For instance, the regular stacking sequence in the hcp structure is ABABABAB, and this can arrange itself as ABABABCABAB, which creates a stacking fault in the crystal. In polycrystalline materials many small crystals or grains with different crystallographic orientation appear. The region, where exists atomic mismatch between two adjacent grains is called grain boundary. Two kinds of grain boundaries exist: the low-angle grain boundary (if the crystallographic misalignment of atomic planes between the adjacent grains is on order of a few degrees) and the high angle grain boundary (if the disorientation angle is larger than 15°).

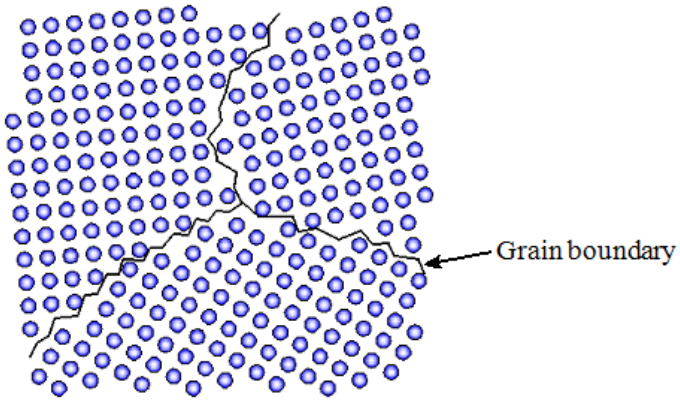

Figure 1. 10: Illustration of planar defects in atomic lattice [51].

Cette thèse est accessible à l'adresse : https://theses.insa-lyon.fr/publication/2023ISAL0011/these.pdf
© [A.J.E. N'Dohi], [2023], INSA Lyon, tous droits réservés

The low-angle boundaries can be described in terms of the orientation of their dislocation arrays. One of the simple forms is referred as tilt boundary that is explained by an array of edge dislocations when disorientation angle is perpendicular to the grain boundary. The other type is called twist boundary that can be described by an array of screw dislocations that are parallel to the disorientation angle. Grain boundaries are more reactive than grains themselves, and impurities tend to segregate along the boundaries due to their higher energy state. Since the total interfacial energy is greater in fine-grained materials than large-grained materials, the grains tend to grow larger in order to minimize the energy [52]. This phenomenon occurs at high temperatures by diffusion

Twin boundary separates two crystalline regions that have a mirror image of one side on the other side. Twin boundary is formed by annealing and mechanical deformation. Figure 1.11 shows a schematic representation of twin boundary and the adjacent atom arrangements.

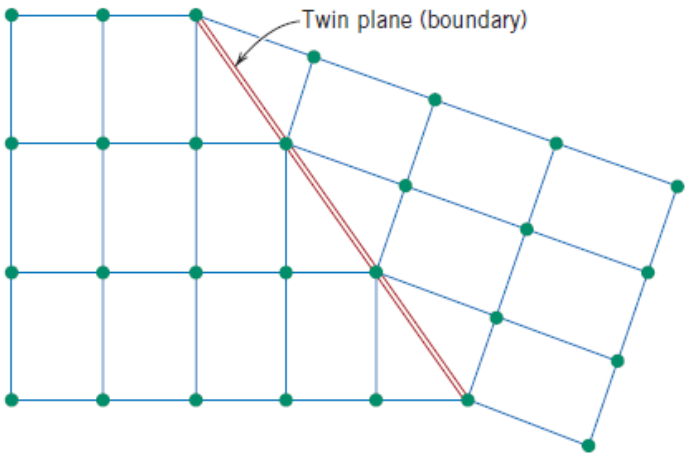

Figure 1. 11: Schematic of twin plane [53].

In addition to dislocations in GaN, two kinds of domain boundaries have also been observed [54]. They lie on {1120} and {1010} planes and according to Xin et al.[54] they are called DB I and DBII respectively. Domain boundaries are either described in terms of a double position boundary (DPB) that consist of a different stacking sequence across the boundary, or an inversion domain boundary (IDB) which is characterized by a polarity inversion across the boundary. In contrast to DBII boundaries that originate at the epilayer substrate interface, the DBI boundaries are found in a GaN sample grown by molecular beam epitaxy (MBE) on GaP extend only a short distance along the c axis [55] . A high-resolution Z contrast image down [0001] reported by Xin et al. [56] shows clearly that DBI has a horizontal displacement of Rh = ½{10-10}. This geometry is also called prismatic stacking fault and is composed of four and eight fold rings along the fault.

Cette thèse est accessible à l'adresse : https://theses.insa-lyon.fr/publication/2023ISAL0011/these.pdf
© [A.J.E. N'Dohi], [2023], INSA Lyon, tous droits réservés

- **Volume defects or bulk defects:** If any three-dimensional regions in a semiconductor are altered from the rest of the crystal, they are called volume defects [57]. They include pores, voids/cracks, clusters/precipitation, foreign inclusions, and other phases. Volume defects appear during the semiconductor processing and fabrication steps and they can affect the mechanical, thermal, electrical, and optical properties of the semiconductor.

The first observation of volume defects such as nano-pipes (hexagonal cross-section) in 2H-GaN was reported by Qian et al. [58] who found them with a density of 10^5-10^7 cm^2 in their material. However, there was also a smaller fraction of nano-pipes that had an almost circular cross-section. The radii of the pipes were between 3.5 to 50 nm, although, as in micro-pipes, the funnel shape of the nanopipes near the crystal surface resulted in much larger radii, of the order of 60-100 nm. With atomic force microscopy (AFM), Qian et al. [59] found the nanopipes to be always at the center of spiral growth hillocks. Moreover, Thi Huong Ngo et al [60] have also recently observed dislocation clusters in GaN epilayers by cathodoluminscence. By inspecting 15 CL images for the GaN sample, they found the dislocation density to be 5-10 $\times$ 10^6 cm^{-2} in areas of 187 500 μm^2 . The mean dislocation density in a dislocation cluster has been estimated to be $2\times10^8 cm^{-2}$ in the 100 μm^2 area by AFM.

1.4. DOPING AND DOPANTS IN GaN

For decades, tuning the doping with different concentrations for GaN and its alloys has been a major issue in the improvement of device performance and technology. Nowadays, researchers are making efforts to handle an appropriate control of the doping level in wide bandgap semiconductors for effective operations of device technology.

Doping in GaN: Doping is the technique used to extend the amount of free charge carriers in materials by substituting a certain quantity of the atoms in the host crystal lattice by other atoms of different nature and type. Two kinds of doping are generally used in materials technology: n-type doping dominating by electrons conductivity and p-type doping where holes concentrations prevail. Some doping may be unintentional during the growth process due to background impurities effects. Thus, a good control of both n-type and p-type doping is necessary to obtain more effective device performance. Moreover, two main techniques are used to dope materials: CVD (MOCVD) technique and the ion implantation technique. The former is based on the introduction of dopant directly into the growth chamber in the form of gas when nitride materials are produced by a chemical vapor deposition. The latter is done as surface treatment that enables an accurate control of doping profile. In

Cette thèse est accessible à l'adresse : https://theses.insa-lyon.fr/publication/2023ISAL0011/these.pdf
© [A.J.E. N'Dohi], [2023], INSA Lyon, tous droits réservés

this process, a high-energy ion beam of between 50-200 KeV is accelerated, directed onto the sample surface to modify its properties.

MOCVD doping of GaN: For N-type GaN, SiH4 has been widely used as a dopant source in the MOCVD technique [61]. The major parameter to calibrate the doping level is the SiH_4 -to-Ga molar ratio (N_{Si} :N_{Ga}). Therefore, it is necessary to vary the SiH_4 flow rate so as to achieve reasonable NSi:NGa ratio, and then Hall measurement is generally used to measure the mobility, resistivity and doping density. As for the P-GaN, the doping was once considered impossible to get, until three Japanese scientists successfully realized it in the 1980s, who also won the Nobel Prize due to this contribution. Akasaki and Amano used the Low-Energy-Electron-Beam-Irradiation (LEEBI) method to activate the p dopant, while Nakamura utilized high temperature thermal annealing [62]. The major challenges of p-GaN growth lie in the three aspects: (1) finding the optimal NMg:NGa ratio, (2) finding the best growth temperature and (3) finding the optimal post-growth annealing condition [63]. The difficulty mainly comes from the extremely small growth temperature window [64]. For instance, the optimal growth temperature is only 25°C; that is very difficult to control.

Ion Implantation Doping of GaN: The first attempts to use ion-implantation doping in GaN were performed in the 70s by Pankove and Hutchby [65], who reported the photoluminescence behavior of the material implanted with a large variety of impurities, demonstrating that Mg could be the shallowest acceptor for GaN. Later on, Pearton et al. [66] demonstrated the concrete possibility of selectively doping GaN by ion-implantation. In reference [67], Si-implantation (200 keV, 5×10^{14} cm^{-2}) followed by annealing at 1050–1100 °C resulted in a sharp decrease in n-type conductivity (decrease of the sheet resistance) associated with an almost complete (93%) activation of the dopant [67]. Next, Zolper et al. [68] successfully obtained n-type and p-type doping of GaN ion-implantation of O and Ca, respectively. Although oxygen exhibited an ionization energy of 29 meV, its activation efficiency was less than 4% after post-implantation annealing at 1050 °C. Tan et al. [69] observed the difficulty in recovering Si ion-implantation induced damage in GaN up to 1100 °C, with the formation of a network of extended defects, which led to amorphization at a high dose ($\geq 2 \times 10^{15}$ cm^{-2}). The formed amorphous layers could recrystallize into a defective polycrystalline material upon annealing in range of 800–1000 °C. For p-type doping, annealing temperatures of GaN in the range of 1400–1500 °C have been preferred to remove implantation-induced defects, and move Mg-dopant into these high temperatures can severely degrade the material, thus making mandatory the adoption of suitable capping layers or innovative annealing methods to prevent the surface degradation. One of the reasons why there are not so many studies on acceptor implantation doping in GaN is that a high background electron concentration in undoped GaN requires a high Mg dose [70]. Unfortunately, ion implantation at a high dose introduces a significant number of defects in the crystal, which favor trapping or compensation of the p-type carriers on a deep level, thus resulting in a poor acceptor activation.

Cette thèse est accessible à l'adresse : https://theses.insa-lyon.fr/publication/2023ISAL0011/these.pdf
© [A.J.E. N'Dohi], [2023], INSA Lyon, tous droits réservés

Dopants in GaN: Fundamentally, two types of dopants exist in semiconductors: donors and acceptors. Donors are atoms of a chemical element having more electrons in the outer electron shell than atoms of the host material, and they provide an excessive electron to the material while acceptors are atoms of a chemical element with lower number of electrons in the outer shell and they give an excess of holes. An important requirement for donor or acceptor atoms is that they should produce sufficient shallow energy levels in the bandgap to enable a reasonable number of electrons and holes into the material at room temperature. In addition, for an element to be used as doping candidate, it needs to be abundant in nature, less costly, and have good solubility and diffusivity. Si is a widely used material in electronics, as group IVA element. As it is located in the periodic table between period III material Ga and period V material N, it can act as both donor and acceptor depending on which atom it substitutes. Its concentration in the nitride layer is typically in the order of 10^{18} cm^{-3}. The silicon dopant is introduced by silane (SiH_4) during the growth process when MOVPE technique is used with a resistivity of n-GaN as low as $1\text{-}10^{-2}$ Ω.cm [71].

Other doping elements such as oxygen (O_2), hydrogen (H) or germanium (Ge) can also be used for n-type GaN materials. Oxygen for instance, is a group VA element that substitutes N and acts as a donor with a shallow level at ~33 meV [72]. The main challenge for GaN based device manufacturers has been to find the proper p-type doping level with the best dopant because the p- doped films are highly resistive and they need to compensate the electron excess in the material before creating an excess of holes. So far, the only promising p- dopant has been magnesium (Mg) which more often forms complexes with hydrogen and lead to dopant passivation. Mg is a group IIA element, an alkaline earth metal, which is the most abundant elements on Earth. When it substitutes Ga in GaN lattice, it acts as an acceptor and creates quite a deep level of around 230 meV. To reduce the resistivity in p-doped GaN layers and eliminate the Mg complexes thermal annealing of the sample inside the reactor after the growth or low energy electron-beam irradiation (LEEBI) have been proposed as a solution to realize p-type conduction in Mg doped GaN [73].

In addition, carbon has been mentioned as a dopant in GaN. Generally, background carbon from trimethyl gallium (TMGa) can be an issue because premature decomposition of the methyl groups is more likely to occur at the higher temperatures, 1000–1100 °C, used to grow GaN films. During carbon doping as reported in ref [74], the carbon concentration generally drops with increasing growth pressure as expected, but, interestingly, it is always greater than the sum of the silicon and oxygen concentration, which are the likely UID n-type dopants (another likely donor V_N was not measured). This means that not all of the carbon occupies nitrogen sites acting as an acceptor. Wright [75] predicted that carbon can occupy an interstitial site and generate midgap defect states. In addition, Seager et al. [76] suggest that carbon can be a shallow donor occupying gallium sites. In all of these studies, the equilibrium site for the carbon is highly dependent on the location of the Fermi energy

Cette thèse est accessible à l'adresse : https://theses.insa-lyon.fr/publication/2023ISAL0011/these.pdf
© [A.J.E. N'Dohi], [2023], INSA Lyon, tous droits réservés

with the nitrogen site being favored in n-type material. If this is truly the case and the carbon concentration always exceeds 10^{16} cm^{-3}, then it will be difficult to obtain controlled n-doping levels below this value unless the occupation state can be controlled kinetically [77]. This, in turn, will limit the maximum breakdown voltage in SDs fabricated from MOCVD-grown films to 1200 V [78]. If the carbon is incorporated in the dislocation core, it is likely that its electrical properties are different than they would be, if it was located in the bulk. It could in fact, account for the carbon concentration being larger than the donor concentration and yet the material is conductive, if the carbon tied up in the dislocation cores is not electrically active. In addition to varying the carbon concentration, changing the pressure affects the growth properties and therefore can affect the topology and crystalline quality of the films. They, in turn, can affect the properties of the diodes as well. Furthermore, MOCVD growth at higher pressures reduces the carbon incorporation, but it still is 10^{16} cm^{-3} setting an approximate lower limit to the level GaN films can be doped and, therefore,an upper limit for breakdown voltage V_b of 1200 V for GaN SDs. The breakdown voltage will usually be lower than 1200 V because both the states created by the carbon impurities, as well as the many dislocations in the film, can cause premature breakdown.

1.5. GAN BASED POWER DEVICES: INDUSTRIAL PROGRESS, ADVANTAGES, STRUCTURE AND CHALLENGES

It is important to know about the progress in the GaN power devices, the advantages, the morphology and the challenges that are essential aspects to consider in GaN based power devices development.

1.5.1. INDUSTRIAL ADVANCES OF GaN BASED POWER DEVICES

GaN material has various possible applications in power electronic commercial platform. At present, GaN-based devices are already commercialized in the photonics area (LED), while it is still in its first stage concerning power HV converters applications. GaN devices can already be found in the electronic market as power charger (100W), HEMT for RF power application.

In 2000, GaN-based power devices appeared for the first time, and the GaN FET was fabricated on a SiC substrate using radio frequency standards. In 2010, the US International Rectifier launched the first GaN commercial integrated power products iP2010 and iP2011, using GaN SBD technology platform. These devices mounted in a flip chip-packaging platform, can bring higher efficiency and more than 2 times switching frequency than silicon integrated power stage devices, and has been

Cette thèse est accessible à l'adresse : https://theses.insa-lyon.fr/publication/2023ISAL0011/these.pdf
© [A.J.E. N'Dohi], [2023], INSA Lyon, tous droits réservés

applied to large-capacity communications, DC-DC converter, electric vehicles and smart appliances [79]. Now, with the availability of high-temperature hydride vapor phase epitaxy freestanding GaN substrates, 600-V GaN Schottky diodes are due to appear in the market to compete with SiC Schottky diodes [80]. Avogy company with the support of the ARPA-E (American Energy Advanced Research Projects Agency) and the military has provided not only 600V GaN SBD commercial products, but also 1700V PN-type diodes, which play a role in solar and wind energy inverters, electric and hybrid vehicles, as well as power conversion and aerospace applications [81]. Commercial GaN Schottky diodes in the 600V – 1.2kV voltage range will also be available in the market in a near future. Khan from APA Optics Company of America manufactured the world's first GaN HEMT device and in 2000, the University of California, Santa Barbara U.K. Mishra team developed a high-voltage AlGaN/GaN HEMT power-switching device for the first time [82]. In July 2014, Transphorm demonstrated a 1 kW single-phase inverter built with its 600V-thick GaN HEMT device, which can be widely used in solar photovoltaic inverter and motor drives with peak efficiency of over 98.6%. Yasukawa Electric used cascode GaN power electronic devices in its mass production of 4.5 kW power regulator, the product is characterized by a maximum conversion efficiency of 98%, switching frequency of 40 kHz ~50 kHz, and the volume is reduced by about 40%. The power losses can be reduced by half [83]. In addition, GaN MOSFET has been developed so far. Compared with GaN HEMT device structure, GaN MOSFET devices are more suitable for high-voltage power conversion applications by using insulating dielectric gate structure to make the gate leakage current greatly reduced. In 2014, Toyota's 600 V GaN power converters made with GaN MOSFETs, with a switching frequency of 2.5 MHz and efficiencies of 97%, are used in the fields of electric vehicles and aerospace. In 2016, Boeing and General Motors Corporation owned research and development laboratories-HRL Labs have fabricated a GaN complementary metal oxide semiconductor (CMOS) [84] to promote the GaN device maturity and industrialization.

1.5.2. MAIN ADVANTAGES

Since decades, Si-based power electronics performance has shown the material limits to satisfy the requirements of high voltage, high frequency, and high power density in power electronic converter [85,86]. The wide-band-gap semiconductor material (GaN) has superior performance compared with the traditional Si, such as high critical breakdown electric field, high saturation electron velocity and high electron mobility, as summarized in Table 1.1. Therefore, power electronic devices based on GaN materials have excellent electrical properties.

Small On-state resistance: GaN devices have a high electron saturation rate (2.8 times than Si material), making GaN devices have a very small on-resistance and low conduction losses.

Cette thèse est accessible à l'adresse : https://theses.insa-lyon.fr/publication/2023ISAL0011/these.pdf
© [A.J.E. N'Dohi], [2023], INSA Lyon, tous droits réservés

Fast switching speed: GaN material has small junction capacitance, and the switching frequency can be as high as the MHz level [87].

High voltage performance: GaN material has three times the band gap of Silicon (Si), the critical breakdown electric field up to 3.3 MV/cm, is 10 times than Si material, therefore GaN device has a higher voltage capacity.

Because of specific polarization characteristics in GaN materials, there is a strong polarization effect between gallium nitride aluminum (AlGaN)/GaN heterojunctions, forming a high concentration of two-dimensional electron gas (2DEG) with a mobility as high as 2000 $cm^2/V•s$ and the surface density is up to $10^{13}cm^{-2}$ [88,89]. GaN-based devices utilize 2DEG to achieve small on-resistance, high current density, so it can achieve a larger power density to meet the severe environmental and performance requirements [90].

1.5.3. BASIC STRUCTURE AND INTEREST

The basic structure of GaN power devices is mainly classified into two categories. One is the horizontal device, fabricated on foreign substrates such as Si or Silicon Carbide (SiC) substrates [91, 92]. The other is the vertical conduction device, which fabricated by homo-epitaxial structure has unique advantages:

Firstly, the breakdown voltage can be higher. Since the drain of the vertical device is on the back of the substrate, on the opposite side of the gate and the source, when the voltage is applied to the drain, the electric field is distributed evenly along the vertical direction without the gate edge spikes of the horizontal device. Therefore, the vertical device is more favorable to obtain the high breakdown voltage than the horizontal device [93].

Secondly, it can mitigate the current collapse effect. The high electric field area of the vertical device is inside the material, away from the surface, which can weaken the effect of surface states and slow down the current collapse effect [94, 95].

Thirdly, it is easier to increase the power density. Since there is no spike electric field, vertical devices do not need to use the field board structure, without increasing the gate leakage spacing to achieve high breakdown voltage, it is easier to improve wafer utilization and improve power density.

Fourthly, the vertical structure with the advantage of being fabricated homoeptaxially has less structural defects because it does not suffer from the lattice mismatch problem as in the hetero epitaxial case.

Cette thèse est accessible à l'adresse : https://theses.insa-lyon.fr/publication/2023ISAL0011/these.pdf
© [A.J.E. N'Dohi], [2023], INSA Lyon, tous droits réservés

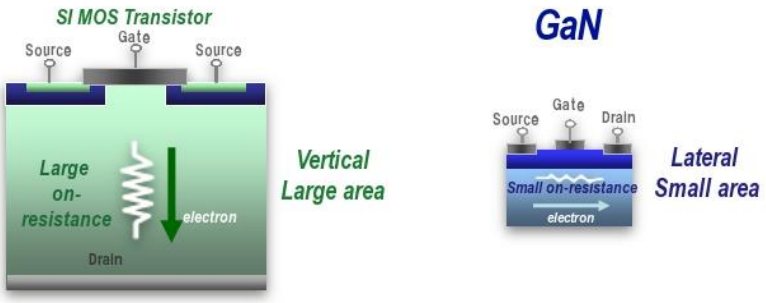

Figure 1. 12: GaN based vertical and lateral devices respectively [96].

1.5.4. STATUS OF VERTICAL GAN POWER DEVICES

Recent works on vertical GaN diodes and transistors performance have renewed the interest in these devices. Since 2010, extensive work has been done to demonstrate high-performance vertical GaN devices on freestanding GaN substrates. In 2014, vertical GaN devices on low-cost Si substrates has been demonstrated [97], with more works on vertical GaN-on-Si diodes in the past years. For GaN vertical pn diodes, Avogy Inc. has found a specific Ron of 2mΩ·cm^2 for a breakdown voltage (BV) of 2.6 kV and 2.9 mΩ·cm^2 for a BV of 3.7 kV [98]. Researchers at Ornell University have shown GaN vertical pn diodes with specific Ron of 0.95 mΩ·cm^2 for a BV of 3.48 kV [99]. For vertical GaN Schottky barrier diodes (SBDs), HRL has fabricated GaN vertical Schottky diodes with a BV over 800 V [100]. Mitsubishi has obtained a record performance with Ron of 0.71 mΩ·cm^2 and a BV over 1100 V [101].

For GaN vertical transistors, UCSB has developed a current aperture vertical electron transistor (CAVET) which combines the high conductivity of 2DEG channel at the AlGaN/GaN heterojunction with the better field distribution in a vertical structure [102]. Vertical GaN MOSFETs have also been demonstrated with similar structures to conventional Si and SiC vertical MOSFETs. Compared to CAVET, vertical MOSFETs do not need the regrowth of AlGaN/GaN channels and are intrinsically normally off.

Finally, a research group has recently fabricated a vertical GaN Fin MOSFET [103]. The Fin MOSFETs have sub-micron GaN Fins with all-around gates, and achieved a R_{on} of 0.36 mΩ·cm^2, a BV of 800 V and normally off operation without the need for p-type GaN materials or epitaxial regrowth.

Cette thèse est accessible à l'adresse : https://theses.insa-lyon.fr/publication/2023ISAL0011/these.pdf
© [A.J.E. N'Dohi], [2023], INSA Lyon, tous droits réservés

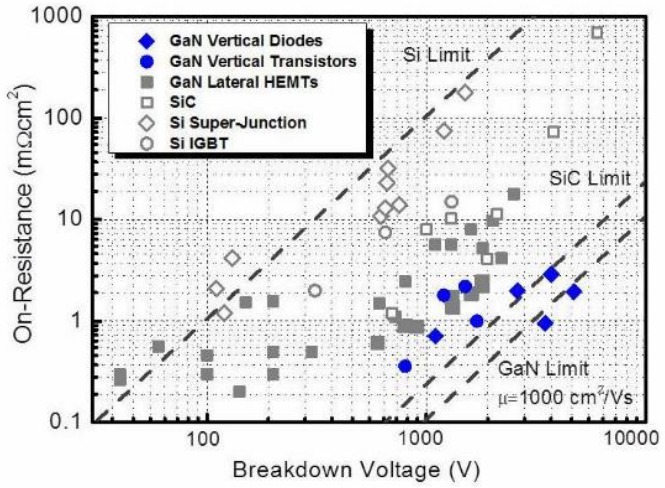

Figure 1. 13:On-resistance vs. breakdown voltage trade-off for the recently demonstrated vertical GaN devices, in comparison with lateral GaN devices, SiC and Si power devices [104].

Figure 1.13 reveals the BV vs. R_{on} trade-off for the recently fabricated GaN vertical diodes and transistors, in comparison with that of GaN lateral HEMTs, SiC power devices, Si super-junction devices and Si IGBT. As shown, the performance of vertical GaN devices has surpassed that of lateral GaN devices. It is even close to or even beyond the GaN theoretical limit (for a channel mobility of 1000 cm^2/Vs).

Although vertical GaN device have various advantages, the existing commercial GaN power devices are still based on planar (horizontal) structure due to the difficulty of material preparation and high cost in fabricating vertical GaN devices [105,106]. At present, the main types of GaN power devices are GaN diodes, GaN high electron mobility transistor (HEMT), Cascode GaN HEMT structure and GaN MOSFET.

1.5.5. CHALLENGES IN GAN BASED VERTICAL POWER DEVICES

Despite the promising performance of vertical GaN power devices, several challenges have hindered the fast commercialization of vertical GaN power devices [107]:

High cost and small diameter of GaN substrates: Currently, almost all vertical GaN power devices have been demonstrated on freestanding GaN substrates. The cost per area of GaN substrates is higher than Si substrates. In addition, the small diameter of GaN substrates will also greatly increase the cost per area of epitaxial material growth and device fabrications. Thus, Cheap-cost alternatives have been greatly desired for the development of vertical GaN power devices.

Cette thèse est accessible à l'adresse : https://theses.insa-lyon.fr/publication/2023ISAL0011/these.pdf
© [A.J.E. N'Dohi], [2023], INSA Lyon, tous droits réservés

Lack of a viable selective area doping or selective area epitaxial regrowth process that yields high-quality p-n junction on patterned GaN surfaces. The full potential of vertical power devices requires the development of selective area p- type doping. For example, merged pn/Schottky diodes could allow for a low turn-on voltage and high BV. Junction termination extensions (p-type GaN rings surrounding the device perimeter) are essential to demonstrate high- voltage vertical devices. However, most of the current approaches, laterally patterned ion implantation and activation or selective area diffusion of p-type dopants (e.g. Mg, Be, Zn) has not produced p-type regions or good-quality (i.e. equivalent to as-grown) p-n junctions.

Complete understanding of BV and leakage current mechanisms: Despite the high BV demonstrated in vertical GaN pn diodes, the understanding for the leakage current and its correlation of dislocation/defect densities is not yet fully covered. High-density dislocation defects and large residual mechanical stress in the material are also parasitic factors that affect the electrical reliability of GaN devices.

Reliability issue: The reliability of GaN devices is still not high enough, and there are many constrains. The degradation of GaN power devices in active state is mainly caused by two important external factors, namely, electric field and junction temperature. Nitrides material appears in the reverse piezoelectric effect under strong electric field [108]. It is shown that the electric field causes the additional tensile strain of AlGaN, which overlaps with the original tensile strain of itself, so that when the voltage increases to a certain critical voltage, the high-voltage field region of gate near the drain will produce cracks or other defects. A large number of hot electrons in the strong electric field can reduce the electron density of the channel, leading to a decrease in saturation current and transconductance. The hot electrons also collide with the lattice to create new defects and aggravate the aging of the device.

Under high power operating condition, the junction temperature of GaN HEMT devices (especially large gate devices) rises, severely limiting the device's output power density and reliability. The seriousness of this problem is that the high junction temperature reduces the thermal conductivity of the substrate, thereby further increasing the junction temperature and seriously deteriorating the reliability of the device.

Consequently, a variety of aspects need to be considered: reducing the material defect density, improving manufacturing process stability and repeatability, optimizing electric field distribution and improving heat dissipation.

Cette thèse est accessible à l'adresse : https://theses.insa-lyon.fr/publication/2023ISAL0011/these.pdf
© [A.J.E. N'Dohi], [2023], INSA Lyon, tous droits réservés

1.6. CONCLUSION

In this chapter, we went through the fundamental aspects of GaN material and devices. We shed light on the physical properties of GaN materials and the recent progress in GaN technology. In addition, we talked about GaN as power device in the lateral and vertical geometry and their respective characteristics. For the scope of the thesis project, we focused on the vertical geometry of GaN based devices due to their advantages and t their perspective on the GaN industrial market.

Cette thèse est accessible à l'adresse : https://theses.insa-lyon.fr/publication/2023ISAL0011/these.pdf
© [A.J.E. N'Dohi], [2023], INSA Lyon, tous droits réservés

REFERENCES

[1] Nakamura S, Senoh MS, Mukai TM. "P-GaN/N-InGaN/N-GaN double-heterostructure blue-light-emitting diodes". Japanese Journal of Applied Physics, 32 (1A):L8. (1993). **DOI** 10.1143/JJAP.32.L8

[2] Millán J, Godignon P, Pérez-Tomás A., Wide band gap semiconductor devices for power electronics, 53(2):107-16 (2012).

[3] Bohnen T, van Dreumel GW, Weyher JL, van Enckevort WJ, Ashraf H, de Jong AE, Hageman PR, Vlieg E. The nucleation of HCl and Cl2-based HVPE GaN on mis-oriented sapphire substrates. Physica status solidi c., 7(7-8):1749-55 (2010).

[4] Fatahilah, Muhammad & Strempel, Klaas & Yu, Feng & Vodapally, Sindhuri & Waag, Andreas & Wasisto, Hutomo. "3D GaN nanoarchitecture for field-effect transistors". Micro and Nano Engineering. 3. 10.1016/j.mne.2019.04.001. (2019).

[5] B. Łucznik, B. Pastuszka, I. Grzegory, M. Boc´kowski, G. Kamler, E. Litwin- Staszewska, S. Porowski, J. Cryst. Growth 281 38 (2005).

[6] Dwiliński, R., R. Doradziński, J. Garczyński, L. P. Sierzputowski, A. Puchalski, Y. Kanbara, K. Yagi, H. Minakuchi, and H. Hayashi. "Excellent crystallinity of truly bulk ammonothermal GaN." Journal of Crystal Growth 310, no. 17, 3911-3916 (2008).

[7] Bohnen T, van Dreumel GW, Weyher JL, van Enckevort WJ, Ashraf H, de Jong AE, Hageman PR, Vlieg E. The nucleation of HCl and Cl2-based HVPE GaN on mis-oriented sapphire substrates. Physica status solidi c., 7(7-8):1749-55 (2010).

[8] Su M, Chen C, Rajan S. Prospects for the application of GaN power devices in hybrid electric vehicle drive systems. Semiconductor Science and Technology, 28(7):074012 (2013).

[9] Koyama K, Aida H, Kim SW, Ikejiri K, Doi T, Yamazaki T. Growth of thick GaN layers on laser-processed sapphire substrate by hydride vapor phase epitaxy. Journal of crystal growth, 403:38-42 (2014).

[10] Hideo, A., et al., Reduction of Bowing in GaN-on-Sapphire and GaN-on-Silicon Substrates by Stress Implantation by Internally Focused Laser Processing. Japanese Journal of Applied Physics, 51(1R): p. 016504 (2012).

[11] Amano, H., et al., Metalorganic vapor phase epitaxial growth of a high quality GaN film using an AlN buffer layer. Applied Physics Letters, 48(5): p. 353-355. (1986).

Cette thèse est accessible à l'adresse : https://theses.insa-lyon.fr/publication/2023ISAL0011/these.pdf
© [A.J.E. N'Dohi], [2023], INSA Lyon, tous droits réservés

[12] H Tokunaga, H Tan, Y Inaishi, T Arai, A Yamaguchi, J Hidaka, Performance of multiwafer reactor GaN MOCVD system, Journal of Crystal Growth, Vol.221, Issues 1–4, P. 616 621(2000).

[13] Ni X, Fu Y, Moon YT, Biyikli N, Morkoc H. Optimization of (112¯0) a-plane GaN growth by MOCVD on (11¯02) r-plane sapphire. Journal of Crystal Growth, 290 (1):166-70 (2006).

[14] Karpiński J, Jun J, Porowski S. Equilibrium pressure of N_2 over GaN and high pressure solution growth of GaN. Journal of Crystal Growth., 66(1):1-0. (1984).

[15] Utsumi W, Saitoh H, Kaneko H, Watanuki T, Aoki K, Shimomura O. Congruent melting of gallium nitride at 6 GPa and its application to single-crystal growth. Nature materials, (11):735-8. (2003).

[16] Dwiliński R, Doradziński R, Garczyński J, Sierzputowski LP, Puchalski A, Kanbara Y, Yagi K, Minakuchi H, Hayashi H. Excellent crystallinity of truly bulk ammonothermal GaN. Journal of Crystal Growth., 310(17):3911-6. (2008).

[17] Kucharski R, Rudziński M, Zając M, Doradziński R, Garczyński J, Sierzputowski L, Kudrawiec R, Serafińczuk J, Strupiński W, Dwiliński R. Nonpolar GaN substrates grown by ammonothermal method. Applied Physics Letters, 95(13), 131119 (2009).

[18] Ptak Aaron Joseph. Growth kinetics and doping of gallium nitride grown by rf-plasma assisted molecular beam epitaxy. West Virginia University, (2001).

[19] Yu PY, Cardona M. Fundamentals of Semiconductors, edited by P. Treiber and C.-D. Bachem, (1996).

[20] Takahashi K, Yoshikawa A, Sandhu A. Wide bandgap semiconductors. Verlag Berlin Heidelberg. (2007).

[21] Ambacher O. Growth and applications of group III-nitrides. Journal of physics D: Applied physics, 31 (20) 2653 (1998).

[22] Sumiya M, Fuke S. Review of polarity determination and control of GaN. Materials Research Society Internet Journal of Nitride Semiconductor Research, 9 (2004).

[23] Yu ET, Dang XZ, Asbeck PM, Lau SS, Sullivan GJ. Spontaneous and piezoelectric polarization effects in III–V nitride heterostructures. Journal of Vacuum Science & Technology B: Microelectronics and Nanometer Structures Processing, Measurement, and Phenomena, (4):1742-9 (1999).

Cette thèse est accessible à l'adresse : https://theses.insa-lyon.fr/publication/2023ISAL0011/these.pdf
© [A.J.E. N'Dohi], [2023], INSA Lyon, tous droits réservés

[24] Ambacher O. Growth and applications of group III-nitrides. Journal of physics D: Applied physics.31 (20):2653. (1998).

[25] Matara Kankanamge, Indika. "Optoelectronic and Structural Properties of Group III-Nitride Semiconductors Grown by High Pressure MOCVD and Migration Enhanced Plasma Assisted MOCVD." (2016).

[26] Yu PY, Cardona M. Fundamentals of Semiconductors, edited by P. Treiber and C.-D. Bachem, (1996).

[27] Semra L, Telia A, Kaddeche M, Soltani A. Effects of spontaneous and piezoelectric polarization on AlInN/GaN heterostructure. In2012 International Conference on Engineering and Technology (ICET), (pp. 1-4). IEEE (2012).

[28] Bernardini F, Fiorentini V, Vanderbilt D. Spontaneous polarization and piezoelectric constants of III-V nitrides. Physical Review B., 56(16):R10024. (1997).

[29] Ambacher O, Foutz B, Smart J, Shealy JR, Weimann NG, Chu K, Murphy M, Sierakowski AJ, Schaff WJ, Eastman LF, Dimitrov R. Two dimensional electron gases induced by spontaneous and piezoelectric polarization in undoped and doped AlGaN/GaN heterostructures. Journal of applied physics, 87(1):334-44 (2000).

[30] Imperfections in Solids, March 20, 2016, http://www.virginia.edu/bohr/mse209/chapter4.htm, consultation date July (2022).

[31] F. K. Yam, L. L. Low, S. A. Oh and Z. Hassan, in Optoelectronics - Materials and Techniques, edited by P. P. Predeep, InTech, (2011).

[32] Murthy, Madhu, Jaime A. Freitas Jr, Jihyun Kim, Evan R. Glaser, and David Storm. "Residual impurities in GaN substrates and epitaxial layers grown by various techniques." Journal of crystal growth 305, no. 2 393-398 (2007).

[33] Van de Walle, Chris G. "Defects and doping in GaN." equilibrium 5, no. 14, 15 (1997).

[34] Katsikini, Maria, K. Papagelis, E. C. Paloura, and S. Ves. "Raman study of Mg, Si, O, and N implanted GaN." Journal of Applied Physics 94, no. 7, 4389-4394 (2003).

[35] JØrgensen, L. V., A. C. Kruseman, H. Schut, A. Van Veen, M. Fanciulli, and T. D. Moustakas. "Investigation of vacancies in GaN by positron annihilation." MRS Online Proceedings Library (OPL) 449 (1996).

Cette thèse est accessible à l'adresse : https://theses.insa-lyon.fr/publication/2023ISAL0011/these.pdf
© [A.J.E. N'Dohi], [2023], INSA Lyon, tous droits réservés

[36] R. Chien, X.J. Ning, S. Stemmer, P. Pirouz, M.D. Bremser and R.F. Davis, Appl. Phys. Lett., 68 2678 (1996).

[37] F. K. Yam, L. L. Low, S. A. Oh and Z. Hassan, in Optoelectronics - Materials and Techniques, edited by P. P. Predeep, InTech, (2011).

[38] McNamara DD. How do eclogites deform subduction and collision zones? , an Alpine study. The University of Liverpool (United Kingdom); (2009).

[39] D. Hull, D.J. Bacon, Introduction to dislocations, 4th ed., Elsevier, https:// doi.org/10.1016/b978-0-7506-4681-9.x5000-7. (2001).

[40] I. Belabbas, J. Chen, G. Nouet, Electronic structure and metallization effects at threading dislocation cores in GaN, Comput. Mater. Sci. 90 71–81, (2014).

[41] D. Hull, D.J. Bacon, Introduction to dislocations, 4th ed., Elsevier, 7. (2001).

[42] D. Mishra, Y.E. Pak, Electroelastic fields for a piezoelectric threading dislocation in various growth orientations of gallium nitride, Eur. J. Mech. A. Solids 61 B 279–292, (2017).

[43] D. Hull, D.J. Bacon, Introduction to dislocations, 4th ed., Elsevier, https:// doi.org/10.1016/b978-0-7506-4681-9.x5000-7. (2001).

[44] I. Belabbas, J. Chen, G. Nouet, Electronic structure and metallization effects at threading dislocation cores in GaN, Comput. Mater. Sci. 90 71–81, (2014).

[45] D. Hull, D.J. Bacon, Introduction to dislocations, 4th ed., Elsevier, https:// doi.org/10.1016/b978-0-7506-4681-9.x5000-7. (2001).

[46] I. Belabbas, J. Chen, G. Nouet, Electronic structure and metallization effects at threading dislocation cores in GaN, Comput. Mater. Sci. 90 71–81, (2014).

[47] R.J. Briggs, A.K. Ramdas, Piezospectroscopic study of the Raman spectrum of cadmium sulfide, Phys. Rev. B: Condensed Matter Mater. Phys. 13 5518–5529, (1976).

[48] G. Irmer, T. Brumme, M. Herms, T. Wernicke, M. Kneissl, M. Weyers, Anisotropic strain on phonons in a-plane GaN layers studied by Raman scattering, J. Mater. Sci.: Mater. Electron. 19, 51, 57. (2008).

[49] N. Kokubo, Y. Tsunooka, F. Fujie, J. Ohara, K. Hara, S. Onda, H. Yamada, M. Shimizu, S. Harada, M. Tagawa, T. Ujihara, Detection of edge component of threading dislocations in GaN by Raman spectroscopy, Appl. Phys. Exp. 11 (2018).

Cette thèse est accessible à l'adresse : https://theses.insa-lyon.fr/publication/2023ISAL0011/these.pdf
© [A.J.E. N'Dohi], [2023], INSA Lyon, tous droits réservés

[50] https://slidetodoc.com/crystal-lattice-imperfections.

[51] http://www.engineeringarchives.com/les_matsci_surface defects.html.

[52] Callister WD, Rethwisch DG. Materials science and engineering: an introduction. New York: Wiley, (2018).

[53] Renu Kumari et al, "Materials Engineering and Metallurgy", https://www.vssut.ac.in/lecture notes/lecture1423814208.pdf.

[54] Z. Sitar, M. J. Paisley, B. Yan, and R. F. Davis, Mater. Res. So c. Symp. Pro c. 162, 537 (1990).

[55] Y. Xin, P. D. Brown and C.J. Humphreys, Appl. Phys. Lett. 70, 1308 (1997).

[56] Y. Xin, S. J. Pennyco ok, N. D. Browning, P. D. Nellist, S. Sivananthan, J.-P. Faurie and P. Gibart, Nitride Semicond. 482 781, edited by F.A. Ponce, S.P. Den Baars, B.K. Meyer, S. Nakamura, S. Strite, Mat. Res. So c., Pennsylvania (1998).

[57] Yacobi BG. Semiconductor materials: an introduction to basic principles. Springer Science & Business Media; (2003).

[58] W. Qian, M. Skowronski, K. Doverspike, L. B. Rowland and D. K. Gaskill, J. Crystal

Growth 151, 396-400 (1995).

[59] W. Qian, G. S. Rohrer, M. Skowronski, K. Doverspike, L. B. Rowland and D. K. Gaskill, Appl. Phys. Let. 67, 2284-2286 (1995).

[60] Ngo, Thi Huong, Rémi Comyn, Eric Frayssinet, Hyonju Chauveau, Sébastien Chenot, Benjamin Damilano, Florian Tendille et al. "Cathodoluminescence and electrical study of vertical GaN-on-GaN Schottky diodes with dislocation clusters." Journal of Crystal Growth 552 125911. (2020).

[61] Koide, N., et al. "Doping of GaN with Si and properties of blue m/i/n/n+ GaN LED with Si-doped n+-layer by MOVPE." Journal of crystal growth 115.1 639-642. (1991).

[62] http://www.nobelprize.org/nobel_prizes/physics/laureates (2014).

[63] Huang, Jen-Wu, et al. "Electrical characterization of Mg-doped GaN grown by metalorganic vapor phase epitaxy." Applied physics letters 68.17 2392-2394. (1996).

[64] Tokunaga, H., et al. "Growth condition dependence of Mg-doped GaN film grown by horizontal atmospheric MOCVD system with three layered laminar flow gas injection." Journal of crystal growth 189: 519-522. (1998).

Cette thèse est accessible à l'adresse : https://theses.insa-lyon.fr/publication/2023ISAL0011/these.pdf
© [A.J.E. N'Dohi], [2023], INSA Lyon, tous droits réservés

[65] Pankove, J.I.; Hutchby, J.A. Photoluminescence of Zn-implanted GaN. Appl. Phys. Lett., 24, 281–283 (1974).

[66] Pearton, S.J.; Vartuli, C.B.; Zolper, J.C.; Yuan, C.; Stall, R.A. Ion implantation doping and isolation of GaN. Appl. Phys. Lett., 67, 1435–1437 (1995).

[67] Pearton, S.J.; Vartuli, C.B.; Zolper, J.C.; Yuan, C.; Stall, R.A. Ion implantation doping and isolation of GaN. Appl. Phys. Lett., 67, 1435–1437 (1995).

[68] Zolper, J.C.; Wilson, R.G.; Pearton, S.J.; Stall, R.A. Ca and O ion implantation doping of GaN Appl. Phys. Lett., 68, 1945–1947, (1996).

[69] Tan, H.H.; Williams, J.S.; Zou, J.; Cockayne, J.H.; Pearton, S.J.; Stall, R.A. Damage to epitaxial GaN layers by silicon implantation. Appl. Phys. Lett., 69, 2364–2366. (1996).

[70] Harris, G.L. Diffusion of Impurities and Ion Implantation. In Properties of Silicon Carbide; Harris, G.L., Ed.; INSPEC, the Institution of Electrical Engineers: London, UK, pp. 151–157. (1995).

[71] Moore WJ, Freitas Jr JA, Lee SK, Park SS, Han JY. Magneto-optical studies of freestanding hydride-vapor-phase epitaxial GaN. Physical Review B., 65(8):081201. (2002).

[72] Amano H, Kito M, Hiramatsu K, Akasaki I. P-type conduction in Mg-doped GaN treated with low-energy electron beam irradiation (LEEBI). Japanese journal of applied physics, 28(12A):L2112. (1989).

[73] Amano H, Kito M, Hiramatsu K, Akasaki I. P-type conduction in Mg-doped GaN treated with low-energy electron beam irradiation (LEEBI). Japanese journal of applied physics, 28(12A):L2112. (1989).

[74] Tompkins, Randy P., Timothy A. Walsh, Michael A. Derange, Kevin W. Kirchner, Shuai Zhou, Cuong B. Nguyen, Kenneth A. Jones et al. "The effect of carbon impurities on lightly doped MOCVD GaN Schottky diodes." Journal of Materials Research 26, no. 23: 2895-2900. (2011).

[75] A.F. Wright: Substitutional and interstitial carbon in wurtzite GaN. J. Appl. Phys. 92, 2575 (2002).

[76] C.H. Seager, A.F. Wright, J. Yu, and W. Gotz: Role of carbon in GaN. J. Appl. Phys. 92, 6553 (2002).

[77] A. Armstrong, C. Poblenz, D.S. Green, U.K. Mishra, J.S. Speck, and S.A. Ringel: Impact of substrate temperature on the mechanism of carbon-related defects and mechanism for semi-insulating behavior in GaN grown by molecular beam epitaxy. Appl. Phys. Lett. 88, 082114 (2006).

Cette thèse est accessible à l'adresse : https://theses.insa-lyon.fr/publication/2023ISAL0011/these.pdf
© [A.J.E. N'Dohi], [2023], INSA Lyon, tous droits réservés

[78] Tompkins, Randy P., Timothy A. Walsh, Michael A. Derenge, Kevin W. Kirchner, Shuai Zhou, Cuong B. Nguyen, Kenneth A. Jones et al. "The effect of carbon impurities on lightly doped MOCVD GaN Schottky diodes." Journal of Materials Research 26, no. 23: 2895-2900. (2011).

[79] Park SS, Park IW, Choh SH. Free-standing GaN substrates by hydride vapor phase epitaxy. Japanese Journal of Applied Physics. 39 (11B):L1141. (2000).

[80] http://www.avogy.com/

[81] Ding X, Zhou Y, Cheng J. A review of gallium nitride power device and its applications in motor drive. CES Transactions on Electrical Machines and Systems 3(1):54-64. (2019).

[82] Nishikawa K. GaN for automotive applications In: Proceedings of Bipolar/BiCMOS Circuits and Technology Meeting. Bordeaux: IEEE, (2013).

[83] Zhang NQ, Moran B, DenBaars SP, Mishra UK, Wang XW, Ma TP. Kilovolt AlGaN/GaN HEMTs as switching devices. Physica status solidi (a), 188 (1):213-7. (2001).

[84] Ikeda N, Tamura R, Kokawa T, Kambayashi H, Sato Y, Nomura T, Kato S. Over 1.7 kV normally off GaN hybrid MOS-HFETs with a lower on-resistance on a Si substrate. In2011 IEEE 23rd International Symposium on Power Semiconductor Devices and ICs (pp. 284-287). IEEE (2011).

[85] Millan J, Godignon P, Perpiñà X, Pérez-Tomás A, Rebollo J. A survey of wide bandgap power semiconductor devices. IEEE transactions on Power Electronics, 29(5):2155-63 (2013).

[86] Ye H, Yang Y, Emadi A. Traction inverters in hybrid electric vehicles. In2012 IEEE Transportation Electrification Conference and Expo (ITEC), (pp. 1-6). IEEE. (2012).

[87] Rodriguez M, Zhang Y, Maksimović D. High frequency PWM buck converters using GaN-on-SiC HEMTs. IEEE transactions on Power Electronics, 29(5):2462-73 (2013).

[88] Ambacher O, Foutz B, Smart J, Shealy JR, Weimann NG, Chu K, Murphy M, Sierakowski AJ, Schaff WJ, Eastman LF, Dimitrov R. Two dimensional electron gases induced by spontaneous and piezoelectric polarization in undoped and doped AlGaN/GaN heterostructures. Journal of applied physics, 87(1):334-44. (2000).

[89] WANG Lei. Studies on Fabrication and Characteristics of AlGaN/GaN Schottky Barrier Diodes. Beijing, Tsinghua University: (2011).

[90] Keller S, Parish G, Fini PT, Heikman S, Chen CH, Zhang N, DenBaars SP, Mishra UK, Wu YF. Metalorganic chemical vapor deposition of high mobility AlGaN/GaN heterostructures. Journal of applied physics, 86 (10):5850-7. (1999).

Cette thèse est accessible à l'adresse : https://theses.insa-lyon.fr/publication/2023ISAL0011/these.pdf
© [A.J.E. N'Dohi], [2023], INSA Lyon, tous droits réservés

[91] Meneghesso G, Meneghini M, Zanoni E. Breakdown mechanisms in AlGaN/GaN HEMTs: an overview. Japanese Journal of Applied Physics, 53(10):100211 (2014).

[92] Hsieh TE, Chang EY, Song YZ, Lin YC, Wang HC, Liu SC, Salahuddin S, Hu CC. Gate recessed quasi-normally OFF Al_2O_3/AlGaN/GaN MIS-HEMT with low threshold voltage hysteresis using PEALD AlN interfacial passivation layer. IEEE Electron Device Letters. 35(7):732-4. (2014).

[93] Sochacki T, Bryan Z, Amilusik M, Bobea M, Fijalkowski M, Bryan I, Lucznik B, Collazo R, Weyher JL, Kucharski R, Grzegory I. HVPE-GaN grown on MOCVD-GaN/sapphire template and ammonothermal GaN seeds: Comparison of structural, optical, and electrical properties. Journal of crystal growth, 394:55-60. (2014).

[94] Mizutani T, Ohno Y, Akita M, Kishimoto S, Maezawa K. A study on current collapse in AlGaN/GaN HEMTs induced by bias stress. IEEE Transactions on Electron Devices. 50(10):2015-20. (2003).

[95] Chen-Hui Y, Xiang-Dong L, Wen-Zheng Z, Qing-Zhou L, Pei-Sheng L. Investigation on the current collapse effect of AlGaN/GaN/InGaN/GaN double-heterojunction HEMTs. ACTA PHYSICA SINICA., 61(20). (2012).

[96] GaN HEMTs – G. Meneghesso- Giornata IU.NET. (2017).

[97] Zhang Y. GaN-based vertical power devices, (Doctoral dissertation, Massachusetts Institute of Technology). (2017).

[98] Kizilyalli IC, Edwards AP, Aktas O, Prunty T, Bour D. Vertical power pn diodes based on bulk GaN. IEEE Transactions on Electron Devices. 62(2):414-22. (2014).

[99] Nomoto K, Hu Z, Song B, Zhu M, Qi M, Yan R, Protasenko V, Imhoff E, Kuo J, Kaneda N, Mishima T. GaN-on-GaN pn power diodes with 3.48 kV and 0.95 mΩ-cm2: A record high figure-of-merit of 12.8 GW/cm2. In2015 IEEE international electron devices meeting (IEDM), (pp. 9-7). IEEE. (2015).

[100] Cao Y, Chu R, Li R, Chen M, Chang R, Hughes B. High-voltage vertical GaN Schottky diode enabled by low-carbon metal-organic chemical vapor deposition growth. Applied Physics Letters. 108(6):062103 (2016).

[101] Saitoh Y, Sumiyoshi K, Okada M, Horii T, Miyazaki T, Shiomi H, Ueno M, Katayama K, Kiyama M, Nakamura T. Extremely low on-resistance and high breakdown voltage observed in vertical GaN Schottky barrier diodes with high-mobility drift layers on low-dislocation-density GaN substrates. Applied Physics Express. 3(8):081001, (2010).

Cette thèse est accessible à l'adresse : https://theses.insa-lyon.fr/publication/2023ISAL0011/these.pdf
© [A.J.E. N'Dohi], [2023], INSA Lyon, tous droits réservés

[102] Yeluri R, Lu J, Hurni CA, Browne DA, Chowdhury S, Keller S, Speck JS, Mishra UK. Design, fabrication, and performance analysis of GaN vertical electron transistors with a buried p/n junction. Applied Physics Letters. 106 (18):183502 (2015).

[103] Sun M, Zhang Y, Gao X, Palacios T. High-performance GaN vertical fin power transistors on bulk GaN substrates. IEEE Electron Device Letters, 38(4):509-12, (2017).

[104] Sun M, Zhang Y, Gao X, Palacios T. High-performance GaN vertical fin power transistors on bulk GaN substrates. IEEE Electron Device Letters, 38(4):509-12, (2017).

[105] Zhou C, Jiang Q, Huang S, Chen KJ. Vertical leakage/breakdown mechanisms in AlGaN/GaN-on-Si structures. In2012 24th International Symposium on Power Semiconductor Devices and ICs (pp. 245-248). IEEE (2012).

[106] Sugimoto M, Kanechika M, Uesugi T, Kachi T. Study on leakage current of pn diode on GaN substrate at reverse bias. Physica status solidi c., (7-8):2512-4, (2011).

[107] Ding X, Zhou Y, Cheng J. A review of gallium nitride power device and its applications in motor drive. CES Transactions on Electrical Machines and Systems. 3(1):54-64 (2019).

[108] Joh J, Del Alamo JA. Mechanisms for electrical degradation of GaN high-electron mobility transistors. In2006 International Electron Devices Meeting 2006, (pp. 1-4). IEEE.

Cette thèse est accessible à l'adresse : https://theses.insa-lyon.fr/publication/2023ISAL0011/these.pdf
© [A.J.E. N'Dohi], [2023], INSA Lyon, tous droits réservés

CHAPTER 2: PHYSICAL CHARACTERIZATIONS METHODS

This section will deal with the main physical characterization techniques used in this work. As said before, it is needed to understand the physical properties of solid-state materials and devices. These physical properties can have an impact on the materials or device's bulk properties, performance, processability, stability and reliability. Here, we focused on two main non-destructive techniques: the micro-Raman spectroscopy and the Cathodo-Luminescence (CL) technique in order to understand physical mechanisms occuring in GaN materials and power devices during and after growth. Details about the results found using these techniques will be given in the next chapters. As for this section, specific and brief information on these techniques and their use in GaN materials will be presented.

2.1. MICRO RAMAN CHARACTERIZATION

Raman spectroscopy is a vibrational technique that provides unique structural information at the atomic scale on inorganic (Crystals, solids) and organic compounds (Molecules). The technique becomes a microprobe with spatial and spectral resolutions of less than 1 µm and 1 cm^{-1} respectively by coupling an optical microscope to a conventional Raman spectrometer. The spatial resolution for instance is characterized by the wavelength of the excitation source and the numerical aperture (NA) of the microscope objective. Historically, the Raman technique and phenomenon has been discovered and observed experimentally by Raman and Krishnan in 1928 [1]. Originally, the experiment was done by focusing the sunlight by a telescope onto a sample which was either a purified liquid. A focusing lens was placed to collect the scattered radiation and a system of optical filters was used to obtain the scattered radiation with an altered frequency from the incident light. This is the basic characteristic of Raman spectroscopy [1]. Various applications of micro-Raman analysis can be found in the field of forensic science, art, jewelry, archeology [2] as it is a well-adapted technique for nondestructive experiments of solids, crystals, and molecules with a good spatial resolution. Recently, it has been used to investigate spatial distribution of physical quantities such as strains and stress, temperature, impurity concentrations, doping and local crystallographic orientation in bulk semiconductors, thin films, and device configurations [3].

2.1.1. THEORY OF RAMAN EFFECT

Cette thèse est accessible à l'adresse : https://theses.insa-lyon.fr/publication/2023ISAL0011/these.pdf
© [A.J.E. N'Dohi], [2023], INSA Lyon, tous droits réservés

The principle of Raman effect is based on the inelastic light-scattering process between incident light and an irradiated substance [4]. In solid-state field, it occurs when light hits a crystal lattice and interacts with the electron cloud of the crystal. During the light–sample interaction, the incident light deforms the electron cloud to form so-called 'virtual states'. Since these levels are not stable, the photons will be scattered immediately to a relatively more stable state [5]. In case the scattered light comes back to the initial ground state, no energy transfer occurs between the incident light and the scattered light, meaning that the photon frequency and its wavelength are conserved. This process is an elastic one and it is known as Rayleigh scattering [6]. However, in the below diagram, the Raman process takes place when the incident photon energy from the ground level and the scattered one are different. The difference between these two types of energy gives rise to a vibrational energy that is known as phonon energy (ω_p).

Generally, the Raman scattering appears in two different forms: The Stokes scattering and the anti-stokes scattering. In case of the Stokes scattering, the scattered photons reach down the first excited vibrational states V_1 with a frequency lower than the incident photon. In the anti-stokes scattering, the scattered photon reachs down the ground state while the initial incident photon is excited from the first vibrational state. In that situation, the scattered photon gets a frequency higher than the incident photon. This mean that the anti-Stokes bands in Raman scattering are of lower intensity than the Stokes bands because very few atoms (crystal case) are excited during the anti-Stokes process. Therefore, the Raman spectrum during measurements comes from the Stokes part generally.

Cette thèse est accessible à l'adresse : https://theses.insa-lyon.fr/publication/2023ISAL0011/these.pdf
© [A.J.E. N'Dohi], [2023], INSA Lyon, tous droits réservés

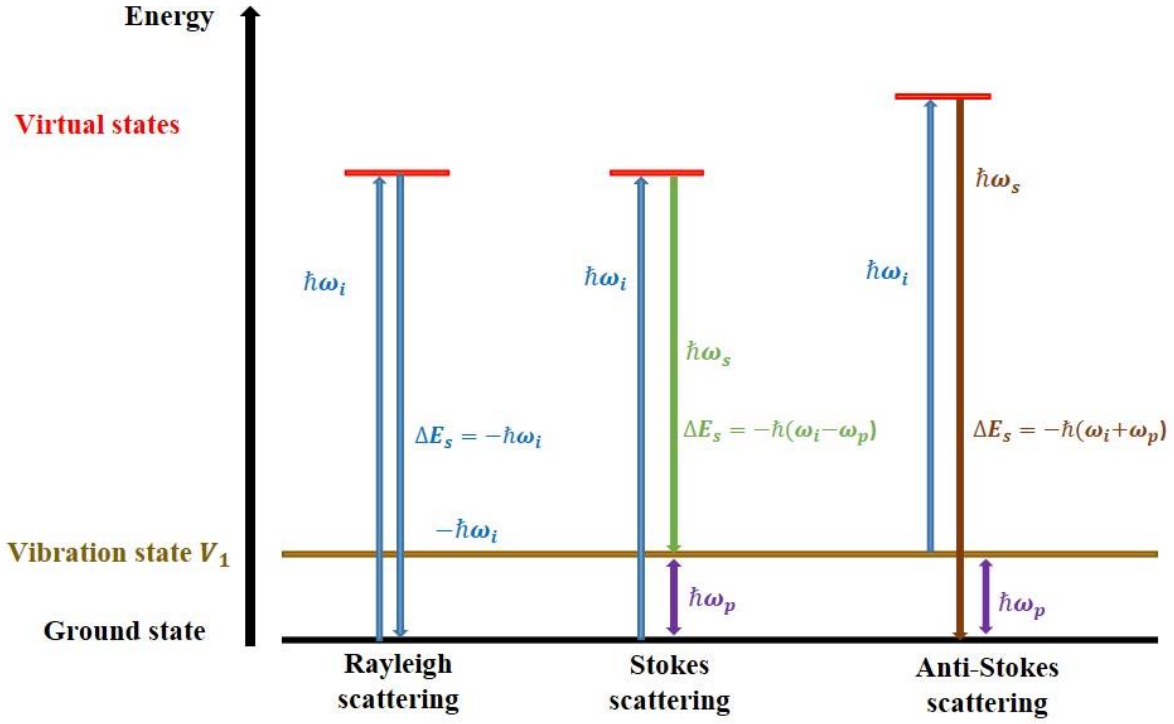

Figure 2. 1:Jablonski diagram for Rayleigh and Raman (Stokes and anti-Stokes) scattering [4]. $\hbar\omega_i$ is the incident energy, $\hbar\omega_s$ is the scattered energy and $\hbar\omega_p$ is the phonon energy.

Classically, Raman scattering effect is driven by the macroscopic description that enables the understanding of Raman scattering and the introduction of basic concepts such as Raman selection rules, Raman tensor and conservation properties. Generally, when photons interact with a vibrating crystal lattice, two physical properties can be defined by the electronic distribution within the crystal lattice in equilibrium state, namely, the dipole moment, P, and electric polarizability, α. These properties change with any deviation in interatomic spacing of the lattice or the time-dependent vibrational motions around the equilibrium position. The polarizability, α, measures the strength of the distortion experienced by the electron cloud during light-crystal interaction. It is a second order tensor representing the volume and shape of the charge distribution in the lattice. When a photon with an incident electric field **E**, interacts with the lattice, it induces a dipole moment that can be expressed by:

$$\mathbf{P} = \varepsilon_0 \alpha \mathbf{E} \qquad (1)$$

With ε_0 the free-space permittivity.

Since atoms in the lattice are vibrating around their equilibrium position during the interaction with the incident electric field, a change in the electric polarizability tensor will occur and it can be

Cette thèse est accessible à l'adresse : https://theses.insa-lyon.fr/publication/2023ISAL0011/these.pdf
© [A.J.E. N'Dohi], [2023], INSA Lyon, tous droits réservés

mathematically described through a Taylor series expansion about the equilibrium position of the lattice atoms for small amplitude of vibration:

$$\alpha = \alpha_0 + \frac{d\alpha}{dq} q + \ldots\ldots\ldots \qquad (2)$$

Where $\alpha_0$the polarizability at the equilibrium is lattice spacing and $q = q_{0,vib}\cos(\omega_p t)$is the time-dependent change in the lattice spacing due to phonon vibrations with amplitude $q_{0,vib}$ and frequency ω_p. Considering the incident electric field of the incident light as a frequency and time dependent plane wave, $E = E_i cos(\omega_i t)$ with E_i as its amplitude and ω_i its frequency, the equation (1) can be re-evaluated as:

$$P = \varepsilon_0 \alpha_0 E_i \cos(\omega_i t) + \frac{d\alpha}{dq} \varepsilon_0 q_0 \cos(\omega_p t) E_i \cos(\omega_i t) \quad (3)\ [7]$$

Where $\omega_0$is the frequency of the phonon vibration and ω_i is the vibrational frequency of the incident photon. By using the trigonometric identity, the equation (3) becomes:

$$P = \varepsilon_0 \alpha_0 E_i \cos(\omega_i t) + \frac{d\alpha}{dq}\frac{E_i}{2} \varepsilon_0 q_0 \cos((\omega_p - \omega_i)t) + \frac{d\alpha}{dq}\frac{E_i}{2} \varepsilon_0 q_0 \cos((\omega_p + \omega_i)t) \quad (4)$$

This equation shows the whole macroscopic model of the classical description of the Raman Scattering developed by Ferraro et al. in [7]. The first term on the right-hand side stands for Rayleigh scattering of photons. The second and third terms result in Stokes and anti-Stokes Raman scattering, respectively where photons are moved away from their incident frequency ω_i by the optical phonon frequency ω_p. The expression $\frac{d\alpha}{dq}$, which is the variation of the polarizability due to lattice displacement, accounts for the Raman tensor $\mathbf{R} = \frac{d\alpha}{dq}\mathbf{q}$. The Raman tensor is the main factor that drives the selection rules in Raman scattering. If $\frac{d\alpha}{dq}$equals to zero, the vibration is not Raman-active. Meaning that, to be Raman active $\frac{d\alpha}{dq}$ needs to be non-zero. Each phonon mode is described by one Raman tensor that transforms like the irreducible representation to which it belongs. The irreducible representations and Raman tensors for phonons in GaN wurtzite crystals will be given next.

Raman selection rules: The selection rules are useful to indicate the vibrations modes that are allowed and active during Raman scattering. Three rules have been elaborated to truly distinguish which Raman mode is active or not. Thus, for a vibration mode to be Raman active these following selections rules need to apply:

Cette thèse est accessible à l'adresse : https://theses.insa-lyon.fr/publication/2023ISAL0011/these.pdf
© [A.J.E. N'Dohi], [2023], INSA Lyon, tous droits réservés

- Energy conservation: $\hbar\omega_s = \hbar\omega_i \pm \hbar\omega_p$ with $\hbar\omega_p$ the phonon energy.

In the above expression, + and – stand for anti-Stokes and Stokes scattering respectively.

- Momentum conservation in the crystal: $\boldsymbol{k_s = k_i \pm q} \Rightarrow \mathbf{0<|q|<2|k|} \Rightarrow \mathbf{0<|q|<}\frac{4\pi n}{\lambda_i}$ ($\Rightarrow$ only small wave vector (close to Brillouin zone center) phonons are seen in the first order (single phonon process) Raman spectra of bulk crystals. k_s is the scattered momentum, k_i is the incident momentum and q is the phonon momemtum.
- Selection rules determined by crystal symmetry and by symmetry of excitations.

Moreover, the intensity of the Stokes scattered radiation can be expressed in terms of the Raman tensor as:

$$I_S \propto |\boldsymbol{e_i}\, \boldsymbol{R}\, \boldsymbol{e_s}\,|^2$$

Where $\boldsymbol{e_i}$ and $\boldsymbol{e_s}$ correspond to the polarisation of the incident and scattered light, respectively. This expression gives the selection rules of the first-order phonon Raman scattering. Since this expression derives from the semi-classical approximation, it does not account for all the possible Raman interactions but it describes well those occurring via the so-called dipole-allowed mechanisms.

2.1.2. RAMAN VIBRATION MODES IN GAN CRYSTAL

GaN is a uniaxial crystal and has a hexagonal structure belonging to the C_{6v}^4 symmetry group. The group theory predicts that there are eight sets of phonon modes at the zone center (Γ point) of the Brillouin zone (momentum reciprocal space near k = 0) of the wurtzite structure: $2A_1 + 2B_1 + 2E_1 + 2E_2$ modes. The A_1, E_1, *and the two* E_2 modes are Raman active, while the two B_1 modes are Raman inactive. Among them, one set of A_1 and E_1 modes are acoustic, where all the atoms move in the same direction in the unit cell. The other six modes $A_1(Z) + 2B_1 + E_1(X,Y) + 2E_2$ are optical modes where the X [100], Y [010], Z [001] in the parentheses represent the polarization directions. In wurtzite GaN, these optical modes are described based on Loudon's model [8] and the atomic displacement of these optical modes is revealed in figure 2.2. The A_1 and B_1 modes result in atomic displacements along the c-axis, while the others, E_1 and E_2, give atomic displacements perpendicular to the c-axis. Moreover, the A_1 and E_1 modes are polar and both Raman and infrared active because their induced dipole moment can couple directly with the incident light. Their vibrations polarize the unit cell and create a long-range electrostatic field which splits the A_1, E_1 modes into longitudinal optical (LO) and transverse optical (TO) modes. Generally, in GaN material,

Cette thèse est accessible à l'adresse : https://theses.insa-lyon.fr/publication/2023ISAL0011/these.pdf
© [A.J.E. N'Dohi], [2023], INSA Lyon, tous droits réservés

the electrostatic forces dominate the anisotropic short-range forces, and consequently lead to the conclusion that the TO-LO energy band splitting becomes normally larger than the A_1–E_1 splitting. The Zinc Blende structure, in contrast has a space group T_d^2 and only one Raman active mode of F2 representation can be detected. This mode has been said to be a polar mode which splits into the TO and LO modes [9].

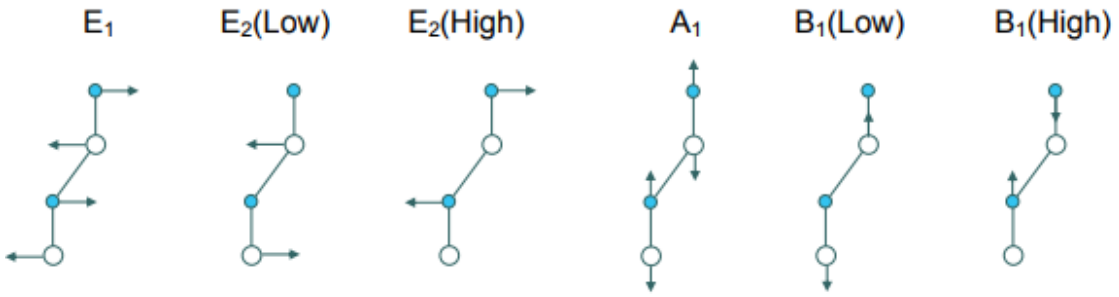

Figure 2. 2: Optical Phonons displacement of Wurtzite GaN [8]. The white circles are the Ga cations and the blue ones are the nitrides anions.

Furthermore, the Raman tensors for the phonon modes are 3 × 3 matrices in a Cartesian basis. For the GaN wurtzite structure, the Raman tensors of the optical active modes are:

$$R[A_1(z)] = \begin{pmatrix} a & 0 & 0 \\ 0 & a & 0 \\ 0 & 0 & b \end{pmatrix} \qquad R[E_1(x)] = \begin{pmatrix} 0 & 0 & c \\ 0 & 0 & 0 \\ c & 0 & 0 \end{pmatrix} \qquad R[E_1(y)] = \begin{pmatrix} 0 & 0 & 0 \\ 0 & 0 & c \\ 0 & c & 0 \end{pmatrix}$$

$$R[E_2] = \begin{pmatrix} 0 & d & 0 \\ d & 0 & 0 \\ 0 & 0 & 0 \end{pmatrix} \qquad R[E_2] = \begin{pmatrix} d & 0 & 0 \\ 0 & -d & 0 \\ 0 & 0 & 0 \end{pmatrix}$$

For polar modes, the coordinate in parentheses denotes the direction of phonon polarization, i. e. the direction of the atomic displacements. As stated above, the propagation direction of these polar phonon modes can be perpendicular or parallel to the atomic motion leading to or LO phonon modes [9].

Table 2.1 shows the selection rules for the Raman scattering under non-resonant conditions for the configurations used in this work. The scattering configurations are given in the Porto notation, that consist in four coordinates corresponding to (1) the incident light propagation direction, (2) the incident light polarization direction, (3) the scattered light polarization direction and (4) the scattered

Cette thèse est accessible à l'adresse : https://theses.insa-lyon.fr/publication/2023ISAL0011/these.pdf
© [A.J.E. N'Dohi], [2023], INSA Lyon, tous droits réservés

light propagation direction. As can be seen in Table 2.1, all the Raman active modes can be observed in backscattering geometry except the E_1 (LO) mode. This mode is only dipole-allowed in the x(y z)y configuration, a scattering configuration that can be difficult to realize in materials with strong optical absorption (such as InN for λexc = 514 nm). However, the E_1 (LO) phonon mode is usually observed under near-resonant condition in the symmetry-forbidden x (zz)$\bar{x}$ configuration due to intra-band Fröhlich interaction [9]. In the following paragraph, we present the first-order Raman spectra of wurtzite GaN in different geometries.

Configuration	E_2^H	$A_1(LO)$	E_2^L	$A_1(TO)$	$E_1(TO)$	E_1(LO)
$z(xx)\bar{z}$	✓	✓	✓			
$z(xy)\bar{z}$	✓		✓			
$x(yy)\bar{x}$	✓		✓	✓		
$x(yz)\bar{x}$					✓	
$x(zz)\bar{x}$				✓		
$x(yz)y$					✓	✓
$x(yy)x$	✓		✓	✓		
$x(yy)z$	✓		✓	✓		

Table 2. 1: Symmetry-allowed Raman modes of the GaN wurtzite structure for different scattering configurations.

Here in this thesis, we worked in the $z\,(xy)\bar{z}$ **and** $z(xx)\bar{z}$ configurations where only E_2 (High), E_2^L and A_1 (LO) are allowed. The modes described in the table 2.1 vibrates each at a specific frequency with a value scattered in the literature. Table 2.2 presents the experimental Raman shift (in cm^{-1}) values of the active Raman modes of GaN extracted from reference [10(bulkGaN), 11(FS GaN), 12 (bulkGaN)].

Cette thèse est accessible à l'adresse : https://theses.insa-lyon.fr/publication/2023ISAL0011/these.pdf
© [A.J.E. N'Dohi], [2023], INSA Lyon, tous droits réservés

Modes	E_2(Low)	A_1(TO)	E_1 (TO)	E_2 (High)	A_1 (LO)	E_1 (LO)
GaN [ref 10]	114	531.8	558.8	567.6	734	741
GaN [ref 11]	114	532.6	560	566.2	735	741
GaN [ref 12]	114	531	560	568	734	741

Table 2. 2: Frequencies of the Raman active phonons of wurtzite GaN (in cm^{-1})

2.1.3. RAMAN INSTRUMENTATION

Raman instruments are more and more widespread in many research laboratories and materials manufacturing industries. Technological breakthrough has recently led to the production of much smaller Raman spectrometers and microscopes with nano and micrometer resolutions. Modern Raman spectrometers require the sample to be presented simply to a microscope that represents an integral part of the spectrometer. The Raman microscope has many advantages; for instance, it is possible to look at extremely small samples and detect small amounts of material despite the weak signal of Raman scattering signal [13]. Here in our thesis project we used a commercial confocal micro Raman instrumentation (Renishaw Invia model) provided by Renishaw company (figure2.3). As mentioned above, we worked out our experiments in the backscattering geometry using a standard confocal mode: the input laser beam coming from the exciting source into the spectrometer is directed to a beam expander. The beam expander increases the diameter of the collimated input beam to a larger collimated output beam. Then, the output beam is steered to the microscope or spectrograph by a mirror for observation or measurement respectively. This expanded beam passes through a rejection filter that filter the beam into Stokes or anti-Stokes Raman signal by removing the Rayleigh scatter. The obtained Raman signal passes through a slit with an adjustable diameter and is collimated by some optical lenses onto a diffraction grating. Finally, the diffracted Raman signal is focused onto a CCD detector by an optical lens. The resulting Raman spectrum shows the intensity of the inelastically scattered light as a function of the Raman shift that is defined as the difference between the incident and scattered light:

$$\text{Raman shift } (\Delta\omega) = \frac{1}{\lambda_i} - \frac{1}{\lambda_s} \quad (1)$$

It is usually expressed in cm^{-1} units. Based on Planck's equation ($E = \hbar\omega = hc/\lambda$) the photon wave number is proportional to the photon energy (therefore to the photon frequency). Here, the idea to use a microscope operating in a 180° backscattering geometry is to eliminate the need to adjust constantly

Cette thèse est accessible à l'adresse : https://theses.insa-lyon.fr/publication/2023ISAL0011/these.pdf
© [A.J.E. N'Dohi], [2023], INSA Lyon, tous droits réservés

the laser onto the sample and to focus the scattered light onto the spectrometer. Our Raman instrumentation mainly includes many parts: a laser source, the collection device, filtering system, optical system, the detector, the diffraction grating and the acquisition electronics.

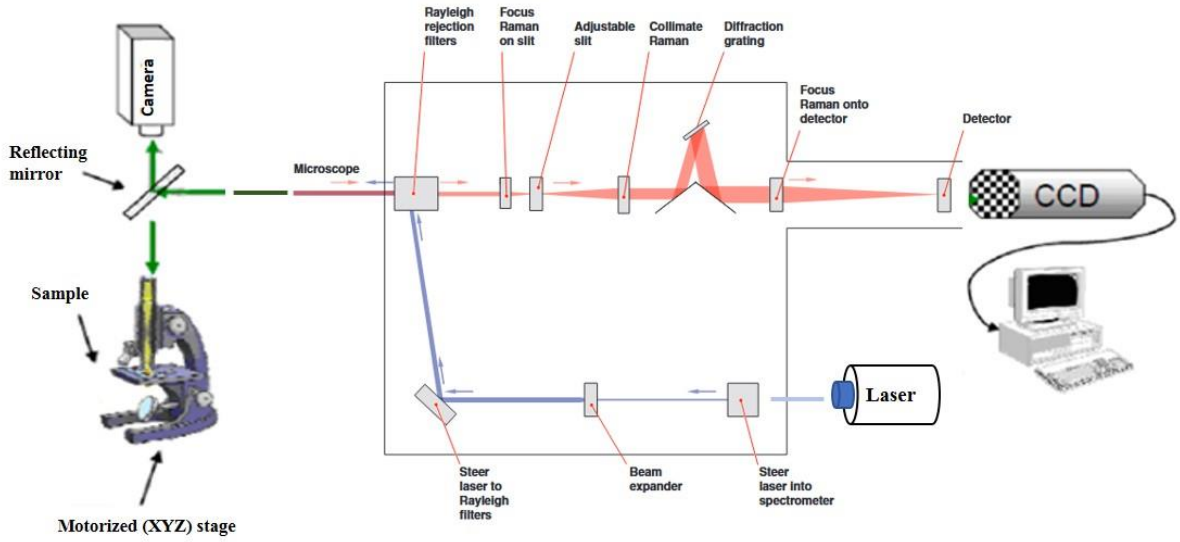

Figure 2. 3: Raman Instrumentation schematic view.

Laser excitation: A green laser diode emitting at 532 nm with a maximum power of 100 Mw has been used in our projet. During measurements we used only 10% of the entire laser power (100mW) in order to avoid sample local heating.

Optical system: As optical system, we have some mirrors to direct the laser beam to a specific direction. Some optical lenses focus and collimate the Raman signal. Other devices such as beam expander and adjustable slit have been inserted for their specific role that is briefly described above.

Diffraction grating: The 2400 l/mm diffraction grating lines has been selected for our measurement to ensure a better spectral resolution and range. The diffraction gratings of the spectrometer can be changed in order to optimize the scattering efficiency for a specific excitation wavelength and to make the choice between highly-dispersive and low-dispersive scattering performance. In addition, our spectrometer also has the 300 l/mm for UV measurements.

Collection and filtering of the scattered light: In our Renishaw model, Notch filters are inserted in the optic system to remove or reduce the Rayleigh scatter of the probe laser's wavelength before it reaches the spectrograph. Gathering the Raman scattered light from the sample is the objective of the microscope. For our measurements, we mainly used the ×100 objective lens to observe the sample and pass the Raman scatter to the spectrograph. Its higher numerical aperture improves the lateral resolution.

Cette thèse est accessible à l'adresse : https://theses.insa-lyon.fr/publication/2023ISAL0011/these.pdf
© [A.J.E. N'Dohi], [2023], INSA Lyon, tous droits réservés

Detectors: Detectors are a key part of a Raman micro spectrometer. They convert photons into a useable electronic signature. The main detector inserted in our commercial Raman microscope is the Charge-Coupled Device (CCD). The CCD is a lattice of pixels that convert light to electronic signals. These pixels are then binned in a horizontal then vertical registers and the data is sent to a computer.

Acquisition electronics: allows the scanning the collection, and the processing of the data. For our measurements, all the collected data are treated by Wire 5.4 software provided by Renishaw company. With this software, we were able to remove the unwanted points (Cosmic ray for example), to fit the Raman spectra, to mask out unwanted data and many other operations such as normalization and baseline operation.

Calibration: In order to get reliable and precise results of the sample, the calibration of the wavelength axis is important. Even though modern microscopes provide continuous calibration for maximum convenience, recalibration is done by estimating a silicon standard. If the equipment is not calibrated continuously, recalibration should be done routinely. Before performing any measurements, our system has been calibrated using an internal silicon sample that is inserted in the microscope. The Raman value of 520.5 cm^{-1} of the silicon central peak has been considered as the calibration reference value.

Lateral and axial and resolution: Based on the diffraction limits theory, the intensity coming from a point observed through a microscope is spread over a so-called "Airy disk". The lateral resolution S is defined as the smallest distance between two points appearing distinctively on the microscope image. Experimentally, it determines the size of the analyzed point which can be called the laser spot size. According to the Rayleigh criterion [14], the lateral resolution can be expressed as:

$$S = \frac{0.61\lambda}{NA} \quad \textbf{(1)}$$

With λ the wavelength of the exciting laser and NA the numerical aperture of the microscope objective. For our measurements, we obtained a spatial resolution of 1µm.

For the axial resolution (Δz) or depth resolution: It has been reported to depend on the depth of field, which is half the width of the axial intensity profile. It can be expressed based on Born and Wolf approximation [15].

$$(\Delta z) = \frac{\lambda}{nsin\theta^2} \Rightarrow (\Delta z)_{n=1,air} = \frac{\lambda}{NA^2} \quad \textbf{(2)}$$

For our measument the Z resolution is of a few micrometers.

Cette thèse est accessible à l'adresse : https://theses.insa-lyon.fr/publication/2023ISAL0011/these.pdf
© [A.J.E. N'Dohi], [2023], INSA Lyon, tous droits réservés

The spectral resolution: It proves the accuracy of the Raman spectrometry. It depends on the laser wavelength and the groove density of the spectrometer's grating. When a grating with a higher groove density is used, the spectral resolution gets better and the Raman spectra become finer and sharper. Information on the Raman spectra and the shift of the band position are affected by the spectral resolution. Thus, when the spectral resolution is not good enough, the band position shift may not be detected correctly. The spectral resolution of our system during measurements was of $0.1cm^{-1}$.

2.1.4. RAMAN IMAGING

Raman imaging or mapping is widely used to characterize the distribution of components within a sample, but additionally it is sensitive to material concentration, phase, stress/strain, and crystallinity. With a single data set, a wide variety of Raman images can be created. In Raman imaging, a confocal microscope is combined with a spectrometer and a Raman spectrum is recorded at every image pixel. For the scope of this thesis, Raman mapping was performed in 2D configurations for GaN materials and devices through a confocal microscope with a standard confocality. In fact, 2D Raman visualizes the distribution of physical parameters such as doping homogeneity, carrier concentration , stress etc… , e.g. on the sample's surface or in a focal plane within the sample (x-y-plane), while 3D Raman imaging enables more complex of the components distribution in three dimensions (x-y-z-plane). This is particularly advantageous for the investigation of comprehensive in depth physical properties of the GaN sample as described above in the 2D case [15]. In order to generate 3D images, confocal 2D Raman images from different focal planes are acquired by automatically scanning through the sample along the z-axis. After data acquisition, evaluation and processing (Wire Software Renishaw model), the data from the image stack is used to generate the 3D image. In addition, from 2D and 3D imaging, physical properties of the materials such as: microstructure configuration, strain, stress and its distribution, carrier concentration and its distribution, structural defects identification and their distribution can be obtained depending on the Raman mode and the specific Raman geometry we used. Information about the extraction of these physical parameters and how their corresponding Raman signal has been processed using Raman mapping in 2D in the backscattering geometry will be presented largely in chapter 6.

2.1.5. RAMAN METROLOGY FOR GAN MATERIALS

Raman micro spectrometry is a very efficient tool to collect a wealth of information from materials as depicted in figure 2.4. Up to now, it is still widely used to investigate semiconductors in bulk, thin films, and device configurations. Typically, from Raman spectroscopy, information on the spatial

Cette thèse est accessible à l'adresse : https://theses.insa-lyon.fr/publication/2023ISAL0011/these.pdf
© [A.J.E. N'Dohi], [2023], INSA Lyon, tous droits réservés

distribution of physical quantities such as strains and stress, atomic fraction in mixed crystals, impurity concentrations, free carrier concentrations, local crystallographic orientation, and device temperature [16]. These physical parameters are useful to evaluate the quality and the performance of the device. Here, a number of them linked to the scope of our project will be tackled and their application in wide band gap material such as GaN will be exposed.

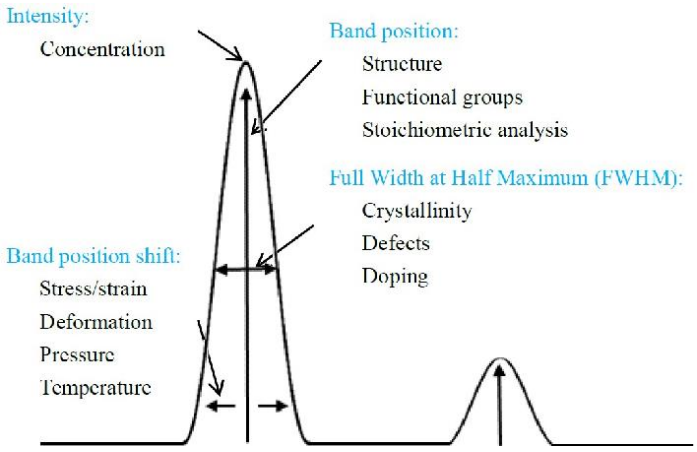

Figure 2. 4: Typical Information from material with Raman spectroscopy [16].

2.1.5.1. STRESS EVALUATION USING RAMAN SPECTRSOCOPY

The strain, stress and Raman shift are closely related. When the material is strained, the crystal structure (or energy level) of the material is altered, thus the Raman shift will be changed [17]. To illustrate the link between the stress and the shift on the Raman signal, the classical model based on spring of force constant $\boldsymbol{k}$ between two objects or atoms can be adopted [18]. Considering the system objects and spring and μ as the reduced mass of the two objects, the dynamic relation, the displacement X of one of the object can be expressed by the equation:

$$\mu\ddot{X} = kX \qquad \textbf{(1)}$$

With $\ddot{X}$ the acceleration of the object. In case of harmonic displacements, the frequency or the resulting peak position, of the normal modes could be written as $\omega = \sqrt{k/\mu}$ independently of the object or atom position. Basically, the spring that connects the two atoms is anharmonic and therefore the force it induces will be varying with any deformation or strain in the system. This variation can be quantified by the equation:

Cette thèse est accessible à l'adresse : https://theses.insa-lyon.fr/publication/2023ISAL0011/these.pdf
© [A.J.E. N'Dohi], [2023], INSA Lyon, tous droits réservés

$$\frac{\partial k}{\partial \varepsilon} = k^1 \varepsilon \quad \textbf{(2)}$$

With ε the applied strain. Considering this fact, the equation 11 will be modified as:

$$\mu \ddot{X} = (k + k^1 \varepsilon)\, X \ \textbf{(3)}$$

This equation stands for the effect of this anharmonicity and its solution accounts for the changes of the normal mode vibrations to be solved as a function of strain. Practically, phonon deformation potentials (PDP) dependence on materials are used as general approximation for the description of the modified spring constant that can be definitely written as follows:

$$k^1 = \mu \times f(p, q, r)$$

With p, q, and r as the PDP. This brings the equation (3) to be solved through a secular equation performed by Ganesan et al. [12]:

$$\begin{bmatrix} p\varepsilon_{11} + q(\varepsilon_{22} + \varepsilon_{33}) - \lambda & 2r\varepsilon_{12} & 2r\varepsilon_{13} \\ 2r\varepsilon_{21} & p\varepsilon_{22} + q(\varepsilon_{11} + \varepsilon_{33}) - \lambda & 2r\varepsilon_{23} \\ 2r\varepsilon_{13} & 2r\varepsilon_{23} & p\varepsilon_{33} + q(\varepsilon_{11} + \varepsilon_{22}) - \lambda \end{bmatrix} = 0 \ \textbf{(4)}$$

ε_{ij} are the strain tensor components and λj are the eigenvalues for phonon polarization modes j. The difference in frequencies of the Raman spectra with (ω_j) and without strain ($\omega_{o,j}$) can be correlated using these eigenvalues according to the relation:

$$\lambda_j = \omega_j^2 - \omega_{o,j}^2 \quad \textbf{(5)}$$

For biaxial strain, usually happening most in microelectronic power devices: $\varepsilon_{12} = \varepsilon_{23} = \varepsilon_{13} = 0$, and the secular equation becomes :

$$\begin{bmatrix} p\varepsilon_{11} + q(\varepsilon_{22} + \varepsilon_{33}) - \lambda & 0 & 0 \\ 0 & p\varepsilon_{22} + q(\varepsilon_{11} + \varepsilon_{33}) - \lambda & 0 \\ 0 & 0 & p\varepsilon_{33} + q(\varepsilon_{11} + \varepsilon_{22}) - \lambda \end{bmatrix} = 0 \ \textbf{(6)}$$

From this equation, the relation between the peak position shift and the stress can be obtained:

$$\omega_j - \omega_{0,j} = \alpha\sigma \qquad \textbf{(7)}$$

With α, a calibration constant or Raman stress factor and σ the stress. The equation (7) clearly displays that the stress sensitivity of the Raman signal comes from a change in the strength of the

Cette thèse est accessible à l'adresse : https://theses.insa-lyon.fr/publication/2023ISAL0011/these.pdf
© [A.J.E. N'Dohi], [2023], INSA Lyon, tous droits réservés

interatomic bonds or distance (spring) due to the response to an elastic deformation (strain). The change in the strength of the interatomic bond leads to the alteration of the resulting vibrational modes frequency felt during Raman scattering. Therefore, by probing Raman peak positions, the stress induced in the material can be quantified. For GaN bulk and epilayers, the stress quantification through Raman spectroscopy is done by analyzing the E_2^h mode because it is more sensitive to biaxial stress. At this mode, all atoms are vibrating in the xy plane. A shift of the E_2 phonon line is a linear function of the biaxial stress and can be expressed as:

$$\Delta\omega = K\sigma_{xx=yy} \quad \textbf{(8)}$$

Where Δω represents the Raman shifts variation of the phonon line ($\Delta\omega = \omega_{raman} - \omega_0$) and $\sigma_{xx=yy}$ is the element of stress tensor, and K is the pressure coefficient that varies depending on the stress applied. Its value (K= 2.56 GPa/cm^{-1}[19], 2.9 GPa/cm^{-1}[20], 4.2 GPa/cm^{-1} [21] to 6.2 GPa/cm^{-1} [22]) and the associate stress can be found in many literatures. As these values are scattered in the literatures, we have not computed quantitatively the stress value in this work but we just focused on the qualitative evaluation of the stress. Following the E_2^h peak position, the generated stress can be compressive when the peak shift is towards higher frequency zone and tensile when it is directed to the lower frequency zones (see figure 2.5)

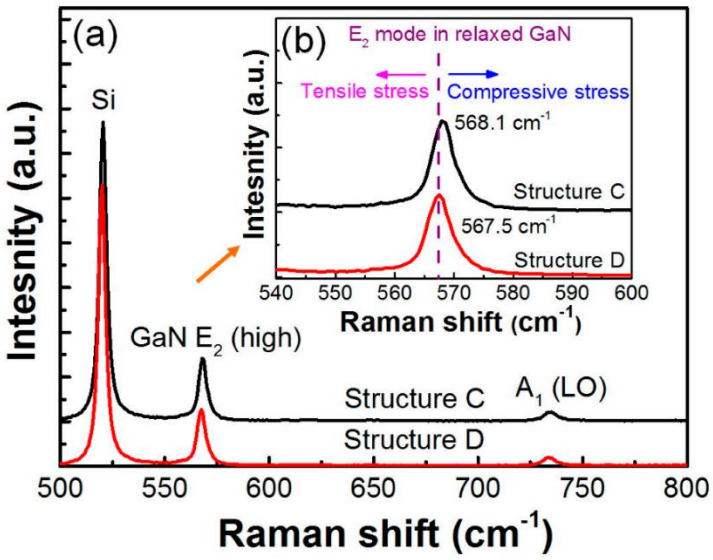

Figure 2. 5: (a) Raman spectra of structures A (black) and B (red) (b) Raman shift of E2 (high) [23].

Cette thèse est accessible à l'adresse : https://theses.insa-lyon.fr/publication/2023ISAL0011/these.pdf
© [A.J.E. N'Dohi], [2023], INSA Lyon, tous droits réservés

2.1.5.2. CARRIER CONCENTRATION AND MOBILTY DETERMINATION BY RAMAN SPECTROSCOPY

Carrier concentration and mobility are one of the main physical parameters that are capital for probing the performance of power electronic devices. Raman scattering is not limited to vibrational phenomena. It is also necessary for studying other excitations such as polaritons, plasmons, and electronic Raman Scattering in wide band gap materials and their polytypes. In polar semiconductors such as GaN, SiC, phonons and photons with approximately the same energy and wave vector may couple strongly. This kind of propagating excitation, called the polariton can no longer be seen as phonon or a photon only, and its dispersion is determined by the material dielectric constant. Azhnyuk et al. [24] investigated the effect of free electrons on the polariton dispersion curve and observed that for nitrogen-doped samples the polariton shift decreased with increasing the free charge carrier concentration. They called that excitation plasmariton because it comes from the interaction between plasmon and polariton. Klein et al. [25] observed in a heavily N-doped sample (6×10^{19} cm^{-3}) a non-symmetric broadening and a shift of the longitudinal optical (LO) phonon that they assigned to the overdamped coupling between LO phonon and plasmon modes [26]. The interaction between these two excitations occurs via their macroscopic electric fields when the frequency of a free-carrier plasma is close to that of the LO phonon. This interaction known as LOPC (Longitudinal Optical Phonon plasmon coupling) is widely used in Raman scattering to probe the carrier concentration and their mobility.

In general, the LOPC mode for semiconductors has two branches (L+ and L-), and their energies are given by the zeros of the real part of the total dielectric function. Three mechanisms generally contribute to the Raman scattering by the LOPC mode [27]: deformation potential (DP), electro-optical (EO) mechanisms and charge-density fluctuation (CDF). In semiconductors, such as GaN having a large band gap and a low carrier mobility the EO and DP mechanisms dominate the scattering process. Moreover, the lower-energy branch (L-) is not observed in the Raman spectra because of the strong damping (overdamping). Our goal is to exploit this shift in LPP mode frequency, known to reflect changes in the plasma frequency, to probe changes in the free-carrier density. The evolution of the LOPC mode with an increase of the carrier concentration can been in figure 2.6 from the reference [28].

Cette thèse est accessible à l'adresse : https://theses.insa-lyon.fr/publication/2023ISAL0011/these.pdf
© [A.J.E. N'Dohi], [2023], INSA Lyon, tous droits réservés

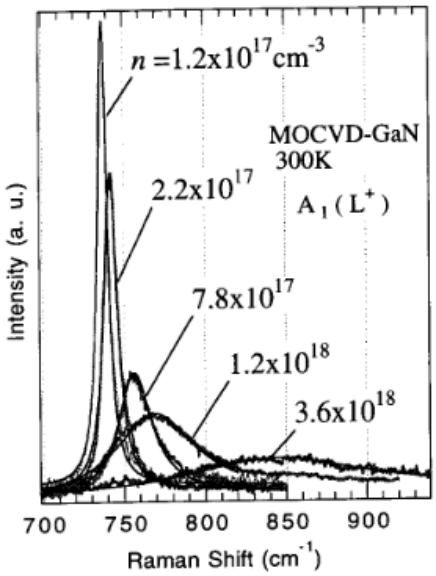

Figure 2. 6: LOPC mode evolution vs carrier concentration.

In literature, a simple harmonic oscillator model can be applied to describe the dielectric function of a coupled plasma-lattice system, from which the zeros define the coupled longitudinal mode [29]. The frequency-dependent dielectric function can be expressed:

$$\varepsilon(\omega) = \varepsilon_\infty \left[1 - \frac{\omega_L^2 - \omega_T^2}{\omega^2 - \omega_T^2} - \frac{\omega_P^2}{\omega^2}\right] \quad (1)$$

ω_L , ω_T are the vibration frequency of the longitudinal and transvers optic modes respectively. ω_P is the vibration frequency of free carrier that we also name as plasma frequency. It can be expressed as follow:

$$\omega_P^2 = \frac{4\pi n e^2}{\varepsilon_0 \varepsilon_\infty m^*} \quad (2)$$

Where n is the free-carrier density, ε_0 is the free-space permittivity, and m* is the effective mass of the free carrier. From the above expression, the carrier concentration can be computed. In literature, the evolution of the doping level vs LOPC mode as the free carrier concentration increases n $>$ 10^{17}cm^{-3} is not linear probably due to the strength of the interaction at this doping level see figure 2.7 [30]. Furthermore, in reference [31], the evolution of the doping level vs the free carrier density was found to be quasi linear for n < 10^{19}cm^{-3} via the equation: $n = 1{,}1.10^{17}(\omega_{L+} - \omega_{LO})^{0.764}$ with n the carrier concentration, ω_{L+} the frequency of the LOPC mode, and ω_{LO} the frequency of the uncoupled LO phonon ω_{LO} = 735 cm^{-1}. Here in the thesis, we probe that behavior when n<10^{17}cm^{-3}. The goal

Cette thèse est accessible à l'adresse : https://theses.insa-lyon.fr/publication/2023ISAL0011/these.pdf
© [A.J.E. N'Dohi], [2023], INSA Lyon, tous droits réservés

was to investigate that range of n-doping for GaN Schottky performance. The results can be found in chapter 5.

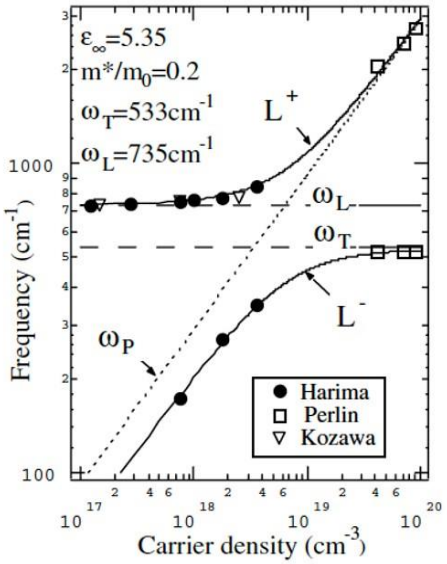

Figure 2. 7: LOPC mode vs carrier concentration for $\mathbf{n \geq 10^{17} cm^{-3}}$**.**

2.1.5.3. DISLOCATIONS IDENTIFICATION BY RAMAN SPECTROSCOPY

Wide band-gap semiconductors such as gallium nitride (GaN) has attracted considerable attention as next-generation power semiconductor materials because of high-temperature operation owing to its large band-gap and higher carrier mobility. Although hydride vapor-phase epitaxy (HVPE)-grown freestanding GaN substrates have become commercially available, the size is only 50 mm and their dislocation densities are still on the order of 10^6 cm^{-2}. These threading dislocations (TDs) are composed of screw dislocations (TSDs), edge dislocations (TEDs), and mixed dislocations (TMDs). The TSDs, TEDs, and TMDs have dislocations propagating to the c-axis with Burgers vectors of b = c [0001], a/3[11-20], and c [0001]+ a/3 [11-20], respectively. The images of the different types of dislocations can be found in chapter 1. It is important to characterize the TDs in GaN crystals because the device performance would be affected by their existence [32]. Several evaluation methods for TDs in GaN crystals are proposed, such as chemical etching, transmission electron microscopy (TEM) [33–34]. X-ray topography, [35] cathodoluminescence (CL) [36] and photoluminescence (PL) [37]. Among them, the chemical etching of GaN bulk crystals is commonly used: however, classification of the dislocations is relatively difficult because the shape of the etch pits depends on the etching conditions and crystal manufacturing methods [38]. TEM can be used to determine the Burgers vector of dislocations [39]. However, it is destructive and the sample must be a thickness of several 100 nm, which requires time. The X-ray spectroscopy is usually used as a nondestructive characterization

Cette thèse est accessible à l'adresse : https://theses.insa-lyon.fr/publication/2023ISAL0011/these.pdf
© [A.J.E. N'Dohi], [2023], INSA Lyon, tous droits réservés

method for determination of the direction of the Burgers vector of TMDs and TSDs in GaN crystals [40] but a synchrotron radiation facility is required to obtain clear contrast images. CL mapping measurements on the other hand, help identify the location of dislocations. However, they must be performed under vacuum conditions. Recently, the three-dimensional imaging of TDs in GaN films was visualized by two-photon excitation PL without any destructive preparations [41]. Now, the micro-Raman spectroscopy mapping is more seen as a nondestructive characterization method for evaluation of TDs in GaN [42]. In the commercially available GaN freestanding substrates, the densities and types of the TDs would vary between wafer venders. It is unrealistic to determine the direction and magnitude of Burgers vectors for all TDs by TEM. By analyzing the Raman mapping of the E_2 (high) peak shift within 0.1 cm^{-1} range, the density, direction, and magnitude of the edge and mixed component of the TDs can be observed and determined [43]. Below are the images of the identification of TDs using Raman mapping [44]. More of them will be presented in chapter 6 of the thesis under correlative analysis with cathodoluminescence images.

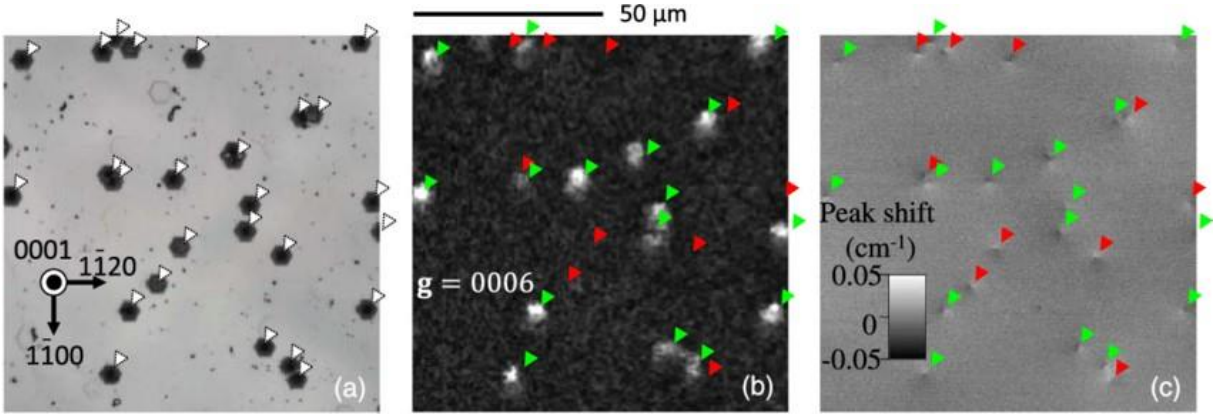

Figure 2. 8: (Color online) 100 × 100 µm2 area images of (a) etch pits, (b) X-ray topography taken along the g=0006, and (c) Raman mapping of the E2 (high) peak shift. The location of the etch pit are illustrated by dotted white triangles. The red and green triangles correspond to the TED and TMD, respectively.

2.2. CATHODOLUMINESCENCE (CL) METHOD

In this part, a brief general theory on the cathodoluminescence spectroscopy will be presented. In this thesis, the cathodoluminescence measurements have been performed in CHREA on GaN Schotttky diodes. The obtained data have been correlated with Raman spectroscopy to understand physical mechanisms in GaN materials and devices in chapter 6.

Cette thèse est accessible à l'adresse : https://theses.insa-lyon.fr/publication/2023ISAL0011/these.pdf
© [A.J.E. N'Dohi], [2023], INSA Lyon, tous droits réservés

2.2.1. PRINCIPLE OF CL MEASUREMENTS

Cathodo-Luminescence (CL) is defined as the emission of electromagnetic radiation as a result of electron bombardment. From this signal one may obtain information on the spatial dependence of luminescence at a sub-pm level and obtain a correlation between structural and optical properties. The cathodoluminescence apparatus is commissioned on the SEM microscope. In CL measurements, the material is exposed to an electron beam resulting in different processes at beam-material interaction. Among these processes, few generate electromagnetic radiation in visible spectral range and are called CL. When an incident electron beam energizes electrons in the ground state to higher energy states, they return to their ground state after their lifetime. When these energized electrons return to their ground state, they emit optical energy leading to fluorescence (see figure 2.9). CL imaging collects and measures the optical energy generated by the e-beam interaction with the material. By moving the incident e-beam, one can scan a pre-defined area of the material with a single-pixel resolution. The emission of light is highly dependent on the material on which electron beam is incident. In case of a GaN layer, no light is emitted when an electron beam is incident on dislocation or crystal defect [45].

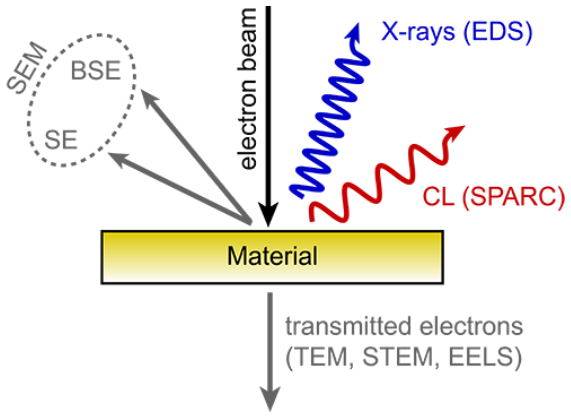

Figure 2. 9: Material analysis based on the incident electron beam.

2.2.2. STATE OF THE ART

CL spectroscopy can be done either at room temperature or at low temperatures. Although the measurements at low temperatures require more complicated experimental set-up, they allow the detection of excitonic transitions and infer relaxation mechanisms [46]. In literature, CL has been used to study structural and physical properties of materials. Zhaoying Chen et al [47] studied a quantitative defect analysis in MOCVD GaN-on-GaN using cathodoluminescence. They observed a strong CL

Cette thèse est accessible à l'adresse : https://theses.insa-lyon.fr/publication/2023ISAL0011/these.pdf
© [A.J.E. N'Dohi], [2023], INSA Lyon, tous droits réservés

intensity contrast that is caused by interfacial impurities at the GaN homoepitaxial interfaces. They also established through the analysis of the recombination mechanisms of electron beam induced non-equilibrium carriers, an analytical model to quantitatively determine the impurity concentration based on CL intensity. Carol Trager-Cowan et al [48] investigated the morphology of GaN thin films using catholuminescence, AFM and SEM. They managed to establish a comparative morphological and spectroscopic studies of GaN films grown on Al_2O_3, GaAs (111) on B and $LiGaO_2$ substrates. They clearly showed that the GaN/GaAs (111)B film exhibit the best surface uniformity and cleanest luminescence. Rosalia Delgado Carrascon et al [49] used CL spectroscopy to determine the band gap energy and get information about impurity incorporation. They mentioned that different energy levels in the band gap of GaN are generated by various point and extended defects such as vacancies and dislocations respectively. In another paper, they estimated from the respective CL maps and the XRD technique, the dislocation densities of both GaN substrate before growth and GaN regrown layer. They mentioned that some energy levels corresponding to strain fields induced by dislocations can be located very close to each other within the bandgap giving rise to non-radiative recombination processes which decrease drastically the CL intensity and hence appearing as dark areas [49]. These dark spots appear near the dislocation centers, which justifies their assignment to dislocations [50, 51]. Thi Huong Ngo et al [52] investigated cathodoluminescence and electrical properties of vertical GaN-on-GaN Schottky diodes with dislocation clusters. They mainly used CL measurements to observe the dislocation clusters in epilayers of the diodes. Their correlative study between CL and electrical measurements shows the role of the dislocations cluster on the performance of the diodes.

2.3. CONCLUSION

In this section, we gave the theoretical details on the physical characterization tools we used in this thesis. We presented the fundamental aspects of micro-Raman spectroscopy. We also presented the recent applications of micro-Raman spectroscopy on GaN material. In addition, we presented the cathodoluminescence spectroscopy as an additional characterization tool to probe the GaN material. We gave a state of the art on the recent applications of cathodoluminescence spectroscopy on GaN material.

Cette thèse est accessible à l'adresse : https://theses.insa-lyon.fr/publication/2023ISAL0011/these.pdf
© [A.J.E. N'Dohi], [2023], INSA Lyon, tous droits réservés

REFERENCES

[1] McCreery, R.L. “Raman Spectroscopy for Chemical Analysis”; Wiley-Interscience: Hoboken, NJ, USA, (2000).

[2] A. Smekal, Naturwissenschaften, "Zur quantentheorie der dispersion." Naturwissenschaften 11, no. 873-875.43, (1923).

[3] Vandenabeele, P.; Edwards, H. G. M.; Moens, L. Chem. ReV. (2007).

[4] Yoshikawa, M.; Ishida, H.; Ishitani, A.; Koisumi, S.; Inuzuka, T. Appl. Phys. Lett. (1991).

[5] Harris, D.C.; Bertolucci, M.D. “Symmetry and spectroscopy: An Introduction to Vibrational and Electronic Spectroscopy”, 1st ed; Oxford University Press: New York, NY, USA, (1978).

[6] Das, R.S.; Agrawal, Y.K. “Raman spectroscopy: Recent advancements, techniques and applications. Vib. Spectroscopy”, (2011).

[7] Mercier, B. Density fluctuations measurement by Rayleigh scattering using a single photomultiplier. Aiaa. J. (2018).

[8] D. A. Long, Raman Spectroscopy (McGraw-Hill, 1977).

[9] R. Loudon, “The Raman effect in crystals”. Advan. Phys. 13:423 (1964).

[10] Núria Domènech i Amador, “Phonons in III-nitride thinfilms, bulk and nanowires: a closer look into InN vibrational properties”, PHD thesis, Barcelona University (2015).

[11] H. Siegle, G. Kaczmarczyk, L. Filippidis, A. P. Litvinchuk, A. Hoffmann, and C. Thomsen, Phys. Rev. B 55, 7000 (1997).

[12] Davydov V Yu, Kitaev Yu E, Goncharuk I N, Smirnov A N, Graul J, Semchinova O, Uffmann D, Smirnov M B, Mirgorodsky A P and Evarestov R A 58 12 899–907, Phys. Rev. B (1998).

[13] V. Y. Davydov, Y. E. Kitaev et al., “Phonon dispersion and Raman scattering in hexagonal GaN and AlN”, Phys. Rev. B 58, 12899 (1998).

[13] L. Rayleigh, Investigations in Optics with special reference to the Spectroscope, Phil. Mag. 8 (1879).

[14] M. Born and E. Wolf, Principles of Optics, Pergamon Press, Oxford, 441 (1985).

[15] B. Prats Mateu, E. Harreither, M. Schosserer, V. Puxbaum, E. Gludovacz, N. Borth, N. Gierlinger, J. Grillari, Label-free live cell imaging by Confocal Raman Microscopy identifies CHO host and producer cell line. Biotechnology Journal (2016).

[16] Huang, Y.; Yu, P.; Charasse, M. N.; Lo, Y.; Wang, S. Appl. Phys. Lett. (1987).

[17] Yoshikawa, M.; Ishida, H.; Ishitani, A.; Koisumi, S.; Inuzuka, T. Appl. Phys. Lett. (1991).

Cette thèse est accessible à l'adresse : https://theses.insa-lyon.fr/publication/2023ISAL0011/these.pdf
© [A.J.E. N’Dohi], [2023], INSA Lyon, tous droits réservés

[18] Xu, Zongwei, Zhongdu He, Ying Song, Xiu Fu, Mathias Rommel, Xichun Luo, Alexander Hartmaier, Junjie Zhang, and Fengzhou Fang. "Topic review: application of Raman spectroscopy characterization in micro/nano-machining." Micromachines 9, no. 7, 361. (2018).

[19] J. M. Wagner and F. Bechstedt, Appl. Phys. Lett. 77, 346 (2000).

[20] Kuei-Ming Chen et al., Stress and Defect Distribution of Thick GaN Film Homoepitaxially Regrown on Free-Standing GaN by Hydride Vapor Phase Epitaxy, Japanese J. Appl. Phys. 49 (2010).

[21] Kisielowski C, Kruger J, Ruvimov S, Suski T, Ager J W III, Jones E, Liliental-Weber Z, Rubin M, Weber E R, Bremser M D and Davis R F Phys. Rev. B 54 17745, (1996).

[22] Kozawa T, Kachi T, Kano H, et al. Raman scattering from LO phonon-plasmon coupled modes in gallium nitride. J Appl Phys, (1994).

[24] Lin, Po-Jung, Ching-Ho Tien, Tzu-Yu Wang, Che-Lin Chen, Sin-Liang Ou, Bu-Chin Chung, and Dong-Sing Wu. "On the Role of AlN Insertion Layer in Stress Control of GaN on 150-mm Si (111) Substrate" Crystals 7, no. 5, 134. (2017).

[24] Amimoto, S.T.; Chang, D.J.; Birkitt. A.D. Stress Measurement in MEMS Using Raman Spectroscopy. In Materials and Device Characterization in Micromachining, Proceedings of SPIE on Micromachining and Microfabrication, Santa Clara, CA, USA, (1998).

[25] Thomas Beechem, Samuel Graham, Sean P. Kearney, Leslie M. Phinney, and Justin R. Serrano, Woodruff School of Mechanical Engineering Georgia Institute of Technology Atlanta, GA 30332 0405.

[26] S. Ganesan, A. Maradudin, and J. Oitmaa, Annals of Physics 56, 556-594 (1970).

[27] M. V. Klein, Light Scattering in Solids, edited by M. Cardona, (Berlin), 1975.

[28] Kozawa T, Kachi T, Kano H, et al. Raman scattering from LO phonon-plasmon coupled modes in gallium nitride. J Appl Phys, (1994).

[29] G. Irmer, V. V. Toporov, B. H. Bairamov, and J. Monecke, Phys. Status Solidi B 119, 595 ,(1983).

[30] Kozawa T, Kachi T, Kano H, Taga Y and Hashimoto M , J. Appl. Phys. 75, 1098–101, (1994).

[31] Wetzel C, Walukiewicz W, Haller E, Ager J III, Grzegory I, Porowski S and Suski T Phys. Rev. B 53, 1322–6, (1996).

[32] B. Kim, D. Moon, K. Joo, S. Oh, Y. K. Lee, Y. Park, Y. Nanishi, and E. Yoon, Appl. Phys. Lett. 104, 102101 (2014).

[33] Z. Liliental-Weber, Jpn. J. Appl. Phys. 53, 100205 (2014).

[34] D. Cherns, W. T. Young, J. W. Steeds, F. A. Ponce, and S. Nakamura, J. Cryst. Growth 178, 201 (1997).

[35] S. Sintonen, M. Rudzinski, S. Suihkonen, H. Jussila, M. Knetzger, E. Meissner, A. Danilewsky, T. O. Tuomi, and H. Lipsanen, J. Appl. Phys. 116, 083504 (2014).

Cette thèse est accessible à l'adresse : https://theses.insa-lyon.fr/publication/2023ISAL0011/these.pdf
© [A.J.E. N'Dohi], [2023], INSA Lyon, tous droits réservés

[36] Y. Yao, Y. Ishikawa, Y. Sugawara, D. Yokoe, M. Sudo, N. Okadaand, and K. Tadatomo, Superlattices Microstruct. 99, 83 (2016).

[37] T. Tanikawa, K. Ohnishi, M. Kanoh, T. Mukai, and T. Matsuoka, Appl. Phys. Express 11, 031004 (2018).

[38] J. L. Weyher, Superlattices Microstruct. 40, 279 (2006).

[39] D. Cherns, W. T. Young, J. W. Steeds, F. A. Ponce, and S. Nakamura, J. Cryst. Growth 178, 201 (1997).

[40] S. Sintonen, M. Rudzinski, S. Suihkonen, H. Jussila, M. Knetzger, E. Meissner, A. Danilewsky, T. O. Tuomi, and H. Lipsanen, J. Appl. Phys. 116, 083504 (2014).

[41] T. Tanikawa, K. Ohnishi, M. Kanoh, T. Mukai, and T. Matsuoka, Appl. Phys. Express 11, 031004 (2018).

[42] N. Kokubo et al., Appl. Phys. Express 11, 061002 (2018).

[43] N. Kokubo et al., Appl. Phys. Express 11, 111001 (2018).

[44] Kokubo, Nobuhiko, Yosuke Tsunooka, Fumihiro Fujie, Junji Ohara, Shoichi Onda, Hisashi Yamada, Mitsuaki Shimizu, Shunta Harada, Miho Tagawa, and Toru Ujihara. "Nondestructive visualization of threading dislocations in GaN by micro Raman mapping." Japanese Journal of Applied Physics 58, no. SC SCCB06, (2019).

[45] E. L. Boulbar, J. Priesol, M. Nouf-Allehiani, G. Naresh-Kumar, S.Fox, C.Trager-Cowan, A. Šatka, D. Allsopp and P. Shields, "Design and fabrication of enhanced lateral growth for dislocation reduction in GaN using nanodashes," Journal of Crystal Growth, vol. 466, pp. 30-38, (2017).

[46] P. Corfdir, J. Risti´c, P. Lefebvre, T. Zhu, D. Martin, A. Dussaigne, J. D. Ganière, N. Grandjean, and B. Deveaud-Plédran, Applied Physics Letters 94, 201115 (2009).

[47] Chen, Zhaoying, Yuxuan Zhang, and Hongping Zhao. "Quantitative defect analysis in MOCVD GaN-on-GaN using cathodoluminescence." Optics Express 28, no. 18 26651-26660 (2020).

[48] Trager-Cowan, Carol, P. G. Middleton, and K. P. O'Donnell. "The morphology and cathodoluminescence of GaN thin films." MRS Internet Journal of Nitride Semiconductor Research 1, no. 1, 1-6 (1996).

[49] Delgado Carrascon, Rosalia. "Epitaxial strategies for defect reduction in GaN for vertical power devices." PhD diss., Linköping University Electronic Press, (2022).

[50] V. Darakchieva, T. Paskova, P. P. Paskov, B. Monemar, N. Ashkenov, and M. Schubert, Phys. Status Solidi A 195, 516 (2003).

[51] T. Paskova, P. P. Paskov, V. Darakchieva, E. M. Goldys, U. Södervall, E. Valcheva, B. Arnaudov, and B. Monemar, Phys. Status Solidi C 0, 209 (2003).

[52] Ngo, Thi Huong, Rémi Comyn, Eric Frayssinet, Hyonju Chauveau, Sébastien Chenot, Benjamin Damilano, Florian Tendille, Bernard Beaumont, Jean-Pierre Faurie, Nabil Nahas, Yvon Cordier

Cette thèse est accessible à l'adresse : https://theses.insa-lyon.fr/publication/2023ISAL0011/these.pdf
© [A.J.E. N'Dohi], [2023], INSA Lyon, tous droits réservés

"Cathodoluminescence and electrical study of vertical GaN-on-GaN Schottky diodes with dislocation clusters." Journal of Crystal Growth 552, 125911 (2020).

Cette thèse est accessible à l'adresse : https://theses.insa-lyon.fr/publication/2023ISAL0011/these.pdf
© [A.J.E. N'Dohi], [2023], INSA Lyon, tous droits réservés

CHAPTER 3: ELECTRICAL CHARACTERIZATION METHODS

Electrical characterization is essential to investigate the electrical behavior of electrical devices. It gives relevant electrical information that helps to predict or diagnose the performance of devices through important parameters. The most useful parameters determined by electrical characterization techniques are: resistivity, carrier concentration, mobility, contact resistance, barrier height, ideality factor, series resistance, turn-on voltage etc. Here in this thesis, we used the current-voltage (I (V)), the capacitance-voltage (C (V)) as electrical characterization techniques. Due to the scope of the thesis, we will focus more on Schottky diodes; especially on GaN based vertical Schottky diodes electrical characterizations. The results of the electrical characterization on the Schottky diodes and the physical parameters extracted from the measurements will be presented in chapter 7 of this thesis.

3.1. SCHOTTKY DIODE

A Schottky diode (see the symbol in **figure 3.1)** is an important majority carrier device that is widely used in radio frequency (RF) applications. It possesses many similarities to the point-contact diode. Unlike conventional semiconductor diodes, which consist of a PN junction, a Schottky diode is a special type of diode with a very low forward-voltage drop, which are based on a metal-semiconductor junction. When current flows through a diode there is a small voltage drop across the diode terminals. A normal diode has between 0.7 and 1.7-volt drops, while a Schottky diode voltage drop is between approximately 0.15 and 0.45 volts [1]. This lower forward voltage requirement allows higher switching speeds and better system efficiency and therefore making it ideal for use in power-rectification and switching applications.

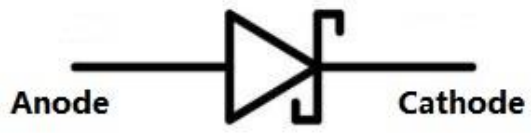

Figure 3.1: Symbol of a Schottky Diode [1].

Cette thèse est accessible à l'adresse : https://theses.insa-lyon.fr/publication/2023ISAL0011/these.pdf
© [A.J.E. N'Dohi], [2023], INSA Lyon, tous droits réservés

3.2. METAL SEMI CONDUCTOR CONTACTS

The metal-semiconductor contact is a vital link between the semiconductor and the outside world. The quality of metal-semiconductor (MS) contact is essential for the performance of various semiconductor devices and integrated circuits and therefore plays a major role in solid state devices. An ideal metal-semiconductor (MS) contact presents the following characteristics: (1) the metal and semiconductor are supposed to be in a very close contact, i.e., no interfacial layer exists between the components. (2) There are no intermixing of the metal and semiconductor (3). There are no surface charges existing at the metal semiconductor interface [2]. During the fabrication process of semiconductor devices, two types of metal-semiconductor contacts need to be set up the Schottky or (rectifying) contacts and the ohmic or (non-rectifying) contacts. A Schottky barrier contact or the rectifying MS contact is an important step and can be found in a number of device structures. A Schottky barrier contact shows an asymmetrical current-voltage (I-V) characteristic when the bias of the externally applied voltage to the contact is changed. Meanwhile, the ohmic or non-rectifying contact shows linear I-V characteristics regardless of the polarity of the bias voltage applied.

3.2.1. SCHOTTKY BARRIERS

Metal-semiconductor (MS) interfaces are essential for all semiconductor electronic and optoelectronic devices. One of the most interesting properties of a MS interface is its Schottky-barrier height (SBH), which is a measure of the difference of the energy levels for majority carriers across the MS interface. The SBH controls the electronic transport across MS interfaces and is, therefore, crucial to the successful operation of any semiconductor device [3] especially in GaN devices in our case. The Schottky barrier can also be used to study the bulk defects and interface properties of a metal-semiconductor system [4]. Thus, this section will describe the physics underlying the MS contacts.

The first-order theory of the formation of a Schottky barrier (SB) is the view attributed to Walter Schottky himself originally and to Neville Mott [5, 6] as well. The Schottky-Mott theory proposes that the SBH between a metal with a work function of Φ_m and a semiconductor with an electron affinity of χ_s should be:

$$\Phi_B = \Phi_m - \chi_s \quad (1)$$

Where Φ_B denotes the SBH measured on an n-type semiconductor. In the absence of interaction, both the metal and the semiconductor are electrically isolated from each other. The metal work function Φ_m is defined as the minimum energy required to raise an electron from the metal surface into free

Cette thèse est accessible à l'adresse : https://theses.insa-lyon.fr/publication/2023ISAL0011/these.pdf
© [A.J.E. N'Dohi], [2023], INSA Lyon, tous droits réservés

space. Each metal has a constant metal work function. The work functions of some metals are given in Table 1.

Table 3. 1: Work Function of some Metals [4].

Metal	Work function (eV)	Metal	Work function (eV)
Al	4.3	Ru	4.7
Ti	4.33	Rh	4.98
V	4.3	Hf	3.9
Cr	4.5	Ta	4.25
Mn	4.1	W	4.55
Fe	4.7	Re	4.96
Co	5	Os	4.83
Ni	5.15	Ir	5.27
Nb	4.3	Au	5.1
Mo	4.6	Pd	5.12
Ag	4.26	Pt	5.65

The work function (Φ_s) of a semiconductor material is the energy difference between the vacuum level and the Fermi energy level. The semiconductor work function (Φ_s), is composed of two distinct parts that can be expressed as:

$$\Phi_s = \chi + (E_C - E_F)_{FB} \quad (2)$$

Where χ is the electron affinity, and is given by $\chi = (E_0 - E_C)_{surface}$. [4]

The electron affinities of several semiconductors are shown in Table 3.2

Cette thèse est accessible à l'adresse : https://theses.insa-lyon.fr/publication/2023ISAL0011/these.pdf
© [A.J.E. N'Dohi], [2023], INSA Lyon, tous droits réservés

Table 3. 2: Electron affinity of some semiconductors [7].

Semiconductors elements	Electron affinity (eV)
Ge (Gemanium)	4.13
Si, (Silicon)	4.01
GaAs, (Gallium Arsenide)	4.07
GaN, (Gallium Nitride)	4.01
3C-SiC	3.83
4H-SiC	3.24
6H-SiC	3.30

Figure 3.2 shows energy band diagrams for a metal and n-type semiconductor system after contact formation. The work function of the semiconductor (Φ_s) is less than that of the metal (Φ_m). That is the essential condition for the formation of Schottky barriers between a metal and a n-type semiconductor. Figure 2a highlights the condition when the metal comes into contact with the semiconductor. Since the Fermi level of the semiconductor is above that of the metal, the system is not in equilibrium. For the system to be under equilibrium, the Fermi energy level must be the same throughout the structure. Consequently, after the contact formation, electrons from the semiconductor will flow into the lower energy states of the metal. The loss of electrons from the semiconductor induces a surface depletion region and results in the potential barrier seen by the electron that increases from the semiconductor to the metal. This situation will go on until the two Fermi levels of the metal and the semi-conductor match respectively.

Cette thèse est accessible à l'adresse : https://theses.insa-lyon.fr/publication/2023ISAL0011/these.pdf
© [A.J.E. N'Dohi], [2023], INSA Lyon, tous droits réservés

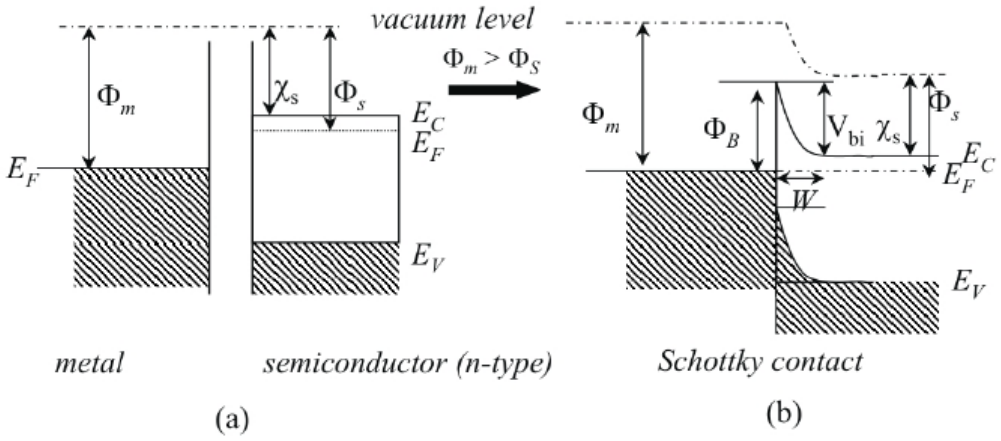

Figure 3.2: Energy band diagram for a metal-semiconductor (n-type) contact, in the case $\Phi_m > \Phi_s$ before (a) and after (b) they are brought into contact, showing the formation of a rectifying contact with a Schottky barrier height Φ_B [8].

The net equilibrium band diagram for an ideal metal to n-type semiconductor contact is shown in Figure 3.2.b. The barrier height for an ideal metal-semiconductor Schottky contact is equal to the difference between the work function of a metal and the electron affinity of a semiconductor. In other words, it is the potential barrier seen by the electrons in the metal trying to move to the semiconductor. For a metal/n-type semiconductor Schottky contact, this is expressed in equation 1. The barrier seen by the electrons in the conduction band trying to move into the metal is known as the built-in potential and is denoted by V_{bi} and is given by:

$$V_{bi} = \Phi_B - \Phi_s \quad (2)$$

However, in many practical cases, a thin interfacial oxide layer is formed between the semiconductor and the metal. As a result, the ideal situation shown in Figure 3.2b can never be reached. Figure 3.3 presents the practical contact with an interfacial layer of usually 10-20 A° thick. As a result, the barrier presented to electrons by this layer is very narrow and the electrons can tunnel through it easily.

Cette thèse est accessible à l'adresse : https://theses.insa-lyon.fr/publication/2023ISAL0011/these.pdf
© [A.J.E. N'Dohi], [2023], INSA Lyon, tous droits réservés

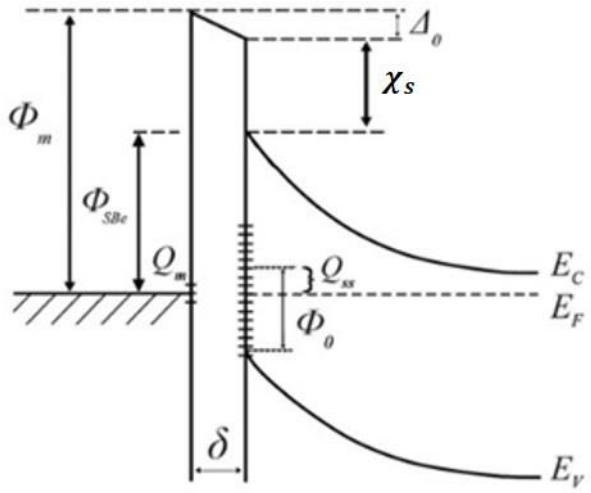

Figure 3.3: Energy band diagram of a contact between a metal and an n-type semiconductor with interface states in the band gap at the semiconductor surface. The charge Q_{ss} in the interface states creates a dipole over a distance d that lowers the barrier height by Δ_0 [4].

When a forward bias voltage $V_A > 0$ is applied to the Schottky contact, electrons in the semiconductor are attracted towards the metal. The Fermi level of the metal is lower than the Fermi level of the semiconductor. As a result, the barrier seen by the electrons in the semiconductor gets reduced and therefore there is a net flow of electrons from the semiconductor to the metal. Increasing the forward bias voltage V_F leads to a rapidly rising forward bias current, since an exponentially increasing number of electrons from the semiconductor are able to surmount the surface barrier (Figure 3.4a). On the other hand, when a reverse bias $V_A < 0$ is applied as shown in Figure 3.4c, the Fermi level of the metal gets above that of the semiconductor and consequently, the flow of electrons from the semiconductor to the metal is blocked. However, some electrons will be able to overcome the barrier while the associated reverse-bias current is small. Since the barrier is the same for all reverse bias, the reverse current is expected to be constant. The general form of the I-V characteristics of the phenomenon described above is also shown below the figure 3.4d.

Cette thèse est accessible à l'adresse : https://theses.insa-lyon.fr/publication/2023ISAL0011/these.pdf
© [A.J.E. N'Dohi], [2023], INSA Lyon, tous droits réservés

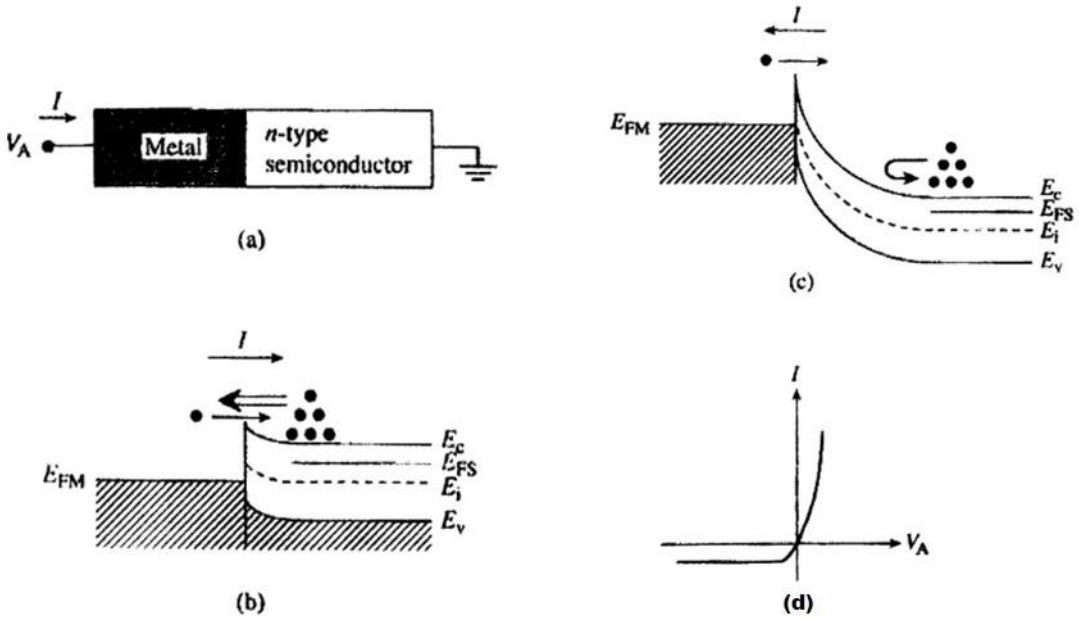

Figure 3.4: Schottky diode behavior under a given bias voltage. (a) Metal-semiconductor (MS) contact under bias. (b) MS contact behavior under positive bias. (C) MS contact behavior under reverse voltage. (d) General I(V)characteristics described in b and C.

In literatures, Schottky barrier contacts on GaN using with different metals have been reported so far. This includes the metals Pt, Pd, Au, Ni ,Re, Ag [9,10,11,12,13,14]. Figure 3.5 gives a summary of reported barrier heights plotted against the work function of the metal from various sources. The data is scattered due to the difference in the ways of metallization and the GaN crystalline quality. The barrier heights obtained by current-voltage (I-V) and capacitance-voltage (C-V) methods differed in value due to image force lowering. The typical values of the barrier height for the metals were 1.5 eV for Pd, [15], 1 eV for Pt [16], 0.9-1.15 eV for Au [17] 0.66-0.99 eV for Ni [9]. The influence of thermal treatments to the Schottky diodes on GaN were also investigated by many research groups. The indium tin-oxide Schottky contacts on n-GaN barrier height of 0.95 eV after annealing at 600°C. The Re [14] Schottky contacts reported a barrier height of 1.06 eV and did not degrade upon annealing until 700°C for 10 min. While the characteristics of other Schottky diodes were reported to degrade after a mild thermal treatment as low as 300 °C for Pd [18] 400°C for Pt, [19] 575°C for Au [20] and 600°C for Ni [21].

Cette thèse est accessible à l'adresse : https://theses.insa-lyon.fr/publication/2023ISAL0011/these.pdf
© [A.J.E. N'Dohi], [2023], INSA Lyon, tous droits réservés

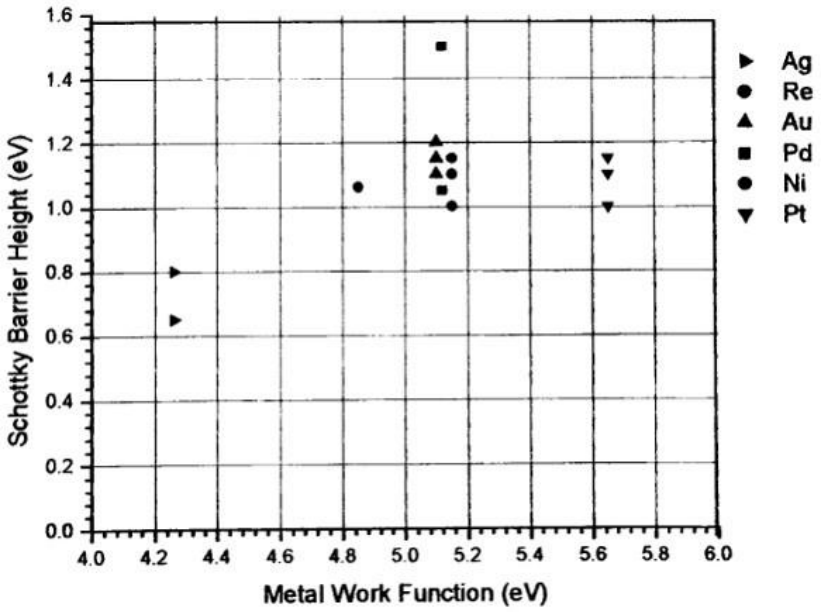

Figure 3.5: Reported Schottky barrier heights versus metal work function of metals [4] on GaN.

3.2.2. OHMIC CONTACT

An ohmic contact is a metal contact to a semiconductor with a very small contact resistance compared to the bulk of the semiconductor. They are essential for extracting electrical characteristics of a semiconductor device and is considered an extremely important process step for fabricating high-performance semiconductor devices and integrated circuits. In other words, an ohmic contact is a non-rectifying contact in which the current-voltage relation under reverse and forward bias conditions is linear and symmetrical. Typical I-V characteristics of an ohmic contact is shown in Figure 3.6.

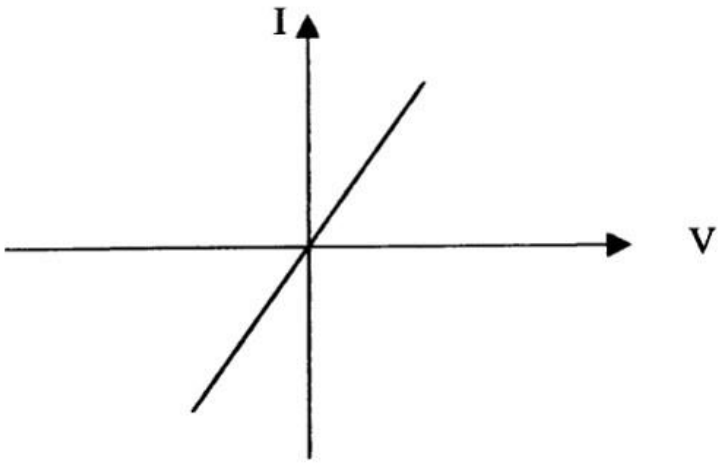

Figure 3.6: I (V) curve for the ohmic contact structure.

Cette thèse est accessible à l'adresse : https://theses.insa-lyon.fr/publication/2023ISAL0011/these.pdf
© [A.J.E. N'Dohi], [2023], INSA Lyon, tous droits réservés

The energy band diagram for a metal and semiconductor with $\Phi_m < \Phi_s$ is shown in Figure 3.7. It is clearly seen that there is no barrier of any kind for electrons to flow from the semiconductor to the metal. Thus, even when a small forward voltage ($V_A > 0$) is applied to the metal-semiconductor contact, it gives rise to a large forward bias current. In the reverse bias condition ($V_A < 0$), a small barrier is encountered by the electrons flow, from the metal to the semiconductor, but the barrier essentially vanishes if the reverse bias exceeds a few tenths of a volt. Therefore, large reverse currents are expected at relatively small reverse biases. In conclusion, MS contact formed from a metal and an n-type semiconductor will be rectifying if $\Phi_m > \Phi_s$ and ohmic if $\Phi_m < \Phi_s$.

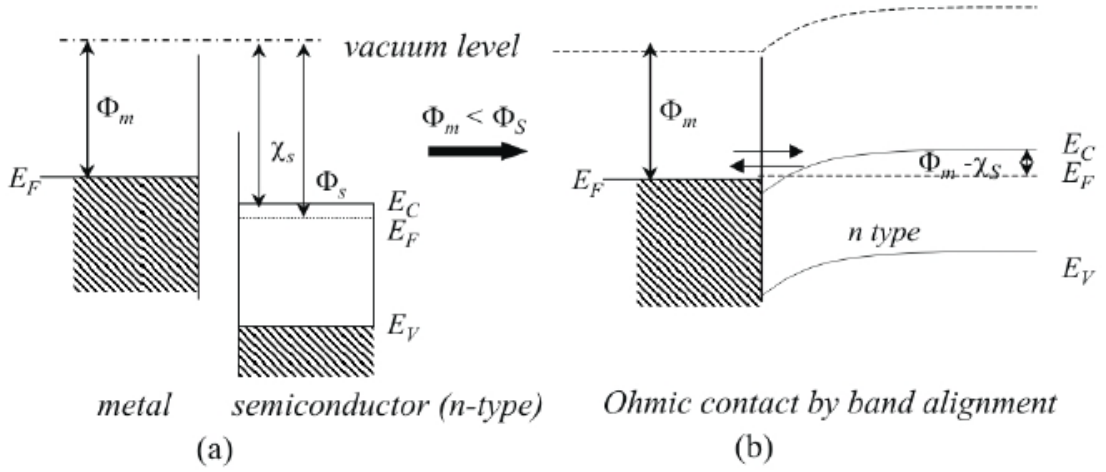

Figure 3.7: Energy band diagram for a metal-semiconductor (n-type) contact, in the case Φm <Φ s before (a) and after (b) they are brought into contact. In this case, ohmic contact formation occurs by band alignment [8].

For nitrides devices, there is a problem in the development of low resistance ohmic contacts due to their wide band gaps. In order to achieve high-performance GaN devices, reliable ohmic contacts are necessary and various combinations of metals have been investigated in literature.

The commonly used ohmic contact to n-GaN is the combination of Ti/Al metallisation. In most cases, a TiN layer was formed as an interface layer and helped in the formation of a low resistance ohmic contact. Researchers have suggested that the formation of the nitride layer through the reaction with GaN causes N vacancies which in turn resulted in the doping of the GaN and thus increased the carrier transport by tunneling. Ultra-low resistive ohmic contacts on n-GaN [23] was reported using Si implantation. Si was implanted at a doping density of 4×10 cm^{-3} to decrease the contact resistance of the contact. Ti/TiN and Zr/ZrN ohmic contacts presents a thermally stable contact at 600°C and also provided a smooth surface morphology.

Cette thèse est accessible à l'adresse : https://theses.insa-lyon.fr/publication/2023ISAL0011/these.pdf
© [A.J.E. N'Dohi], [2023], INSA Lyon, tous droits réservés

Table 3. 2: summarizes recent reports of ohmic contacts on n-GaN [22].

Metallization (nm)	Annealing Conditions	n-concentration(cm^{-3})
Ti/Al/Ni/Au (15/220/40/50)	900°C, 30 sec	$4x10^{17}$
Ti/Al (20/100)	900°C, 30 sec	10^{17}
Ti/Al (35/115)	600°C, 15sec	$5x10^{17}$
Ti (20)	975°C, 30 sec	$5x10^{17}$
Ti/TiN (5/200)	800°C, 60 sec	$7x10^{17}$
Ti/Ag (15/150)	No anneal	$1.7x10^{19}$
Ti/Ni (5/25)	1040°C, 30 sec	$1x10^{18}$
Ti/Au (3/300)	No anneal	$4x10^{20}$
Ti/Pd/Ni (5/5/25)	990°C, 20 sec	$1x10^{18}$
TiN (200)	800°C, 60 sec	$7x10^{17}$
Al (150)	600°C, 60-480sec in Ar/H_2	$7x10^{17}$
Al (250)	No anneal	$5x10^{19}$
W (50)	600-1000°C, 60sec	$1.5x10^{19}$
Zr/ZrN (20/80)	1000°C, 60sec	$2x10^{18}$
Pd/Al (12.5/100)	650°C, 30 sec	$2.8x10^{17}$
Ta/Al (35/115)	600°C, 15sec	$7x10^{17}$

Ti/Al/Ni/Au combination exhibited better surface morphology than the Ti/Al contact. Tungsten (W) contact was found to produce low resistance ohmic contacts to n-GaN with less interaction between the semiconductor and the metal till 800°C [24]. Thus, for high temperature electronic device applications, refractory metal contacts like W is preferred.

Cette thèse est accessible à l'adresse : https://theses.insa-lyon.fr/publication/2023ISAL0011/these.pdf
© [A.J.E. N'Dohi], [2023], INSA Lyon, tous droits réservés

3.2.3. SCHOTTKY DIODE FABRICATION

In this work, the studied GaN-on-GaN Schottky diodes have been developed and provided by CRHEA (Centre de Recherche sur l'Hetero-Epitaxie). Standard ultraviolet-photolithography [25], e-beam evaporation, lift-off, and reactive ion etching (RIE) are used for the fabrication of Ni frames and the SBDs, as described in figure 3.8. On the front side of the GaN wafer, 40 nm thick Ni frames are first deposited. Before fabrication of the metal contacts, the virtual locations of diodes are determined within the Ni frames and shown by using blue circles figure 8a. The fabricated diodes are of 200 µm, 100 µm, 50 µm (high) and 50 µm (low) wide (diameter). This technique allows us to inspect the arrangement of dislocations in the GaN layers before the fabrication of metal contacts. For the proposed high quality Schottky diodes, a clean contact between metal and semiconductor is required. Therefore, the Ni/Au contacts are evaporated before making the mesa isolation in order to limit as much as possible parasitic contaminations at the interface between Ni and the GaN epilayer. Inside the Ni frames, the circular Ni/Au (20/200 nm) Schottky contacts are deposited, followed by an additional 200 nm Au pad at the center of the diodes to facilitate the electrical contact with needle probes figure 8c. Then the diodes are isolated by mesa etching with an etching depth of 400 nm using $Cl_2/Ar/CH_4$ based RIE (Reactive Ion Etching). The mesa etching was performed using an additional lithography step with another mask-set. In this mask-set each mesa pattern is wider than the Schottky contact by 10 µm. Finally, Ti/Al/Ni/Au (30/180/40/200 nm) stacks are deposited at the backside of the n+-GaN substrate to make Ohmic contacts Figure 8b.

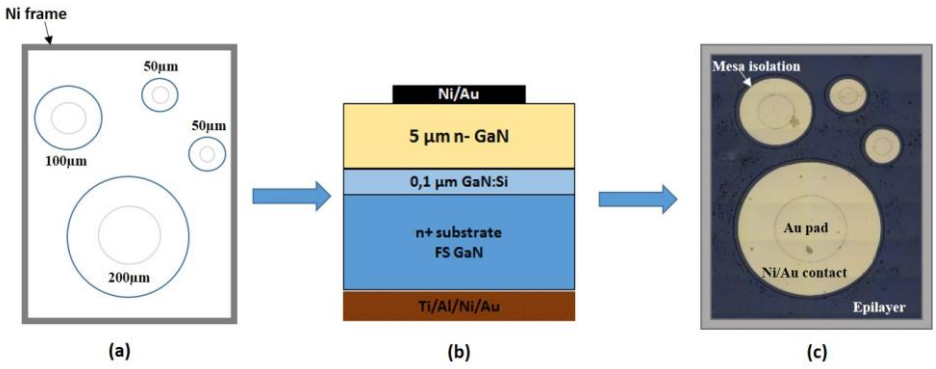

Figure 3.8: (a) Cross section of the mask design before metallization. (b) Cross section of the vertical GaN Schottky diodes. (c) Optical image of the diodes after metallization. Scale bar for the image in figure c is 100µm.

Cette thèse est accessible à l'adresse : https://theses.insa-lyon.fr/publication/2023ISAL0011/these.pdf
© [A.J.E. N'Dohi], [2023], INSA Lyon, tous droits réservés

3.3. ELECTRICAL CHARACTERIZATION

3.3.1. CARRIERS TRANSPORT IN SCHOTTKY DIODES

The current flow through a Schottky contact can be described by well-known Thermionic Emission (TE) theory. The current-voltage I (V) relationship of Schottky diodes is given by [26]:

$$I = I_0 \exp\left(\frac{qV}{nkT}\right)\left[1 - \exp\left(\frac{-qV}{kT}\right)\right]$$

With $I_0 = AA^*T^2\exp(\frac{-q\Phi_B}{kT})$

The barrier height Φ_B can be calculated from I_0 using: $\Phi_B = \frac{kT}{q}\ln(\frac{AA^*T^2}{I_0})$

The quantities A, A*, T, k, and q are the diodes area, the effective Richardson's constant of 26.4 A cm^{-2} K^{-2} for n-GaN [27], the temperature is given in Kelvin, the Boltzman constant and the electric charge, respectively. The ideality factor (n) from Eq. (1) for ($V \geq 3$ kT/q) represents the deviation of the ideal TE current transport mechanism. It is usually extracted from the slope of the I (V) curve.

$$n = \frac{q}{kT}\left(\frac{dV}{dlnI}\right)$$

Typical I-V characteristic of a Schottky diode in different scale is:

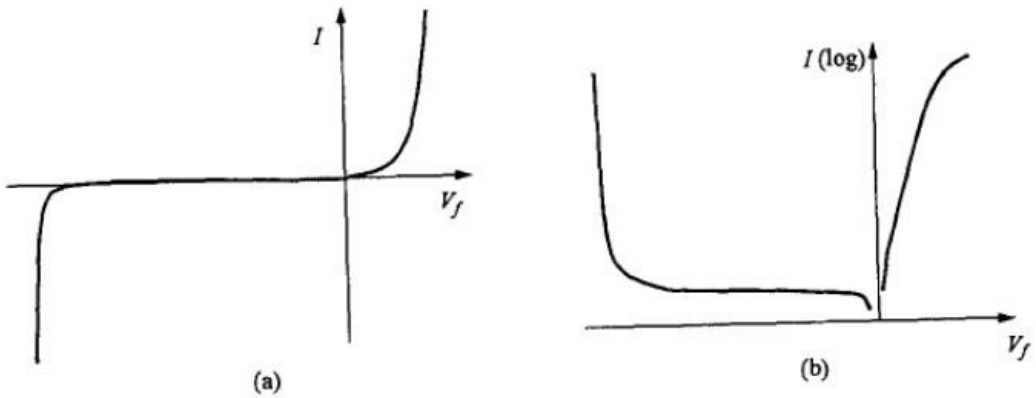

Figure 3.9: (a) is plot in linear scale; (b) is plot in log scale [28].

Cette thèse est accessible à l'adresse : https://theses.insa-lyon.fr/publication/2023ISAL0011/these.pdf
© [A.J.E. N'Dohi], [2023], INSA Lyon, tous droits réservés

3.3.2. CURRENT –VOLTAGE I (V) MEASUREMENTS

Current-voltage measurement is a necessary tool to characterize the performance of the devices and to extract parameters such as Schottky barrier height, ideality factor and series resistance. The principle is simple: voltage is applied to the device, and the passing through current is measured. Here we used low field I-V measurements because low field I-V system has a good accuracy to detect small currents. Figure 3.10 shows the low field I-V measurement system, which comprises of a Keithley 2410 source measure unit (SMU) and a probe station. It can provide a voltage up to 1100 V and measure a current up to 1A. All of Keithley's source measure unit (SMU) instruments deliver voltage and measure the current of the device under test. All are fully programmable instruments that can stand alone as complete source, measurement, and automation solutions. They are also easy to integrate into larger systems. Keithley's SMU instruments are faster, easier to use, and more economical than using individual power supplies and measurement instruments that are harnessed together. Additionally, they provide more accurate and repeatable results Keithley's SMU instruments are ideal for production and automation, yet precise and sensitive enough for laboratory applications.

Cette thèse est accessible à l'adresse : https://theses.insa-lyon.fr/publication/2023ISAL0011/these.pdf
© [A.J.E. N'Dohi], [2023], INSA Lyon, tous droits réservés

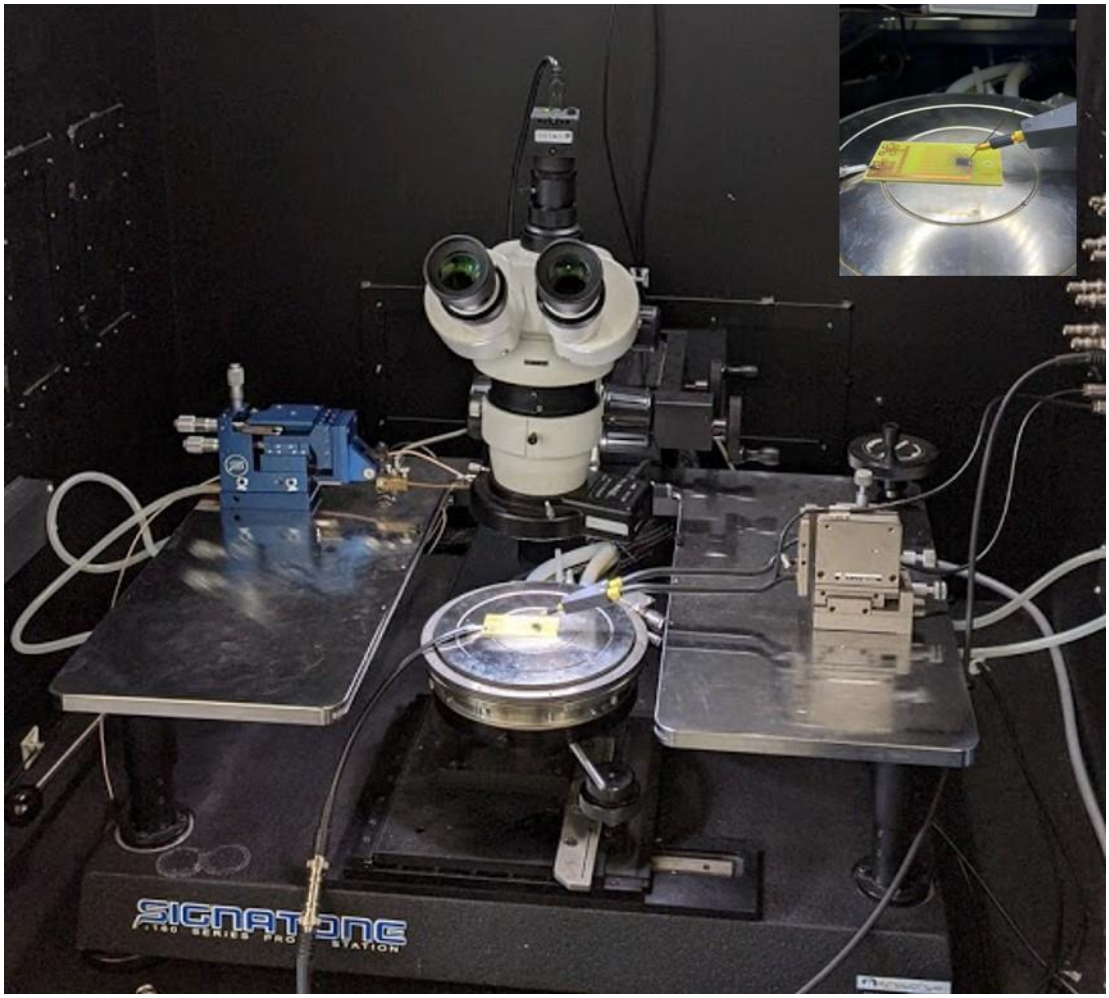

Figure 3.10: I (V) measurement station. The insert is the zoom of device under test.

In principle, SMU instruments can be used as stand-alone constant voltage or constant current sources and as stand-alone voltmeters or ammeters. However, their real strength is their ability to simultaneously source and measure applying voltage to a device under test (load) and measuring the current flowing through it, or supplying current to a load and measuring the voltage drop across it. The SMU instrument topology (Figure 3.10) protects the device under test (DUT) from damage due to accidental overloads, thermal runaway, and other problems. Both the current and voltage source are programmable with readback to maximize device measurement integrity if the readback reaches a programmed compliance limit, then the source is clamped at the limit, providing fault protection. Keithley's SMU instruments are core instruments for I-V characterization tests. Their ability to source voltage while simultaneously measuring current or source current while simultaneously measuring voltage can be combined with both DC and sweep operations to perform measurements such as forward voltage (VF), reverse leakage, and reverse breakdown voltage (BV) without changing a single connection to the device under test. A SMU instrument can store data from a sweep in its buffer, thus

Cette thèse est accessible à l'adresse : https://theses.insa-lyon.fr/publication/2023ISAL0011/these.pdf
© [A.J.E. N'Dohi], [2023], INSA Lyon, tous droits réservés

reducing data transfer time to a computer. A family of curves could also be produced using pulse-sweeps to reduce power dissipation within a device.

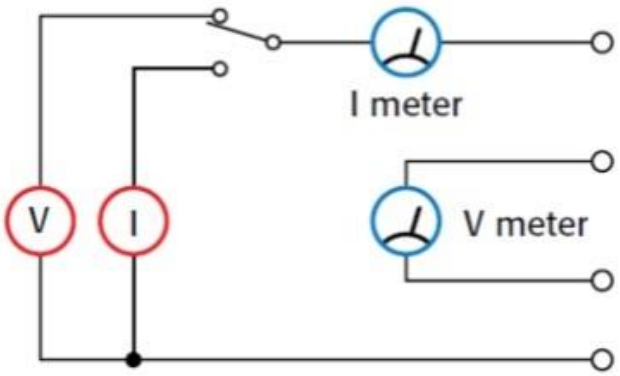

Figure 3. 1: Basic SMU instrument topology [29].

Figure 3.12 illustrates various hardware and software solutions for I-V characterization. In the first example, 2400 series Source Meter SMU instruments is connected to a PC. This is similar to our connection system.

Cette thèse est accessible à l'adresse : https://theses.insa-lyon.fr/publication/2023ISAL0011/these.pdf
© [A.J.E. N'Dohi], [2023], INSA Lyon, tous droits réservés

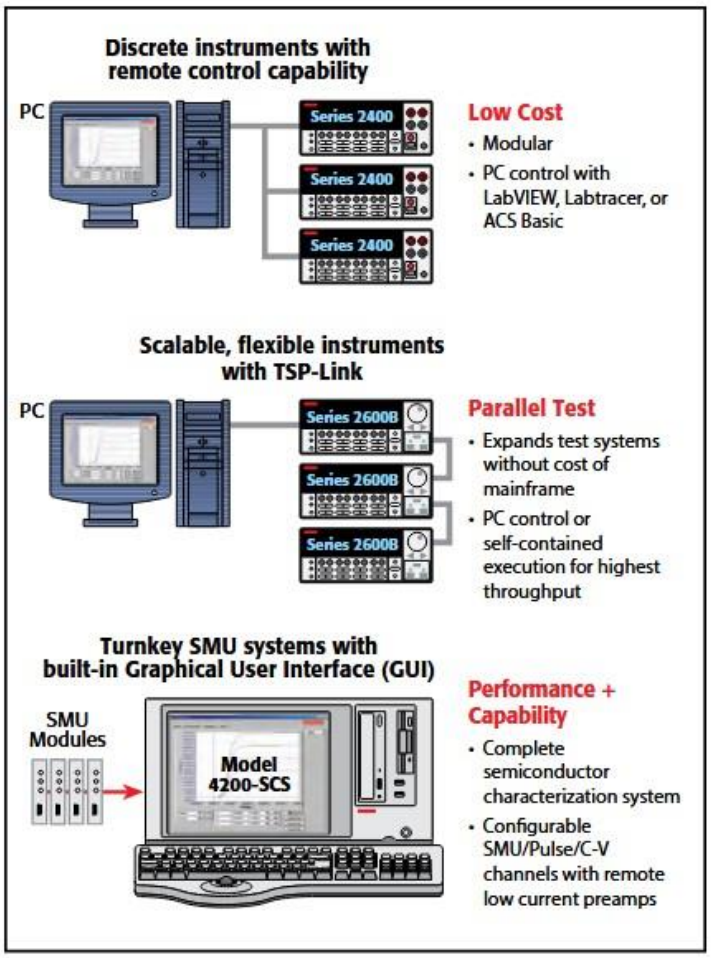

Figure 3.2: Examples of I-V characterization solutions [30].

I(V) measurement description : The GaN wafer containing the vertical Schottky diodes has been mounted on a printed circuit board (PCB) before practical electrical measurements (see figure 10). Then, under a semi - automatic I-V probe station, the Au pad of the metallization helps to the connection of the anode. As the cathode, the backside of the diodes is directly stuck and linked to the PCB with some gold lines and we wired it with a coaxial cable. All the electrical connection was done through a combination of coaxial-triaxial cables to ensure better conductivity. Before any measurements:

- The semi-automatic table with a chuck needs to be set well via a software
- A vacuum pump needs to be active to maintain the wafer on the chuck and avoid its sudden movement during measurement.

After that, we first measured the forward characteristics by setting the compliance to 10mA and 1V for the forward current and voltage bias respectively. As for the reverse characteristics, we first turned off the lighting system in the station to minimize the noise during measurement due to the sensitivity of

Cette thèse est accessible à l'adresse : https://theses.insa-lyon.fr/publication/2023ISAL0011/these.pdf
© [A.J.E. N'Dohi], [2023], INSA Lyon, tous droits réservés

the GaN material with light. Secondly, we set the reverse compliance to 100µA and -150V for the current and the voltage bias respectively in order to avoid premature burning of the diodes since the diode periphery is not fully well protected except a part from the presence of the mesa. The software (CaractIV) for the data readout has been made in our lab based on a LabVIEW program.

3.3.3. CAPACITANCE–VOLTAGE (C–V) MEASUREMENTS

C–V measurements yield accurate information about doping concentrations of majority carriers as a function of distance (depth) from the junction. C–V measurements can quantitatively describe the free carrier concentrations together with information about traps. Defects appearing as traps at energies deep within the forbidden gap of a semiconductor can add or remove free carriers. C–V profiling to determine the doping profile of the mobile majority carriers in a semiconductor is a powerful quantitative technique. Some precautions must be taken, especially in dealing with multiple-layered structures such as high-to-low doping levels, quantum wells, and the presence of traps. In principle, the capacitance at a p–n or MS junction depends upon the properties of the charge-depletion layer formed at the junction. The depletion region is near the p–n junction and is “depleted” of free carriers (Fig. 3.13a) due to the drift field (Fig. 3.13b) required to maintain charge neutrality. The fluctuations of charge in the depletion region gives rise to capacitance. For C-V measurements, many probing procedures can be used: mercury probe contacts, electrochemical profiling, classical tip probe, Hall measurements. However, for the scope of our work, mercury probe contacts have been used to evaluate the carrier concentration in the epilayer of the vertical GaN Schottky diodes. The measurements have been performed in CRHEA. Below is just a general view of the mercury probe contact method

Cette thèse est accessible à l'adresse : https://theses.insa-lyon.fr/publication/2023ISAL0011/these.pdf
© [A.J.E. N’Dohi], [2023], INSA Lyon, tous droits réservés

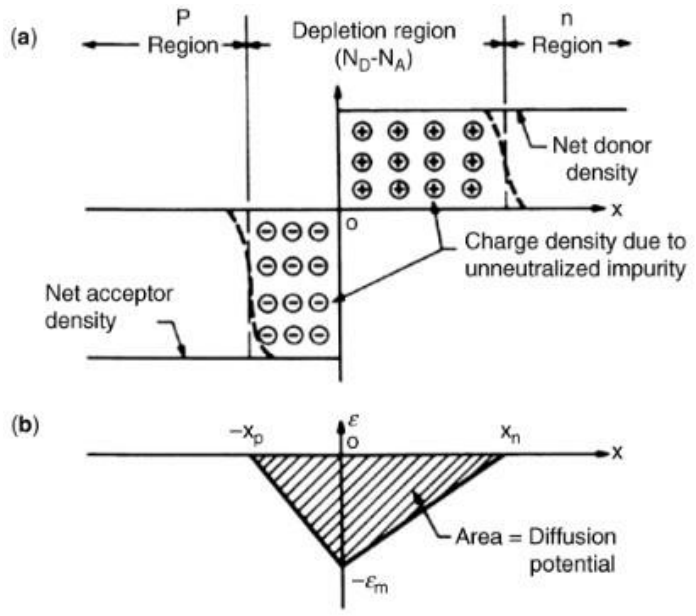

Figure 3.13: Abrupt p–n junction in thermal equilibrium (no bias), after Sze (1981). (a) Space charge distribution in the depletion approximation. The dashed lines indicate the majority carrier distribution tails. (b) Electric field across the depletion region [31]

Mercury Probe Contacts: The disadvantage of all carrier concentration measurement techniques is the need to establish contacts to the material under investigation. For Schottky barriers, a metal of precise area is deposited onto the wafer using photolithographic techniques. A low-resistance ohmic contact must also be formed in order to complete the circuit. These procedures are destructive, and the material is lost to further use. In an attempt to eliminate these Schottky barrier fabrication procedures, mercury probes have been developed to make temporary contact to the semiconductor surface. A schematic representation of a mercury (Hg) probe is shown in Figure 3.13 (Schroder, 2006). The mercury probe is an electrical probing device to make swift and non-destructive contact to a sample for electrical characterization. Its primary application is semiconductor measurements where otherwise time-consuming metallization or photolithographic processing are needed to make contact to a sample. The mercury probe applies mercury contacts of well-defined areas to a flat sample. In principle, the Hg is forced against the semiconductor by pulling it down against a precisely defined area using a vacuum. Simultaneously the Hg is siphoned up against the semiconductor making intimate contact (Jones and Corbett, 1989). The larger area contact in the figure 3.13 is the second contact to complete the circuit. Its area is many times that of the profiling contact, so that the two capacitances in series essentially look like the small reverse biased probing capacitance acting alone. Unfortunately, reproducible results are difficult to obtain, requiring careful surface preparation, very clean Hg, and careful cleaning of the semiconductor surface after use. Furthermore, as Hg is toxic, safe procedures must be observed.

Cette thèse est accessible à l'adresse : https://theses.insa-lyon.fr/publication/2023ISAL0011/these.pdf
© [A.J.E. N'Dohi], [2023], INSA Lyon, tous droits réservés

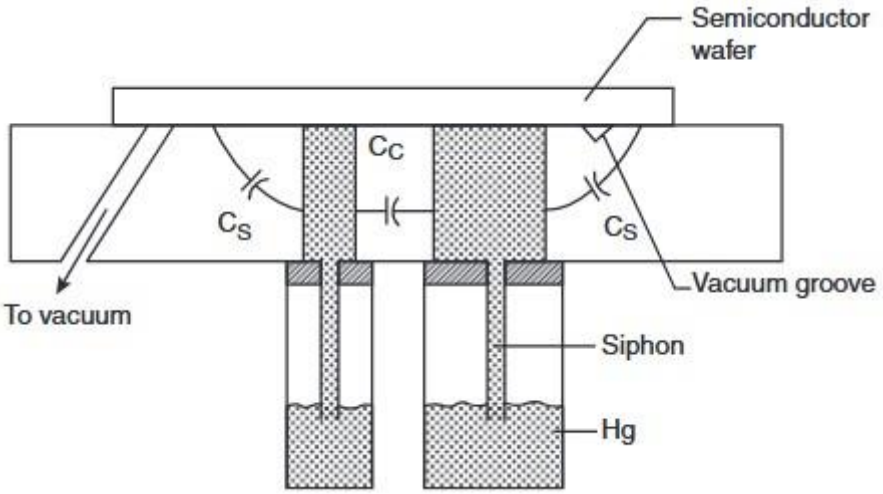

Figure 3.14: Typical mercury probe. The smaller contacting area is the reverse-biased Schottky barrier. (After Schroder, 2006.) [31].

Figure 3.14 is the theoretical image of a typical mercury probe. The one that has been used in the CHREA during measurements on our GaN samples is shown in figure 3.15 below. It is a keysight Agilent 4284A Precision MDC LCR Meter (20 Hz – 1 MHz), that can also measure impedance at 10 kHz with the extraction of parameters such as capacitance and resistance in parallel. The central dot image can be seen at the right-hand side of the Agilent instrument.

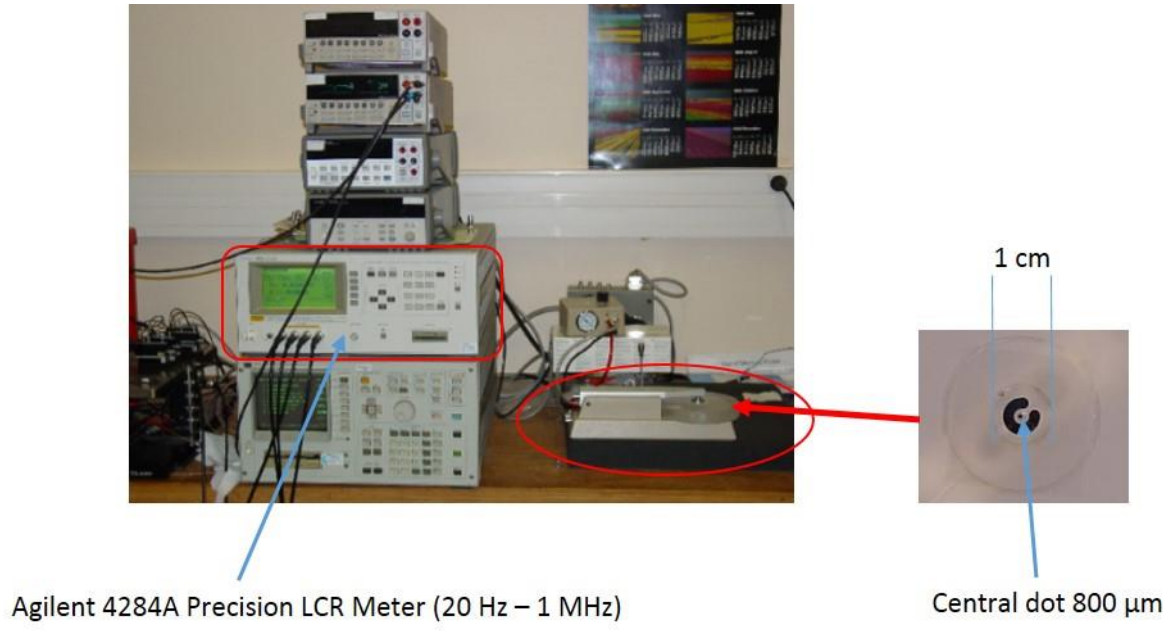

Figure 3. 15: Image of the CV measurement source of our GaN samples.

Cette thèse est accessible à l'adresse : https://theses.insa-lyon.fr/publication/2023ISAL0011/these.pdf
© [A.J.E. N'Dohi], [2023], INSA Lyon, tous droits réservés

3.4. CONCLUSION

In this chapter, we tackled the fundamental physics in the electrical characterization of diodes. As the scope of the thesis was focused on GaN Schottky diodes, we presented the way they have fabricated and the different electrical methods (I (V), C(V)) and instruments we used to characterized them. The characterization results on the diodes are fully commented on chapter 7.

Cette thèse est accessible à l'adresse : https://theses.insa-lyon.fr/publication/2023ISAL0011/these.pdf
© [A.J.E. N'Dohi], [2023], INSA Lyon, tous droits réservés

REFERENCES

[1] Tom Smy, Devices materials and properties, Elec 4705, lecture 13, fall (2009).

[2] Robert F. Pierret, Semiconductor Device Fundamentals. Addison-Wesley, Publication (1996).

[3] Çankaya G, Ucar N. Schottky barrier height dependence on the metal work function for p-type Si Schottky diodes. Zeitschrift für Naturforschung A. 59(11), 795-8 (2004).

[4] Veena Vijaya, Schottky diodes on GaN semiconductors, Texas Tech University, Thesis (2000).

[5] W. Schottky, Naturwissenschaften 26, 843 (1938).

[6] N. F. Mott, Proc. Cambridge Philos. Soc. 34, 568 (1938).

[7] Ming-Chang Lee, Integrated Photonic Devices, Introduction to Solid State Physics,

[8] Francesco La Via, Fabrizio Roccaforte, Vito Raineri, Ohmic contacts to SiC, (2006).

[9] J.D.Guo, M.S.Feng, R.J.Guo, F.M.Pan, and C.Y.Chang, Appl. Phys. Lett. 67, 2657 (1995).

[10] L. Wang, M.I.Nathan, T H.Lim, M. Akhan, and Q.Chen, Appl. Phys. Lett. 68, 1267 (1996).

[11] Z. Z. Bandic, P.M.Bridger, E.C.Piquette, and T.C. McGiH, Appl. Phys. Lett. 74, 1266 (1999).

[12] AC.Schmitz, AT.Ping, M.AKhan, J.W.Yang, and I.Adesida, Semicond. Sci. technol. (UK) 11 1464-7 (1996).

[13] HS.Venugopalan and S.E. Mohney, Appl. Phys. Lett. 73, 1242 (1998).

[14] AC.Schmitz, A.T.Ping, M.A.Khan,Q.Chen, J.W.Yang, I.Adesida, J. Electron. Mater (USA) 27 255 60 (1998).

[15] AT.Ping, AC.Schmitz, M.AKhan, andI.Adesida, Electron. Lett. 32, 68(1996).

[16] S.N.Mohammad, Z.Fan, AE.Botchkarev, W.Kim, O.Aktas, ASalvador, and H.Morkov, Electron. Lett. 32, 598 (1996).

[17] M.RH.Khan, T.Detchprom, P.Hacke, K.Hiramatsu, and N.Sawaki, J. Phys. D 28, 1169(1995).

[18] AC.Schmitz, AT.Ping, M.AKhan, Q.Chen, J.W.Yang, I.Adesida. Electron. Lett, 32 1832(1996).

[19] Q.Z.Liu, L.S.Yu, S.S.Lau, J.M.Redwing, N.R.Perkins, T.D.Kuech. Appl. Phys. Lett. 70, 1275 (1997).

Cette thèse est accessible à l'adresse : https://theses.insa-lyon.fr/publication/2023ISAL0011/these.pdf
© [A.J.E. N'Dohi], [2023], INSA Lyon, tous droits réservés

[20] J.S. Forensi, T.D. Moustakas. Appl. Phys. Lett, 62, 2859 (1993).

[21] H.S.Venugopalan and S.E. Mohney, Mater. Res. Soc. Symp. Proc, 512 (1998).

[22] James H.Edgar, Samuel Strite, Isamu Akasaki, Hirushi Amano and Christian Wetzel, "Properties, Processing and Applications of Gallium Nitride and related Semiconductors." INSPEC, London, United Kingdom. (1999).

[23] Jinwook B Burm, K.Chu, W.A.Davis, W.J.Schaff, L.F.Eastman, T.J.Eustis. Appl. Phys. Lett, 70,464 (1997).

[24] M.W.Cole, F.Ren, and S.J.Pearton, J.Electrochem. Soc. 144, L275; Appl. Phys. Lett. 71, 3004 (1997).

[25] Ngo TH, Comyn R, Frayssinet E, Chauveau H, Chenot S, Damilano B, Tendille F, Beaumont B, Faurie JP, Nahas N, Cordier Y. Cathodoluminescence and electrical study of vertical GaN-on-GaN Schottky diodes with dislocation clusters. Journal of Crystal Growth. 552,125911, (2020).

[26] S.M. Sze, Physics of Semiconductor Devices, 2nd edition, Wiley, New York, (1981).

[27] M. Drechsler, D.M. Hofmann, B.K. Meyer, T. Detchprohm, H. Amano, I. Akasaki, Japan. J. Appl. Phys. 34, L1178 (1995).

[28] Hui Xu, Fabrication and electrical/optical characterization of bulk GaN based Schottky diodes, Phd thesis, Auburn University, Alabama (2009).

[29] Test & Measurement, Keithley Product Catalog, (2016).

[30] Technical information: Source Measure Unit (SMU) Instruments, Keithley Product Catalog, (2016).

[31] Peter A. Barness, Cacitance-voltage characterization of semiconductors, Department of Physics and Astronomy, Clemson University Clemson, SC, USA, dited by Elton N. Kaufmann. Copyright, (2012).

Cette thèse est accessible à l'adresse : https://theses.insa-lyon.fr/publication/2023ISAL0011/these.pdf
© [A.J.E. N'Dohi], [2023], INSA Lyon, tous droits réservés

CHAPTER 4: MICRO RAMAN STUDY OF GAN SUBSTRATES FOR VERTICAL DEVICE TECHNOLOGY

The growth and the performance of vertical devices require a highly doped with a good crystalline quality native substrate. This is necessary to assure a good ohmic contact at the backside of the device. Therefore, in this section, in order to get high quality vertical GaN Schottky diodes, we investigated some freestanding n-doped GaN substrates with Si, Ge and O_2 using Raman spectroscopy. Here we focused on the physical properties of the GaN substrates: the GaN crystal symmetry, their crystalline quality and their residual stress level.

4.1. INTRODUCTION

Wide-Bandgap (WBG) semiconductors such as silicon carbide (SiC) or Gallium Nitride (GaN) are particularly interesting for power electronics. Especially, nitride-based devices such as ultraviolet (UV)-blue-green emitters, high-power transistors, etc., have become commercially available with hetero-epitaxial methods by employing a variety of foreign substrates including, sapphire, silicon carbide, and silicon. However, their performances are highly limited by the structural quality of these materials due to the well-known disadvantages of the hetero-epitaxy, such as lattice mismatch, thermal expansion coefficient mismatch and chemical incompatibility leading to high-dislocation density, mosaic crystal structure, biaxial induced stress, and wafer bowing [1]. GaN technology is presently being used in applications up to 650 V by means of horizontally configured high electron mobility transistors (HEMTs) [2]. Although GaN HEMT technology is exhibiting impressive performance, there are several limitations caused by the growth of GaN epi-layers in a metamorphic way on foreign substrates such as sapphire (Al_2O_3), silicon (Si) and SiC. These limitations can be reduced by using native GaN substrate or freestanding GaN substrate to favor the homoepitaxial growth of vertical GaN power devices. Such devices can withstand more than 1 kV [3, 4] drain voltage depending mainly on the crystalline quality of the active epi layers and the crystal quality of the substrate. Therefore, high-quality GaN substrates are needed to bring the performance of the GaN transistors to a value that has never been achieved. Fundamentally, the quality of GaN samples can be evaluated by probing the stress level and distribution in the samples, the doping level, as well as the effect of both point and extented defects such as threading dislocations (TDs) throughout the samples. Indeed, the control of TDs density during GaN crystal growth is a key issue for having good quality samples. The lower the TDs density in the crystal, the better its quality will be.

Cette thèse est accessible à l'adresse : https://theses.insa-lyon.fr/publication/2023ISAL0011/these.pdf
© [A.J.E. N'Dohi], [2023], INSA Lyon, tous droits réservés

Besides structural characterization techniques such as X-ray diffraction (XRD), AFM and SEM, Raman spectroscopy appears as a more powerful and non destructive alternative to detect these structural defects and study their deleterious effect on GaN crystal. Previous studies have revealed the interest of using micro-Raman spectroscopy to probe the stress in GaN samples. D. G. Zhao et al. reported on the stress and its effect on optical properties of GaN films grown on Si (111), SiC and c-plane sapphire [5]. S. Fritze et al. have investigated on the stress induced by Si and Ge in GaN films on sapphire with a doping concentration as high as 2×10^{19} cm^{-3} [6]. Lei Zhang et al. have also studied the influence of stress in GaN crystals grown by HVPE on MOCVD-GaN/6H-SiC substrate [7]. In addition, C. L. Chao et al. [8] have reported on a Freestanding (FS) high quality GaN substrate by associated GaN nanorods self-separated hydride vapor-phase epitaxy (HVPE) in which the (FS) GaN substrate was uncommonly obtained from nanorods array. They found no residual tensile stress in the substrate and no additional information on the doping level and its effect of the FS GaN substrate have been mentioned. The majority of stress evaluation in GaN samples in literature have been conducted on heteroepitaxially grown GaN films from which the origin of stress was attributed to the lattice mismatch and the thermal expansion coefficient discrepancy between the epilayer and the substrate. Some works on optical [9] and electrical [10] properties of doped GaN substrates as well as doped vertical GaN Schottky barrier diodes [11] have also been reported so far. Nevertheless, studies on mechanical stress in intentionally n-doped HVPE-grown FS GaN substrates using micro-Raman technology still lack deep and clear investigations.

Here, in this chapter, we present the micro-Raman investigation of the residual mechanical stress in five epi-ready freestanding GaN wafers. The substrates are doped with three different dopants: Si, Ge, O_2, with roughly the same carrier concentration. By investigated the E_2^h mode, we evaluated the microscopic residual stress level that effectively occur during growth process. The study of the residual stress in these n-doped GaN substrates will shed light on the quality of the GaN substrates for the efficiency of the vertical device technology. Moreover, this work proves that micro-Raman spectroscopy is a powerful tool to characterize GaN substrates.

4.2. EXPERIMENTAL METHOD

We investigated five epi-ready freestanding GaN wafers grown by the common HVPE (Hydride Vapor Phase Epitaxy) method [12] at Saint-Gobain Lumilog. The details on the HVPE method for GaN substrates growth can be found in the first chapter of the manuscript. These five samples are 2-inch diameter wide and 300 µm thick. Two of them have been doped with Oxygen (O_2), one has been doped with Silicium (Si) and other two have been doped with Germanium (Ge). The free carrier

Cette thèse est accessible à l'adresse : https://theses.insa-lyon.fr/publication/2023ISAL0011/these.pdf
© [A.J.E. N'Dohi], [2023], INSA Lyon, tous droits réservés

concentration of the n-type doping process was approximately kept at 2×10^{18} cm^{-3}. The doping concentration is not homogeneous all over the wafers. As the local variation of the doping is not negligeable in each wafer, the sample provider (Saint Gobain) has just given the mean value of the doping concentration.

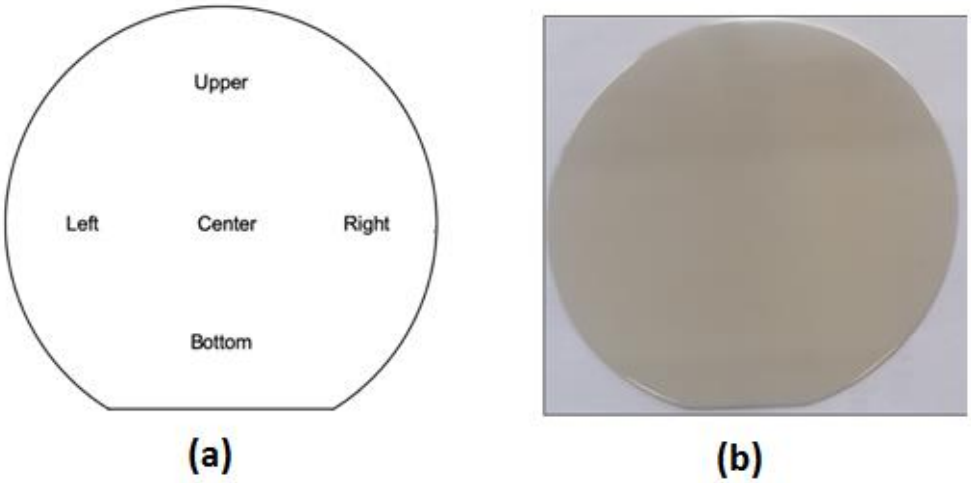

Figure 4. 1: (a) Schematic representation of a GaN substrate (top view) with localization of the five micro-Raman measurements zone. (b) Image of the fabricated freestanding GaN substrate.

Some of the physical characteristics of the wafers are summarized in the table 4.1. They were obtained by XRD measurements and were realized by Saint-Gobain Lumilog. The threading dislocations density (TDDs) calculated from the X-ray diffraction (XRD) measurements was on average between 10^6 cm^{-2} and 10^7 cm^{-2} for the substrates. The FWHM has been obtained from the analysis of the (002) XRD reflection plane. According to Kappers et al. [13], the FWHM of the (002) reflection is related to the screw or mixed dislocations. The bow of -3µm indicates a slight concave form of the substrates as compared to the ones mentioned in reference [14]. The reason of this bowing state comes from the HVPE growth of the substrates [12]. Thus, because of this bowing morphology, some inhomogeneities of physical parameters such as doping concentration, stress may be found throughout each substrate surface from one edge to another one. The high doping concentration ($1\sim2\times10^{18}$ cm^{-3}) of the substrates was intentional because it is necessary for good ohmic contacts during device technology fabrication.

Cette thèse est accessible à l'adresse : https://theses.insa-lyon.fr/publication/2023ISAL0011/these.pdf
© [A.J.E. N'Dohi], [2023], INSA Lyon, tous droits réservés

Substrate Name	Dopant	XRD (002) FWHM	Bow (µm)	Average dislocation density (cm^{-2})	N carrier concentration (cm^{-3})
Sample 1	O_2	86	-3	5×10^{6}	$1\sim2\times10^{18}$
Sample 2	O_2	120	-3	10^{7}	$1\sim2\times10^{18}$
Sample 3	Ge	124	-3	10^{7}	$1\sim2\times10^{18}$
Sample 4	Ge	120.5	-3	10^{7}	$1\sim2\times10^{18}$
Sample 5	Si	75	-3	$< 5\times10^{6}$	$1\sim2\times10^{18}$

Table 4. 1: Summary of the different GaN substrates studied by Raman spectroscopy.

The micro-Raman spectroscopy was performed at room temperature under a 532 nm laser source. A commercial confocal micro-Raman spectrometer (Renishaw Invia model) was used in back scattering geometry, with ×100 objective and a 2400 l/mm diffraction grating. The spatial and spectral resolutions were around 0.1µm and 0.1cm^{-1} respectively. For Raman measurements, cartographies of 150 µm × 150 µm with a 3 µm step size were performed at different zones on each substrate. Then, from one Raman cartography, series of more than 2600 spectra have been obtained. See (Figure 4.2a and 4.2b).

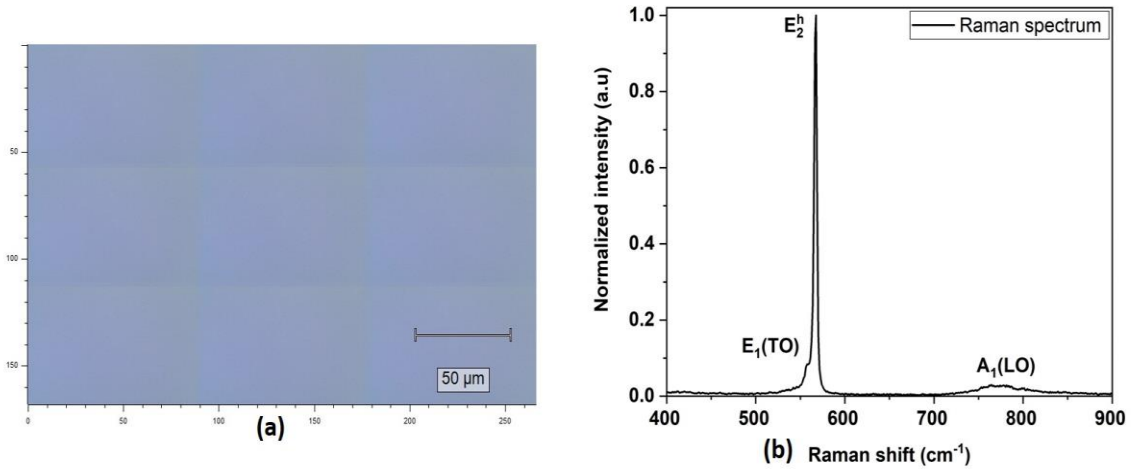

Figure 4. 2: (a) Raman microscope image of the GaN substrate surface. (b) Raman spectrum from the cartography.

Cette thèse est accessible à l'adresse : https://theses.insa-lyon.fr/publication/2023ISAL0011/these.pdf
© [A.J.E. N'Dohi], [2023], INSA Lyon, tous droits réservés

We fitted the obtained spectra with a mixed (Gaussian - Lorentzian) function. We fitted the E_2^h and the E_1 (TO) peaks together, but for the stress analysis, we just considered the E_2^h peaks fit values. Before the fittings, we have done basic data processings: pic normalization with regard to the highest intensity peak (E_2^h) and cosmic rays removal. Finally, the study of the residual stress in the substrates was conducted by the analysis of the E_2^h Raman maps derived from the fittings. Let us remind that the data treatment was done by using the "wire" software provided by Renishaw.

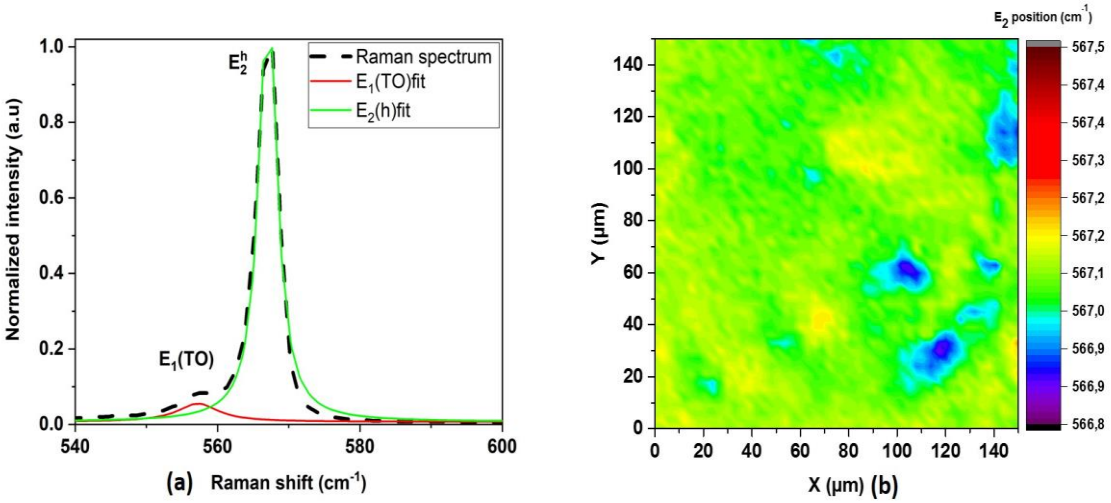

Figure 4. 3: (a) Zoom and fitting of the E_2^h peak. (b) E_2^h position map extracted from the fitting results.

4.3. RESULTS AND DISCUSSIONS

4.3.1. SYMMETRY OF GaN SUBSTRATES

From each position of a substrate as described in the cross-section image (figure 4.1a), we carried out Raman measurements and analyzed the E_2^h peak behavior in order to investigate the residual stress and structural defects. Figure 4.4 presents the normalized Raman spectra recorded at the center (cartography measurement) of each GaN substrate wafer. The spectra normalization has been done with regard to the highest peak E_2^h peak intensity. The two peaks E_2^h and A_1 (LO) mainly appear in the recorded data because our measurements have been performed in the backscattering geometry. The E_2^L mode is absent since our spectral frequency range was fixed between 200 cm^{-1} and 1000 cm^{-1} and the E_2^h mode is reported to display the highest intensity in that geometry. The peak at the shoulder of the E_2^h mode is ascribed to E_1 (TO) mode. Hence, by considering generally E_2^h and A_1 (LO) modes of these Raman signals we can conclude that the GaN substrates are of the hexagonal symmetry that is the

Cette thèse est accessible à l'adresse : https://theses.insa-lyon.fr/publication/2023ISAL0011/these.pdf
© [A.J.E. N'Dohi], [2023], INSA Lyon, tous droits réservés

preferred configuration for the device fabrication. However as the doping concentration is not homogeneous on each wafer, we just studied the E_2^h peak behavior.

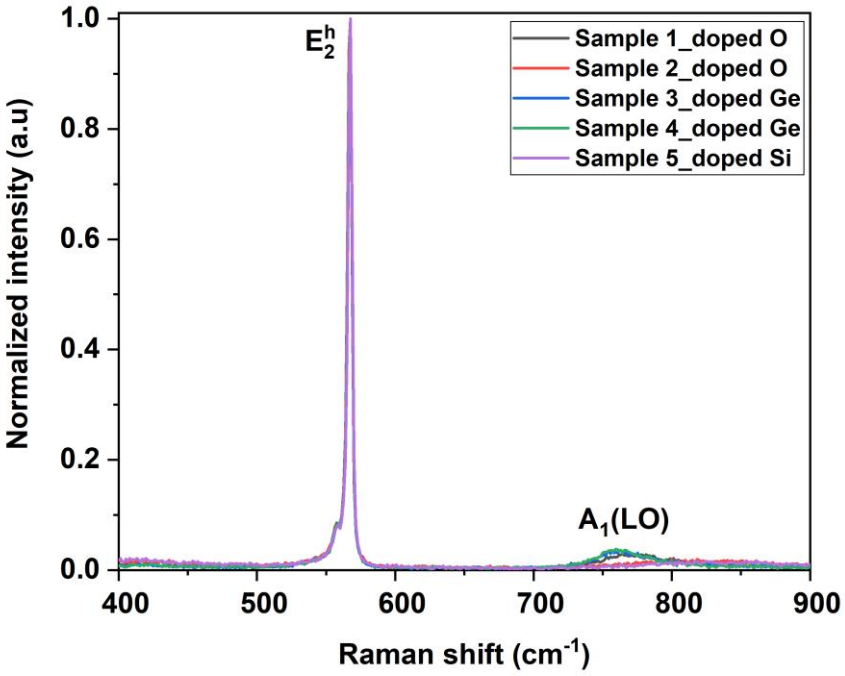

Figure 4.4: Raman spectra obtained from the center of the different substrates.

4.3.2. STUDY OF THE E_2^h RAMAN MODE

As presented in chapter 2, in epitaxial GaN samples, the stress is biaxial and the E_2^h mode (position and width) is reported to be sensitive to the biaxial stress and the crystalline quality respectively [15] by the equation [16]:

$$\Delta\omega = \boldsymbol{K}\sigma_{xx=yy} \qquad (1)$$

Where $\Delta\omega$ is the shift of phonon line (cm^{-1}), $\sigma_{xx=yy}$ (GPa) is the biaxial stress and $\boldsymbol{K}$ is the pressure coefficient or the stress coefficient (cm^{-1}/GPa). Here we could not quantify exactly the stress because of the scattered values of the stress coefficient shown in chapter 2. However, when tracking and quantifying the E_2^h mode position and width by 2D Raman cartographies, we evaluated the qualitative stress level and distribution in the substrates.

Cette thèse est accessible à l'adresse : https://theses.insa-lyon.fr/publication/2023ISAL0011/these.pdf
© [A.J.E. N'Dohi], [2023], INSA Lyon, tous droits réservés

Substrate Name	dopants	FWHM (mean value) (cm^{-1})	FWHM (standard deviation) (cm^{-1})	Average dislocation density (cm^{-2})
Sample1	O_2	3,6±0,1	0,03	5×10^6
Sample2	O_2	3,6±0,1	0.04	10^7
Sample3	Ge	3,6±0,1	0.03	10^7
Sample4	Ge	3,6±0,1	0.05	10^7
Sample5	Si	3,6±0,1	0.05	$< 5\times10^6$

Table 4.2: Summary of the different GaN substrates E_2^h Raman mode FWHM for each sample and their respective standard deviation.

Cette thèse est accessible à l'adresse : https://theses.insa-lyon.fr/publication/2023ISAL0011/these.pdf
© [A.J.E. N'Dohi], [2023], INSA Lyon, tous droits réservés

Substrate Name	dopants	E_2^h position (mean value) (cm^{-1})	E_2^h position standard deviation (cm^{-1})	Average dislocation density (cm^{-2})
Sample1	O_2	567.0±0,1	0,02	5×10^6
Sample2	O_2	567.1±0,1	0.03	10^7
Sample3	Ge	567.1±0,1	0.04	10^7
Sample4	Ge	567.3±0,1	0.02	10^7
Sample5	Si	567.5±0,1	0.04	$< 5\times10^6$

Table 4.3: **Summary of the different GaN substrates E_2^h Raman mode position for each sample and their respective standard deviation.**

Table 4.2 is the summary of the quantification result derived from the E_2^h width maps. The substrates have all the same E_2^h width mean value of 3.6 cm^{-1}. This means that they have the same crystalline quality. This value is also an indication of a good crystalline quality even though the doping level is around 2×10^{18} cm^{-3} with different dopants. Another reason for that good crystallinity is that the dislocations rate (5×10^6 cm^{-2} - 6×10^7 cm^{-2}) is a reasonable one for HVPE grown GaN samples and does not influence the crystalline quality of the substrates. Moreover, the standard deviation from the E_2^h width mean value shows that the O_2 doped sample with less dislocations (sample 1) is more homogeneous (crystalline homogeneity) than the Si doped one with almost the same dislocation density. This can be due to the physical properties of the Si and O as the two main donor dopants in GaN [17].

Table 4.3 shows the results for E_2^h position shift. We observe that the shift is less for O_2 doped substrates (samples1 and 2) and more or less for the Ge doped ones. However, it is significant for the Si doped substrate. This indicates that the stress is more significant in Si doped sample than in the O_2 doped ones. In addition, we clearly see that at the same order of carrier concentration 10^{18} cm^{-3}, the E_2^h position shifts gradually to high frequency from O_2 doped (567.0 ±0,1cm^{-1}) to Si doped (567.5±0,1 cm^{-1}) samples. It reveals that the stress is more compressive in the Si doped case. Also, we denote a shift gap of 0.5±0,1 cm^{-1} between sample 1 and sample 5 even though they show nearly the same dislocation rate. This supports the fact dislocations may not affect the shift we observed. Rather,

Cette thèse est accessible à l'adresse : https://theses.insa-lyon.fr/publication/2023ISAL0011/these.pdf
© [A.J.E. N'Dohi], [2023], INSA Lyon, tous droits réservés

it may be due to the dopant effect as explained in reference [20], where it has been reported that the impurity dopant incorporation affects the atomic lattice by its size effect through the atomic radius difference between both the impurity and the host atom. Here, the covalent radius of Ge (1.22 Å) atom is similar to that of Ga (1.26 Å) and the metal-nitrogen bond length changes by only 1.4% with Ge, compared to 5.5% with Si (1.17 Å) [18, 19, 20] while, on the other hand, the covalent radius of O (0.73 Å) is close to that of N (0.75 Å) [21]. We can conclude that Si creates more atomic lattice distortions than Ge and O and therefore making the E_2^h position shift more significant.

In addition, we calculated the standard deviation of the E_2^h position by using the mathematical method to quantify the stress distribution in the samples. We particularly found that for the same order of dislocation rate, the standard deviation is of 0.02 for sample 1 and 0.04 for sample 5. This indicates that the stress distribution is more significant with Si doped sample than O_2 doped one.

Furthermore, in the E_2^h position maps of each sample we observed some blue spots (see figure 4.5) corresponding to tensile stress that we suppose to be some dislocations or dislocations clusters in the substrates. More details about that will be presented in the next chapters.

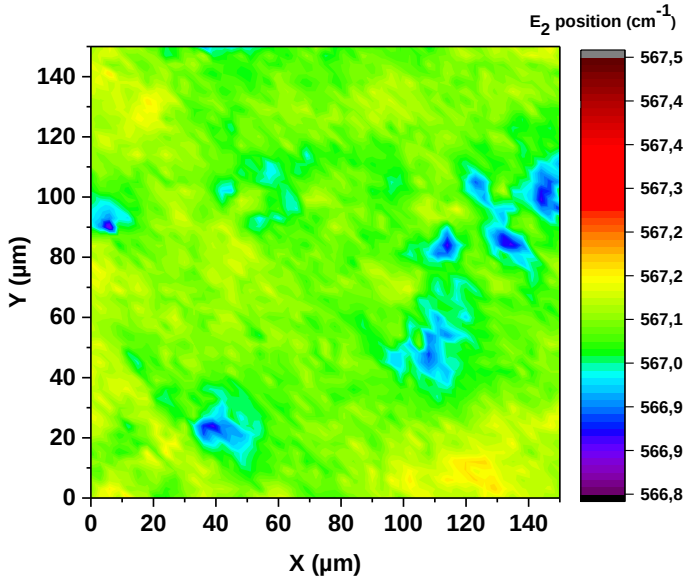

***Figure 4. 5**: E_2^h position map example of one substrate. The blue spots may be some dislocations during substrate growth*

Cette thèse est accessible à l'adresse : https://theses.insa-lyon.fr/publication/2023ISAL0011/these.pdf
© [A.J.E. N'Dohi], [2023], INSA Lyon, tous droits réservés

4.4. CONCLUSION

In summary, we investigated the stress and crystalline quality of five n-doped freestanding GaN substrates by investigating the E_2^h mode using Raman spectroscopy. On one hand, we noticed that the studied substrates have all the same crystalline quality due to their similar E_2^h width mean value. In addition, the samples 1 and 5 doped with O_2 and Si respectively do not have the same crystalline homogeneity even though they contain the same order of dislocation rate. On the other hand, from the E_2^h position shift evaluation, we observed that the stress is more compressive and significant in Si doped sample than the ones doped with O_2 and Ge even though it has the smallest dislocations density. The E_2^h position shift observed here and its related stress may come from the effect of the dopant, its incorporation in the GaN samples and also the activity of the dislocation presence in the samples. This study illustrates the efficiency of micro-Raman spectroscopy in probing structural and the mechanical properties of GaN substrates for power device applications.

Cette thèse est accessible à l'adresse : https://theses.insa-lyon.fr/publication/2023ISAL0011/these.pdf
© [A.J.E. N'Dohi], [2023], INSA Lyon, tous droits réservés

REFERENCES

[1] Foronda, Humberto M., Alexey E. Romanov, Erin C. Young, Christian A. Robertson, Glenn E. Beltz, and James S. Speck. "Curvature and bow of bulk GaN substrates." Journal of Applied Physics 120, no. 3 035104. (2016).

[2] Xiao, Ming, Xiang Gao, Tomás Palacios, and Yuhao Zhang. "Leakage and breakdown mechanisms of GaN vertical power FinFETs." Applied Physics Letters 114, no. 163503, 16 (2019).

[3] Xiao, Ming, Xiang Gao, Tomás Palacios, and Yuhao Zhang. "Leakage and breakdown mechanisms of GaN vertical power FinFETs." Applied Physics Letters 114, no. 163503, 16 (2019).

[4] Nie, Hui, Quentin Diduck, Brian Alvarez, Andrew P. Edwards, Brendan M. Kayes, Ming Zhang, Gangfeng Ye, Thomas Prunty, Dave Bour, and Isik C. Kizilyalli. "1.5-kV and 2.2 mΩ/cm^2 Vertical GaN Transistors on Bulk-GaN Substrates." IEEE Electron Device Letters 35, no. 9, 939-941 (2014).

[5] Zhao, D. G., S. J. Xu, M. H. Xie, S. Y. Tong, and Hui Yang. "Stress and its effect on optical properties of GaN epilayers grown on Si (111), 6H-SiC (0001), and c-plane sapphire." Applied physics letters 83, no. 4, 677-679 (2003).

[6] Fritze, S., A. Dadgar, H. Witte, M. Bügler, A. Rohrbeck, J. Bläsing, A. Hoffmann, and A. Krost. "High Si and Ge n-type doping of GaN doping-Limits and impact on stress." Applied Physics Letters 100, no. 12, 122104 (2012).

[7] Zhang, Lei, Jiaoxian Yu, Xiaopeng Hao, Yongzhong Wu, Yuanbin Dai, Yongliang Shao, Haodong Zhang, and Yuan Tian. "Influence of stress in GaN crystals grown by HVPE on MOCVD-GaN/6H-SiC substrate." Scientific Reports 4, no. 1, 1-6 (2014).

[8] Chao, C. L., C. H. Chiu, Ya-Ju Lee, Hao-Chung Kuo, Po-Chun Liu, Jeng Dar Tsay, and Shun-Jen Cheng. "Freestanding high quality GaN substrate by associated GaN nanorods self-separated hydride vapor-phase epitaxy." Applied Physics Letters 95, no. 5, 051905 (2009).

[9] Khromov, Sergey, Carl Hemmingsson, Bo Monemar, Lars Hultman, and Galia Pozina. "Optical properties of C-doped bulk GaN wafers grown by halide vapor phase epitaxy." Journal of Applied Physics 116, no. 22, 223503 (2014).

[10] Bogusławski, P., and J. Bernholc. "Doping properties of C, Si, and Ge impurities in GaN and AlN." Physical Review B 56, no. 15, 9496 (1997).

Cette thèse est accessible à l'adresse : https://theses.insa-lyon.fr/publication/2023ISAL0011/these.pdf
© [A.J.E. N'Dohi], [2023], INSA Lyon, tous droits réservés

[11] Gu, Hong, Feifei Tian, Chunyu Zhang, Ke Xu, Jiale Wang, Yong Chen, Xuanhua Deng, and Xinke Liu. "Recovery performance of Ge-doped vertical GaN Schottky barrier diodes." Nanoscale Research Letters 14, no. 1, 1-6 (2019).

[12] Ban, Vladimir S. "Mass spectrometric and thermodynamics studies of the CVD of some III–V compounds." Journal of Crystal Growth 17, 19-30 (1972).

[13] Kappers, M. J., R. Datta, R. A. Oliver, F. D. G. Rayment, M. E. Vickers, and C. J. Humphreys. "Threading dislocation reduction in (0 0 01) GaN thin films using SiNx interlayers." Journal of Crystal Growth 300, no. 1, 70-74 (2007).

[14] Shim, Jae-Hyoung, Jin-Seong Park, and Jea-Gun Park. "A bow-free freestanding GaN wafer." RSC advances 10, no. 37, 21860-21866 (2020).

[15] Barchuk, Motylenko, M. Motylenko, T. Schneider, M. Förste, C. Röder, A. Davydok, S. Lazarev et al. "Defect-rich GaN interlayer facilitating the annihilation of threading dislocations in polar GaN crystals grown on (0001)-oriented sapphire substrates." Journal of Applied Physics 126, no. 8 085301 (2019).

[16] Li, H. D., S. L. Zhang, H. B. Yang, G. T. Zou, Y. Y. Yang, K. T. Yue, X. H. Wu, and Y. Yan. "Raman spectroscopy of nanocrystalline GaN synthesized by arc plasma." Journal of applied physics 91, no. 7, 4562-4567 (2002).

[17] Van de Walle, Chris G. "Defects and doping in GaN." equilibrium 5, no. 14 (1997): 15.

[18] Cargill III, G. S., J. Angilello III, and K. L. Kavanagh. "Lattice compression from conduction electrons in heavily doped Si: As." Physical review letters 61, no. 15, 1748. (1988).

[19] Ajay, A., J. Schörmann, M. Jiménez-Rodriguez, C. B. Lim, F. Walther, M. Rohnke, I. Mouton et al. "Ge doping of GaN beyond the Mott transition." Journal of Physics D: Applied Physics 49, no. 44 445301, (2016).

[20] Neugebauer, Jörg, and Chris G. Van de Walle. "Chemical trends for acceptor impurities in GaN." Journal of applied physics 85, no. 5, 3003-3005 (1999).

[21] Kobayashi, H., and W. M. Gibson. "Lattice location of Si in ion implanted GaN." Applied physics letters 73, no. 10, 1406-1408 (1998).

Cette thèse est accessible à l'adresse : https://theses.insa-lyon.fr/publication/2023ISAL0011/these.pdf
© [A.J.E. N'Dohi], [2023], INSA Lyon, tous droits réservés

CHAPTER 5: MICRO RAMAN CHARACTERIZATION OF HOMOEPITAXIAL N DOPED GAN LAYERS FOR VERTICAL DEVICE APPLICATION

Here homo-epitaxially grown n-doped GaN layers with different concentration have been investigated by Raman spectroscopy. For vertical device technology, lightly n-doped homo-epitaxial layers (i.e $n<10^{17}cm^{-3}$) are needed as fundamental steps. Practically, the first steps during the fabrication of vertical GaN Schottky diodes take into account the growth of a GaN native substrate and a subsequent growth of GaN layers. Other additional steps such lithography for mask layout and metallization deposition come next. In addition, in a Schottky diode configuration for instance, the epilayer is of a great importance. It is considered as the drift layer of the device that withstands one of the most important electrical parameters of the device: breakdown voltage (BV). Therefore, a deep study on the epitaxial layers with a non-destructive physical approach such as Raman spectroscopy is vital to get an overview of the performance of the device after fabrication.

5.1. INTRODUCTION

Vertical-type GaN (Gallium Nitride) power devices are reported to show better electrical performance than their lateral counterparts because of less leakage paths, high current density and better reliability [1, 2, 3]. The growth of such devices requires good quality homo-epitaxially grown layers on native GaN substrates. Up to date, native GaN substrates can be manufactured with highly sophisticated technologies such as HVPE (Hydride Vapor Phase Epitaxy), ammonothermal method and low-pressure solution growth [4]. In addition, homo-epitaxially fabricated vertical GaN devices have been mentioned to sustain more than 1 kV [5, 6] as a blocking voltage depending on the device drift layer thickness. Such an expected device performance is possible through an accurate control of the doping level and the crystalline quality of the active epilayer [7]. Indeed, a lower doping of the drift layer increases the breakdown voltage in the device, and a homogeneous doping induces a uniform electric field distribution in the device. A physical characterization approach of the doping concentration and the structural defects is therefore necessary to understand the roots of the electrical performance limitations of the vertical GaN devices.

Micro-Raman spectroscopy is a powerful optical non-destructive tool to study the crystalline quality of GaN material by probing different phonon vibrational modes. In backscattering geometry and for a hexagonal GaN structure, the E_2^h mode is analyzed to evaluate the biaxial stress in GaN [8, 9, 10] as

Cette thèse est accessible à l'adresse : https://theses.insa-lyon.fr/publication/2023ISAL0011/these.pdf
© [A.J.E. N'Dohi], [2023], INSA Lyon, tous droits réservés

mentioned in chapter 2 in the bibliography work. Many studies on GaN crystal quality using Raman tool have been conducted mainly on hetero-epitaxial samples [11, 12]. So far only a few of them have given detailed explanations of the physics underlying the effect of the charge carrier density on the homo-epitaxial GaN crystal quality when a doping concentration ranges between 10^{17} - 10^{19} cm^{-3} [13, 14]. In this range, the A_1(LO) behavior is reported to be drastically changing with the carrier density due to a strong coupling with the plasmons. However, to our knowledge, investigations in the low doping range 10^{14} -10^{17} cm^{-3} are still fully lacking in literature. Vertical GaN SBDs (Schottky Barrier Diodes) have been reported to always suffer from high reverse leakage current and premature breakdown voltage. To solve that challenge, one solution is to lower the doping concentration of the drift layer below 10^{17} cm^{-3} [15, 16].

In this work, we used the micro-Raman tool to investigate quantitatively the quality of Si-doped homo-epitaxial GaN samples from an unintentionally doped state n < 10^{14} cm^{-3} to a highly doped one n > 10^{18} cm^{-3}. By tracking the position and the FWHM (Full Width Half Maximum) of the E_2^h and A_1(LO) Raman modes as the carrier density increases, the quality of the homo-epitaxial samples was carefully probed. Furthermore, a calibration of the A_1(LO) position as a function of Si concentration was performed to quantify its sensitivity at low and high doping levels and then we deduced the physical mechanism underlying the A_1(LO) behavior vs the carrier density.

5.2 . EXPERIMENTAL METHOD AND RESULTS

A batch of eight homo-epitaxial GaN samples was grown by MOCVD (Metal Organic Chemical Vapor Deposition) method [17] on 50 mm diameter n-doped freestanding GaN substrates provided by Lumilog [18] (see experimental method section for GaN substrates). GaN films were grown in CRHEA (Centre de recherche pour l'hetero epitaxie appliquée) in a close-coupled showerhead reactor. Ammonia, trimethylgallium, and hydrogen carrier gas were used to grow the films at 1020 °C with a growth rate of 2 µm·h^{-1}. Diluted silane was added to the vapor phase in order to dope the GaN films. Before the growth of the thick low-doped films, a thin highly doped GaN buffer layer of 0.1 µm thickness was grown on top of the substrate (see figure 5.1). The epilayers thickness was kept at 5 µm (except for sample Epi 06 which was 10 µm) with a Si carrier concentration ranging from an unintentionally doped level inferior to 10^{14} cm^{-3} (non-intentionally doped sample) to a high-doped state of 1.8 × 10^{18} cm^{-3}. Prior the Raman measurements, the capacitance-voltage (C-V) by mercury probe method was used to determine the doping level (Nd-Na measurement) in CRHEA.

Cette thèse est accessible à l'adresse : https://theses.insa-lyon.fr/publication/2023ISAL0011/these.pdf
© [A.J.E. N'Dohi], [2023], INSA Lyon, tous droits réservés

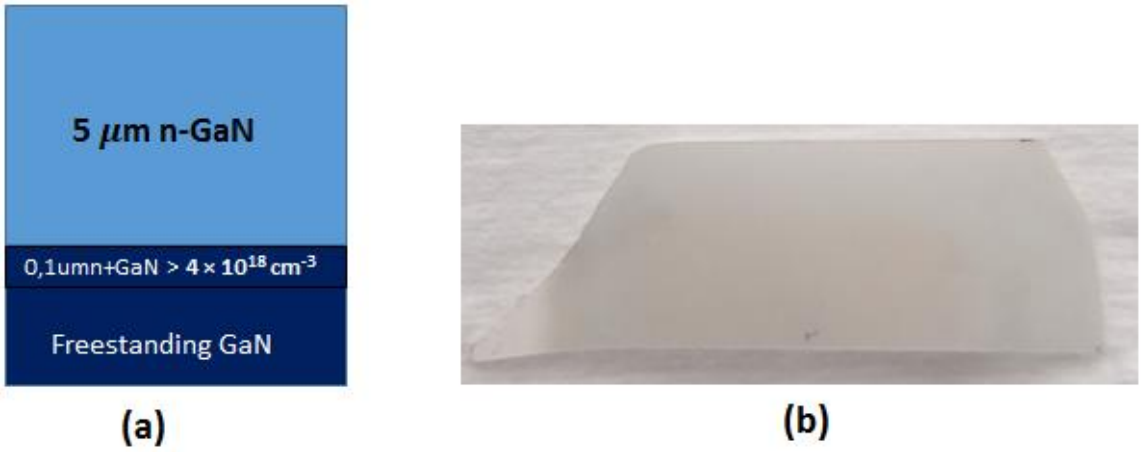

Figure 5. 1: (a) Schematic cross section image of the homo-epitaxial sample with a highly doped (n+ doping) GaN buffer layer (0.1µm thickness) on a freestanding GaN substrate. (b) Image of the n doped GaN epilayer.

Micro-Raman spectroscopy measurements were carried out at room temperature. For that, a confocal micro-Raman spectrometer (Renishaw Invia model) was used in back scattering geometry, with a ×100 objective and a 2400 l/mm diffraction grating. All the samples were excited with a 532 nm laser source (maximum power 10 mW to avoid local heating). The spectral and spatial resolutions were around 0.1 cm^{-1} and 1 µm respectively. Prior to any measurements, a calibration of the Raman shift was made with a silicon reference at 520.5 cm^{-1}. Figure 5.2 shows the whole Raman spectra recorded at the center of each sample in backscattering geometry. Two main peaks can be observed: the E_2^h and the A_1(LO) peaks. This confirms the hexagonal crystal structure of the films. The small peak at the shoulder of the E_2^h can be ascribed to the E_1 (TO) (558 cm^{-1}) mode [19] and has been already observed during the substrate investigation in chapter 4. The obtained Raman spectra have been processed and normalized with respect to the E_2^h peak intensity.

Cette thèse est accessible à l'adresse : https://theses.insa-lyon.fr/publication/2023ISAL0011/these.pdf
© [A.J.E. N'Dohi], [2023], INSA Lyon, tous droits réservés

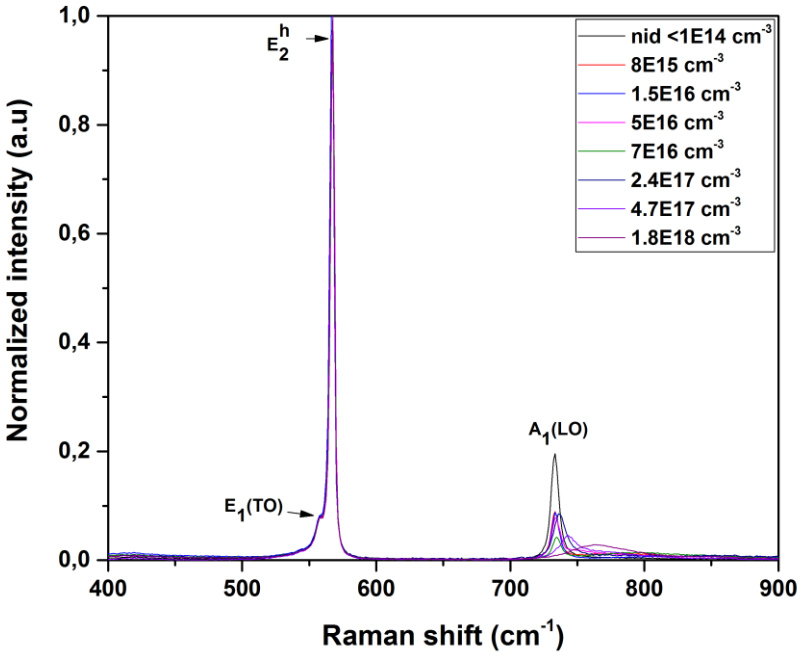

Figure 5. 2: Raman spectra of the Si-doped epilayers. The nid layer is the non-intentionally doped layer. The A_1(LO) modes clearly changes with the n carrier concentration.

During measurements, Raman mappings of 150 µm × 150 µm square dimension with a step size of 3 µm were made on different zones of each sample. An average of more than 2600 spectra extracted from each Raman map was obtained. The acquisition time during mapping was fixed at 1sec for all samples to get better Raman spectra. The quantitative analysis of the E_2^h and the A_1(LO) modes has been made by processing these modes with standard operations described in previous chapters and fitting their spectra by a mixed Gaussian-Lorentzian function with the Wire 5 Renishaw software (figure 5.3). For the A_1(LO) modes fittings, we fitted both the substrate A_1(LO) peak (dome-like curve, figure 5.3) and the A_1(LO) peak of the studied layers. As the GaN substrate is highly n-doped, the two A_1(LO) peaks can be easily separated and we keep just the A_1(LO) contribution from the studied layer. In addition, we have drawn and visualized the E_2^h and the A_1(LO) position maps. Finally, we then considered the mean values of the E_2^h and the A_1(LO) position and FWHM deduced from all the Raman maps in our analyses.

Cette thèse est accessible à l'adresse : https://theses.insa-lyon.fr/publication/2023ISAL0011/these.pdf
© [A.J.E. N'Dohi], [2023], INSA Lyon, tous droits réservés

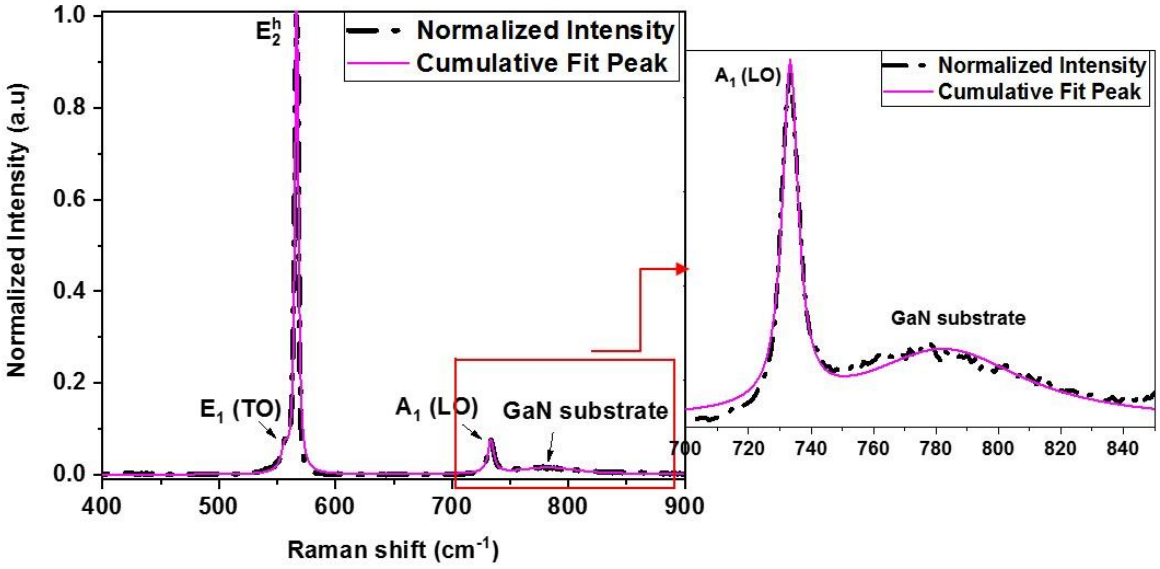

Figure 5. 3: A1 (LO) fittings for A1 (LO) Raman maps extraction. The fittings have been performed by taking account of the GaN substrate signal in order to subtract its quantitative influence.

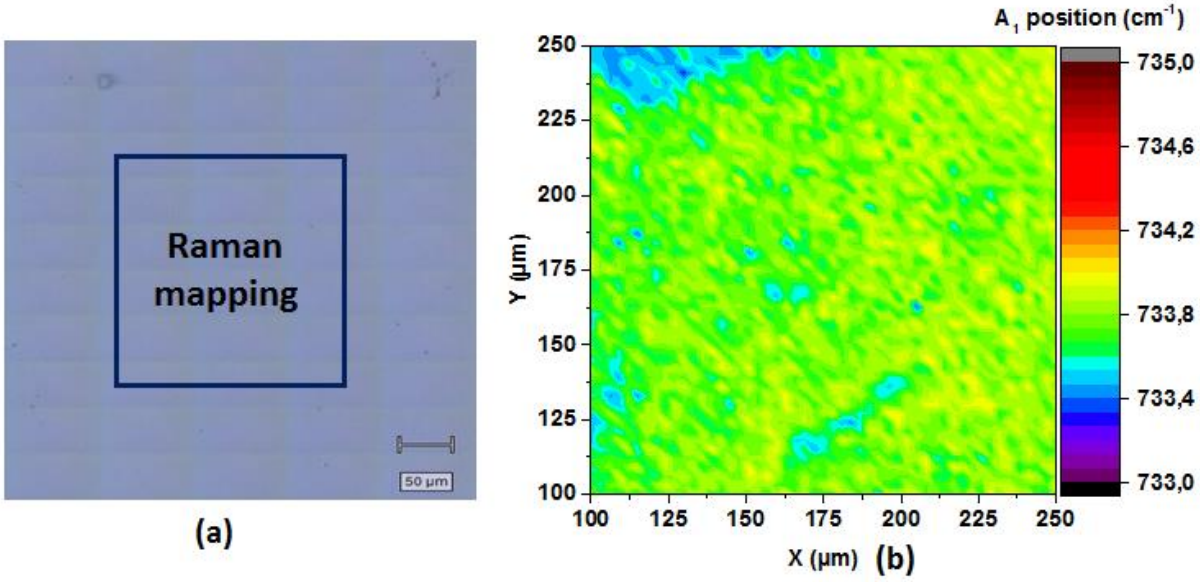

Figure 5.4: (a) Optical image of the sample surface. (b) Raman mapping of the A1 (LO) position of one zone of the sample.

We remind that the A_1 (LO) position and width Raman maps have been extracted for all studied GaN samples in accordance with the fitting operation displayed in figure 5.3. We only exposed an example of them (figure 5.4) to avoid figure caption redundancy.

Cette thèse est accessible à l'adresse : https://theses.insa-lyon.fr/publication/2023ISAL0011/these.pdf
© [A.J.E. N'Dohi], [2023], INSA Lyon, tous droits réservés

The table 5.1 summarizes the values extracted from the data processing. The calculated errors are the systematic errors based on the mean values.

Sample	epilayers thickness (µm)	Si carrier concentration (cm^{-3})	A_1(LO) Position (cm^{-1})	A_1(LO) width (cm^{-1})	E_2(h) Position (cm^{-1})	E_2(h) Width (cm^{-1})
Epi 01	**5**	**$\leq 10^{14}$ (NID)**	**733.3 ± 0.1**	**6.3 ± 0.1**	**567.1 ± 0.1**	**3.5 ± 0.1**
Epi 02	**5**	**8×10^{15}**	**733.4 ± 0.1**	**6.9 ± 0.1**	**567.1 ± 0.1**	**3.3 ± 0.1**
Epi 03	**5**	**1.5×10^{16}**	**733.6 ± 0.1**	**7.0 ± 0.1**	**567.1 ± 0.1**	**3.5 ± 0.1**
Epi 04	**5**	**5×10^{16}**	**734.0 ± 0.2**	**7.1 ± 0.1**	**567.1 ± 0.1**	**3.5 ± 0.1**
Epi 05	**5**	**7×10^{16}**	**734.2 ± 0.2**	**7.2 ± 0.1**	**567.1 ± 0.1**	**3.5 ± 0.1**
Epi 06	**10**	**2.4×10^{17}**	**737.3 ± 0.1**	**10.9 ± 0.3**	**567.1 ± 0.1**	**3.5 ± 0.1**
Epi 07	**5**	**4.7×10^{17}**	**743.6 ± 0.2**	**14.9 ± 0.7**	**567.1 ± 0.1**	**3.5 ± 0.1**
Epi 08	**5**	**1.8×10^{18}**	**764.2 ± 1.2**	**48 ± 2**	**567.1 ± 0.1**	**3.5 ± 0.1**

Table 5. 1: Summary of the E_2^h and the A_1 (LO) mean values derived from the Gauss-Lorentzian fitting.

5.3. RESULT ANALYSIS AND DISCUSSIONS

As reported in the literature, the E_2^h mode can be used to probe the biaxial stress in GaN because of its non-polar behavior [20] while the A_1(LO) is more sensitive to the doping level and allows to determine the free carrier concentration due to its longitudinal and polar features [8]. The analyses in this section will be focused on the study of the above-cited Raman modes behavior with the n carrier concentration influence.

5.3.1. STUDY OF THE E_2^h PEAK VS CARRIER CONCENTRATION

The E_2^h mode behavior shows no change as the carrier density increases. From the quantitative point of view (Table 5.1), E_2^h position and width remain constant with average values of 567.1 cm^{-1} and 3.5 cm^{-1} respectively for all the studied samples. Indeed, as compared to the reference [21], the Si-doping up to 1.8×10^{18} cm^{-3} does not disturb the crystalline quality of the GaN layers grown on GaN substrate.

Cette thèse est accessible à l'adresse : https://theses.insa-lyon.fr/publication/2023ISAL0011/these.pdf
© [A.J.E. N'Dohi], [2023], INSA Lyon, tous droits réservés

We can therefore notice no influence of the Si impurities on the structural quality of the samples. In addition, the non-variation of the E_2^h position and width with the Si concentration confirms its non-sensitivity to the carrier concentration due to its in-plane non-polar displacement during lattice vibration. Moreover, the E_2^h width shift mean value (3.5 cm^{-1}) of the epilayers is close the one found for the GaN substrates (3.6 cm^{-1}) in chapter 4. This indicates that there is barely no crystalline modification between the substrates and the epilayers. As for the stress evaluation, the Epi01 has been taken as the stress-free sample reference due to its non-intentionally doped state. Let us remind that the evaluation of the stress here was only qualitative due to the scatter value of the stress coefficient as mention in chapter 4. Thus, from the table 1, the E_2^h position shift mean value 567.1cm^{-1} is the same as the Si concentration increases. This means that the incorporation of the Si atoms up to the mentioned concentration rate (table 5.1) do not induce any particular stress in the epilayers as compare to the stress free sample. The stress level is the same in each sample despite the increase of the Si concentration up to 1.8×10^{18} cm^{-3}.

5.3.2. STUDY OF THE A_1(LO) PEAK VS CARRIER CONCENTRATION

The A_1(LO) mode was sensitive to the free carrier density. When zooming on the A_1(LO) mode features (figure 5.5), we clearly observe that as the Si concentration increases with moderate levels from 10^{14} cm^{-3} to 7×10^{16} cm^{-3}, the A_1(LO) peak position shifts slightly of +0.9 cm^{-1} (deduced from table 5.1) as well as the width increases by a small amount of +0.9 cm^{-1} (deduced from table 5.1). This position shift and the width broadening, even though small, are only seen for the A_1(LO) mode and not on the E_2^h mode. That reveals that these changes observed in the A_1(LO) behavior are not due to the presence of dislocations or the residual stress effect (Not even observed in the E_2^h mode). Thus, we conclude that they can be solely attributed to a variation of the doping level. In addition, the sharp peak shape at the initial nid state

On the other hand, at higher doping levels starting from 2.4×10^{17} cm^{-3} up to 1.8×10^{18} cm^{-3}, the shift of A_1(LO) peak position becomes important and the width gets larger. Indeed, a gap of 31 cm^{-1} and 42 cm^{-1} can be seen in the A_1(LO) peak position and width respectively. Moreover, the peak intensity is decreasing when the doping increases. These changes in the A_1(LO) behavior as a function of the n-carrier concentration is due to the coupling of the A_1(LO) mode with the carrier oscillation, called Plasmon, through their macroscopic electric field [11, 19] changing the A_1(LO) mode into the LOPC mode. This can be seen in the shape of A_1(LO) mode. The dome-like shape (figure 5.5) at 1.8×10^{18}

Cette thèse est accessible à l'adresse : https://theses.insa-lyon.fr/publication/2023ISAL0011/these.pdf
© [A.J.E. N'Dohi], [2023], INSA Lyon, tous droits réservés

cm^{-3} confirms the presence of interacting quasi-particles such as phonon and plasmon. Indeed, as the carrier density is lower, the coupling of their electric field with that of the A_1(LO) mode is weak. This explains the origin of the small quantification values of the variations of the A_1(LO) position and width found for such doping level. Meanwhile, when the carrier density increases, their electric field coupling with the one of the A_1(LO) modes becomes stronger, inducing the high frequency shift and the broadening of the A_1(LO) peak.

In addition, the sharp A_1(LO) peak shape at the initial NID (non-intentionally doped) sample state expresses the lack of this phonon plasmon interaction. Here only the electric field of the A_1(LO) phonon gets into action during lattice vibration. The intensity of the A_1(LO) phonon remains undamped and higher as well due to the very low carrier concentration. However, the decrease of the phonon intensity with the increase of the carrier concentration indicates the presence of a damping effect that emanates from the progressive influence of the plasmon induced electric field.

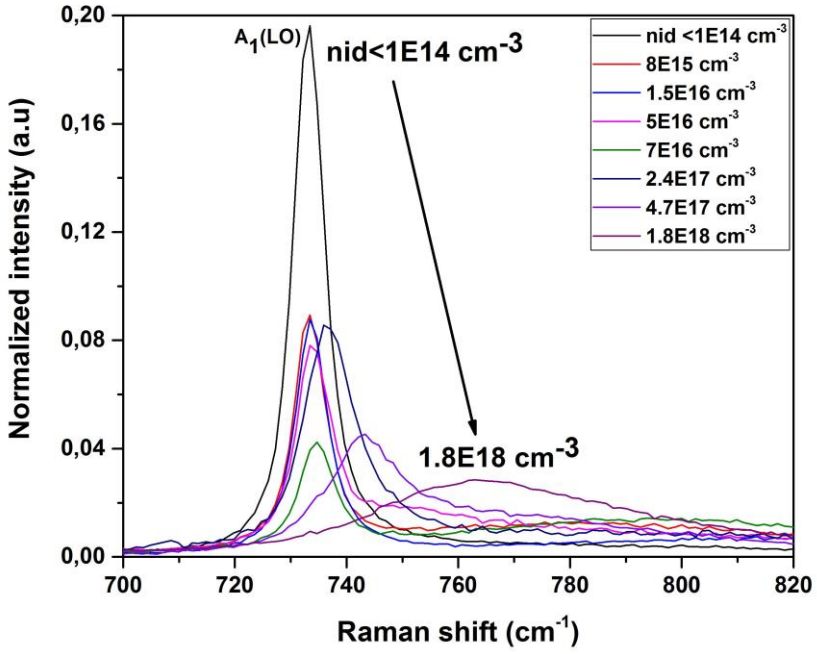

Figure 5. 5: Zoom of the A_1 (LO) Raman peak as the carrier density increases. The nid layer is the non-intentionally doped layer.

Moreover, as the A_1(LO) mode evolves with the free carrier density, we calibrated its frequency position as a function of the carrier concentration. Figure 5.6 shows the evolution of the A_1 (LO) peak position as function of the effective n-carrier density (in log scale). We found out that the overall trend

Cette thèse est accessible à l'adresse : https://theses.insa-lyon.fr/publication/2023ISAL0011/these.pdf
© [A.J.E. N'Dohi], [2023], INSA Lyon, tous droits réservés

of the curve follows a sigmoid growth trend with a Boltzmann fitting as the best matching fit. In details, we can see from the curve that at light doping levels up to 7×10^{16} cm^{-3}, the A_1(LO) position does not shift significantly; while at high doping levels up to 1.8×10^{18} cm^{-3}, its position shifts at higher wavenumber. This means that at higher doping levels, as the carrier density is higher, the coupling with the A_1(LO) mode is stronger and therefore the LOPC mode appears completely. In the transition region from 7×10^{16} cm^{-3} to 2.4×10^{17} cm^{-3}, the plot shows a concave curvature that may indicate the rise of the coupling between the carrier density and the A_1(LO) mode. We suggest that this transition stands for the change of A_1(LO) mode into LOPC mode.

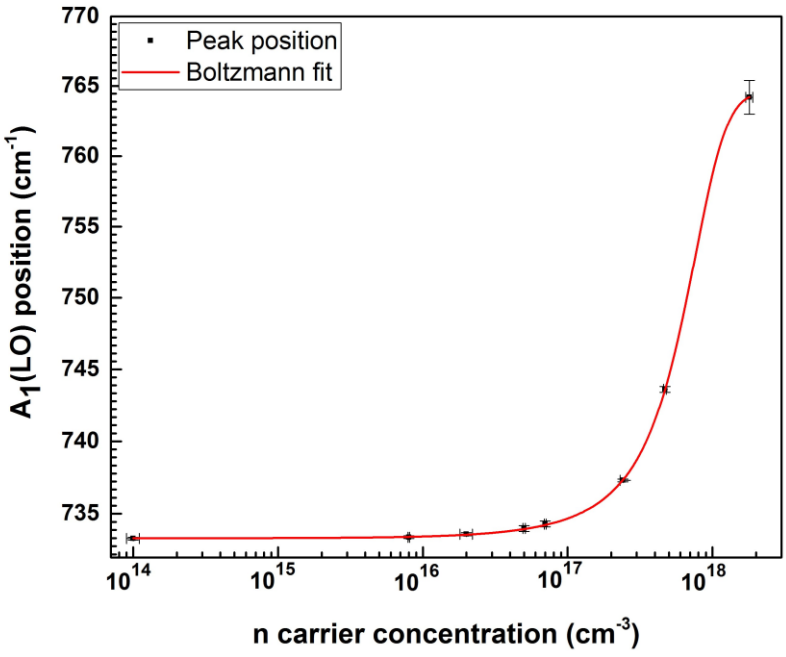

Figure 5. 6: Calibration of the A_1(LO) position as function of the n-doping concentration in log scale. The square dark dots are the experimental data and the red line is the fitting Boltzmann evolution growth curve.

Cette thèse est accessible à l'adresse : https://theses.insa-lyon.fr/publication/2023ISAL0011/these.pdf
© [A.J.E. N'Dohi], [2023], INSA Lyon, tous droits réservés

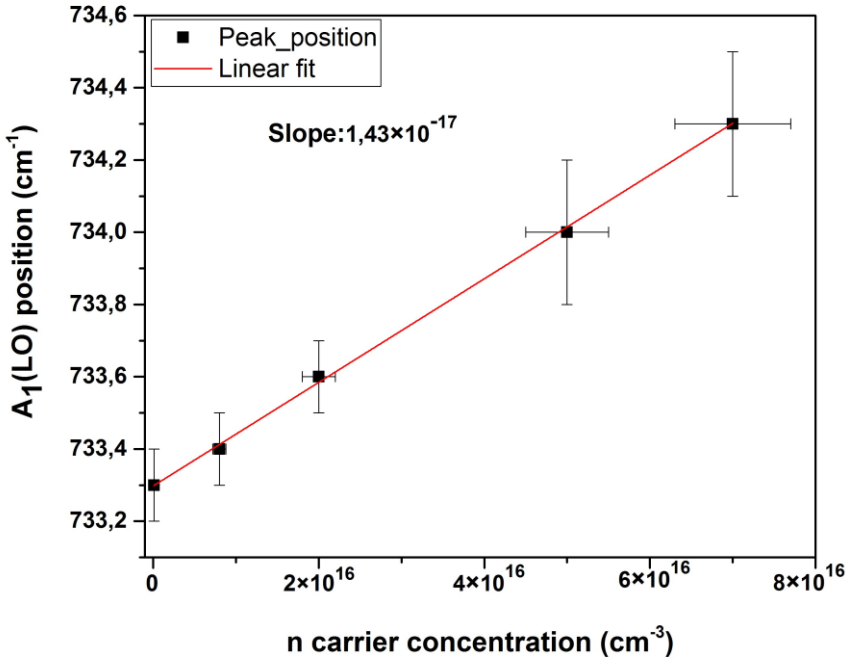

Figure 5. 7: Zoom in the light doping region n < 1017 cm-3 with a linear approximation fit. The error bars of the carrier concentration have been set based on 10% of the initial Si concentration for each sample.

Most importantly, when zooming in the light doping region (figure 5.7), we found out that a linear approximation could be considered as a fitting option, which we expressed in terms of linear equation:

$$\omega_1 = 1.4 \times 10^{-17} n + \omega_0 \quad (1)$$

Where *n* is the n-carrier concentration in cm^{-3}, $\omega_1(A_1(LO)$ is the Raman shift in cm^{-1}) and ω_0 is an offset value of 733.3 cm^{-1} deduced from the plot. The linear approximation in the light doping region may be due to the weak coupling strength between the $A_1(LO)$ electric field and the small carrier density in that region. This linear calibration for the light doping region is newly reported for thin homo-epitaxial GaN layers on freestanding substrate and the considered doping level n < 10^{17} cm^{-3} falls within the usable doping range of GaN Schottky diodes [22]. This light carrier doping is a crucial parameter to get a higher breakdown voltage of the vertical GaN Schottky diodes. In the future, we intend to use this calibration to probe the doping level and the doping homogeneity of GaN epilayers for GaN on GaN vertical Schottky diodes by making 2D maps throughout their respective surface; because homogenous high quality GaN drift layers, (epilayers) are necessary for making high voltage vertical devices [23]. This method would also be adapted to heteroepitaxial GaN samples.

Cette thèse est accessible à l'adresse : https://theses.insa-lyon.fr/publication/2023ISAL0011/these.pdf
© [A.J.E. N'Dohi], [2023], INSA Lyon, tous droits réservés

5.4. CONCLUSION

In this chapter, we show that Raman spectroscopy can be used to probe the structural and electronic properties of n-doped epilayers grown on freestanding GaN substrate by a quantitative analysis of both A_1 (LO) and E_2^h position and FWHM as the carrier density increases from light doping to a higher doping. The A_1 (LO) behavior changes drastically as a function of carrier concentration; especially at a high doping its position, intensity and width shift significantly. Meanwhile the E_2^h mode remains unchanged as the carrier concentration increases. Furthermore, a calibration of the A_1 (LO) position as a function of carrier density was performed to monitor its sensitivity to the doping level. Most importantly, we showed that a linear approximation could be considered to express the A_1 (LO) peak position as function of the n-doping concentration for $n < 10^{17}$ cm^{-3}. Thus, this study shows that micro-Raman is an efficient tool to examine the effect of doping concentration on the crystal quality in GaN material. In the next chapter, we will prospectively examine the homogeneity of the n doping concentration and the crystalline quality in the light doping region of vertical GaN Schottky diodes.

Cette thèse est accessible à l'adresse : https://theses.insa-lyon.fr/publication/2023ISAL0011/these.pdf
© [A.J.E. N'Dohi], [2023], INSA Lyon, tous droits réservés

REFERENCES

[1] Sang, L., Ren, B., Sumiya, M., Liao, M., Koide, Y., Tanaka, A., Cho, Y., Harada, Y., Nabatame, T., Sekiguchi, T. and Usami, S., "Initial leakage current paths in the vertical-type GaN-on-GaN Schottky barrier diodes "Applied Physics Letters, 111(12), pp.122102 (2017).

[2] Yeluri, R., Lu, J., Hurni, C.A., Browne, D.A., Chowdhury, S., Keller, S., Speck, J.S. and Mishra, U.K. "Design, fabrication, and performance analysis of GaN vertical electron transistors with a buried p/n junction." Applied Physics Letters, 106(18), pp.183502 (2015).

[3] Zhang, Y., Sun, M., Liu, Z., Piedra, D., Lee, H.S., Gao, F., Fujishima, T. and Palacios, T., "Electrothermal Simulation and Thermal Performance Study of GaN Vertical and Lateral Power Transistors, » IEEE Transactions on Electron Devices, 60(7), pp.2224-2230 (2013).

[4] Paskova, T., Hanser, D.A. and Evans, K.R., "GaN substrates for III-nitride devices." Proceedings of the IEEE, 98(7), pp.1324-1338 (2009).

[5] Shibata, D., Kajitani, R., Ogawa, M., Tanaka, K., Tamura, S., Hatsuda, T., Ishida, M. and Ueda, T.,"1.7 kV/1.0 mΩcm^2 normally-off vertical GaN transistor on GaN substrate with regrown p-GaN/AlGaN/GaN semipolar gate structure." IEEE International Electron Devices Meeting (IEDM), pp. 10-1 (2016).

[6] Nie, H., Diduck, Q., Alvarez, B., Edwards, A.P., Kayes, B.M., Zhang, M., Ye, G., Prunty, T., Bour, D. and Kizilyalli, I.C.,"1.5-kV and 2.2mΩ-cm^2 Vertical GaN Transistors on Bulk-GaN Substrates." IEEE Electron Device Letters, 35(9), pp.939-941 (2014).

[7] Fu, H., Huang, X., Chen, H., Lu, Z., Baranowski, I. and Zhao, Y., "Ultra-low turn-on voltage and on-resistance vertical GaN-on-GaN Schottky power diodes with high mobility double drift layers." Applied Physics Letters, 111(15), pp.152102 (2017).

[8] Demangeot, F., Frandon, J., Renucci, M.A., Briot, O., Gil, B. and Aulombard, R.L, “Raman determination of phonon deformation potentials in α-GaN”, Solid State communications, 100(4), pp.207-210 (1996).

[9] Wagner, J.M. and Bechstedt, F., "Phonon deformation potentials of α-GaN and-AlN: An ab initio calculation." Applied Physics Letters , 77(3), pp.346-348 (2000).

[10] Chen, K.M., Yeh, Y.H., Wu, Y.H., Chiang, C.H., Yang, D.R., Gao, Z.S., Chao, C.L., Chi, T.W., Fang, Y.H., Tsay, J.D. and Lee, W.I., "Stress and defect distribution of thick GaN film homoepitaxially regrown on free-standing GaN by hydride vapor phase epitaxy", Japanese Journal of Applied Physics, 49(9R), pp.091001 (2010).

Cette thèse est accessible à l'adresse : https://theses.insa-lyon.fr/publication/2023ISAL0011/these.pdf
© [A.J.E. N’Dohi], [2023], INSA Lyon, tous droits réservés

[11] Park, M., Cuomo, J.J., Rodriguez, B.J., Yang, W.C., Nemanich, R.J. and Ambacher, O., "Micro-Raman study of electronic properties of inversion domains in GaN-based lateral polarity heterostructures." Journal of applied physics, 93(12), pp.9542-9547 (2003).

[12] Hushur, A., Manghnani, M.H. and Narayan, J., "Raman studies of GaN/sapphire thin film heterostructures." Journal of Applied Physics, 106(5), pp.054317 (2009).

[13] Harima, H., Sakashita, H. and Nakashima, S.I., "Raman microprobe measurement of under-damped LO-phonon-plasmon coupled mode in n-type GaN." In Materials Science Forum, 264, pp. 1363-1366 (1998).

[14] Richter, E., Stoica, T., Zeimer, U., Netzel, C., Weyers, M. and Tränkle, G., "Si doping of GaN in hydride vapor-phase epitaxy." Journal of electronic materials, 42(5), pp.820-825 (2013).

[15] Harima, H., Sakashita, H., Inoue, T. and Nakashima, S.I, "Electronic properties in doped GaN studied by Raman scattering." Journal of crystal growth, 189, pp.672-676 (1998).

[16] Baliga, B.J, "Gallium nitride devices for power electronic applications." Semiconductor Science and Technology, 28(7), pp.074011 (2013).

[17] Gomila, G. and Bulashenko, "Effects of the epitaxial layer thickness on the noise properties of Schottky barrier diodes." Journal of applied physics, 86(2), pp.1004-1012 (1999).

[18] Fujito, K., Kubo, S., Nagaoka, H., Mochizuki, T., Namita, H. and Nagao, S., "Bulk GaN crystals grown by HVPE." Journal of Crystal Growth, 311(10), pp.3011-3014 (2009).

[19] Ban, V.S, "Mass spectrometric and thermodynamics studies of the CVD of some III–V compounds." Journal of Crystal Growth, 17, pp.19-30 (1972).

[20] Amilusik, M., Wlodarczyk, D., Suchocki, A. and Bockowski, M., "Micro-Raman studies of strain in bulk GaN crystals grown by hydride vapor phase epitaxy on ammonothermal GaN seeds." Japanese Journal of Applied Physics, 58(SC), pp.SCCB32 (2019).

[21] Zhihao, X., Jincheng, Z., Huantao, D., Zhongfen, Z., Qingwei, Z., Hao, X. and Yue, H.,"Stress, structural and electrical properties of Si-doped GaN film grown by MOCVD." Journal of Semiconductors, 30(12), pp.123003 (2009).

[22] Munir, T., Aziz, A.A. and Abdullah, M.J, "Epilayer Thickness and Doping Density Variation Effects on Current-Voltage (IV) Characteristics of n-GaN Schottky Diode." In IEEE International Conference on Semiconductor Electronics, pp. 892-895, (2006).

[23] Schoen, K.P., Woodall, J.M., Cooper, J.A. and Melloch, M.R., "Design considerations and experimental analysis of high-voltage SiC Schottky barrier rectifiers." IEEE Transactions on electron devices, 45(7), pp.1595-1604 (1998).

Cette thèse est accessible à l'adresse : https://theses.insa-lyon.fr/publication/2023ISAL0011/these.pdf
© [A.J.E. N'Dohi], [2023], INSA Lyon, tous droits réservés

Cette thèse est accessible à l'adresse : https://theses.insa-lyon.fr/publication/2023ISAL0011/these.pdf
© [A.J.E. N'Dohi], [2023], INSA Lyon, tous droits réservés

CHAPTER 6: PHYSICAL CHARACTERIZATION OF VERTICAL GAN SCHOTTKY DIODES

Following the previous chapters 4 and 5, we now focus on the GaN based vertical device in this chapter. Through physical characterizations, the studied vertical GaN Schottky diodes physical properties are addressed. These physical properties will be helpful for understanding the electrical performance of this Schottky diodes. Hence, Micro Raman, cathodoluminescence and SIMS have been used concomitantly to shed light on the physical behavior of the Schottky diodes. Details about the physics background of these two characterization tools can be found in chapter 2.

6.1. INTRODUCTION

GaN is interesting for power electronic applications due to its high saturated electron velocities of 2.3×10^7 cm/s [1, 2] its wide band gap of 3.4 eV, its high critical breakdown field of 3.3×10^6 V/cm [3, 4] and also its stability at high temperature. Schottky barriers diodes are of great importance for the electronic device's operations. The structure of most existing GaN power devices is lateral since they are made by epitaxial growth of GaN on a foreign substrate such as sapphire or SiC. However, it has been reported that most conventional high-capacity GaN power devices are of vertical structure [5], because vertical devices provide a higher area efficiency, larger-current density, higher breakdown voltage than lateral devices. Vertical GaN Schottky diodes fabrication includes:

- Low dislocation density that indicates low current leakage resulting from crystalline disturbance of the drift layer and the substrate [6].
- Developing an organometallic vapor phase epitaxial (OMVPE) growth technique applicable to GaN substrates [7].
- Low doping level of the drift layer.

Hence, efficient vertical GaN Schottky diodes will result from the good quality of their drift layer and substrate. That efficiency is usually manifested through their fast switching behavior during operation, their high BV and their low current leakage. This means that a good GaN rectifier has to show fundamentally good physical and microstructural properties after fabrication.

Here in this chapter, we address the structural defects presence and the effective doping homogeneity effects on the quality of the GaN diodes. To investigate these defects, we used mainly a combination of two non-destructive physical techniques such as micro-Raman spectroscopy and cathodoluminescence (CL). The association of the two techniques helps us to study the physical

Cette thèse est accessible à l'adresse : https://theses.insa-lyon.fr/publication/2023ISAL0011/these.pdf
© [A.J.E. N'Dohi], [2023], INSA Lyon, tous droits réservés

properties of the diodes. Thanks to the Raman spectroscopy performed in the backscattering geometry, 2D mappings have been made to observe the structural defects, [8] their activity and the n-doping concentration distribution [9]. The E_2^hpeak shift and width have been used to probe the structural defects and stress distribution in the diodes. The A1 (LO) peak shift has been tracked to analyze the n carrier distribution in the epitaxial layer. The CL measurements helped to highlight the presence of dislocation clusters due to their non-radiative recombination activity. We also conducted the SIMS measurements on the epi drift layer that the presence of background impurities such as carbon (C) and oxygen (O). Thus, this chapter reveals the efficiency of Raman spectroscopy in probing the physical properties of GaN based devices and be a good correlative characterization tool with other physical microelectronics metrology tool.

6.2. EXPERIMENTAL METHOD

The vertical GaN Schottky diodes (SBDs) with different diameters (200 µm, 100 µm and 50 µm) have been fabricated by standard photolithography technique. The circular shape of the diodes comes from the mask design during the lithography process. The Schottky contact (Ni/Au) and the back-side ohmic contact (Ti/Al/Ni/Au) have been made by electron beam deposition technique as mentioned in chapter 3. This Schottky contact was deposited on a five (5µm) µm GaN epilayer, which is generally consider as the drift layer of the diodes. The 5 µm homo-epi-structure has been grown by MOCVD (Metal Organic Chemical Vapor Deposition) method on a GaN HVPE grown freestanding substrate from Saint-Gobain Lumilog [10] and doped with Si. For the scope of this project; Epi02 (8×10^{15} cm^{-3}) and Epi03 ($\sim 2 \times 10^{16} cm^{-3}$) GaN epilayer (see chapter 5) with different Si concentration have been chosen for the Schottky diodes fabrication because their low effective carrier concentration ($n<10^{17} cm^{-3}$). During the doping process, diluted silane (vapor phase) was used to dope the GaN films. The effective doping concentration ($N_d - N_a$ value) of the drift layers was determined initially by Capacitance Voltage (C-V) technique using mercury probe method. These diodes have been displayed and arranged in a Ni frame on a GaN wafer (see chapter 3). Figure 6.1 is the GaN wafers used for this study. We can see the Ni frame containing the diodes and referenced by lines and columns. For example, in Epi02 wafer, the frame L45C36 refers to diodes in the line 45 and column 36 and so on for the other frames.

Cette thèse est accessible à l'adresse : https://theses.insa-lyon.fr/publication/2023ISAL0011/these.pdf
© [A.J.E. N'Dohi], [2023], INSA Lyon, tous droits réservés

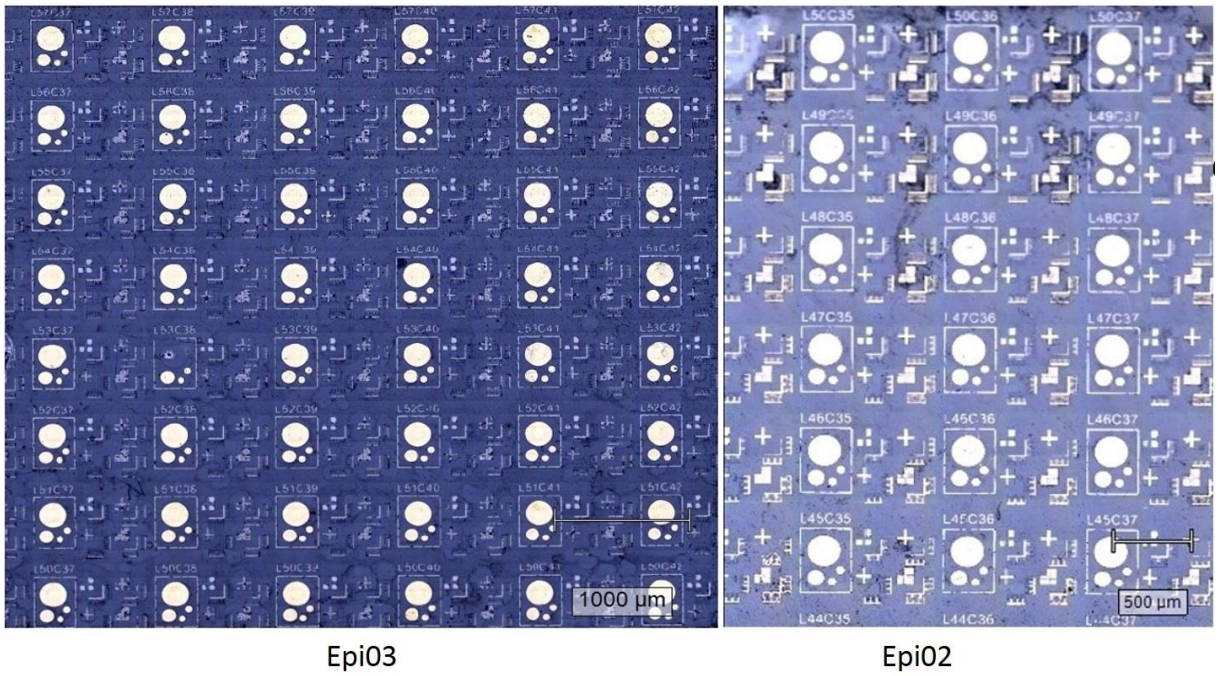

Figure 6. 1: GaN wafer microscope image. Left is GaN Wafer for Epi03) and right is GaN wafer for Epi02

Micro-Raman spectroscopy measurements were carried out at room temperature using a confocal spectrometer (Renishaw Invia model) in back scattering geometry with a ×100 objective lens and a 2400 l/mm diffraction grating. The micro-Raman measurements were carried out after the complete removal of the Ni/Au Schottky contact. The excitation laser source was of 532 nm. The spectral and spatial resolutions were around 0.1cm^{-1} and 1µm respectively. For the Raman measurements, 2D Raman maps have been made on the epilayer of the diodes before metallization. During 2D Raman measurements, cartographies of 500 × 350 µm size with a step size of 5 µm have been performed on each frame containing the diodes (see figure 6.2). From these measurements, series of E_2^h and A_1 (LO) Raman spectra have been obtained and fitted using a mixed Gaussian–Lorentzian function with the Wire 5 Renishaw software (see chapter 4 and 5). Consequently, we extracted from these fitting results, specific E_2^h and A_1 (LO) Raman maps that have been useful to probe the physical properties of the diodes.

Cette thèse est accessible à l'adresse : https://theses.insa-lyon.fr/publication/2023ISAL0011/these.pdf
© [A.J.E. N'Dohi], [2023], INSA Lyon, tous droits réservés

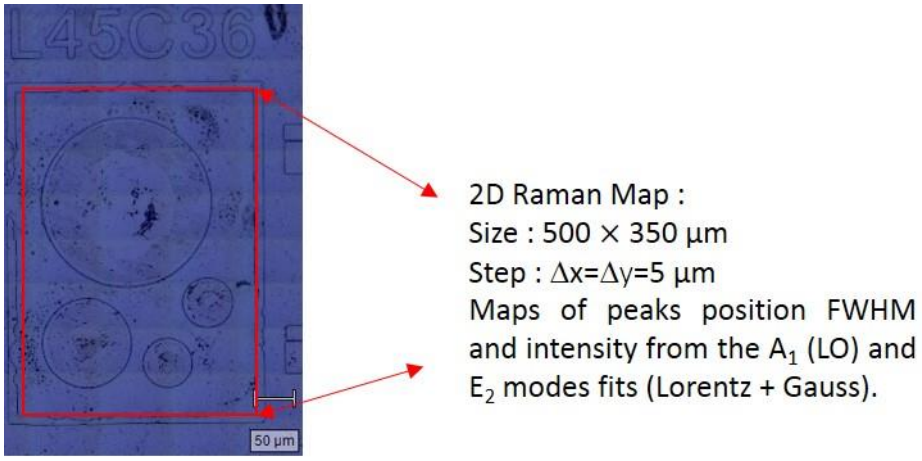

Figure 6. 2: Example of 2D Raman mapping parameters from Epi02 (column C36). Idem for Epi03 (column C38).

As for CL investigation, the images were recorded at room temperature using an acceleration voltage of 10 kV and a magnification of 500× or 1000×. By inspection of 15 CL images for each sample, the dislocation density is found to be 5~10 × 10^6 cm^{-2} in areas of 187 × 500 µm² [11]. The measurements have been conducted in CHREA. We remind that the CL were performed before the metallization and the micro-Raman measurements have been done after removal of the metallization with chemical solution in CHREA in order to explore accurately the drift layer of the diodes. Figure 6.3 is the CL results on L45C36 frames before metallization.

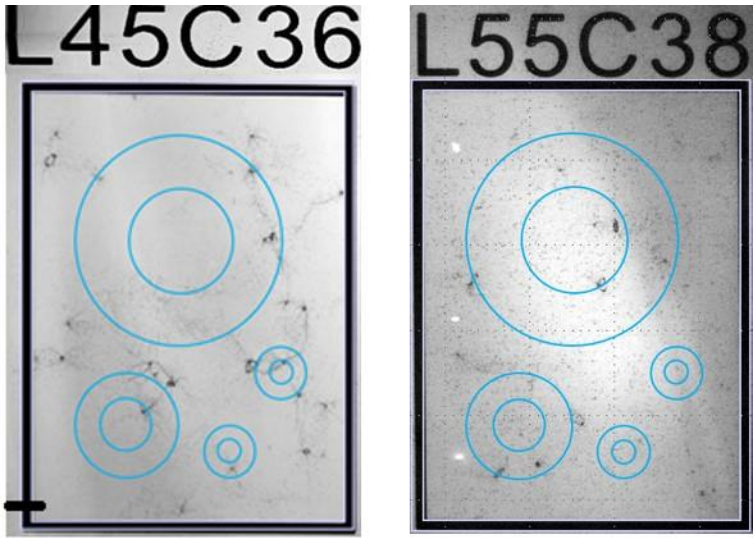

Figure 6. 3: Example of cathodoluminescence images. Left is from Epi02 and right is from Epi03.

In addition, SIMS measurements have been conducted to examine the rate and the presence of (background) impurities in the drift layer of the diodes. Figure 6.4 illustrates the SIMS depth profile for the Si-doped Epi02 GaN film. We clearly see the presence of background impurities such as carbon and oxygen in the drift layer after growth. Close to the surface, very high Si concentration is noticed from the SIMS profile like in the literature reports [12-13]. The depth of this dopant tail from

Cette thèse est accessible à l'adresse : https://theses.insa-lyon.fr/publication/2023ISAL0011/these.pdf
© [A.J.E. N'Dohi], [2023], INSA Lyon, tous droits réservés

the surface to the bulk is about 100 nm. The tail formation may be visualized as follows [12]: during SIMS measurements, the primary ion-beam sputtering can knock the dopant atoms from surface contaminations into a certain depth (about 50 nm) in the epilayer. The tails can be further extended due to the out-diffusion process through the dislocations and grain boundaries. However, beyond this tail (~100 nm), a nearly uniform Si doping density (~2.5×10^{16}cm^{-3}) is observed in the epilayer. A thin layer of highly-doped GaN is regrown on top of the free-standing GaN substrate to ensure that the series resistance will not be limited by the interface contamination (particularly with carbon impurity). For this reason, high concentration of Si-dopants is detected in the regrown region located beyond the depth of 4.2 µm. Overall, the SIMS results reveal that the silicon doping concentration is almost uniform (~2.5×10^{16} cm^{-3}) in the GaN active layer. The presence of carbon and oxygen impurities is not negligible. Even near the surface they also exist in high density as in Si case. From the surface up to 4 µm deep in the epilayer, O and C density is dominant and constant before varying up and down to a certain value respectively when reaching 5 µm deepness. Oxygen is present in the films due to the contamination from ammonia source [14]. The presence of the carbon is due to the methyl group during MOCVD process [15]. We remind that the Epi02 and Epi03 are 5µm thick. The SIMS results are also true for Epi03.

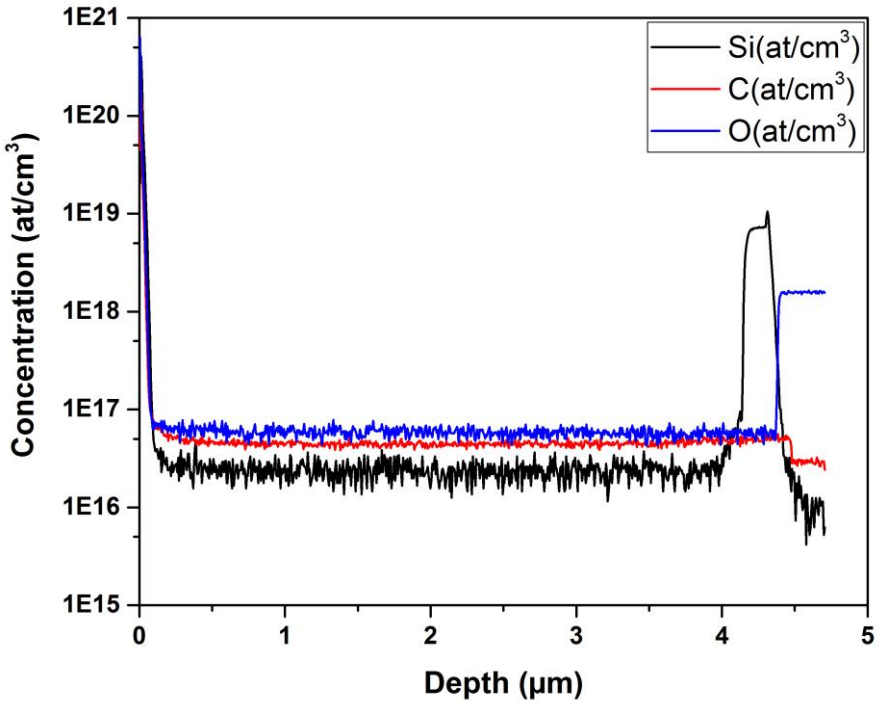

Figure 6. 4: SIMS results on Epi02 sample. The black curve highlights presence of Si dopants (main dopant). The red and the blue curves represent the background impurities in the sample respectively. This result can also be applied to Epi03 samples because they have been grown on the same way with the same instruments.

Cette thèse est accessible à l'adresse : https://theses.insa-lyon.fr/publication/2023ISAL0011/these.pdf
© [A.J.E. N'Dohi], [2023], INSA Lyon, tous droits réservés

6.3. RESULTS AND DISCUSSIONS

6.3.1. STUDY OF THE E_2^h PEAK BEHAVIOR ON EPI02 AND EPI03

Here, by investigating 2D E_2^h Raman maps obtained as described earlier in the experimental method on each Ni frame, the stress and the crystal quality of the diodes drift layer have been assessed. We remind that the Epi02 and Epi03 have a net carrier concentration of 8×10^{15} cm^{-3} and $1\sim 2\times10^{16}$ cm^{-3} respectively. Figure 6.5 shows the E_2^h Raman maps performed on four different frames on the GaN wafer of Epi02 (frames from column C36).

Cette thèse est accessible à l'adresse : https://theses.insa-lyon.fr/publication/2023ISAL0011/these.pdf
© [A.J.E. N'Dohi], [2023], INSA Lyon, tous droits réservés

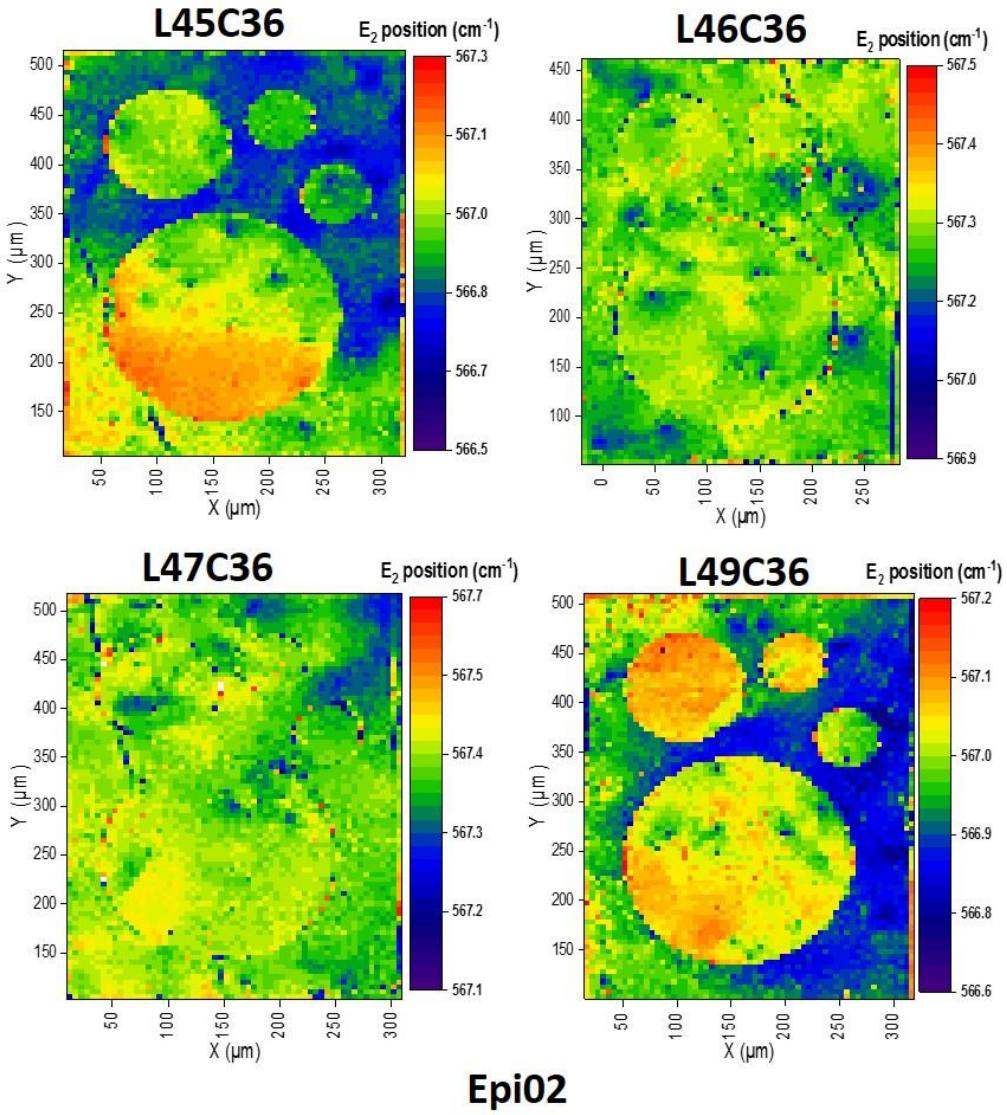

Figure 6. 5: E_2^h position on the four frames (Epi02)

Actually, the wafer of the Epi02 has been cut into two batches. The first batch contains frames from column C36 as mentioned above and the second studied batch contains frames from column C39. However, as the Epi02 second wafer batch has been extremely measured during many experiments such SEM, I (V) T, Raman, it may have been deteriorated after these operations. Therefore, we only examine some of its initial Raman maps in order to show the dislocations that are present on it and correlate them with the cathodoluminescence data. Apart from that, for convenience, all results from Epi02 sample come from the first wafer batch. Table 6.1 summarizes the supporting quantification results extracted from the E_2^h position and width maps obtained by fittings.

Cette thèse est accessible à l'adresse : https://theses.insa-lyon.fr/publication/2023ISAL0011/these.pdf
© [A.J.E. N'Dohi], [2023], INSA Lyon, tous droits réservés

Table 6. 1: E_2^h position and width quantification result for Epi02

Frame Name	E_2^h position (mean value) (cm^{-1})	E_2^h width (mean value) (cm^{-1})
L45C36	567 ± 0.1	3.6 ± 0.1
L46C36	567.3 ± 0.1	3.6 ± 0.1
L47C36	567.4 ± 0.1	3.6± 0.1
L49C36	567 ± 0.1	3.6± 0.1

When considering each frame of the Epi02 epilayer, we clearly see that the E_2^h position mean value does vary from one frame to another one. It starts from 567 cm^{-1} for L45C36 and L49C36 frames to 567.4 cm^{-1} for L47C36 frame. We can notice a gap of 0.4 cm^{-1} on average that is relatively four times higher than the spectral resolution value of our Raman measurements (0.1 cm^{-1}). The average mean value of E_2^h position deduced from the Epi02 is of 567.2 cm^{-1}. This fluctuation indicates that the stress distribution in Epi02 is not homogeneous and therefore the diodes fabricated on it may undergo this stress inhomogeneity. This may be due either to the contribution of some structural defects (dislocations or impurities) presence in Epi02 before fabrication or to the device fabrication such as the mesa etching. However, to confirm that observation, more analyses and measurements based on additional characterization tool would be necessary. Here we only give qualitative description of the stress because of the reason evoked in previous chapter 4 and 5 concerning the computation of the stress.

From the E_2^h width maps fittings (table 6.1), we observe the same order of the width mean value of v = 3.6 ± 0.1 cm^{-1} in all frames either for Epi02. This reveals that all the studied diodes in the Epi02 frames have the same crystalline quality. When referring to ref [16], this value of 3.6 cm^{-1} indicates a good crystalline quality of Si-doped epilayer of the diodes. In addition, based on our measurements, we can see different colors on the E_2^h position maps that correspond to a specific shift in the E_2^h position. As stated previously, a shift of E_2^h position indicates a specific stress level. Therefore, a shift toward the blue zone or the red zone will indicate a lower or higher stress state relatively.

For Epi03, the E_2^h mode behavior was different from the Epi02. Figure 6.6 is the E_2^h Raman maps from four different frames on the GaN wafer of Epi03 (frames from column C38) and table 6.2 shows the supporting quantification results as extracted in the Epi02.

Cette thèse est accessible à l'adresse : https://theses.insa-lyon.fr/publication/2023ISAL0011/these.pdf
© [A.J.E. N'Dohi], [2023], INSA Lyon, tous droits réservés

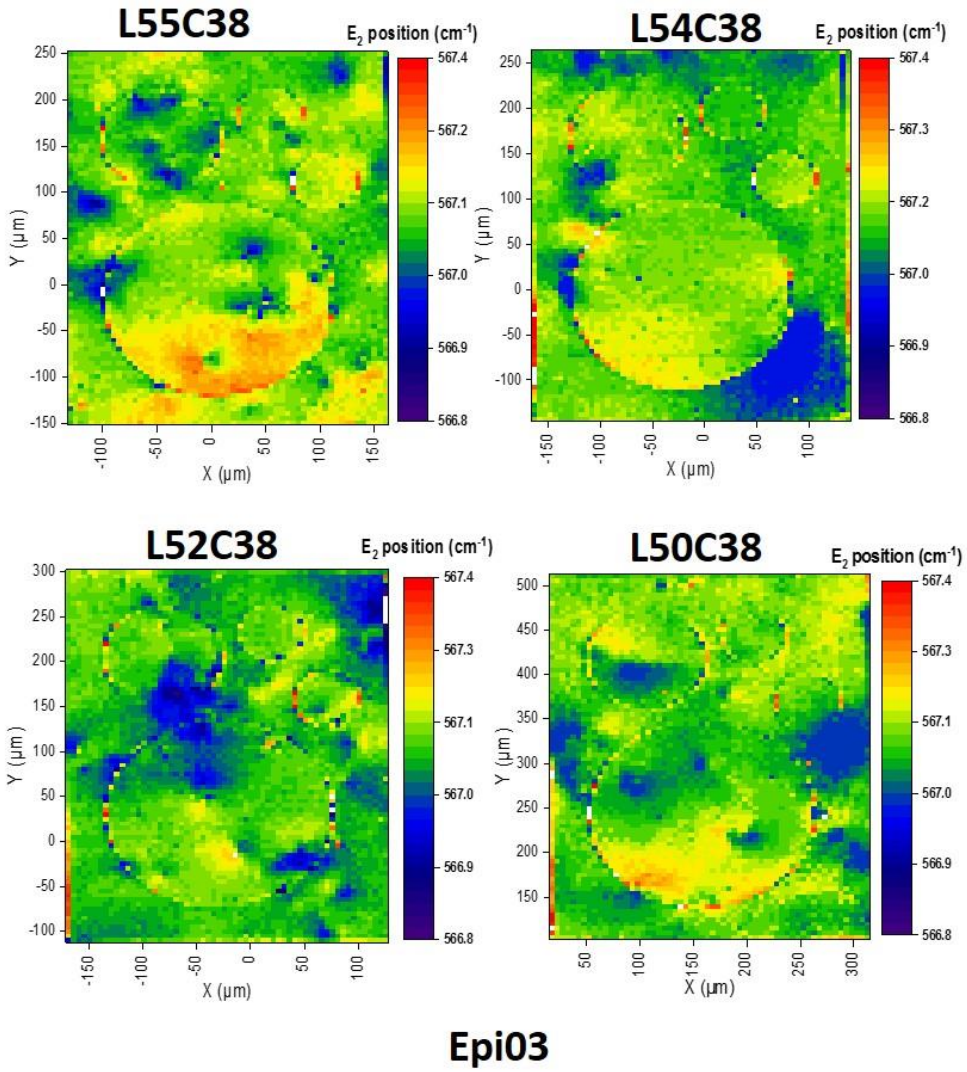

Figure 6. 6: E_2^h position on the four frames (Epi02)

Table 6. 2: E_2^h position and width quantification result for Epi03

Frame Name	E_2^h position (mean value) (cm^{-1})	E_2^h width (mean value) (cm^{-1})
L50C38	567.1 ± 0.1	3.6 ± 0.1
L52C38	567.1 ± 0.1	3.6 ± 0.1
L54C38	567.1± 0.1	3.7 ± 0.1
L55C38	567.1± 0.1	3.7 ± 0.1

Cette thèse est accessible à l'adresse : https://theses.insa-lyon.fr/publication/2023ISAL0011/these.pdf
© [A.J.E. N'Dohi], [2023], INSA Lyon, tous droits réservés

We see that the E_2^h position is constant for the four frames. The mean value of 567.1 ± 0.1 is found. The non-variation in the E_2^h position in this case reveals that the stress level is the same for the four frames and then the diodes fabricated on the Epi03 may have the same stress level. From the E_2^h width maps fittings (table 6.2), we observe on average the same order of the width mean value of around v = 3.6 ± 0.1 cm^{-1} in all frames either for Epi02. This indicates that the crystalline quality of the diodes is also as good as in Epi02.

As interpretation from what we have observed for the two epilayers, we see that the crystalline quality of the drift layer of the diodes is not disturbed although the n carrier concentration increased by order of 10 (Epi03). The Si doping at this n carrier concentration (2 $\times 10^{16}$ cm^{-3}) does not affect the atomic lattice homogeneity in the diodes drift layer. As for the stress state, it is approximately the same in the two drift layers as the average mean value of E_2^h position shift in Epi03 (567.1 cm^{-1}) is close to the one in Epi02 (567.2 cm^{-1}). This means that the E_2^h mode is not really affected by the Si doping as the n carrier concentration increases by order of 10. This confirms what we have found out in chapter 5 concerning the E_2^h mode vs the n carrier concentration. However, that shift observed in Epi02 may be due to the influence of other structural defects such as threading dislocations. In terms of stress distribution, the Epi03 shows a better stress distribution than the Epi02 because the E_2^h position shift fluctuation between the frames in Epi02 is relatively significant than in Epi03. Hence the diodes in Epi03 may experience a better stress distribution than the ones in Epi02.

6.3.2. DISLOCATIONS IN EPI02 AND EPI03

From the E_2^h position Raman maps, we identified the presence of the dislocations observed in the cathodoluminescence image for both Epi02 and Epi03. The E_2^h mode is useful for observing dislocations related defects due to its non-polar in plane behavior during atomic lattice vibration. It is therefore sensitive to any in-plane physical phenomenon that GaN material will undergo. To establish this correlative part, we selected the same frames on which both cathodoluminescence and Raman spectroscopy have been performed. Hence, the observed dislocations in Raman images have been matched zone by zone in accordance with the cathodoluminescence images (figure 6.7 and 6.8). These dislocations are highlighted in blue color, which correspond to a decrease of the E_2^h position, and then appear as low stress area. In the Epi02, that blue zone spans between (566.5 cm^{-1} to 566.8 cm^{-1}), while in Epi03, it extends from 566.8 cm^{-1} to 567.0 cm^{-1}. As stated in chapter 2, three kinds of threading dislocations exist: the edge dislocations (TEDs), the screw dislocations (TSDs) and the mixed

Cette thèse est accessible à l'adresse : https://theses.insa-lyon.fr/publication/2023ISAL0011/these.pdf
© [A.J.E. N'Dohi], [2023], INSA Lyon, tous droits réservés

dislocations (edge and screw) (TMDs). In reference [17], it has been reported that the TSDs do not affect the E_2^h peak shift because the shear strain, which is described as TSDs, has less influence on E_2^h shift. Thus, the screw type dislocations are not detectable by means of Raman peak shift. However, it is still challenging to identify TED and TMD types when they are both present in a GaN sample. Kokubo et al [18] have successfully identified them using Raman spectroscopy. By comparing the contrast spot in E_2^h position maps, they have identified both TEDs and TMDs. The TMDs shows a higher contrast than the TEDs. This implies that the TMDs appear more in the high frequency zone, while the TEDs appear in low frequency zone in the E_2^h position maps. This observation was also supported in reference [19] where theoretical calculations revealed that TMDs have a stronger and more far-reaching stress field. In our study, it seems that the observed dislocation clusters appear only in blue on the Raman E_2^h position map and then correspond to area with a lower stress. This reveals that dislocation clusters may induce a tensile stress in the drift layer of studied the diodes. In addition, it is possible that either the step used for our mapping is too large to observe the compressive stress or that the dislocations observed here are dislocation clusters locally decreasing the stress. Nonetheless, more investigations are requested to reach to that conclusion effectively. Although, we see a good correlation between Raman spectroscopy and the CL method, which confirms the efficiency of the micro-Raman spectroscopy as a powerful and non-destructive tool to probe the presence of the TDs.

Cette thèse est accessible à l'adresse : https://theses.insa-lyon.fr/publication/2023ISAL0011/these.pdf
© [A.J.E. N'Dohi], [2023], INSA Lyon, tous droits réservés

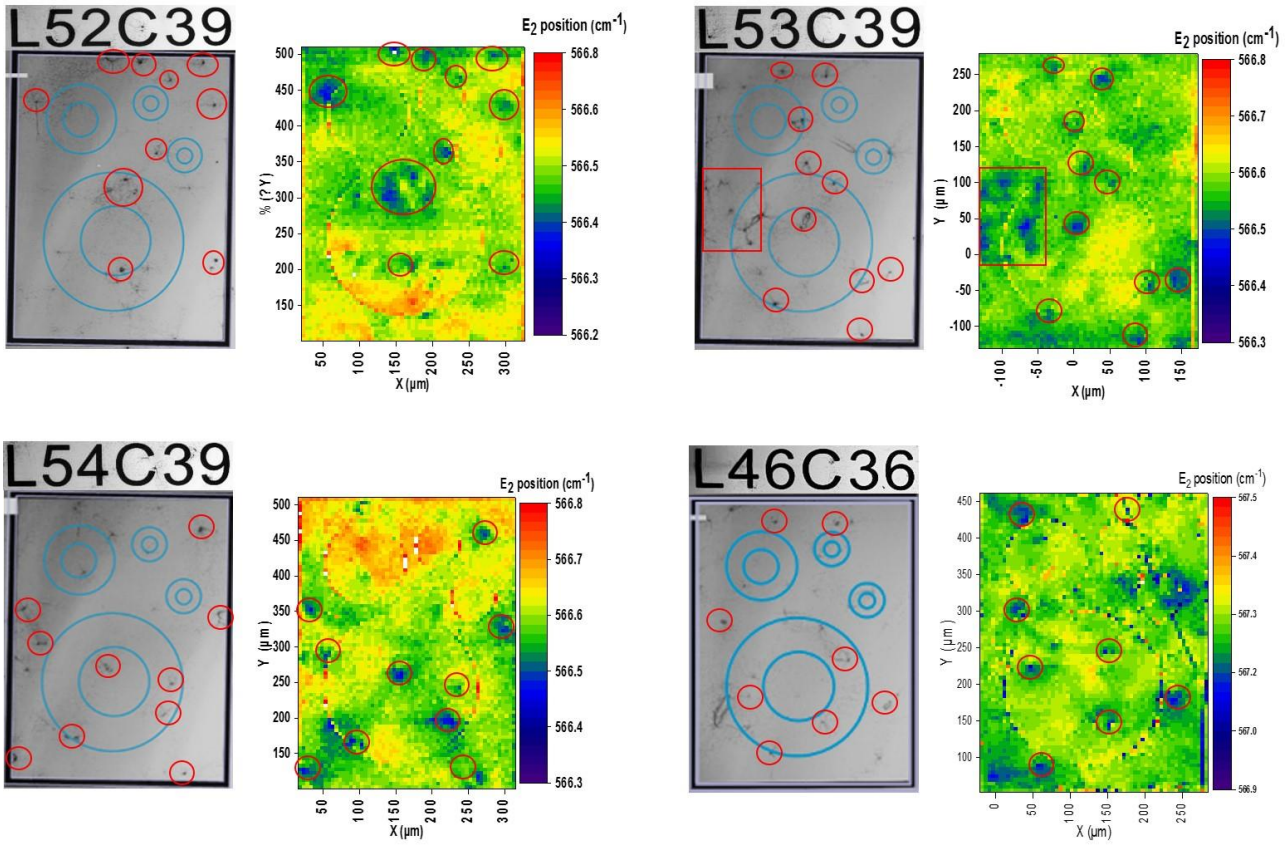

Figure 6. 7: E_2^h position 2D Raman map alongside their corresponding cathodo-luminescence images (scale bar: 100 µm) performed on the diodes for Epi02 (column C39 and C36).

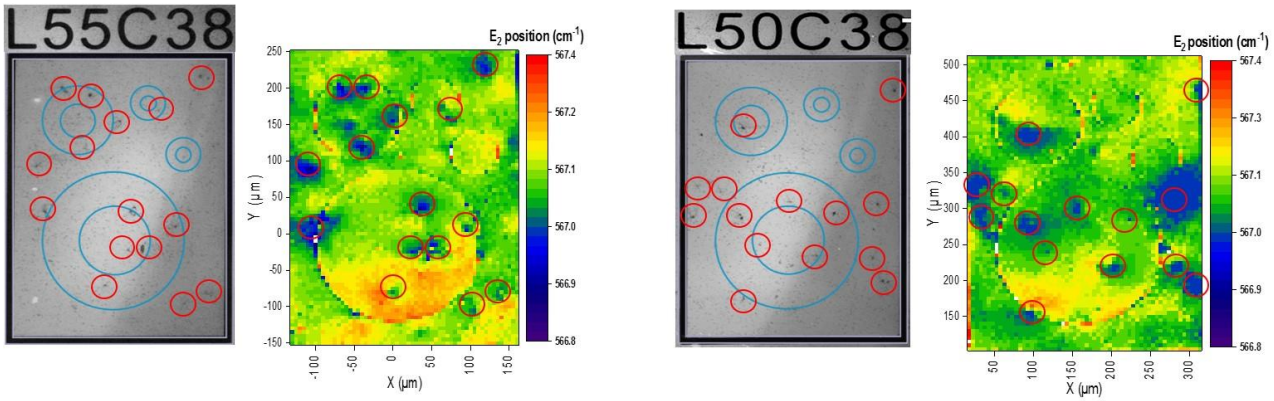

Figure 6. 8: E_2^h position 2D Raman map alongside their corresponding cathodo-luminescence images (scale bar: 100 µm) performed on the diodes for Epi03 (column C38).

Cette thèse est accessible à l'adresse : https://theses.insa-lyon.fr/publication/2023ISAL0011/these.pdf
© [A.J.E. N'Dohi], [2023], INSA Lyon, tous droits réservés

6.3.3. STUDY OF THE A1 (LO) PEAK BEHAVIOR ON EPI02 AND EPI03

The evaluation and the optimization of the carrier concentration of GaN based devices drift layer is important for their electrical performance. The shift in A_1 (LO) position is known to reflect changes in the plasma frequency and therefore necessary to estimate the free-carrier density [20, 21, 22]. By tracking the A_1 (LO) position shift through a Raman mapping, we determined the effective carrier concentration of the diodes. We have shown (see chapter 5) that for n-doped GaN layers with concentration below $n < 10^{17}$ cm^{-3}, the A_1 (LO) position shift is a linear function of the carrier concentration through the equation (2):

$$\omega_1 = 1.4 \times 10^{-17} n + \omega_0 \quad (2)$$

Where n is the n-carrier concentration, ω_1(A_1(LO) is the Raman shift in cm^{-1}) and ω_0 is an offset value of 733.3 cm^{-1} deduced from the plot [23]. This means that any A_1 (LO) position shift value corresponds to a specific carrier concentration and any shift below the offset value will correspond to an undoped region.

From A_1(LO) 2D position maps from the frames in Epi02 as displayed in figures 6.9, we extracted the mean value of A_1(LO) position shift in each frame for Epi02. As we can see, the low doped region is highlighted in blue color because it corresponds to a low value of the A_1(LO) position shift based on the equation 2. The contrast in the four frames is dominated by the many blue zones (733.2 cm^{-1} to 733.4 cm^{-1}) meaning that they have many low and undoped regions. This situation may be due to the presence of peculiar structural defects or impurities (highlighted in blue) linked to the doping process and that actually affect the effective carrier concentration of the Epi02. According to the SIMS results, they may be background impurities such as Oxygen (O) or Carbon (C) or an agglomeration of them since they all exist together in the probed epilayer thickness (5µm). Further analyses are requested to determine the exact nature of the defect that creates this kind of issue.

Cette thèse est accessible à l'adresse : https://theses.insa-lyon.fr/publication/2023ISAL0011/these.pdf
© [A.J.E. N'Dohi], [2023], INSA Lyon, tous droits réservés

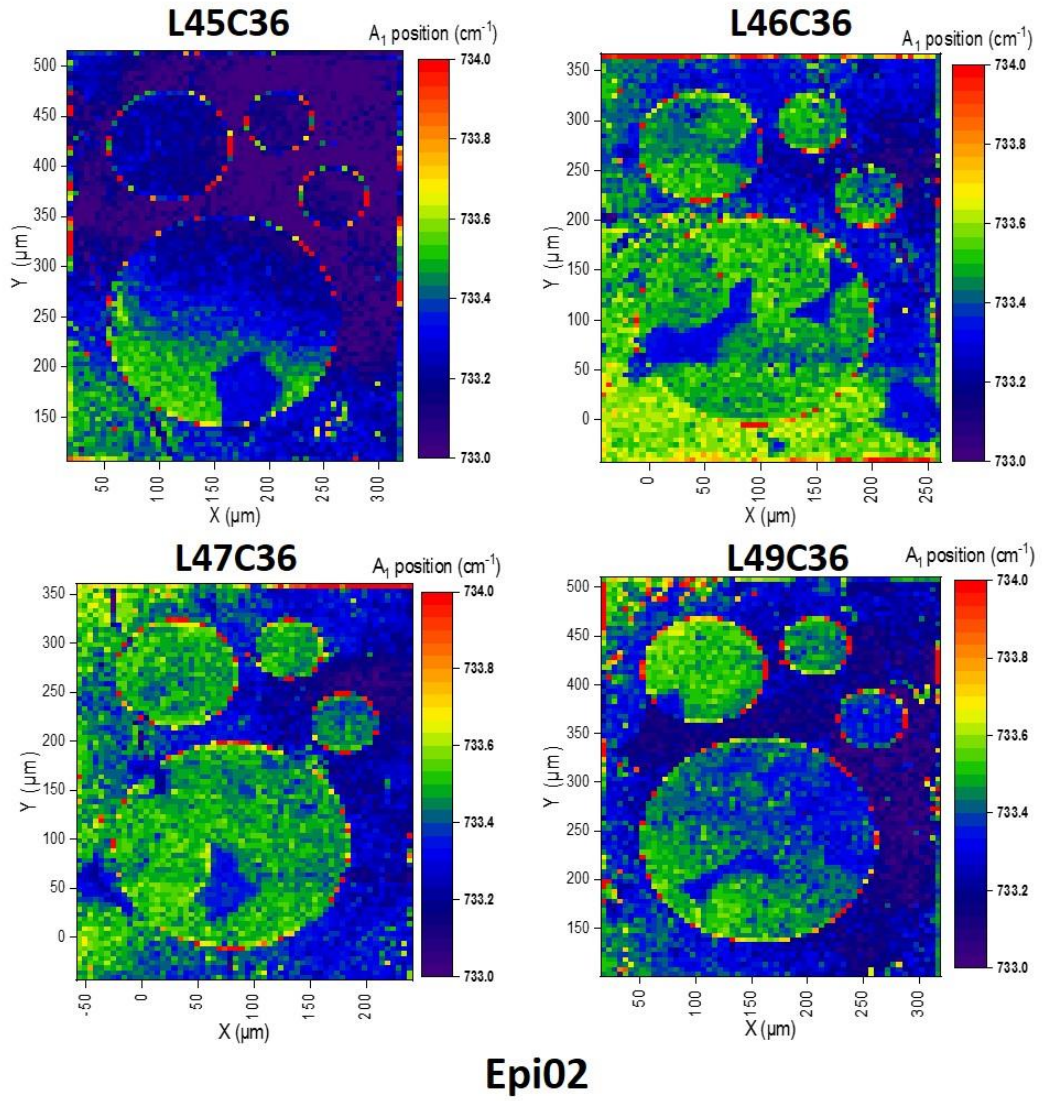

Figure 6. 9: A_1(LO) position maps on the four frames (Epi 02).

Table 6. 3: A_1(LO) position and n carrier concentration quantification result (Epi02).

Frame Name	A_1 (LO) position (mean value) (cm^{-1})	n carrier concentration (mean value) (cm^{-1})
L45C36	733.2 ± 0.1	$<1 \times 10^{15}$± 10%
L46C36	733.4 ± 0.1	9.8×10^{15} ± 10%
L47C36	733.4 ± 0.1	9.8×10^{15} ± 10%
L49C36	733.4 ± 0.1	9.8×10^{15} ± 10%

Cette thèse est accessible à l'adresse : https://theses.insa-lyon.fr/publication/2023ISAL0011/these.pdf
© [A.J.E. N'Dohi], [2023], INSA Lyon, tous droits réservés

Table 6.3 is the computed n carrier concentration in Epi02 frames based on the equation 2. The A_1(LO) position shift mean value varies between 733.2 cm^{-1} (L45C36) and 733.4 cm^{-1} (L47C36). This mean that the n doping is not homogeneous in that epilayer. Using equation 2, the n carrier concentration in the epilayer will vary between the undoped level ($n<10^{14}cm^{-3}$) to nearly $n = 9.8 \times 10^{15}$ cm^{-3}.

From the A_1(LO) 2D intensity maps (Figure 6.10) we observed in Epi02 the presence of red patches (type I) that actually appear in blue in the 2D position maps. In the position maps, they are in the low frequency zone while in the intensity maps they are in the higher intensity zone. This means that they make the A_1(LO) phonon mode shift to lower position with a higher intensity corresponding to a decrease of the n carrier concentration. These patches did not appear in the E_2^h maps. Therefore, they cannot be ascribed to dislocations. Rather, they may stand for impurities (such as carbon or oxygen) inhomogeneous incorporation during the MOCVD growth process.

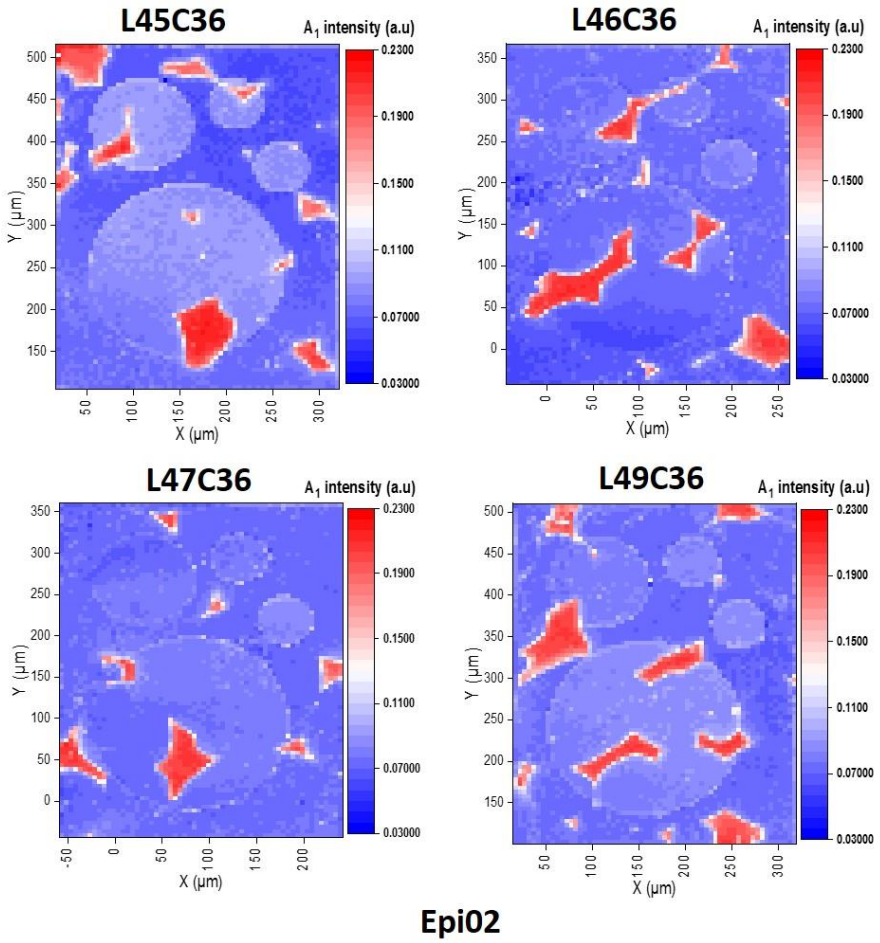

Figure 6. 10: A_1 (LO) intensity maps on the four frames (Epi 02).

Cette thèse est accessible à l'adresse : https://theses.insa-lyon.fr/publication/2023ISAL0011/these.pdf
© [A.J.E. N'Dohi], [2023], INSA Lyon, tous droits réservés

In Epi03, the A_1(LO) position shift mean value is higher than in Epi02. The value is generally around 733.5 cm^{-1} for most of the frames apart from the frame L50C38 which shows a value of 733.44 cm^{-1} ($n = 9.8 \times 10^{15}$ cm^{-3}). This value corresponds to a relatively low carrier concentration as compared to the other frames ($n = 1.6 \times 10^{16}$ cm^{-3}) as we can see in table 4. This is due to the fact that it is significantly covered by the blue zone or less doped regions than the others which significantly lower the effective carrier concentration. Generally, the contrast in the four frames shows less blue zone than in Epi02 frames. Rather, they are relatively covered by a green contrast (733.4 cm^{-1} to 733.6 cm^{-1}) which corresponds to a zone with a relatively higher carrier concentration (see figure 6.11). The presence of different color zones in these frames indicates that the A_1(LO) position shift is not constant over the probed area and therefore the doping in the Epi03 drift layer is not homogeneous. Notably, in the L52C38 and L55C38 frames, we observed some patches (highlighted in black circle) that makes the A_1(LO) position shift to higher frequency or higher concentration zone. This red patch may be due to a defect linked to the doping process.

Cette thèse est accessible à l'adresse : https://theses.insa-lyon.fr/publication/2023ISAL0011/these.pdf
© [A.J.E. N'Dohi], [2023], INSA Lyon, tous droits réservés

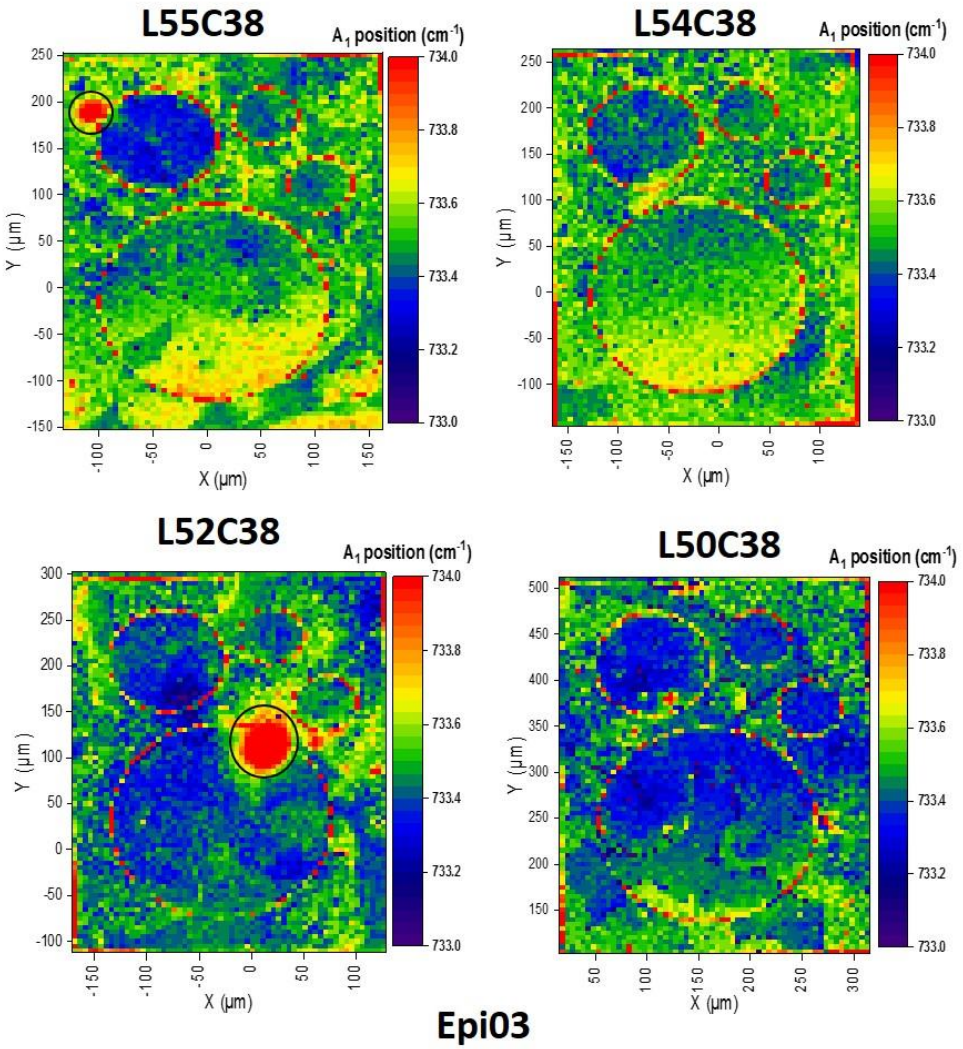

Figure 6. 11: A1 (LO) position maps on the four frames (Epi 03)

The A_1 (LO) intensity maps of the four frames show the same red patches observed in Epi02 (see figure 6.12). These red patches are randomly dispersed across the frames. The L54C38 frame seems to have less of them on its surface while the others have their diodes nearly overlapped by the red patches. This may indicate the activity of these patches on the diodes as they propagate across the frames. Also, they mostly appear in the higher intensity zone as in the Epi02 case. This implies that they decrease the n carrier concentration in the frames.

Cette thèse est accessible à l'adresse : https://theses.insa-lyon.fr/publication/2023ISAL0011/these.pdf
© [A.J.E. N'Dohi], [2023], INSA Lyon, tous droits réservés

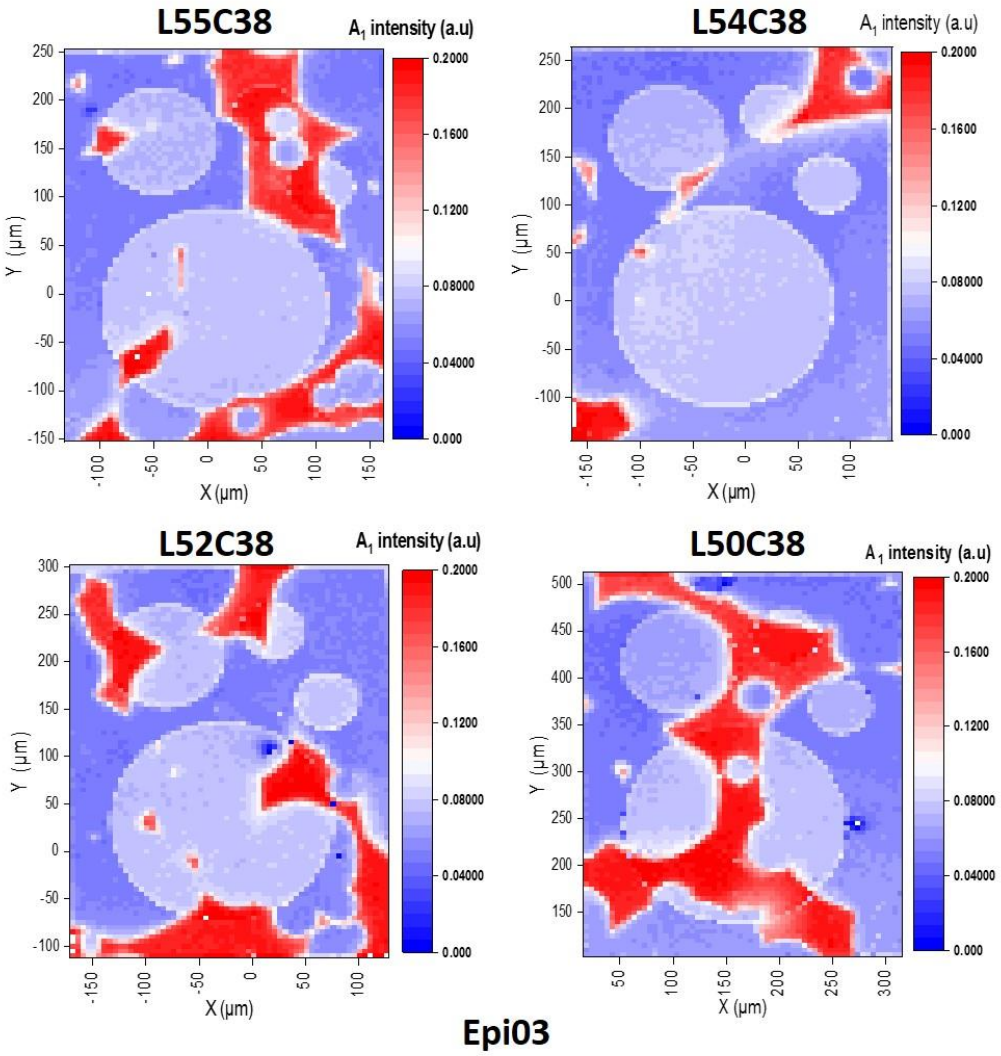

Figure 6. 12: A1 (LO) intensity maps on the four frames (Epi 03).

Table 6. 4: A_1(LO) position and n carrier concentration quantification result (Epi03).

Frame Name	A_1(LO) position (mean value) (cm^{-1})	n carrier concentration (mean value) (cm^{-1})
L50C38	733.4 ± 0.1	9.8×10^{15} ± 10%
L52C38	733.5 ± 0.1	1.6×10^{16}± 10%
L54C38	733.5 ± 0.1	1.6×10^{16}± 10%
L55C38	733.5 ± 0.1	1.6×10^{16}± 10%

Cette thèse est accessible à l'adresse : https://theses.insa-lyon.fr/publication/2023ISAL0011/these.pdf
© [A.J.E. N'Dohi], [2023], INSA Lyon, tous droits réservés

As an interpretation, we can say that the estimated n carrier concentration in the Epi02 and Epi03 based on the equation 2 shows a good correlation between Raman spectroscopy method and C-V mercury probe methods in carrier concentration determination. For instance, in Epi02 and Epi03 the calculated n carrier concentration is n = 8 × 10^{15} cm^{-3} and n = 1.6× 10^{16} cm^{-3} respectively which correlates with the nominal carrier concentration found by CV method. In addition, from the A_1(LO) maps we observed in both cases (Epi02 and Epi03) the presence of red patches (type I) that actually appear in blue in the 2D position maps. In the position maps, they are in the low frequency zone while in the intensity maps they are in the higher intensity zone. This means that they make the A_1(LO) phonon mode shift to lower position with a higher intensity corresponding to a decrease of the n carrier concentration. Therefore, they may be atoms impurities coming from the doping process during fabrication or a spatial inhomogeneity of the n doping. The red patches (type II) observe in A_1(LO) position map of the L52C38 and L50C38 frame in Epi03 appear blue in the intensity map. It makes A_1(LO) mode shift to higher position with a lower intensity. We see that this patch has an opposite behavior than the ones observed above. It induces an increase in the carrier concentration while the one observed above induce a decrease in the carrier concentration. Hence, even though both types of patches that we consider as atom impurities linked to the doping process, we are attempted to classify them based on their role in the doping level. The type I may stand for a p type impurity while the Type II may stand for an n type impurity. Importantly, both types of impurities appear significantly and coexist in the Epi03. It means that the Epi03 drift layer may contains more significant doping defects than the Epi02. Moreover, types I patches appear more elongated and wider in Epi03 than in Epi02. It seems like as the carrier concentration increases by 10 (Epi03), the type I patches tend to agglomerate over the surface, becoming wider and thicker. These patches did not appear in the E_2^h maps. Therefore, they cannot be ascribed to dislocations. Rather, according to the SIMS results, these patches or impurities may stand for impurities (such as carbon or oxygen) inhomogeneous incorporation during the MOCVD growth process. As a result, they seem to affect the doping and its homogeneity in the diodes by apparently locally decreasing the n free carrier concentration.

6.4. CONCLUSION

This chapter shows the efficiency of micro-Raman spectroscopy as a tool to probe structural and electronic properties of GaN based devices. From 2D E_2^h Raman position maps, we observed threading dislocations that correlate well with the cathodoluminescence results from Epi02 and Epi03 GaN films with different Si concentration. In addition, 2D A_1 (LO) position maps from Epi02 and Epi03 have been used respectively to estimate the carrier concentration in the diodes drift layer in correlation with

Cette thèse est accessible à l'adresse : https://theses.insa-lyon.fr/publication/2023ISAL0011/these.pdf
© [A.J.E. N'Dohi], [2023], INSA Lyon, tous droits réservés

the CV mercury probe. Furthermore, from the 2D A_1 (LO) intensity maps mainly, we observed peculiar patches getting thicker and extended in Epi03 than in Epi02. This means that as the n carrier concentration increases (Epi03) these patches morphology also changes. Hence, as they are linked to the A_1 (LO) maps (intensity, position), they may be ascribed to residual impurities from the doping process. From the SIMS results, they may be of C or O background impurities that can affect the local doping homogeneity. In the next and final chapter, we will examine the electrical performance of the diodes in the presence of the observed dislocations clusters and the background impurities.

Cette thèse est accessible à l'adresse : https://theses.insa-lyon.fr/publication/2023ISAL0011/these.pdf
© [A.J.E. N'Dohi], [2023], INSA Lyon, tous droits réservés

REFERENCES

[1] Y. Cao, R. Chu, R. Li, M. Chen, R. Chang, and B. Hughes, Appl. Phys. Lett. 108, 062103 (2016).

[2] R. Chu, A. Corrion, M. Chen, R. Li, D. Wong, D. Zehnder, B. Hughes, and K. Boutros, IEEE Electron Device Lett. 32, 632 (2011).

[3] J. Kolnik, I. H. Oguzman, K. F. Brennan, Wang Rongping, and P. P. Ruden, J. Appl. Phys. 81, 726 (1997).

[4] S. C. Jain, M. Willander, J. Narayan, and R. Van Overstraeten, J. Appl. Phys. 87, 965 (2000).

[5] Ren, Bing, Meiyong Liao, Masatomo Sumiya, Linjun Wang, Yasuo Koide, and Liwen Sang. "Nearly ideal vertical GaN Schottky barrier diodes with ultralow turn-on voltage and on-resistance." Applied Physics Express 10, no. 5, 05, 1001 (2017).

[6] Sumiyoshi, Kazuhide, Masaya Okada, Masaki Ueno, Makoto Kiyama, and Takao Nakamura. "Low on-resistance high breakdown voltage GaN diodes on low dislocation density GaN substrates." SEI Tech. Rev 77: 113. (2013).

[7] T. Horii, T. Miyazaki, Y. Saito, S. Hashimoto, T. Tanabe, M. Kiyama, SEI Technical Review, No.174, p.p.77-80 (2009).

[8] M. Amilusik, D. Wlodarczyk, A. Suchocki, M. Bockowski. Japanese Journal of Applied Physics, 58, SCCB32, (2019).

[9] T. Kozawa, T. Kachi, H. Kano, Y. Taga, M. Hashimoto, N. Koide, K. Manabe, Journal of Applied Physics, 75(2), 1098 (1994).

[10] D. Gogova, H. Larsson, A. Kasic, G.R. Yazdi, I. Ivanov, R. Yakimova, B. Monemar, E. Aujol, E. Frayssinet, J.-P. Faurie, B. Beaumont, P. Gibart, Jpn. J. Appl. Phys., 44, 3, (2005).

[11] T. H. Ngo, R. Comyn, E. Frayssinet, H. Chauveau, S. Chenot, B. Damilano, F. Tendille, Y. Cordier, Journal of Crystal Growth, 552, 125911, (2020).

[12] M.A Reshchikov, M. Vorobiov, O Andrieiev, K Ding, N Izyumskaya, V. Avrutin, A. Usikov, Helava H, Y Makarov. Determination of the concentration of impurities in GaN from photoluminescence and secondary-ion mass spectrometry. Sci Rep 10:.1-7. (2020).

[13] Jr JA Freitas, WJ Moore, BV Shanabrook, GC Braga, SK Lee, SS Park, JY Han, DD Koleske. Donors in hydride-vapor-phase epitaxial GaN. J Cryst Growth, 246: 307-14, (2002).

[14] Popovici, Galina, Wook Kim, Andrei Botchkarev, Haipeng Tang, Hadis Morkoc, and James Solomon. "Impurity contamination of GaN epitaxial films from the sapphire, SiC and ZnO substrates." Applied physics letters 71, no. 23 3385-3387 (1997).

[15] Ciarkowski, Timothy, Noah Allen, Eric Carlson, Robert McCarthy, Chris Youtsey, Jingshan Wang, Patrick Fay, Jinqiao Xie, and Louis Guido. "Connection between carbon incorporation and growth rate for GaN epitaxial layers prepared by OMVPE." Materials 12, no. 15 2455 (2019).

Cette thèse est accessible à l'adresse : https://theses.insa-lyon.fr/publication/2023ISAL0011/these.pdf
© [A.J.E. N'Dohi], [2023], INSA Lyon, tous droits réservés

[16] C. Nenstiel, M. Bügler, G. Callsen, F. Nippert, T. Kure, S. Fritze, A. Dadgar, Physica status solidi (RRL)–Rapid Research Letters 9, 12, 716-721, (2015).

[17] J.-M. Wagner and F. Bechstedt, Phys. Rev. B 66, 115202 (2002).

[18] N. Kokubo, Y. Tsunooka, F. Fujie, J. Ohara, S. Onda, H. Yamada, M. Shimizu, S. Harada, M. Tagawa, T. Ujihara, Japanese Journal of Applied Physics, 58, SCCB06. (2019).

[19] I. Belabbas, A. Béré, J. Chen, P. Ruterana, G. Nouet, Investigation of the atomic core structure of the (a+c)-mixed dislocation in wurtzite GaN, Phys. Status Solidi C 4 2940–2944, (2007).

[20] T. Kozawa, T. Kachi, H. Kano, Y. Taga, M. Hashimoto, N. Koide, and K. Manabe. Journal of Applied Physics, 75, 1098-1101, (1994).

[21] K.M. Chen, Y.H. Yeh, Y. H. Wu, C. H. Chiang, D. R. Yang, Z.S. Gao, C.L. Chao, Japanese Journal of Applied Physics, 49, 091001,(2010).

[22] C. Nenstiel, M. Bügler, G. Callsen, F. Nippert, T. Kure, S. Fritze, A. Dadgar, Physica status solidi (RRL)–Rapid Research Letters 9,12, 716-721, (2015).

[23] E. N'Dohi, C. Sonneville, L.V. Phung, T. H. Ngo, P. De Mierry, E. Frayssinet, H. Maher, Y. Cordier, D. Planson, AIP Advances, 12, 025126, (2022).

Cette thèse est accessible à l'adresse : https://theses.insa-lyon.fr/publication/2023ISAL0011/these.pdf
© [A.J.E. N'Dohi], [2023], INSA Lyon, tous droits réservés

CHAPTER 7: ELECTRICAL CHARACTERIZATION OF VERTICAL GAN SCHOTTKY DIODES

This chapter deals with the electrical characteristics of the Schottky diodes studied in Chapter 6. These diodes have been fabricated on the Epi02 and Epi03 drift layer. One of the reasons of the choice of these two GaN epilayers is that their nominal n doping level is suitable for Schottky diodes electrical performance. Electrical parameters from I (V) forward and reverse characteristics will be addressed. Through that, tentative explanation and conclusion on the quality and the performance of the diodes will be drawn.

7.1. INTRODUCTION

Lateral GaN power devices built on foreign substrates structures have shown good performance with high frequency and high breakdown field [1, 2, 3]. However, structural defects such as lattice mismatch-induced dislocations or current collapse from surface-interface states leads to insufficient power con- version efficiency and current density. Vertical structures are considered to be more suitable for high-power applications since high current density and voltage can be reached alternatively for the same device with reduced on-resistance and less effects from surface-interface states because of the recent availability of free-standing GaN substrates with low threading dislocation (TD) density (on the order of 10^6 cm^{-2} or less). It has been reported that Schottky barrier diodes (SBDs) can show good electrical properties (low on-resistance (R_{on}) and low turn-on voltages (V_{on})) since they do not have the minority carrier storage issue and have higher electron mobility, which is essential for high-power and high-frequency switching applications [4,5]. Recently, some progress has been made in the development of vertical GaN SBDs by increasing the area to increase the output current, optimizing the doping concentration, or controlling the unintentional impurities incorporation [6, 7, 8]. The physical properties of the drift layer will determine the electrical performance of the diodes. Previously, we studied the physical properties of two epilayers (Epi02 and Epi03) on which the GaN Schottky diodes have been designed and fabricated. Here, by analyzing the I(V) characteristics of the vertical diodes under Epi02 and Epi03 with the increase in the n doping level, more information on the performance of the diodes and their quality has been given in addition to their physical properties. Electrical parameters such as ideality factor, turn-on voltage, barrier height and reverse leakage current have been computed and an eventual assessment has been made on the performance of the diodes on Epi02 and Epi03 drift layers. However, to establish an effective

Cette thèse est accessible à l'adresse : https://theses.insa-lyon.fr/publication/2023ISAL0011/these.pdf
© [A.J.E. N'Dohi], [2023], INSA Lyon, tous droits réservés

correlation between the electrical and the physical properties of the diodes, it would be needed to study more devices.

7.2. EXPERIMENTAL METHOD

The vertical GaN Schottky diodes have been homoepitaxially grown on GaN freestanding substrate with a standard photolithography method. Details about that can be found in chapter 3. The I (V) measurements have been performed using SMU power supply (see chapter 3). Low compliance parameters have been set to avoid premature diode burning. The compliance current was 1mA for forward measurement and 100µA for reverse current. The reserve voltage was set at -120V to protect the diodes from breakdown. As the tip, we used for the measurements on the probe station, has a bigger radius, we only measured the 200µm and 100µm diodes from Epi02 and Epi03 drift layers. To reduce the noise signal during the reverse bias measurements of the diodes, we turned off the light of the I (V) station and we conducted all the measurements (forward and reverse) at room temperature.

7.3. RESULTS AND DISCUSSIONS

Here are the results obtained from the I (V) measurements for both Epi02 ($8\times10^{15}cm^{-3}$) and Epi03 ($1\sim2\times10^{16}cm^{-3}$) diodes (100µm, 200µm) in both forward and reverse bias. To probe the electrical performances of the diodes structurally studied in chapter 6, we analyzed exactly the same frame with I(V) measurements.

7.1.1. ELECTRICAL MEASUREMENTS ON THE EPI02 DIODES

Figure 1 and 2 are the forward I (V) plots of both 100µm and 200µm diodes in linear and semi-log scales. From the linear scale, we see that all the diodes show a Schottky diode behavior with a turn-on voltage of at least 0.5V. The turn-on voltage is usually determined by linear interpolation [9] of the I(V) curve. In the semi-log scale, we notice that the diodes have all the same trend below and beyond the average turn-on voltage (0.5V). This implies that the forward current density is independent of the diode size. It also shows that they are dominated by the same forward current conduction mechanism. Previous experimental I (V, T) work on this sample (Epi02) have revealed that they are dominated by the standard thermionic emission (TE) model [10], through the emission of electrons from the semiconductor to the metal over the potential barrier:

Cette thèse est accessible à l'adresse : https://theses.insa-lyon.fr/publication/2023ISAL0011/these.pdf
© [A.J.E. N'Dohi], [2023], INSA Lyon, tous droits réservés

$$J_{TE} = J_s \exp\left(\frac{q(V - IR_s)}{nkT} - 1\right) \qquad (1)$$

$$J_s = A^* T^2 \exp\left(-\frac{q\Phi_B}{kT}\right) \qquad (2)$$

where J_s is the saturation current density, q is the elementary charge, V is the applied bias voltage, I is the resultant current, R_s is the series resistance, k is the Boltzmann constant, T is the temperature, A^* is the Richardson's constant for GaN (26.9 A/cm^{2}K^2 [11]), n is the ideality factor, Φ_B is the Schottky barrier height (SBH). Here the series resistance is not negligible when considering the semi-log plots. Therefore, it needs to be taken into account when evaluating the forward characteristics parameters.

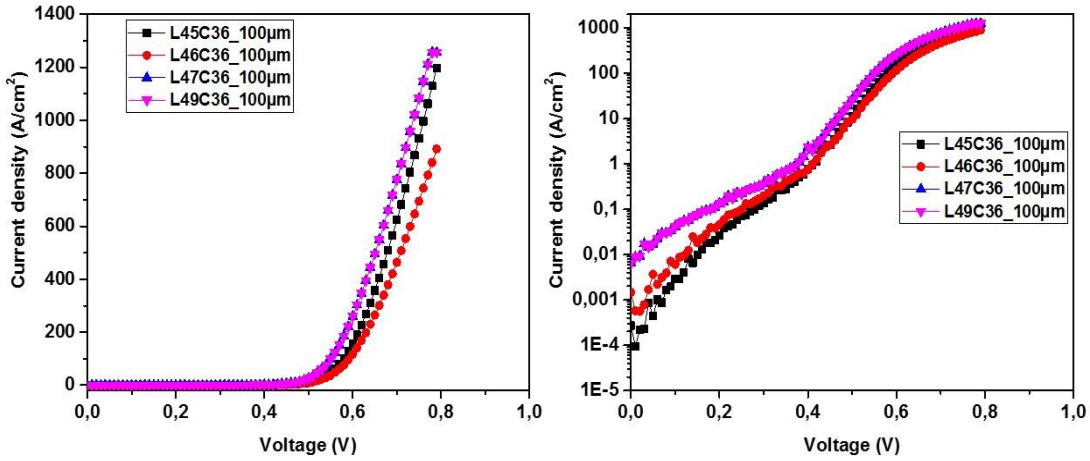

Figure 7. 1: Forwards I (V) plots of 100µm diodes of Epi02 drift layer. Left hand side is the linear scale plot and right hand side is the semi-log scale plot.

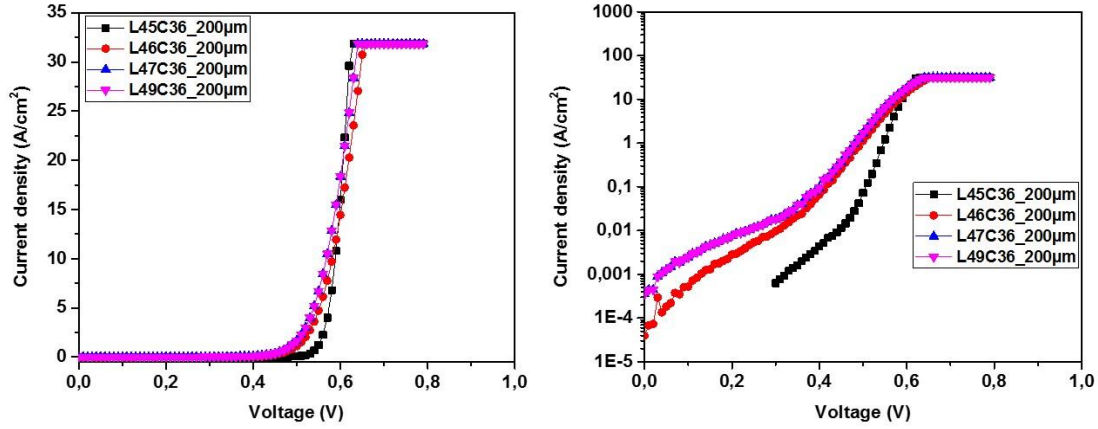

Figure 7. 2: Forwards I (V) plots of 200µm diodes of Epi02 drift layer. Left hand side is the linear scale plot and right hand side is the semi-log scale plot. The constant current density is due to the limitation of the compliance value.

Cette thèse est accessible à l'adresse : https://theses.insa-lyon.fr/publication/2023ISAL0011/these.pdf
© [A.J.E. N'Dohi], [2023], INSA Lyon, tous droits réservés

In reference [12], it has been reported that the SBD parameters (n, Φ_B, and R_s) extracted from the Cheung's method are also consistent with the TE model evaluation of I (V) curve:

$$\frac{\partial V}{\partial \ln(J)} = JA^* R_S + \frac{nkT}{q}$$

With $\frac{\partial V}{\partial \ln(J)}$ the variation of the voltage with regard to the variation of the logarithm value of the current density. The slope of the curve gives the on specific resistance. From the y intercept of the curve, we deduce the ideality factor and therefore compute the barrier height.

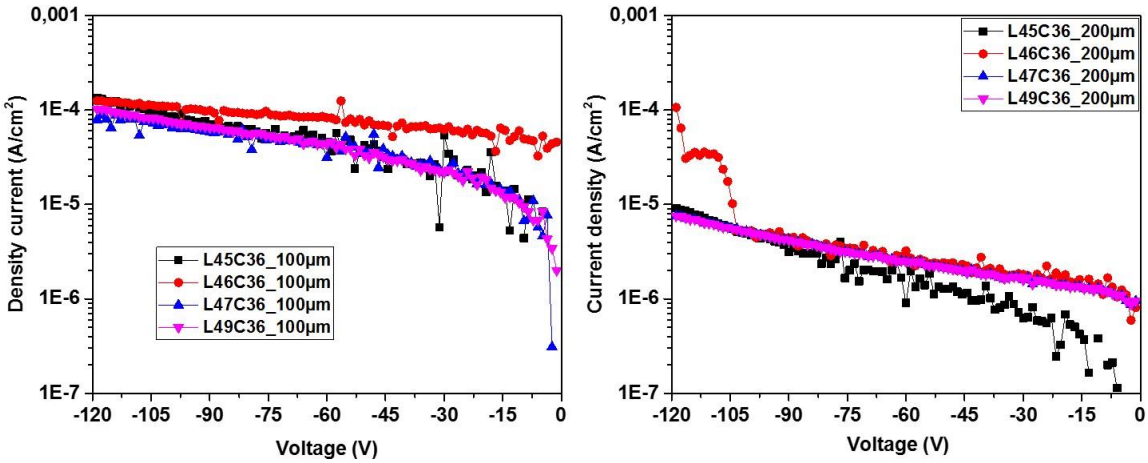

Figure 7. 3: Reverse I (V) semi-log plots of 100µm (left) and 200µm (right) diodes of Epi02 drift layer.

Figure 7. 3 shows the reserve bias behavior of the diodes (100µm_left and 200µm_right) in semi-log scales. In this study, we did not perform any breakdown measurements in order to avoid the total destruction of the diodes. The 100µm diodes have their reverse leakage current density between 8.8×10^{-5}A/cm^2 and 1.1×10^{-4} A/cm^2. The 200µm diodes display a smaller reverse current density from 8.7×10^{-6}A/cm^2 to 1.05×10^{-4} A/cm^2. We also observe that even within each frame the reverse current density is not the same between the 100µm and the 200µm diodes. The L45C36_100µm, L46C36_100µm, L47C36_100µm, L49C36_100µm, and the L46C36_200µm diodes show a higher leakage current density while the L45C36_200µm L47C36_200µm, L49C36_200µm have a lower leakage current density. Hence, we suspect that this discrepancy may be caused by the inhomogeneity of the defect distribution, such as threading dislocations and/or presence of impurity locally modifying the doping as observed in chapter 6, in the Epi02 drift layer. Also, we think that the discrepancy in the reverse leakage current density between 100µm and 200µm can be due to the effet of the perimeter/surface ratio which more important in the 100µm diodes. To wrap this conclusion up efficiently, we suggest more additional characterization methods such as DLTS (deep level transient

Cette thèse est accessible à l'adresse : https://theses.insa-lyon.fr/publication/2023ISAL0011/these.pdf
© [A.J.E. N'Dohi], [2023], INSA Lyon, tous droits réservés

spectroscopy) or EBIC (electron beam induced current) to complete these observations [13, 14]. The value of the parameters, extracted from forwards and reverse electrical characteristics, for all the the diodes of the Epi02 sample are summarized in table 7.1.

Table 7. 1: Extracted values of **n, Φ_B, R_s** *and* J_R *(Reverse leakage current density) for Epi02*

Diodes column C36	Rs [mΩ.cm^2]	n	Φ_B[eV]	Leakage current density [A . cm^{-2}] at -120V
L45C36_100µm	0.61	1.04	0.48	1.40×10^{-4}
L46 C36_100µm	0.68	1.63	0.52	1.26×10^{-4}
L47 C36_100µm	0.42	1.76	0.51	8.8×10^{-5}
L49 C36_100µm	0.23	1.26	0.52	1.1×10^{-4}
L45 C36_200µm	0.05	1.10	0.53	9.62×10^{-5}
L46 C36_200µm	0.87	1.14	0.53	1.05×10^{-4}
L47 C36_200µm	1.17	1.07	0.53	7.70×10^{-6}
L49 C36_200µm	1.86	1.08	0.53	8.70×10^{-6}

We see that the specific on-resistance for both 100µm and 200µm diodes is low from 0.05 to 1.86 mΩ.cm^2. These values are even lower than the ones found in reference [14] where Tsung-Han Yang et al, found a low on specific on-resistance of vertical GaN Schottky diodes (from 1.16 to 1.59 mΩ.cm^2) with field rings. This implies that whatever the size of the diodes, losses will be minimized in these diodes during operation. The ideality factor n varies between 1.04 and 1.76, meaning that they generally conserve their rectifying behavior. The studied diode showing higher ideality factor (L46C36_100µm and L47C36_100µm) or ideality factor not very close to unity may present some secondary mechanisms at the metal-semiconductor interface. In reference [15], it has been reported that these secondary mechanisms may be due to: interfacial dipoles caused by the organic interlayer or a specific interface structure or even fabrication-induced interfacial defects, presence of a wide distribution of low-Schottky barrier patches caused by a laterally inhomogeneous barrier [16], the image-force effect, recombination-generation and tunneling are all possible mechanisms that could lead to an ideality factor greater than unity [17]. These effects actually decrease the quality of the metal-semiconductor contact. Apart from that, the studied diodes showing the ideality factor close to

Cette thèse est accessible à l'adresse : https://theses.insa-lyon.fr/publication/2023ISAL0011/these.pdf
© [A.J.E. N'Dohi], [2023], INSA Lyon, tous droits réservés

unity (L45C36_100µm and L47C36_200µm, L49C36_200µm) have a better metal-semiconductor contact.

Moreover, the barrier height is generally of the same order 0.5eV, it does not really vary with the size of the diode. The 200µm diodes especially have the same barrier height value of 0.53eV; this implies that the diodes may have the same metal-semiconductor interface properties. When considering both diodes size in the same frame, we see that the barrier height value is nearly the same. This also indicates that within the same frame the diodes have the same metal-semiconductor interface properties. As for the reverse leakage current density, the value is scattered within or out of the frames even if this is low in general. The reason behind that discrepancy may be due to what we have said earlier: inhomogeneity in the defect (i.e dislocations and/or presence of impurity) and/or in the stress distribution.

7.1.2. ELECTRICAL MEASUREMENTS ON EPI03 DIODES

We similarly conducted the I (V) measurements on Epi03 diodes as in the Epi02 case. Figure 4 and 5 show the forwards I (V) plots of both 100µm and 200µm diodes in linear and semi-log scales. From the linear scale plot, the 100µm diodes show the rectifying behavior with a turn-on voltage generally around 0.6V. The semi-log plot shows that they all have the same rectifying property. As in the previous case, this rectifying behavior is also dominated by the thermionic emission mechanism. For the 200µm diodes, only diodes from three frames (L50C38, L54C38, L55C38) have the rectifying behavior with a turn-on voltage between 0.5V and 0.6V. The L52C38_200µm diodes however does not show the rectifying behavior. Its behavior from the linear and semi-log plots reveals a huge deviation from a normal Schottky diode. It rather tends to follow a quasi-ohmic behavior. This may be due to a deterioration of the Schottky contact in this diode after fabrication.

Cette thèse est accessible à l'adresse : https://theses.insa-lyon.fr/publication/2023ISAL0011/these.pdf
© [A.J.E. N'Dohi], [2023], INSA Lyon, tous droits réservés

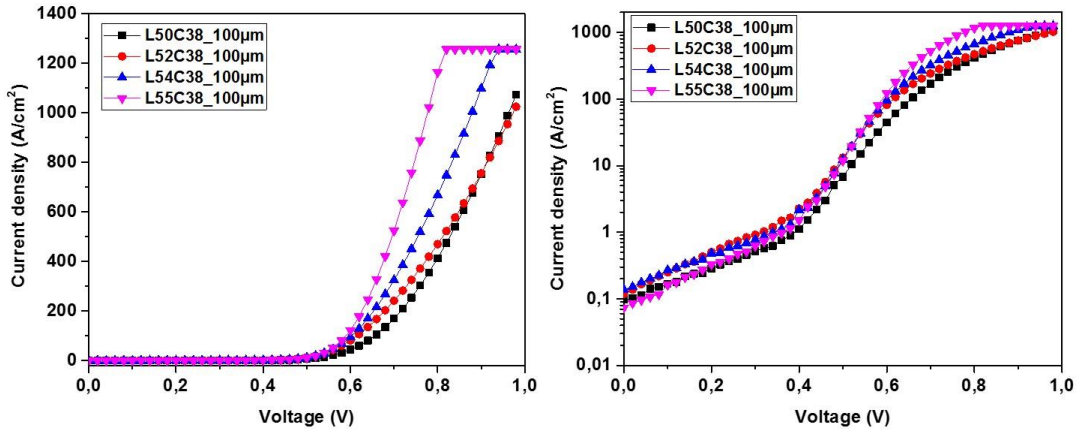

Figure 7. 4: Forward I (V) plots of 100µm diodes of Epi03 drift layer. Left hand side is the linear scale plot and right hand side is the semi-log scale plot.

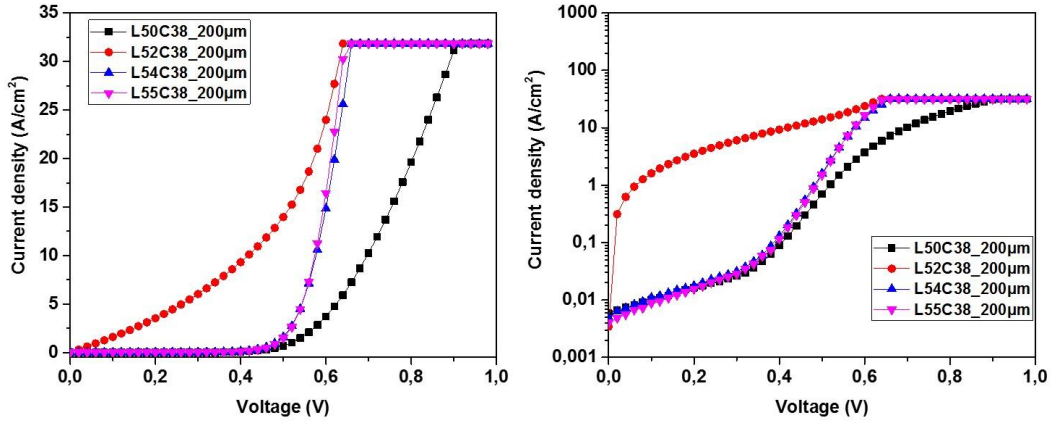

Figure 7. 5: Forward I (V) plots of 200µm diodes of Epi03 drift layer. Left hand side is the linear scale plot and right hand side is the semi-log scale plot.

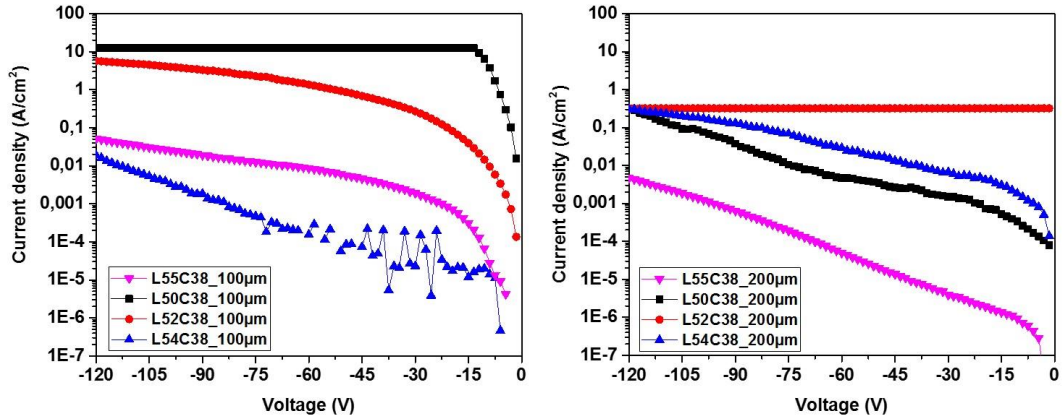

Figure 7. 6: Reverse I (V) semi-log plots of 100µm (left) and 200µm (right) diodes of Epi03 drift layer.

Cette thèse est accessible à l'adresse : https://theses.insa-lyon.fr/publication/2023ISAL0011/these.pdf
© [A.J.E. N'Dohi], [2023], INSA Lyon, tous droits réservés

In reverse bias region (0V $to - 120V$), the 100µm (figure 6_right side) diodes display a pretty higher leakage current density varying between 10^{-2}A/cm^2 $\sim$ 12A/cm^2 order of variation. Among them, the L50C38_100µm and the L52C38_100µm show the highest leakage current density. This may be due to the presence of structural defects (dislocations or impurities) that create more leakage paths in the diodes. For the 200µm diodes (figure 6: left side), the leakage current density is also higher (10^{-3} A/cm^2 $\sim$ 10^{-1}A/cm^2) but less than for the 100µm. The straight line of the L52C38_200µm diode all over the reverse bias region implies that the diode is completely deteriorated. Therefore, we did not go further in evaluating its Schottky parameters. Table 7.2 summarizes the calculated Schottky parameters based on the Cheung's method as in the Epi02 case.

Table 7. 2: Extracted values of* n, Φ_B, R_s *and* J_R *(Reverse leakage current density) for Epi03

Diodes column C38	Rs [m$\Omega.cm^2$]	n	Φ_B[eV]	Leakage current density [A . cm^{-2}] at -120V
L50C38_100µm	0.07	2,11	0,48	12,84
L52C38_100µm	0.06	1,70	0.48	5,92
L54C38_100µm	0.07	1,64	0,49	2×10^{-2}
L55C38_100µm	0.04	1,37	0,50	$5{,}3 \times 10^{-2}$
L50C38_200µm	0.25	1,66	0,39	$3{,}4 \times 10^{-1}$
L52C38_200µm	NO	NO	NO	$3{,}3 \times 10^{-1}$
L54C38_200µm	0.05	1,16	0,51	$3{,}2 \times 10^{-1}$
L55C38_200µm	0.24	1,19	0,52	$4{,}9 \times 10^{-3}$

We see that the specific on-resistance is low for both 100µm and 200µm apart from the L52C38_200µm diode. It is generally between 0.04 and 0.24 m$\Omega.cm^2$, which is even lower than the Epi02 case. This means that during operation losses will be lower in these diodes. Two diodes (L54C38 and L55C38 200 microns) present a rather good ideality factor closed to the unity (1.16 and 1.19 respectively). However for the other diodes, the ideality factor is t far from the unity (1.64 to 2.11) and even higher than in the Epi02 case. This implies that the Schottky contact in these diodes is affected by some interfacial states or defects that create some inhomogeneities at the metal-semiconductor interface. The barrier height value (0.39 $\sim$ 0.52eV) is also lower for most of the diodes as compared with the Epi02 case. There is a slight dispersion in the barrier value for diodes within the

Cette thèse est accessible à l'adresse : https://theses.insa-lyon.fr/publication/2023ISAL0011/these.pdf
© [A.J.E. N'Dohi], [2023], INSA Lyon, tous droits réservés

same frame or out of the frame for both 100µm and 200µm diodes. This indicates an inhomogeneous Schottky barrier height distribution due to interfacial oxide or interface states, at the metal–semiconductor interface as the ideality factor gets higher [18]. The dispersion also in the reverse leakage current density may also be due to some inhomogeneity in the carrier distribution or the defects that create leakage path in the diodes.

7.1.3. MULTI BARRIERS EFFECT IN DIODES OF EPI02 AND EPI03

More importantly, we observe that in the forwards region in particular, the diodes whatever their size, present for both Epi02 ane Epi03 similar trend in the semilog scale (see figure 7.1 and 2, 7.4 and 5). That trend is dominated by a phenomenon called a double barrier effect [19] with a knee at around 0.4V. In the same reference [19], it is said that that phenomenon representing the inhomogeneity of the barrier height, affect the value of the barrier and other forwards parameters such as serie resistance and ideality factor. This explains the low values of the barrier heights and the serie resistance found in our case. In addition, as repoted in references [20, 21], the non-ideality contact of our diodes, is due to the double barrier height effect in parallel displayed by the diodes. The forwards plots in the semi log scale all show a deviation from the nearly ideal case [20]. This also explains the value of the ideality factor of many of our diodes far from the unity (ideal case). In order to understand the physical mechanism behind this effect, it has been concluded in reference [19] that isolated defects, such as point defects, screw dislocations, micropipes, EBIC dark spots, and stacking faults, donot significantly affect the measured barrier heights at room temperature. However, when these defects (specifically point defects, EBIC dark spots, and stacking faults) are clustered in a local area, creating a high local density of defects, a low Schottky barrier height region is created, lowering the effective barrier height of the Schottky contacts and resulting in a nonideal contact. Here in our case, the dislocations clusters and their random distribution in the Epi02 and Epi03 found from the cathodoluminecence measurements may cause this double barrier height phenomenon based on the above-cited reasons. To confirm this assumption in our case, more characterizations are needed as said above.

7.1.4. ELECTRICAL BEHAVIOR AND DOPING CONCENTRATION VARIATION

The impact of the doping concentration can impressively be seen in the I(V) behavior, especially for the reduction of the reverse leakage currents. Also, the performance of the diode in the forward polarisation changes with doping [18]. Here we probe the effect of the doping concentration on the Schottky diodes (100µm, 200µm) as the n carrier concentration increases by almost 10 from $8\times10^{15}cm^{-3}$ (Epi02) to $1\sim2\times10^{16}cm^{-3}$ (Epi03).

Cette thèse est accessible à l'adresse : https://theses.insa-lyon.fr/publication/2023ISAL0011/these.pdf
© [A.J.E. N'Dohi], [2023], INSA Lyon, tous droits réservés

100µm diodes : Table 3 is the evaluation of forward and reverse leakage current parameters for 100µm diodes as the n carrier concentration increases by order of 10. We clearly observe that the forward electrical characteristics are influenced by the carrier concentration. When the n carrier concentration is at $8\times10^{15}cm^{-3}$, the specific on resistance varies between 0.23 and 0.68 $m\Omega.cm^2$. As the carrier concentration increases up to 2×10^{16} cm^{-3} the specific resistance variation becomes lower between 0.04 and 0.07 $m\Omega.cm^2$. This means that the increase in carrier concentration will induce a decrease in the depletion width of the drift layer and therefore the carrier can easily cross the barrier. But this does not mean that diodes with higher carrier concentration are good, rather those with lower carrier concentration will show better performance characteristics. We notice an increase in the ideality factor as the carrier concentration increases. It starts between 1.04 *and* 1.76 at $8\times10^{15}cm^{-3}$ and increases between the interval of 1.37 and 2.11 at $1\text{-}2\times10^{16}cm^{-3}$. This increase in the carrier concentration may affect the quality of the Schottky contact by inducing some doping related defects or impurities that will affect the performance of the Schottky contact. In addition, the barrier height gets slightly lower with the increase in the carrier concentration. This indicates that higher doping level will create some doping related inhomogeneities or defects (type II defects mentioned in chapter 6) in the barrier height distribution and therefore affect the device performance.

Table 7. 3: Evaluation of forward and reverse leakage current parameters for 100µm as the n carrier concentration increases by 10 for Epi02 and Epi03 drift layer.

Diodes column C36 vs C38	Rs [$m\Omega.cm^2$]	n	Φ_B[eV]	Leakage current density [$A.cm^{-2}$] at -120V	Carrier concentration [cm^{-3}]
L45C36_100µm	**0.61**	**1,04**	**0,48**	**$1{,}40\times10^{-4}$**	**8×10^{15}**
L46 C36_100µm	**0.68**	**1,63**	**0,52**	**$1{,}26\times10^{-4}$**	**8×10^{15}**
L47 C36_100µm	**0.42**	**1,76**	**0,51**	**$8{,}8\times10^{-5}$**	**8×10^{15}**
L49 C36_100µm	**0.23**	**1,26**	**0,52**	**$1{,}1\times10^{-4}$**	**8×10^{15}**
L50C38_100µm	0.07	2,11	0,48	12,84	2×10^{16}
L52C38_100µm	0.06	1,70	0.48	5,92	2×10^{16}
L54C38_100µm	0.07	1,64	0,49	2×10^{-2}	2×10^{16}
L55C38_100µm	0.04	1,37	0,50	$5{,}3\times10^{-2}$	2×10^{16}

Cette thèse est accessible à l'adresse : https://theses.insa-lyon.fr/publication/2023ISAL0011/these.pdf
© [A.J.E. N'Dohi], [2023], INSA Lyon, tous droits réservés

As for the reverse the leakage current density, we clearly observe that as the carrier concentration increases, the reverse current density gets higher. Here for the 100µm diodes an increase up 12.84 A/cm^2 is noticed. This is very huge for a vertical Schottky diode of this size. This is due to a reduced resistance as the doping concentration increases. Figure 7 is the semi-log plot of the reverse current density as the carrier concentration increases. It confirms the effect of the doping concentration on the diode electrical performance.

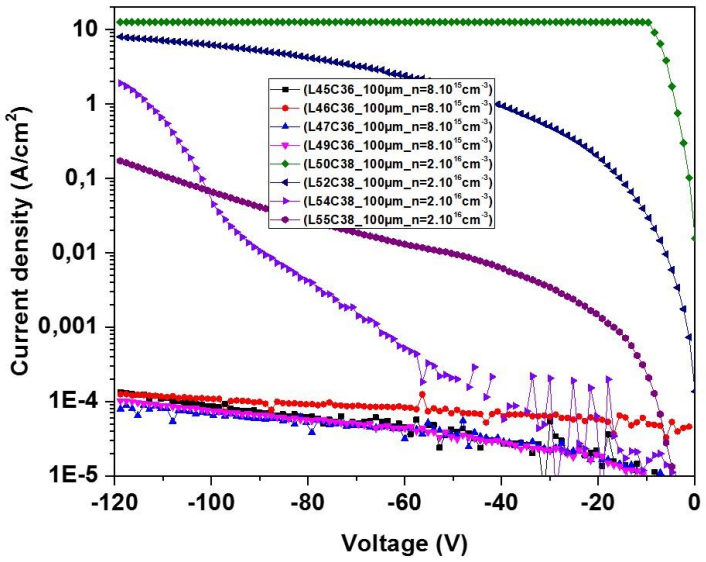

Figure 7. 7: Reverse I(V) plot for 100µm as the n carrier concentration increases by 10 for Epi02 and Epi03 drift layer.

200µm diodes: For the 200µm diodes, the increase of the carrier concentration also affects the forward and the reverse characteristics (Table 7.4). In forward characteristics, we see that the specific on resistance is much lower at 2×10^{16} cm^{-3}, the ideality factor also increases while the barrier height gets lower. This trend was also observed in reference [18], where with higher doping concentration, the ideality factor increases and at the same time the barrier height Φ_B decreases. It has been mentioned in that reference that higher doping normally leads to larger contributions of tunneling currents and also the image force barrier lowering due to the shift of the Fermi level which actually is one of the reasons that creates the observed trend. In addition, the reverse leakage current density is also affected by the carrier concentration. From the table 4 we see that there is a multiplication factor of 10^3 in the reverse leakage current density is noticed when the carrier concentration increases from 8×10^{15} cm^{-3} to 1-2×10^{16} cm^{-3}. This gap (figure 8) indicates that more leakage paths are created in the diodes due to the increase of the doping concentration.

Cette thèse est accessible à l'adresse : https://theses.insa-lyon.fr/publication/2023ISAL0011/these.pdf
© [A.J.E. N'Dohi], [2023], INSA Lyon, tous droits réservés

Table 7. 4: Evaluation of forward and reverse leakage current parameters for 200µm as the n carrier concentration increases by 10 for Epi02 and Epi03 drift layer.

Diodes column C36 vs C38	Rs [mΩ.cm^2]	n	Φ_B[eV]	Leakage current density [A . cm^{-2}] at -120V	Carrier concentration [cm^{-3}]
L45C36_200µm	0.05	1 ,10	0,53	$9{,}62\times 10^{-5}$	8×10^{15}
L46 C36_200µm	0.87	1,14	0,53	$1{,}05\times 10^{-4}$	8×10^{15}
L47 C36_200µm	1.17	1,07	0,53	$7{,}70\times 10^{-6}$	8×10^{15}
L49 C36_200µm	1.86	1,08	0,53	$8{,}70\times 10^{-6}$	8×10^{15}
L50C38_200µm	**0.25**	**1,66**	**0,39**	$\mathbf{3{,}4\times 10^{-1}}$	$\mathbf{2\times10^{16}}$
L52C38_200µm	**NO**	**NO**	**NO**	$\mathbf{3{,}3\times 10^{-1}}$	$\mathbf{2\times10^{16}}$
L54C38_200µm	**0.05**	**1,16**	**0,51**	$\mathbf{3{,}2\times 10^{-1}}$	$\mathbf{2\times10^{16}}$
L55C38_200µm	**0.24**	**1,19**	**0,52**	$\mathbf{4{,}9\times 10^{-3}}$	$\mathbf{2\times10^{16}}$

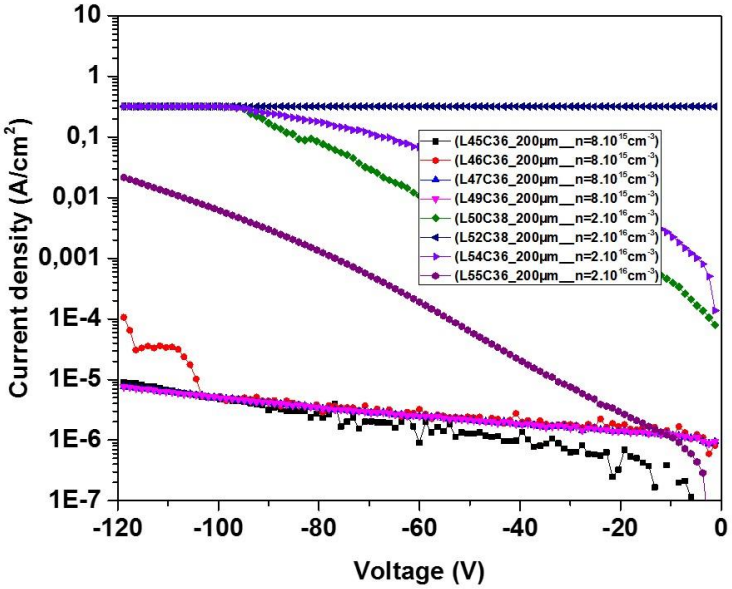

Figure 7. 8: Reverse I(V) plot for 200µm as the n carrier concentration increases by 10 for Epi02 and Epi03 drift layer.

Cette thèse est accessible à l'adresse : https://theses.insa-lyon.fr/publication/2023ISAL0011/these.pdf
© [A.J.E. N'Dohi], [2023], INSA Lyon, tous droits réservés

7.1.5. RAMAN MAPPING AND ELECTRICAL CHARACTERISTICS

We suspect that one of the leakage paths may be linked to the doping process. In chapter 6, we found from the A_1 (LO) Raman maps that defects (type I and II defects) linked to the doping process appear in the drift layer of the diodes and they expand all over the active area of the diodes. For instance, the L50C38 and L52C38 frames cases are more interesting. The type II defects (highlighted in black circles) appear in the drift layer in addition to the type I defects (extended red patches in the intensity maps) when considering their A_1 (LO) Raman maps (figures 7.9 and 10).

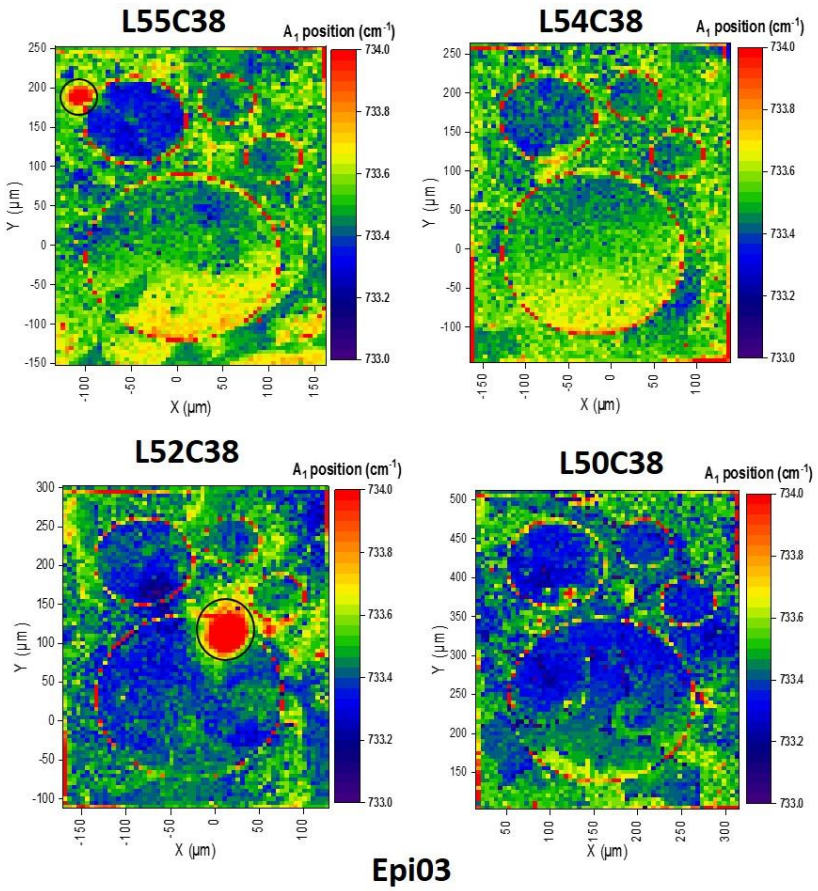

Figure 7. 9: A1 (LO) position maps on the four frames (Epi 03). The type II defects are in black circles.

Cette thèse est accessible à l'adresse : https://theses.insa-lyon.fr/publication/2023ISAL0011/these.pdf
© [A.J.E. N'Dohi], [2023], INSA Lyon, tous droits réservés

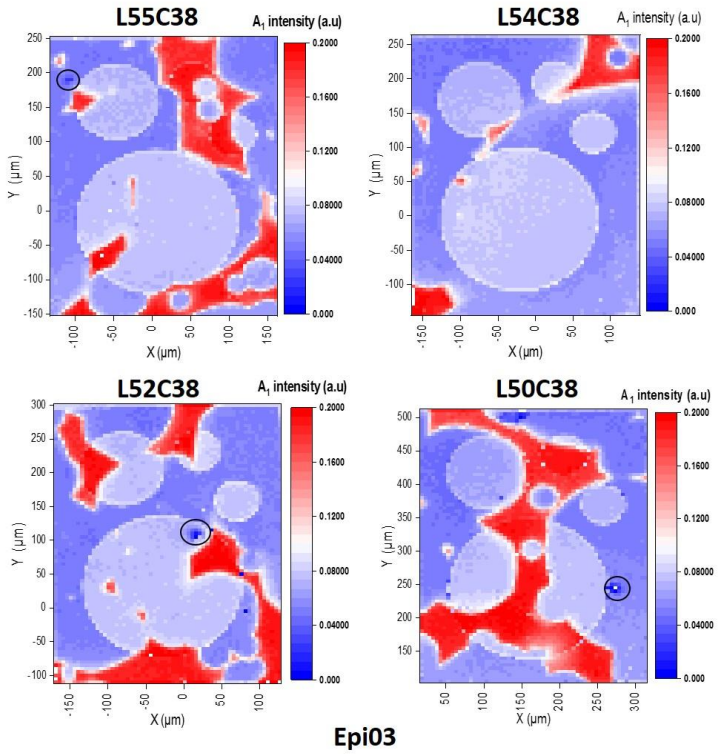

Figure 7. 10: A1 (LO) intensity maps on the four frames (Epi 03). The types I defects are the extended red patches and the type II defects are in black circles.

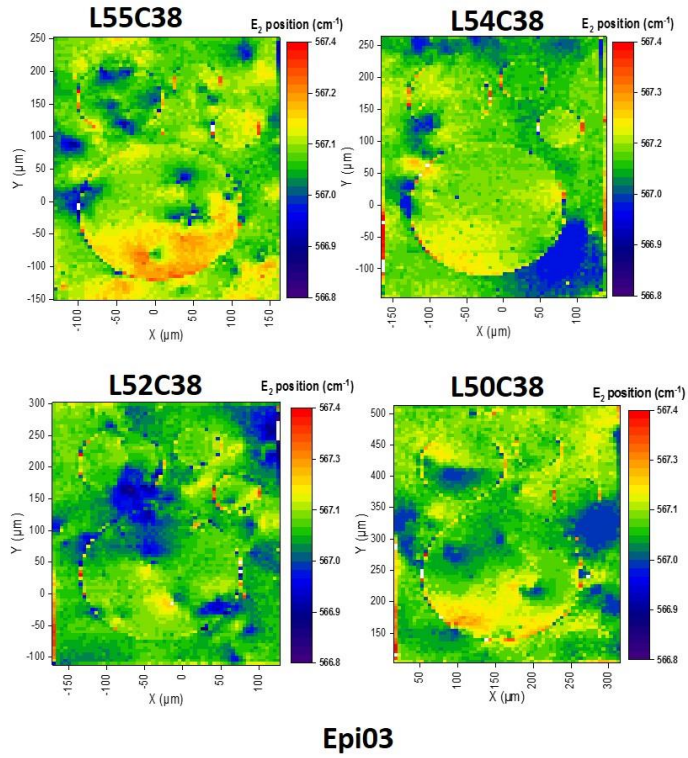

Figure 7. 11: A1 (LO) intensity maps on the four frames (Epi 03). The types I defects are the extended red patches and the type II defects are in black circles.

Cette thèse est accessible à l'adresse : https://theses.insa-lyon.fr/publication/2023ISAL0011/these.pdf
© [A.J.E. N'Dohi], [2023], INSA Lyon, tous droits réservés

According to their Raman characteristics (increase of the A_1 (LO) position and decrease of its intensity), these type II defects seem to corresponds to a local increase of the n-carrier concentration. We then suspect that these types of defects may create more leakage paths due to the doping in the diodes of the frames that contain them.

Also, the presence of the threading dislocations found in chapter 6 is not negligible as they may also be considered as leakage paths that influence the performance of the diode. For instance, in the E_2^h maps of Epi03 (see fig 7.11), the L55C35 (200µm) diodes and L54C38 (100 and 200µm) diodes active area have less dislocations clusters (blue spots) than L50C38 and L52C38 (100 and 200µm) diodes. This may also explain their lower leakage current density found previously. However, we need more additional characterization tool such as DLTS and to chazacterize more devices to conclude on that observation. As for now, we expect that dislocations and the background impurities (type I and II defects) linked to the doping process may be the leakage paths in the drift layer of the diodes and their influence is more visible as the n carrier concentration increases, especially for those linked to the doping process.

7.4. CONCLUSION

We have probed the electrical characteristics of the GaN Schottky diodes of 100µm and 200µm using classical I (V) measurements in both forward and reverse bias region. We noticed that the n carrier concentration plays an important role on both characteristics. In the forward bias, we see that the specific resistance gets lower, the ideality factor increases while the barrier height diminishes. In the reverse bias, the increase in the doping concentration creates an increase in the reverse leakage current density. We infer that the structural defects (dislocations) found in the previous chapter 6 may be responsible of that. Also, as the increase of the reverse current density follows the increase of doping concentration, we suspect that defects as presence of impurities found in the A_1(LO) Raman maps and that are related to the doping process may be responsible of that by creating additional leakage paths in the diodes. In the effort to correlate the physical properties of the diodes in chapter 6 to the electrical properties of the same diodes in this chapter, we suggest that more electrical and physical characterizations such as OBIC (optical beam induced current), 3D Raman spectroscopy, IVT and DLTS will be needed to conclude efficiently on these observations.

Cette thèse est accessible à l'adresse : https://theses.insa-lyon.fr/publication/2023ISAL0011/these.pdf
© [A.J.E. N'Dohi], [2023], INSA Lyon, tous droits réservés

REFERENCES

[1] G. T. Dang, A.P. Zhang, F. Ren, X.A. Cao, S.J. Pearton, H. Cho, J.Han, J.-I. Chyi, C.-M. Lee, C.-C. Cho, S.N.G. Chu, R.G. Wilson, "High voltage GaN schottky rectifiers," IEEE Transactions on Electron Devices, vol. 47, no. 4, pp. 692-696, (2000).

[2] B. Zhang, T. Egawa, G. Zhao, H. Ishikawa, M. Umeno, and T. Jimbo, "Schottky diodes of Ni/Au on n-GaN grown on sapphire and SiC substrates," Applied Physics Letters, vol. 79, no. 16, pp. 2567-2569, (2001).

[3] Y. Zhang, M. Yuan, N. Chowdhury, K. Cheng, and T. Palacios, "720-V/0.35-mΩ·cm2 Fully Vertical GaN-on-Si Power Diodes by Selective Removal of Si Substrates and Buffer Layers," IEEE Electron Device Letters, vol. 39, no. 5, pp. 715-718, (2018).

[4] Wang, Yaqi, Siddharth Alur, Yogesh Sharma, Fei Tong, Resham Thapa, Patrick Gartland, Tamara Issacs-Smith et al. "Ultra-low leakage and high breakdown Schottky diodes fabricated on free standing GaN substrate." Semiconductor Science and Technology 26, no. 2, 022002. (2010).

[5] Zhou, Yi, Mingyu Li, Dake Wang, Claude Ahyi, Chin-Che Tin, John Williams, Minseo Park, N. Mark Williams, and Andrew Hanser. "Electrical characteristics of bulk GaN-based Schottky rectifiers with ultrafast reverse recovery." Applied physics letters 88, no. 11: 113509, (2006).

[6] Saitoh, Yu, Kazuhide Sumiyoshi, Masaya Okada, Taku Horii, Tomihito Miyazaki, Hiromu Shiomi, Masaki Ueno, Koji Katayama, Makoto Kiyama, and Takao Nakamura. "Extremely low on-resistance and high breakdown voltage observed in vertical GaN Schottky barrier diodes with high-mobility drift layers on low-dislocation-density GaN substrates." Applied Physics Express 3, no. 8, 081001. (2010).

[7] Ren, Bing, Meiyong Liao, Masatomo Sumiya, Linjun Wang, Yasuo Koide, and Liwen Sang. "Nearly ideal vertical GaN Schottky barrier diodes with ultralow turn-on voltage and on-resistance." Applied Physics Express 10, no. 5, 051001. (2017).

[8] Tanaka, Nariaki, Kazuya Hasegawa, Kota Yasunishi, Noriaki Murakami, and Tohru Oka. "50 A vertical GaN Schottky barrier diode on a free-standing GaN substrate with blocking voltage of 790 V." Applied Physics Express 8, no. 7, 071001. (2015).

[9] Fu K, Fu H, Huang X, Yang TH, Cheng CY, Peri PR, Chen H, Montes J, Yang C, Zhou J, Deng X. Reverse leakage analysis for as-grown and regrown vertical GaN-on-GaN Schottky barrier diodes. IEEE J Electron Devices Soc; 8:74-83, (2020).

Cette thèse est accessible à l'adresse : https://theses.insa-lyon.fr/publication/2023ISAL0011/these.pdf
© [A.J.E. N'Dohi], [2023], INSA Lyon, tous droits réservés

[10] Maeda, Takuya, Masaya Okada, Masaki Ueno, Yoshiyuki Yamamoto, Tsunenobu Kimoto, Masahiro Horita, and Jun Suda. "Temperature dependence of barrier height in Ni/n-GaN Schottky barrier diode." Applied Physics Express 10, no. 5, 051002 (2017).

[11] Ngo, Thi Huong, Rémi Comyn, Eric Frayssinet, Hyonju Chauveau, Sébastien Chenot, Benjamin Damilano, Florian Tendille et al. "Cathodoluminescence and electrical study of vertical GaN-on-GaN Schottky diodes with dislocation clusters." Journal of Crystal Growth 552, 125911. (2020).

[12] Ha, Sieu D., R. Jaramillo, D. M. Silevitch, Frank Schoofs, Kian Kerman, John D. Baniecki, and Shriram Ramanathan. "Hall effect measurements on epitaxial SmNiO 3 thin films and implications for antiferromagnetism." Physical Review B 87, no. 12, 125150. (2013).

[13] D. V. Lang, "Deep-level transient spectroscopy: A new method to characterize traps in semiconductors," J. Appl. Phys., vol. 45, no. 7, pp. 3023-3032, (1974).

[14] A. Pugatschow, R. Heiderhoff, and L. J. Balk. Microelectronics Reliability 47, 1529-1533, (2007).

[15] Yang, Tsung-Han, Houqiang Fu, Kai Fu, Chen Yang, Jossue Montes, Xuanqi Huang, Hong Chen et al. "Vertical GaN-on-GaN Schottky barrier diodes with multi-floating metal rings." IEEE Journal of the Electron Devices Society 8: 857-863. (2020).

[16] Janardhanam, V., I. Jyothi, Ji-Hyun Lee, Jae-Yeon Kim, V. Rajagopal Reddy, and Chel-Jong Choi. "Electrical properties and carrier transport mechanism of Au/n-GaN schottky contact modified using a copper pthalocyanine (CuPc) interlayer." Materials Transactions: M2013449. (2014).

[17] Tung, R. T. "Electron transport at metal-semiconductor interfaces: General theory." Physical Review B 45, no. 23 13509. (1992).

[18] Contacts, Metal-Semiconductor. "E.H Rhoderick and R.H. Williams." Clarendon, Oxford 1-70. (1988).

[17] Iucolano, Ferdinando, Fabrizio Roccaforte, Filippo Giannazzo, and Vito Raineri. "Temperature behavior of inhomogeneous Pt⁄ Ga N Schottky contacts." Applied Physics Letters 90, no. 9: 092119. (2007).

[18] Witte, W., D. Fahle, H. Koch, M. Heuken, H. Kalisch, and A. Vescan. "Electrical properties of quasi-vertical Schottky diodes." Semiconductor Science and Technology 27, no. 8: 085015. (2012).

Cette thèse est accessible à l'adresse : https://theses.insa-lyon.fr/publication/2023ISAL0011/these.pdf
© [A.J.E. N'Dohi], [2023], INSA Lyon, tous droits réservés

[19] Ewing, D. J., L. M. Porter, Q. Wahab, X. Ma, T. S. Sudharshan, S. Tumakha, M. Gao, and L. J. Brillson. "Inhomogeneities in Ni⁄4 H-Si C Schottky barriers: Localized Fermi-level pinning by defect states." Journal of applied physics 101, no. 11 114514. (2007).

[20] Defives, D., O. Noblanc, C. Dua, C. Brylinski, M. Barthula, and F. Meyer. "Electrical characterization of inhomogeneous Ti/4H–SiC Schottky contacts." Materials Science and Engineering: B 61 395-401. (1999).

[21] Skromme, B. J., E. Luckowski, K. Moore, M. Bhatnagar, C. E. Weitzel, T. Gehoski, and D. Ganser. "Electrical characteristics of Schottky barriers on 4H-SiC: The effects of barrier height nonuniformity." Journal of Electronic Materials 29, no. 3 376-383. (2000).

Cette thèse est accessible à l'adresse : https://theses.insa-lyon.fr/publication/2023ISAL0011/these.pdf
© [A.J.E. N'Dohi], [2023], INSA Lyon, tous droits réservés

CONCLUSION

In this thesis, we have confronted the physical and electrical properties of GaN material and devices through multiphysics characterizations approach. A combination of non-destructive characterization tools such as micro-Raman spectroscopy and cathodolumiscence tool was mainly used to probe the physical properties of the GaN material and devices and the classical I(V) measurements were performed to probe the electrical behavior of the devices. Starting from the theoretical background on GaN and the state of the art on GaN devices in chapter 1, we went into details on the fundamental aspects of the physical characterization's methods and the electrical measurements we used during this project in chapter 2 and 3 respectively. The understanding of the physics that supports these methods helped us to address the problematic of the thesis project stated in the general introduction. Hence, our approach in facing the thesis project starts from the investigation of GaN materials quality to the GaN device performance. Therefore, in chapter 4, we investigated some freestanding n-doped GaN substrates with Si, Ge and O_2 using Raman spectroscopy because having a good devices performance requires a highly doped and good crystalline quality native substrate. In these substrates, we probed the residual stress and crystalline quality of n-doped freestanding GaN substrates quantitatively by tracking the E_2^h mode using Raman spectroscopy. We shed light on the possible effect of the dopants in the microstructural properties of the substrates. This study also confirmed the efficiency of micro-Raman tool for quantitative microstructural analysis of GaN materials.

Then, in chapter 5, we went on probing some n-doped homo-epitaxial GaN epi samples with n concentration ranging between $10^{14}cm^{-3}$ to $10^{18}cm^{-3}$. The main dopant here was silicon (Si) atom. By using micro-Raman spectroscopy in the backscattering configuration, we mainly tracked the behavior of the A_1 (LO) phonon position shift versus the n carrier concentration by performing Raman mappings in different zones of each sample. Then, we calibrated intentionally that behavior in the low-doped region ($10^{14}cm^{-3}$ to $10^{16}cm^{-3}$). We found a linear response that is due to a low interaction strength between the A_1 (LO) phonon electric field and the low carrier density electric field. From that study, we managed to show that micro-Raman is an efficient tool to examine the effect of doping concentration on the crystal quality in GaN material. We also extracted a linear calibration from that low doping zone ($10^{14}cm^{-3}$ to $10^{17}cm^{-3}$).

Further, in chapter 6, we studied the physical properties of vertical GaN Schottky diodes based on the combination of micro-Raman spectroscopy and cathodoluminescence (CL) method mainly. The CL measurements showed the presence of dislocation clusters in the GaN epilayers and with Raman spectroscopy, we performed 2D Raman mappings to observe the structural defects and n-doping concentration distribution. In this work, the E_2 (high) peak shift and width have been used to probe the

Cette thèse est accessible à l'adresse : https://theses.insa-lyon.fr/publication/2023ISAL0011/these.pdf
© [A.J.E. N'Dohi], [2023], INSA Lyon, tous droits réservés

structural defects and stress distribution, while the A_1 (LO) peak shift has been employed to analyze the n carrier distribution in the epitaxial layer. We found out a good correlation between Raman spectroscopy and the CL method in identifying threading dislocations in GaN samples. This also shows the efficiency of the micro-Raman spectroscopy as a powerful and non-destructive tool to probe the presence of the TDs and evaluating the n carrier concentration in GaN material and devices. In addition, from the A_1 (LO) intensity 2D maps mainly, we observed peculiar patches that tend to affect the effective n carrier concentration in the diodes epilayers. We suspected that these patches may be linked to the doping process as atom impurities because the SIMS results performed earlier on these epilayers revealed the presence of the background impurities such as Oxygen and Carbon. Thus, more analyses are required to confirm that.

Finally, in chapter 7, the electrical behavior of the vertical GaN Schottky diodes (100µm, 200µm) have been analyzed with two doping concentration $8\times 10^{15}cm^{-3}$ and $1\text{-}2\times 10^{16}cm^{-3}$. Through the I(V) measurements at room temperature, we investigated the effects of the structural defects found in chapter 6 on the performance of the diodes. For that, we evaluated the forward and the reverse parameters based on the physical properties studied in chapter 6. We also probed the influence of doping concentration on these diodes. In both cases, we observed some changes in the forward and the reverse parameters such as the ideality factor, the series resistance, the barrier height and the reverse leakage current density, which both increase with the n carrier concentration. These parameters are affected by the double barrier effect in the diodes. Thus, we tentatively infer that the structural defects and the doping concentration variation plays an important role in the electrical behavior of the Schottky diodes by creating more leakage paths and some interface inhomogeneities that affect their quality. However, to correlate efficiently the physical properties to the electrical behavior, we suggest that more electrical and physical characterizations on many diodes at once will be helpful to draw a final conclusion on that and this can be done as a future work to extend this thesis project. As a future characterization work, I intend to use OBIC to check on the efficiency of the diodes periphery protection and probe the local variation of the electric field in the diodes. This will help to get the active defect inside the diodes. In addition, I intend to perform I (V) T, DLTS, and 3D Raman spectroscopy on the diodes in order to correlate efficiently the physical and the electrical properties.

Cette thèse est accessible à l'adresse : https://theses.insa-lyon.fr/publication/2023ISAL0011/these.pdf
© [A.J.E. N'Dohi], [2023], INSA Lyon, tous droits réservés

RESUME DE LA THESE

EN FRANCAIS

INTRODUCTION : Cette thèse traite de la caractérisation multiphysique du nitrure de Gallium sous forme de matériaux et aussi sous forme de composant électronique. Face aux limitations du silicium pour opérer à haute fréquence, à température élevée et sous haute tension au risque de claquage prématurée, l'utilisation de matériaux alternatifs comme le nitrure de gallium présentant une large bande interdite qui lui permet de combler les déficits technologiques du silicium sous haute tension. Ainsi dans cette thèse nous avons traité cet aspect à l'aide d'outils de caractérisation physique non destructifs comme la spectroscopie micro-Raman et la cathodoluminescence qui ont permis de sonder les propriétés physiques du GaN en tant que matériaux et aussi en tant que composant. Ces mesures ont été suivies par des caractérisations électriques de type courant-tension (I(V)) qui ont permis de sonder les performances électriques des composants GaN. Cette thèse s'est étendue sur sept chapitres. Le chapitre 1 présente la partie théorique liée à la connaissance du GaN en tant que matériaux et en tant que composant. L'état de l'art général sur les récentes activités liées à la technologie GaN a été abordé. Les chapitres 2 et 3 traitent des aspects fondamentaux et pratiques de la spectroscopie micro Raman, de la cathodoluminescence et de la caractérisation électrique par courant-tension I(V). Dans le chapitre 4 nous avons étudié les substrats GaN dopé Si, Ge, O. Nous avons sondé la contrainte mécanique résiduelle liée au type de dopants dans ces substrats en utilisant la spectroscopie micro-Raman. Au chapitre 5, nous avons investigué les couches homo-épitaxiées GaN dopé Si à différentes concentrations allant de 10^{14} cm^{-3} à $10^{18}cm^{-3}$. L'effet du dopage sur la qualité cristalline de la couche épitaxiée a été quantitativement évalué à l'aide de la microscopie micro Raman. Ensuite, dans la gamme de faible dopage ($10^{14}cm^{-3}$ à $10^{16}cm^{-3}$), nous avons obtenu une influence linéaire du dopage sur l'évolution du phonon A_1(LO). Dans le chapitre 6, les propriétés physiques des diodes Schottky GaN ont été évaluées en utilisant le couplage entre la spectroscopie Raman et la cathodoluminescence. Enfin au chapitre 7, les propriétés électriques de ces diodes Schottky ont été étudiées par la méthode courant-tension. Nous avons essayé de corréler l'influence des propriétés physiques sur les performances électriques à l'issue de cette étude.

Cette thèse est accessible à l'adresse : https://theses.insa-lyon.fr/publication/2023ISAL0011/these.pdf
© [A.J.E. N'Dohi], [2023], INSA Lyon, tous droits réservés

CHAPITRE 1 : GENERALITE SUR LE GAN ET LES COMPOSANTS GAN

Dans ce chapitre, nous abordons les aspects théoriques et fondamentaux sur le GaN et les composants en GaN. Un état de l'art général sur l'évolution de la technologie sera présenté.

GENERALITES SUR LE GAN : Le nitrure de gallium (GaN) a une large bande interdite de 3,4 eV et un fort champ électrique critique (E_c) d'environ 10 fois celui du silicium (Si) qui permet des performances électriques pour les applications haute tension. Ses propriétés physiques sont matérialisées par les paramètres physiques listés dans le tableau 1.1 [2] ainsi que dans la figure 1.1. Ces paramètres sont des facteurs essentiels qui donnent au matériau GaN la capacité de fonctionner à haute tension, haute température et haute fréquence pour les applications de commutation de puissance.

Tableau 1.1 : Propriétés physiques des semi-conducteurs à large bande interdite. [2]

Matériaux	E_g **(eV) à 300 K**	μ_n **(cm²/V.S)**	μ_p **(cm²/V.S)**	v_{sat} **(cm/.S)**	E_c **(V/cm)**	ε_r
Si	1,1	1450	450	10^7	3.10^5	11.7
SiC (4H, 6H, 3C)	3.2-2.9-2.3	450-1000	45-115	2.10^7	2.10^6	10
GaN (wurtzite)	3.4	1000	35	2.10^7	5.10^6	8.9
Diamant	5.6	2200	1800	3.10^7	$5{,}6.10^6$	5.7

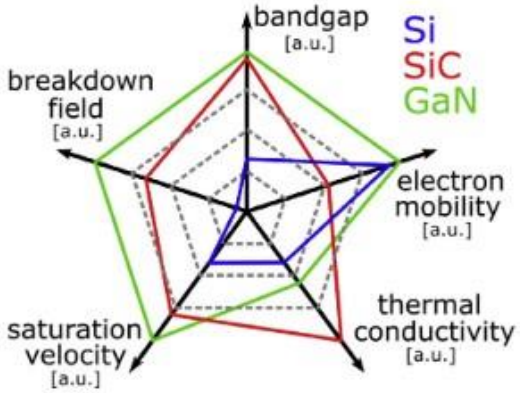

Figure.1.1 : Comparaison des propriétés des matériaux pertinents pour l'électronique de puissance Si, SiC et GaN [2].

La technique de croissance des matériaux GaN peut être divisée en deux catégories : la croissance cristalline massive, qui est plus liée à la croissance du substrat et la croissance épitaxiale qui est plus orientée sur la croissance des couches epitaxiales. La croissance du substrat GaN peut être effectuée par épitaxie en phase vapeur aux halogénures (HVPE) [3], sublimation, solution liquide à haute pression, méthodes ammonothermiques [4]. Pour la croissance des couches épitaxiées de GaN de haute qualité, deux types de croissance peuvent être synthétisés : la croissance homo et hétéro-épitaxiée. Il existe une variété de méthodes de synthèse par croissance pour obtenir des couches de GaN épitaxiées, parmi lesquelles l'épitaxie par jet moléculaire (MBE), le dépôt chimique organique en phase vapeur métallique (MOCVD) et le HVPE sont les principales techniques de traitement.

Le tableau 1.2 résume les avantages et les désavantages des différentes méthodes de croissance du GaN.

Cette thèse est accessible à l'adresse : https://theses.insa-lyon.fr/publication/2023ISAL0011/these.pdf
© [A.J.E. N'Dohi], [2023], INSA Lyon, tous droits réservés

Tableau 1.2 : Résumé des techniques de croissance du GaN.

Technique de croissance	**Avantages**	**Désavantages**
Épitaxie en phase vapeur d'hydrure (HVPE)	Taux de croissance élevé (200 – 300 $\mu m.h^{-1}$)	Densité de défauts élevée (10^9 cm^{-2})
Vapeur chimique organo métallique déposition (MOCVD)	Faibles densités de défauts (10^5 cm^{-2})	Taux de croissance faible (1-2 $\mu m.h^{-1}$)
Épitaxie en phase vapeur d'hydrure (masse)	Taux de croissance élevé (200 – 300 $\mu m.h^{-1}$)	Fissuration à l'interface et courbure du wafer
Ammono thermique	Densité de défauts très faible (5×10^3 cm^{-2})	Long temps de croissance
Epitaxie par jet moléculaire (MBE)	Bon contrôle des épaisseurs au niveau atomique	Taux de croissance très faible

Le GaN et ses alliages peuvent cristalliser à la fois en phase wurtzite (WZ) appelée (phase α) ou hexagonale et en structure zinc blende (ZB) appelée (phase β). En raison de certaines conditions thermodynamiques, la structure wurtzite semble être la forme la plus stable et la plus utile pour la croissance des composants GaN. La figure 1.5 montre l'aspect cristallin des polytypes Wurtzite et Zinc blende.

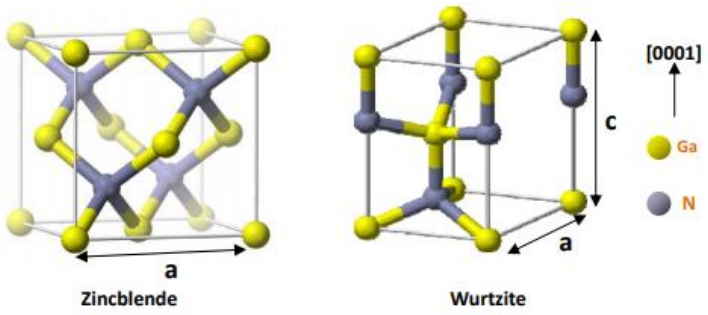

Figure 1.2 : Polytypes zinc blende et Wurtzite GaN [6].

Défauts structuraux dans le GaN : Des défauts sont retrouvés dans les matériaux nitrures quelle que soit la technologie de croissance (MBE, MOCVD ou VPE) utilisée pour les faire croître. Les défauts perturbent généralement la forme continue du réseau pendant la nucléation du cristal et créent des états d'énergie indésirables à l'intérieur de la bande interdite. Ils se forment généralement au cours de la croissance et peuvent être classés en défauts ponctuels (défauts adimensionnels), défauts linéaires (défauts unidimensionnels), défauts plans (défauts bidimensionnels) et défauts volumiques (défauts tridimensionnels). Il est rapporté que l'oxygène est le donneur unique le plus actif dans le GaN. D'après les références [7, 8], les défauts natifs de type n les plus probables dans les cristaux de GaN sont les lacunes Ga (VGa) en raison de leur faible énergie de formation même dans des conditions de cristallisation fortement riches en Ga [9]. De plus, l'incorporation de Mg (type p) dans la solution de croissance influence extrêmement les propriétés électriques des cristaux de GaN en augmentant leur résistivité de plusieurs ordres de grandeur. Quant aux défauts extensifs, la plupart sont des dislocations de type vis, coins et mixtes (vis et coins). Ces types de défauts sont très souvent à la base de la contrainte mécanique résiduelle dans le GaN après croissance. Les défauts plans sont la discontinuité de la structure cristalline idéale sur un plan 2D. Le défaut d'empilement, les joints de grains et les joints de macles

Cette thèse est accessible à l'adresse : https://theses.insa-lyon.fr/publication/2023ISAL0011/these.pdf
© [A.J.E. N'Dohi], [2023], INSA Lyon, tous droits réservés

peuvent être considérés comme des défauts plans dans le GaN. Les défauts volumiques comprennent les pores, les vides/fissures, les amas/précipitations, les inclusions étrangères et d'autres phases [10].

Dopage dans le GaN : Le nitrure de gallium peut être aussi dopé n pour renforcer les propriétés intrinsèques en introduisant intentionnellement des impuretés donneuses. Pour doper le GaN,on peut utiliser du carbone, de l'oxygène ou du silicium. Le carbone n'est pas un bon candidat car il se comporte comme accepteur site C et son énergie de formation en site Ga reste très grand (4eV). On peut aussi doper le GaN avec l'oxygène (O), mais comme ce dernier a un rayon covalent très proche de celui du l'azote, il va s'incorporer en substitution de l'azote et ne permettra donc pas le dopage n. Le dopant le plus utilisé pour doper n le GaN est le silicium (Si). Malgré son petit rayon covalent (r_{Si} = 1.17 Å) qui cause des effets de contraction de la maille wurtzite, il est énergétiquement plus stable [16]. Ensuite, deux techniques principales sont utilisées pour doper les matériaux GaN : la technique CVD (MOCVD) [11] et la technique d'implantation ionique [12]. La première est basée sur l'introduction de dopant directement dans la chambre de croissance sous forme de gaz lorsque des matériaux nitrurés sont produits par un dépôt chimique en phase vapeur. La dernière est réalisée sous forme de traitement de surface qui permet un contrôle précis du profil de dopage. Dans ce processus, un faisceau d'ions de haute énergie compris entre 50 et 200 keV est accéléré, dirigé sur la surface de l'échantillon pour modifier ses propriétés.

COMPOSANTS ELECTRONIQUES A BASE DU GAN : Il est important de connaître les progrès des dispositifs de puissance GaN, les avantages, la morphologie et les défis qui sont des aspects essentiels à prendre en compte dans le développement des dispositifs de puissance à base de GaN. En 2000, des dispositifs de puissance à base de GaN sont apparus pour la première fois et le GaN FET a été fabriqué sur un substrat SiC en utilisant des normes de radiofréquence. En 2010, l'entreprise International Rectifier a lancé les premiers produits d'alimentation intégrés commerciaux GaN iP2010 et iP2011, en utilisant la plate-forme technologique GaN SBD. En 2016, les laboratoires de recherche et de développement appartenant à Boeing et à General Motors Corporation -HRL ont fabriqué un semi-conducteur à oxyde métallique complémentaire (CMOS) [13] pour promouvoir la maturité et l'industrialisation du dispositif GaN. La structure de base des dispositifs de puissance GaN est principalement classée en deux catégories : on a le dispositif latéral, fabriqué sur des substrats étrangers tels que des substrats en Si ou en carbure de silicium (SiC) [14, 15] et le dispositif à conduction verticale, qui est fabriqué par la méthode homo-épitaxiale et qui présente des avantages uniques comparés à celle de la structure horizontale : une tension de claquage plus élevée, atténuation de l'effet d'effondrement du courant, la densité de puissance plus élevée, faible densité de défauts structuraux.

Des travaux récents et approfondis [16, 17, 18, 19] sur les performances des GaN verticales et des transistors ont renouvelé l'intérêt pour ces dispositifs. Comme indiqué (figure 1), les performances des dispositifs GaN verticaux ont dépassé celles des dispositifs GaN latéraux. Elle est même proche voire au-delà de la limite théorique du GaN (pour une mobilité de canal de 1000 cm^2/Vs).

Cette thèse est accessible à l'adresse : https://theses.insa-lyon.fr/publication/2023ISAL0011/these.pdf
© [A.J.E. N'Dohi], [2023], INSA Lyon, tous droits réservés

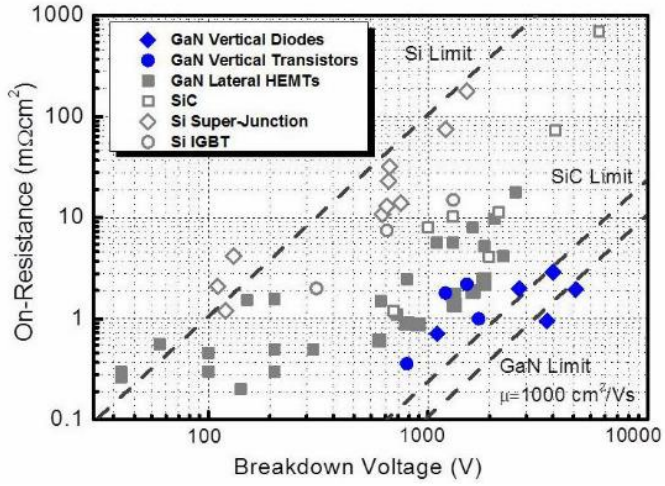

Figure 1.3 : Comparaison entre la résistance à l'état passant et la tension de claquage pour les dispositifs GaN verticaux récemment démontrés, par rapport aux dispositifs GaN latéraux, aux dispositifs de puissance SiC et Si [20].

Malgré les performances prometteuses des dispositifs de puissance GaN verticaux, plusieurs défis ont entravé la commercialisation rapide des dispositifs de puissance GaN verticaux [21] parmi lesquels : Le coût élevé des substrats GaN, l'absence d'une zone de dopage sélectif viable, la compréhension complète des mécanismes de courant de fuite, et les problèmes de fiabilité.

CONCLUSION : Dans ce chapitre, nous avons passé en revue les aspects fondamentaux du matériau et des dispositifs GaN. Nous avons mis en lumière les propriétés physiques des matériaux GaN et les progrès récents de la technologie GaN. De plus, nous avons parlé du GaN en tant que dispositif de puissance dans la géométrie latérale et verticale et de leurs caractéristiques respectives. Dans le cadre du projet de thèse, nous nous sommes concentrés sur la géométrie verticale des dispositifs à base de GaN en raison de leurs avantages et de leur perspective sur le marché industriel du GaN.

REFERENCES

[1] Millán J, Godignon P, Pérez-Tomás A., Wide band gap semiconductor devices for power electronics, 53(2):107-16 (2012).

[2] Fatahilah, Muhammad & Strempel, Klaas & Yu, Feng & Vodapally, Sindhuri & Waag, Andreas & Wasisto, Hutomo. "3D GaN nanoarchitecture for field-effect transistors". Micro and Nano Engineering. 3. 10.1016/j.mne.2019.04.001. (2019).

[3] B. Łucznik, B. Pastuszka, I. Grzegory, M. Boc´kowski, G. Kamler, E. Litwin- Staszewska, S. Porowski, J. Cryst. Growth 281 38 (2005).

[4] Dwiliński, R., R. Doradziński, J. Garczyński, L. P. Sierzputowski, A. Puchalski, Y. Kanbara, K. Yagi, H. Minakuchi, and H. Hayashi. "Excellent crystallinity of truly bulk ammonothermal GaN." Journal of Crystal Growth 310, no. 17, 3911-3916 (2008).

[5] https://microelectronique.univ-rennes1.fr/fr/ch4c.htm 12/12/2022.

[6] H Tokunaga, H Tan, Y Inaishi, T Arai, A Yamaguchi, J Hidaka, Performance of multiwafer reactor GaN MOCVD system, Journal of Crystal Growth, Vol.221, Issues 1–4, P. 616 621(2000).

[7] Dwiliński R, Doradziński R, Garczyński J, Sierzputowski LP, Puchalski A, Kanbara Y, Yagi K, Minakuchi H, Hayashi H. Excellent crystallinity of truly bulk ammonothermal GaN. Journal of Crystal Growth., 310(17):3911-6. (2008).

Cette thèse est accessible à l'adresse : https://theses.insa-lyon.fr/publication/2023ISAL0011/these.pdf
© [A.J.E. N'Dohi], [2023], INSA Lyon, tous droits réservés

[8] Kucharski R, Rudziński M, Zając M, Doradziński R, Garczyński J, Sierzputowski L, Kudrawiec R, Applied Physics Letters, 95(13), 131119 (2009).

[9] Yu PY, Cardona M. Fundamentals of Semiconductors, edited by P. Treiber and C.-D. Bachem, (1996).

[10] Van de Walle, Chris G. "Defects and doping in GaN." equilibrium 5, no. 14, 15 (1997).

[11] JØrgensen, L. V., A. C. Kruseman, H. Schut, A. Van Veen, M. Fanciulli, and T. D. Moustakas. "Investigation of vacancies in GaN by positron annihilation." MRS Online Proceedings Library (OPL) 449 (1996).

[12] Yacobi BG. Semiconductor materials: an introduction to basic principles. Springer Science & Business Media; (2003).

[13] Koide, N., et al. "Doping of GaN with Si and properties of blue m/i/n/n+ GaN LED with Si- doped n+-layer by MOVPE." Journal of crystal growth 115.1 639-642. (1991).

[14] Pankove, J.I.; Hutchby, J.A. Photoluminescence of Zn-implanted GaN. Appl. Phys. Lett., 24, 281–283 (1974).

[15] Ikeda N, Tamura R, Kokawa T, Kambayashi H, Sato Y, Nomura T, Kato S. Over 1.7 kV normally off GaN hybrid MOS-HFETs with a lower on-resistance on a Si substrate. In2011 IEEE 23rd International Symposium on Power Semiconductor Devices and ICs (pp. 284-287). IEEE (2011).

[16] Meneghesso G, Meneghini M, Zanoni E. Breakdown mechanisms in AlGaN/GaN HEMTs: an overview. Japanese Journal of Applied Physics, 53(10):100211 (2014).

[17] Zhang Y. GaN-based vertical power devices, (Doctoral dissertation, Massachusetts Institute of Technology). (2017).

[18] Kizilyalli IC, Edwards AP, Aktas O, Prunty T, Bour D. Vertical power pn diodes based on bulk GaN. IEEE Transactions on Electron Devices. 62(2):414-22. (2014).

[19] Nomoto K, Hu Z, Song B, Zhu M, Qi M, Yan R, Protasenko V, Imhoff E, Kuo J, Kaneda N, Mishima T. GaN-on-GaN pn power diodes with 3.48 kV and 0.95 mΩ-cm2: A record high figure-of-merit of 12.8 GW/cm2. In2015 IEEE international electron devices meeting (IEDM), (pp. 9-7). IEEE. (2015).

[20] Cao Y, Chu R, Li R, Chen M, Chang R, Hughes B. High-voltage vertical GaN Schottky diode enabled by low-carbon metal-organic chemical vapor deposition growth. Applied Physics Letters. 108(6):062103 (2016).

[21] Ding X, Zhou Y, Cheng J. A review of gallium nitride power device and its applications in motor drive. CES Transactions on Electrical Machines and Systems. 3(1):54-64 (2019).

Cette thèse est accessible à l'adresse : https://theses.insa-lyon.fr/publication/2023ISAL0011/these.pdf
© [A.J.E. N'Dohi], [2023], INSA Lyon, tous droits réservés

CHAPITRE 2 : METHODES DE CARACTERISATIONS PHYSIQUES

Cette section traitera des principales techniques de caractérisation physique que nous avons utilisées dans nos travaux : la spectroscopie micro Raman et la technique de cathodo-luminescence afin de comprendre les mécanismes physiques intervenant dans les matériaux GaN et les dispositifs de puissance pendant et après la croissance.

LA SPECTROSCOPIE MICRO RAMAN : Le principe de l'effet Raman est basé sur le processus de diffusion inélastique de la lumière entre la lumière incidente et une substance irradiée [1]. De manière classique, lorsque les photons interagissent avec un réseau cristallin vibrant, deux propriétés physiques peuvent être définies due à la distribution électronique au sein du réseau cristallin à l'état d'équilibre, à savoir le moment dipolaire, P, et la polarisabilité électrique, α. La polarisabilité, α, mesure la force de la distorsion subie par le nuage d'électrons lors de l'interaction lumière-cristal. C'est un tenseur du second ordre représentant le volume et la forme de la distribution de charge dans le réseau. Lorsqu'un photon avec un champ électrique incident E, interagit avec le réseau, il induit un moment dipolaire qui peut s'exprimer par :

$$\mathbf{P} = \varepsilon_0 \alpha \mathbf{E} \qquad (1)$$

Avec ε_0 la permittivité du vide.

Étant donné que les atomes du réseau vibrent autour de leur position d'équilibre lors de l'interaction avec le champ électrique incident, un changement du tenseur de polarisabilité électrique se produira et il peut être décrit mathématiquement par une expansion en série de Taylor autour de la position d'équilibre des atomes du réseau pour de petites amplitudes de vibration :

$$\alpha = \alpha_0 + \frac{d\alpha}{dq} q + \ldots\ldots\ldots \qquad (2)$$

Où α_0 la polarisabilité à l'équilibre et $q = q_{0,vib}\cos(\omega_p t)$ est le changement en fonction du temps de l'espacement du réseau dû aux vibrations des phonons avec une amplitude $q_{0,vib}$ et la fréquence ω_p. Considérant le champ électrique incident de la lumière incidente comme une onde plane dépendant de la fréquence et du temps $E = E_i \cos(\omega_i t)$ avec E_i comme amplitude and ω_i comme fréquence. L'équation (1) peut être réévaluée comme suit :

$$P = \varepsilon_0 \alpha_0 E_i \cos(\omega_i t) + \frac{d\alpha}{dq} \varepsilon_0 q_0 \cos(\omega_p t)\, E_i \cos(\omega_i t) \quad (3)\ [2]$$

Où ω_p est la fréquence de vibration du phonon et ω_i est la fréquence vibrationnelle du photon incident. En utilisant l'identité trigonométrique, l'équation (3) devient :

$$P = \varepsilon_0 \alpha_0 E_i \cos(\omega_i t) + \frac{d\alpha}{dq}\frac{E_i}{2} \varepsilon_0 q_0 \cos((\omega_p - \omega_i)t) + \frac{d\alpha}{dq}\frac{E_i}{2} \varepsilon_0 q_0 \cos((\omega_p + \omega_i)t) \quad (4)$$

Cette équation montre l'ensemble du modèle macroscopique de la description classique de la diffusion Raman développée par Ferraro et al. [7]. Le premier terme du côté droit représente la diffusion Rayleigh des photons. Les deuxième et troisième termes se traduisent par une diffusion Raman Stokes et anti-Stokes, respectivement où les photons sont éloignés de leur fréquence incidente ω_i par la fréquence des phonons optiques ω_p. L'intensité du rayonnement diffusé de Stokes peut être exprimée en termes de tenseur de Raman comme suit :

Cette thèse est accessible à l'adresse : https://theses.insa-lyon.fr/publication/2023ISAL0011/these.pdf
© [A.J.E. N'Dohi], [2023], INSA Lyon, tous droits réservés

$$I_S \propto |\boldsymbol{e_i}\, \boldsymbol{R}\, \boldsymbol{e_s}\,|^2$$

Où $\boldsymbol{e_i}$ et $\boldsymbol{e_s}$ correspondent respectivement à la polarisation de la lumière incidente et diffusée. Cette expression donne les règles de sélection de la diffusion Raman des phonons du premier ordre. Les règles de sélection Raman sont déterminées par ces tenseurs Raman et sont directement reliées à la symétrie du cristal. Pour GaN wurtzite, les tenseurs Raman sont donnés par :

$$R[A_1(z)] = \begin{pmatrix} a & 0 & 0 \\ 0 & a & 0 \\ 0 & 0 & b \end{pmatrix} \qquad R[E_1(x)] = \begin{pmatrix} 0 & 0 & c \\ 0 & 0 & 0 \\ c & 0 & 0 \end{pmatrix} \qquad R[E_1(y)] = \begin{pmatrix} 0 & 0 & 0 \\ 0 & 0 & c \\ 0 & c & 0 \end{pmatrix}$$

$$R[E_2] = \begin{pmatrix} 0 & d & 0 \\ d & 0 & 0 \\ 0 & 0 & 0 \end{pmatrix} \qquad R[E_2] = \begin{pmatrix} d & 0 & 0 \\ 0 & -d & 0 \\ 0 & 0 & 0 \end{pmatrix}$$

Pour les modes polaires, la coordonnée entre parenthèses indique la direction de polarisation des phonons, i. e. la direction des déplacements atomiques. Dans le GaN wurtzite, ces modes polaires optiques sont décrits sur la base du modèle de Loudon [3] et le déplacement atomique de ces modes optiques est révélé sur la figure 2.1. Les modes A_1 et B_1 donnent des déplacements atomiques le long de l'axe c, tandis que les autres, E_1 et E_2, donnent des déplacements atomiques perpendiculaires à l'axe c. De plus, les modes A_1 et E_1 sont polaires et actifs à la fois Raman et infrarouge car leur moment dipolaire induit peut se coupler directement avec la lumière incidente. Leurs vibrations polarisent la cellule unitaire et créent un champ électrostatique à longue portée qui divise les modes A_1, E_1 en modes optique longitudinal (LO) et optique transversal (TO).

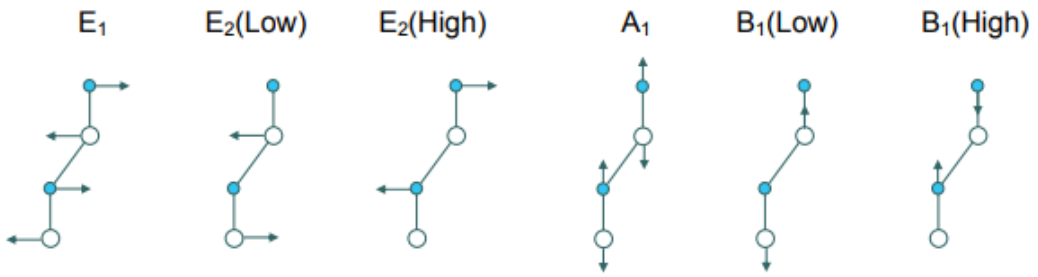

Figure.2.1 : Déplacement des phonons optiques du GaN wurtzite [3]. Les cercles blancs sont les cations Ga et les bleus sont les anions nitrures.

Le tableau 2.1 montre les règles de diffusion Raman dans les conductions pour différentes configurations de rétrodiffusion. Ces configurations de rétrodiffusion sont données par la notation de Porto. Ils sont constitués par quatre coordonnées (exemple X_1 (X_2 X_3) X_4) correspondant à (X_1) direction de propagation de l'onde incident, (X_2) direction de polarisation de l'onde incident, (X_3) direction de polarisation de l'onde diffusée et (X_4) direction de propagation de l'onde diffusée. En se référant aux données du tableau 2.1, on peut aussi dire que sauf le mode E_1(TO) tous les autre modes Raman du GaN wurtzite sont observables en géométrie de rétrodiffusion. Cependant ce mode sera visible dans son spectre car nos échantillons ne sont pas parfaitement plats.

Cette thèse est accessible à l'adresse : https://theses.insa-lyon.fr/publication/2023ISAL0011/these.pdf
© [A.J.E. N'Dohi], [2023], INSA Lyon, tous droits réservés

Tableau 2.1 : Modes Raman à symétrie autorisée de la structure wurtzite GaN pour différentes configurations de diffusion.

Configuration	E_2^H	$A_1(LO)$	E_2^L	$A_1(TO)$	$E_1(TO)$	E_1(LO)
$z(xx)\bar{z}$	✓	✓	✓			
$z(xy)\bar{z}$	✓		✓			
$x(yy)\bar{x}$	✓		✓	✓		
$x(yz)\bar{x}$					✓	
$x(zz)\bar{x}$				✓		
$x(yz)y$					✓	✓
$x(yy)x$	✓		✓	✓		
$x(yy)z$	✓		✓	✓		

Ici, dans cette thèse, nous avons travaillé dans la configuration z(xy)**z** où principalement E_2 (H) et A_1 (LO) sont autorisés. Les modes décrits dans le tableau 2.1 vibrent chacun à une fréquence spécifique avec une valeur dispersée dans la littérature. Ci-dessous le tableau 2 présentant les valeurs de fréquence expérimentales des modes Raman actifs du GaN extraites de la référence [4, 5, 6].

Modes (cm^{-1})	E_2(Low)	A_1(TO)	E_1 (TO)	E_2 (High)	A_1 (LO)	E_1 (LO)
ref [4]	114	531.8	558.8	567.6	734	741
ref [5]	114	532.6	560	566.2	735	741
ref [6]	114	531	560	568	734	741

Tableau 2.2 : Fréquences des phonons actifs Raman du wurtzite GaN (en cm^{-1})

Les instruments Raman sont de plus en plus répandus dans de nombreux laboratoires de recherche et industries de fabrication de matériaux. Ici, dans notre projet de thèse, nous avons utilisé une instrumentation micro Raman confocale commerciale (modèle Renishaw Invia) fournie par la société Renishaw (figure 2.2). Nous avons élaboré nos expériences dans la géométrie de rétrodiffusion en utilisant un mode confocal standard : le faisceau laser d'entrée provenant de la source excitante dans le spectromètre est dirigé vers un expanseur de faisceau. Le détendeur de faisceau augmente le diamètre du faisceau d'entrée collimaté à un faisceau de sortie collimaté plus grand. Ensuite, le faisceau de sortie est dirigé vers le microscope ou le spectrographe par un miroir pour l'observation ou la mesure respectivement. Ce faisceau passe à travers un filtre de rejet qui filtre le faisceau en signal Raman de Stokes ou anti-Stokes en supprimant la diffusion de Rayleigh. Le signal Raman obtenu passe à travers une fente de diamètre réglable et est collimaté par des lentilles optiques sur un réseau de diffraction. Enfin, le signal Raman diffracté est focalisé sur un détecteur CCD par une lentille optique. Le spectre Raman résultant montre l'intensité de la lumière diffusée inélastiquement en fonction du décalage Raman qui est défini comme la différence entre la lumière incidente et diffusée :

$$\text{Raman shift } (\Delta\omega) = \frac{1}{\lambda_i} - \frac{1}{\lambda_s} \qquad (1)$$

Il est généralement exprimé en unités cm^{-1}. D'après l'équation de Planck ($E = \hbar\omega = hc/\lambda$), le nombre d'ondes de photons est proportionnel à l'énergie du photon (donc à la fréquence des photons). Ici la longueur d'onde la lumière incidente vaut $\lambda_i = 532nm$ et λ_s est la longueur d'onde de la lumière diffusée inélastiquement par spectroscopie Raman du mode de vibration considéré.

Cette thèse est accessible à l'adresse : https://theses.insa-lyon.fr/publication/2023ISAL0011/these.pdf
© [A.J.E. N'Dohi], [2023], INSA Lyon, tous droits réservés

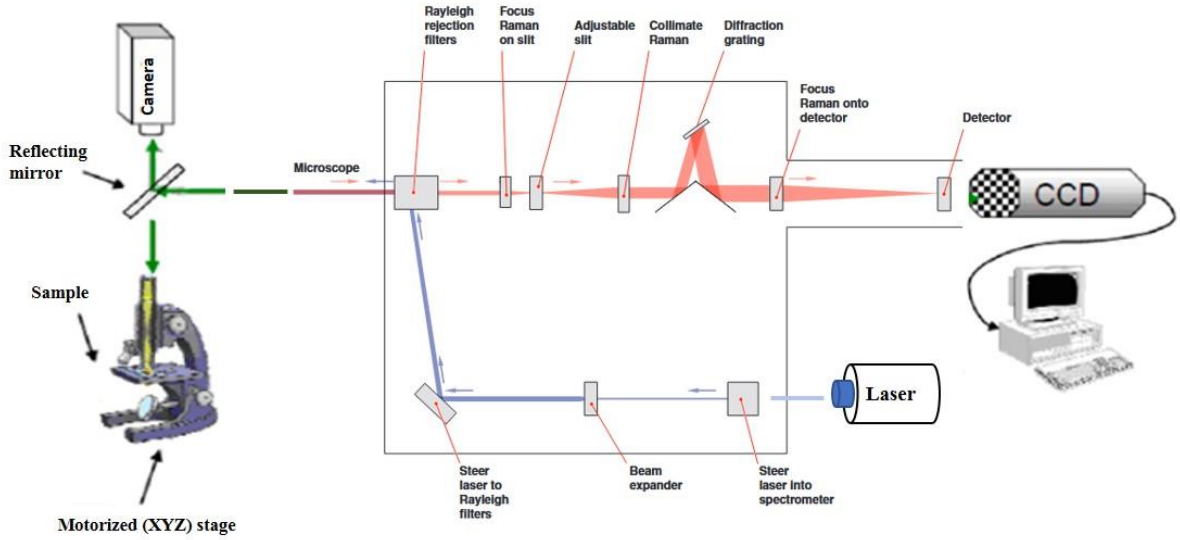

Figure.2.2 : Vue schématique de Raman Instrumentation.

Pour la portée de cette thèse, des cartographies Raman ont été réalisées dans des configurations 2D pour les matériaux et dispositifs GaN à l'aide d'un microscope confocal avec une confocalité standard. En effet, la cartographie Raman 2D visualise la distribution de paramètres physiques tels que l'homogénéité du dopage, la concentration du porteur, le stress etc., par exemple sur la surface de l'échantillon ou dans un plan focal à l'intérieur de l'échantillon (x-y-plane). Lors de cette thèse, la cartographie Raman a été utilisée pour étudier la contrainte mécanique résiduelle [8] dans le matériau GaN, l'homogénéité du dopage de la couche épitaxiée [9], et l'identification de défauts structuraux comme les dislocations [10].

Contrainte mécanique résiduelle : la quantification des contraintes par spectroscopie Raman se fait en analysant le mode car il est plus sensible aux contraintes biaxiales. Un décalage de la ligne de phonons E_2 est une fonction linéaire de la contrainte biaxiale et peut être exprimé comme suit :

$$\Delta\omega = K\sigma_{xx=yy} \quad (8)$$

Où $\Delta\omega$ représente la variation des décalages Raman de la raie des phonons et est l'élément du tenseur des contraintes, et K est le coefficient de pression qui varie en fonction de la contrainte appliquée. Sa valeur (K= 2,56 GPa/cm^{-1}[11], 2,9 GPa/cm^{-1} [12], 4,2 GPa/cm^{-1} [13] à 6,2 GPa/cm^{-1} [14]) et la contrainte associée se retrouvent dans de nombreuses littératures, ces valeurs étant dispersées dans la littérature, nous n'avons pas calculé quantitativement la valeur de la contrainte dans ce travail, mais nous nous sommes concentrés sur l'évaluation qualitative de la contrainte. Suivant la position du pic, la contrainte générée peut être compressive lorsque le pic se déplace vers une zone de fréquence plus élevée et tendue lorsqu'elle est dirigée vers les zones de basse fréquence.

Concentration des porteurs de charge: La concentration et la mobilité des porteurs sont l'un des principaux paramètres physiques qui sont capitaux pour sonder les performances des dispositifs électroniques de puissance. Dans les semi-conducteurs, tels que le GaN ayant une large bande interdite et une faible mobilité des porteurs, les mécanismes EO et DP dominent le processus de diffusion. De plus, la branche de plus faible énergie (L-) n'est pas observée dans les spectres Raman en raison du fort amortissement (suramortissement). Notre objectif est d'exploiter ce décalage de fréquence du mode LPP, connu pour refléter les changements de fréquence du plasma, pour sonder les changements de densité de porteurs libres. L'évolution du mode LOPC avec une augmentation de la concentration en porteurs peut être représentée sur la figure 2.3 à partir de la référence [15].

Cette thèse est accessible à l'adresse : https://theses.insa-lyon.fr/publication/2023ISAL0011/these.pdf
© [A.J.E. N'Dohi], [2023], INSA Lyon, tous droits réservés

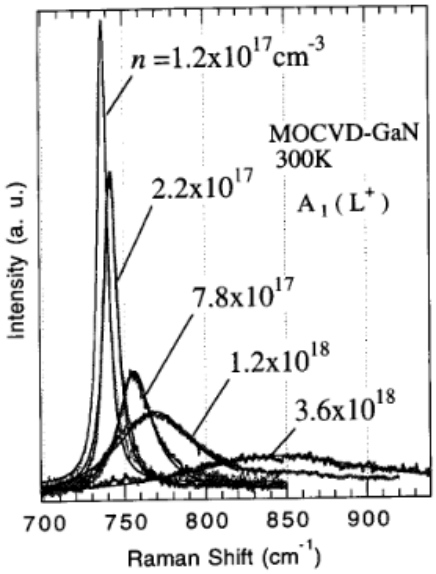

Figure 2.3 : Évolution du mode LOPC en fonction de la concentration en porteurs.

Dislocations dans le GaN : la cartographie par spectroscopie micro-Raman est davantage considérée comme une méthode de caractérisation non destructive pour l'évaluation des TD dans le GaN [16]. Dans les substrats autonomes de GaN disponibles dans le commerce, les densités et les types de TD varieraient entre les vendeurs de plaquettes. Il n'est pas réaliste de déterminer la direction et l'amplitude des vecteurs de Burgers pour tous les TD par TEM. En analysant la cartographie Raman du décalage de pic E_2 (élevé) dans une plage de 0,1 cm-1, la densité, la direction et l'amplitude du bord et de la composante mixte des TD peuvent être observées et déterminées [17]. Ci-dessous, les images de l'identification des TD par cartographie Raman [18]. Plus d'entre eux seront présentés dans le chapitre 6 de la thèse sous l'analyse corrélative avec des images de cathodoluminescence.

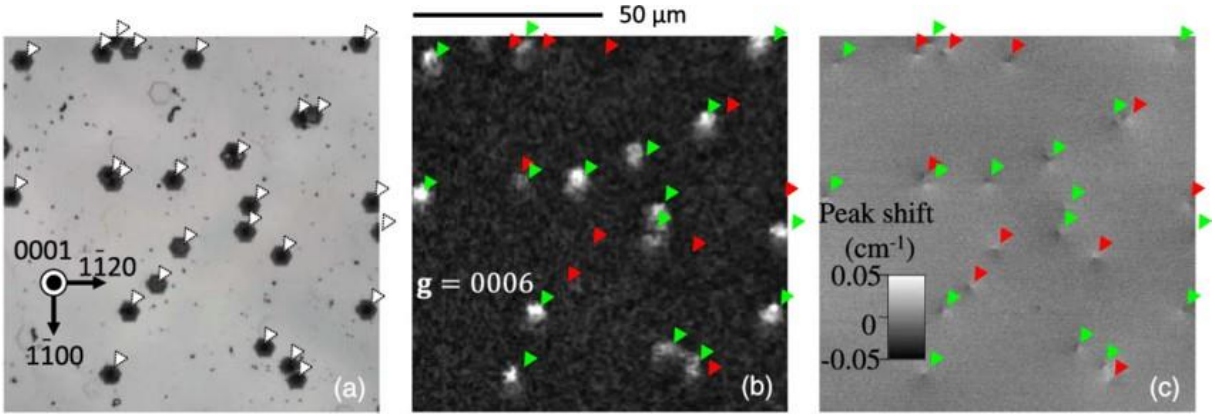

Figure 2.4 : (Couleur en ligne) Images de zone de 100 × 100 µm2 de (a) fosses de gravure, (b) topographie aux rayons X prise le long du g = 0006 et (c) cartographie Raman du décalage de crête E2 (élevé). L'emplacement de la fosse de gravure est illustré par des triangles blancs en pointillés. Les triangles rouges et verts correspondent respectivement au TED et au TMD.

LA CATHODOLUMINESCENCE: La cathodoluminescence est définie comme l'émission de rayonnement électromagnétique à la suite d'un bombardement d'électrons. L'appareil de cathodoluminescence (CL) est mis en service sur le microscope SEM. Dans les mesures CL, le matériau

Cette thèse est accessible à l'adresse : https://theses.insa-lyon.fr/publication/2023ISAL0011/these.pdf
© [A.J.E. N'Dohi], [2023], INSA Lyon, tous droits réservés

est exposé à un faisceau d'électrons, ce qui entraîne différents processus d'interaction faisceau-matériau. Parmi ces processus, certains génèrent un rayonnement électromagnétique dans la gamme spectrale visible et sont appelés CL. Lorsqu'un faisceau d'électrons incident alimente les électrons dans l'état fondamental vers des états d'énergie plus élevés, ils reviennent à leur état fondamental après leur durée de vie. Lorsque ces électrons sous tension reviennent à leur état fondamental, ils émettent de l'énergie optique conduisant à la fluorescence (voir figure 2.3). L'imagerie CL recueille et mesure l'énergie optique générée par l'interaction du faisceau électrique avec le matériau. En déplaçant le faisceau électrique incident, on peut balayer une zone prédéfinie du matériau avec une résolution d'un pixel. L'émission de lumière dépend fortement du matériau sur lequel le faisceau d'électrons est incident. Dans le cas d'une couche de GaN, aucune lumière n'est émise lorsqu'un faisceau d'électrons est incident sur une dislocation ou un défaut cristallin [11].

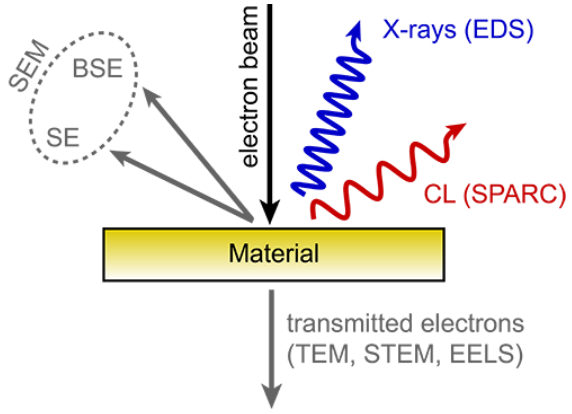

Figure. 2.3 : Analyse des matériaux basée sur le faisceau d'électrons incident.

Dans la littérature, le CL a été utilisé pour étudier les propriétés structurelles et physiques des matériaux. Zhaoying Chen et al [12] ont étudié une analyse quantitative des défauts dans le GaN-on-GaN MOCVD en utilisant la cathodoluminescence. Rosalia Delgado Carrascon et al [13] ont utilisé la spectroscopie CL pour déterminer l'énergie de la bande interdite et obtenir des informations sur l'incorporation d'impuretés. Ils ont mentionné que différents niveaux d'énergie dans la bande interdite du GaN sont générés par divers défauts ponctuels et étendus tels que les vides et les dislocations respectivement.

CONCLUSION : Dans cette section, nous avons donné les détails théoriques sur les outils de caractérisation physique que nous avons utilisés dans cette thèse. Nous avons présenté les aspects fondamentaux de la spectroscopie micro-Raman. Nous avons également présenté les applications récentes de la spectroscopie micro-Raman sur le matériau GaN. De plus, nous avons présenté la spectroscopie cathodoluminescence comme un outil de caractérisation supplémentaire pour sonder le matériau GaN. Nous avons donné un état de l'art sur les applications récentes de la spectroscopie cathodoluminescence sur le matériau GaN.

REFERENCES

[1] Yoshikawa, M; Ishida, H.; Ishitani, A.; Koisumi, S.; Inuzuka, T. Appl. Phys. Lett. (1991).

[2] Mercier, B. Density fluctuations measurement by Rayleigh scattering using a single photomultiplier. Aiaa. J. (2018).

[3] R. Loudon, "The Raman effect in crystals". Advan. Phys. 13:423 (1964).

[4] Núria Domènech i Amador, "Phonons in III-nitride thinfilms, bulk and nanowires: a closer look into InN vibrational properties", PHD thesis, Barcelona University (2015).

Cette thèse est accessible à l'adresse : https://theses.insa-lyon.fr/publication/2023ISAL0011/these.pdf
© [A.J.E. N'Dohi], [2023], INSA Lyon, tous droits réservés

[5] H. Siegle, G. Kaczmarczyk, L. Filippidis, A. P. Litvinchuk, A. Hoffmann, and C. Thomsen, Phys. Rev. B 55, 7000 (1997).

[6] Davydov V Yu, Kitaev Yu E, Goncharuk I N, Smirnov A N, Graul J, Semchinova O, Uffmann D, Smirnov M B, Mirgorodsky A P and Evarestov R A 58 12 899–907, Phys. Rev. B (1998).

[7] Huang, Y.; Yu, P.; Charasse, M. N.; Lo, Y.; Wang, S. Appl. Phys. Lett. (1987).

[8] J. M. Wagner and F. Bechstedt, Appl. Phys. Lett. 77, 346 (2000).

[9] M. V. Klein, Light Scattering in Solids, edited by M. Cardona, (Berlin), 1975.

[10] E. L. Boulbar, J. Priesol, M. Nouf-Allehiani, G. Naresh-Kumar, S.Fox, C.Trager-Cowan, A. Šatka, D. Allsopp and P. Shields, "Design and fabrication of enhanced lateral growth for dislocation reduction in GaN using nanodashes," Journal of Crystal Growth, vol. 466, pp. 30-38, (2017).

[11] J. M. Wagner and F. Bechstedt, Appl. Phys. Lett. 77, 346 (2000).

[12] Kuei-Ming Chen et al., Stress and Defect Distribution of Thick GaN Film Homoepitaxially Regrown on Free-Standing GaN by Hydride Vapor Phase Epitaxy, Japanese J. Appl. Phys. 49 (2010).

[13] Kisielowski C, Kruger J, Ruvimov S, Suski T, Ager J W III, Jones E, Liliental-Weber Z, Rubin M, Weber E R, Bremser M D and Davis R F Phys. Rev. B 54 17745, (1996).

[14] Kozawa T, Kachi T, Kano H, et al. Raman scattering from LO phonon-plasmon coupled modes in gallium nitride. J Appl Phys, (1994).

[15] Kozawa T, Kachi T, Kano H, et al. Raman scattering from LO phonon-plasmon coupled modes in gallium nitride. J Appl Phys, (1994).

[16] N. Kokubo et al., Appl. Phys. Express 11, 061002 (2018).

[17] N. Kokubo et al., Appl. Phys. Express 11, 061002 (2018).

[18] Kokubo, Nobuhiko, Yosuke Tsunooka, Fumihiro Fujie, Junji Ohara, Shoichi Onda, Hisashi Yamada, Mitsuaki Shimizu, Shunta Harada, Miho Tagawa, and Toru Ujihara. "Nondestructive visualization of threading dislocations in GaN by micro Raman mapping." Japanese Journal of Applied Physics 58, no. SC SCCB06, (2019).

[11] Chen, Zhaoying, Yuxuan Zhang, and Hongping Zhao. "Quantitative defect analysis in MOCVD GaN-on-GaN using cathodoluminescence." Optics Express 28, no. 18 26651-26660 (2020).

[12] Trager-Cowan, Carol, P. G. Middleton, and K. P. O'Donnell. "The morphology and cathodoluminescence of GaN thin films." MRS Internet Journal of Nitride Semiconductor Research 1, no. 1, 1-6 (1996).

[13] Delgado Carrascon, Rosalia. "Epitaxial strategies for defect reduction in GaN for vertical power devices." PhD diss., Linköping University Electronic Press, (2022).

Cette thèse est accessible à l'adresse : https://theses.insa-lyon.fr/publication/2023ISAL0011/these.pdf
© [A.J.E. N'Dohi], [2023], INSA Lyon, tous droits réservés

CHAPITRE 3: METHODES DE CHARCTERISATIONS ELECTRIQUES

Dans cette thèse, nous avons utilisé les mesures de caractéristiques électriques courant-tension (I (V)), et la capacité en fonction de la tension (C (V)). Nous sommes concentrés davantage sur les diodes Schottky; et en particulier sur les caractérisations électriques des diodes Schottky à base de GaN. Les résultats de la caractérisation électrique sur les diodes Schottky et les paramètres physiques extraits des mesures seront présentés dans le chapitre 7 de cette thèse.

Une diode Schottky: une diode Schottky (voir le symbole dans la figure 3.1) est un important dispositif à porteurs majoritaires largement utilisé dans les applications de radiofréquence (RF). Lorsque le courant traverse une diode, il y a une petite chute de tension aux bornes de la diode. Une diode bipolaire présente une chute de tension comprise entre 0,7 et 1,7 volt, tandis qu'une diode Schottky présente une chute de tension comprise entre 0,15 et 0,45 volt environ [1].

Figure 3.1: Symbole d'une diode Schottky [1].

Le contact métal-sémiconducteur : Le contact métal-semiconducteur est un lien vital entre le semi-conducteur et le monde extérieur. Au cours du processus de fabrication des dispositifs semi-conducteurs, deux types de contacts métal-semiconducteur doivent être établis : les contacts Schottky ou (redresseurs) et les contacts ohmiques ou (non redresseurs). Le contact Schottky présente une caractéristique courant-tension (I-V) asymétrique lorsque la polarisation de la tension appliquée extérieurement au contact est modifiée. Parallèlement, le contact ohmique ou non redresseur présente des caractéristiques I-V linéaires quelle que soit la polarité de la tension de polarisation appliquée. Une des propriétés les plus intéressantes d'une interface métal-semiconducteur (MS) est sa hauteur de barrière Schottky (SBH), qui est une mesure de la différence des niveaux d'énergie pour les porteurs majoritaires à travers l'interface MS. La hauteur de la barrière Schottky contrôle le transport électronique à travers les interfaces MS et est, par conséquent, cruciale pour le bon fonctionnement de tout dispositif semi-conducteur [2], en particulier dans les dispositifs GaN dans notre cas. La barrière Schottky peut également être utilisée pour étudier les défauts et les propriétés d'interface d'un système métal-semiconducteur. La théorie du premier ordre de la formation d'une barrière de Schottky (SB) est le point de vue attribué à Walter Schottky lui-même à l'origine et à Neville Mott [3] également. Elle propose que la SBH entre un métal avec une fonction de travail de Φ_m et un semi-conducteur avec une affinité électronique de χ_s soit :

$$\Phi_B = \Phi_m - \chi_s \quad (1)$$

Où Φ_B représente le SBH mesuré sur un semi-conducteur de type n. En l'absence d'interaction, le métal et le semi-conducteur sont électriquement isolés l'un de l'autre. La fonction de travail du métal Φ_m est définie comme l'énergie minimale requise pour élever un électron de la surface du métal vers l'espace libre. Chaque métal a une fonction de travail métallique constante. La fonction de travail de certains métaux et l'affinité électronique des semi-conducteurs à grand gap sont connues dans la littérature [4]. La condition essentielle pour la formation de barrières Schottky entre un métal et un semi-conducteur de type n est établie lorsque le travail d'extraction du semi-conducteur (Φs) est inférieur à celui du métal (Φm).

Cette thèse est accessible à l'adresse : https://theses.insa-lyon.fr/publication/2023ISAL0011/these.pdf
© [A.J.E. N'Dohi], [2023], INSA Lyon, tous droits réservés

Lorsqu'une tension de polarisation directe $V_A > 0$ est appliquée au contact Schottky, les électrons du semi-conducteur sont attirés vers le métal. Le niveau de Fermi du métal est inférieur au niveau de Fermi du semi-conducteur. Par conséquent, la barrière vue par les électrons dans le semi-conducteur est réduite et il y a donc un flux net d'électrons du semi-conducteur vers le métal. L'augmentation de la tension de polarisation directe V_F entraîne une augmentation rapide du courant de polarisation directe, car un nombre exponentiellement croissant d'électrons du semi-conducteur est capable de surmonter la barrière de surface (figure 3.2a). D'autre part, lorsqu'une polarisation inverse $V_A < 0$ est appliquée comme le montre la figure 3.2c, le niveau de Fermi du métal devient supérieur à celui du semi-conducteur et par conséquent, le flux d'électrons du semi-conducteur vers le métal est bloqué. Cependant, certains électrons seront capables de surmonter la barrière alors que le courant de polarisation inverse associé est faible. Comme la barrière est la même pour toutes les polarisations inverses, le courant inverse devrait être constant. La forme générale des caractéristiques I-V du phénomène décrit ci-dessus est également illustrée sous la figure 3.2d.

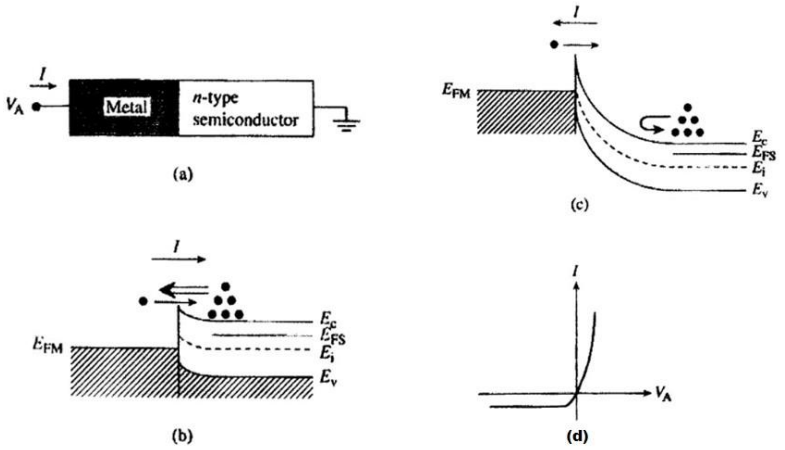

Figure 3.2 : Le comportement de la diode Schottky sous une tension de polarisation donnée. (a) Contact métal-semiconducteur (MS) sous polarisation. (b) Comportement du contact MS sous une polarisation positive. (C) Comportement du contact MS sous tension inverse. (d) Caractéristiques générales I(V)décrites en b et C. [2]

Le contact ohmique: Un contact ohmique est un contact métallique avec un semi-conducteur dont la résistance de contact est très faible par rapport à celle du semi-conducteur. C'est un contact non redresseur dans lequel la relation courant-tension dans des conditions de polarisation inverse et directe est linéaire et symétrique. Il est essentiel pour extraire les caractéristiques électriques d'un dispositif semi-conducteur et est considéré comme une étape extrêmement importante du processus de fabrication de dispositifs semi-conducteurs et de circuits intégrés de haute performance. Pour les dispositifs à base de nitrures, le développement de contacts ohmiques à faible résistance pose un problème en raison de leurs larges bandes interdites. Afin de réaliser des dispositifs GaN de haute performance, des contacts ohmiques fiables sont nécessaires et diverses combinaisons de métaux ont été étudiées dans la littérature [5].

Fabrication des diodes GaN Schottky : Dans ce travail, les diodes Schottky GaN-on-GaN étudiées ont été développées et fournies par le CRHEA (Centre de Recherche sur l'Hetero-Epitaxie). La photolithographie ultraviolette standard [6], l'évaporation par faisceau d'électrons, le lift-off et la gravure ionique réactive (RIE) ont été utilisés pour la fabrication des diodes (figure 3.3). Sur la face avant de la tranche de GaN, des cadres de Nickel (Ni) de 40 nm d'épaisseur sont d'abord déposés. Avant la fabrication des contacts métalliques, les emplacements virtuels des diodes sont déterminés à l'intérieur des cadres de Ni et représentés par des cercles bleus sur la figure 3.3a. Les diodes fabriquées sont de 200 µm, 100 µm, 50 µm (haut) et 50 µm (bas) de largeur (diamètre). Pour les diodes GaN Schottky de

Cette thèse est accessible à l'adresse : https://theses.insa-lyon.fr/publication/2023ISAL0011/these.pdf
© [A.J.E. N'Dohi], [2023], INSA Lyon, tous droits réservés

haute qualité proposées, un contact propre entre le métal et le semi-conducteur est nécessaire. C'est pourquoi les contacts Ni/Au sont évaporés avant de réaliser l'isolation mesa afin de limiter au maximum les contaminations parasites à l'interface entre le Ni et le GaN. A l'intérieur des cadres de Ni, les contacts Schottky circulaires Ni/Au (20/200 nm) sont déposés, suivis d'un dépôt Au supplémentaire de 200 nm au centre des diodes pour faciliter le contact électrique avec les pointes figure 3.8c. Ensuite, les diodes sont isolées par gravure mésa avec une profondeur de gravure de 400 nm en utilisant la technique RIE (Reactive Ion Etching) à base de $Cl_2/Ar/CH_4$. La gravure mésa a été réalisée en utilisant une étape de lithographie supplémentaire avec un autre jeu de masques. Dans ce jeu de masques, chaque motif de mésa est plus large que le contact Schottky de 10 µm. Enfin, des empilements métalliques de Ti/Al/Ni/Au (30/180/40/200 nm) sont déposés à l'arrière du substrat n+-GaN pour réaliser des contacts ohmiques Figure 3.3b.

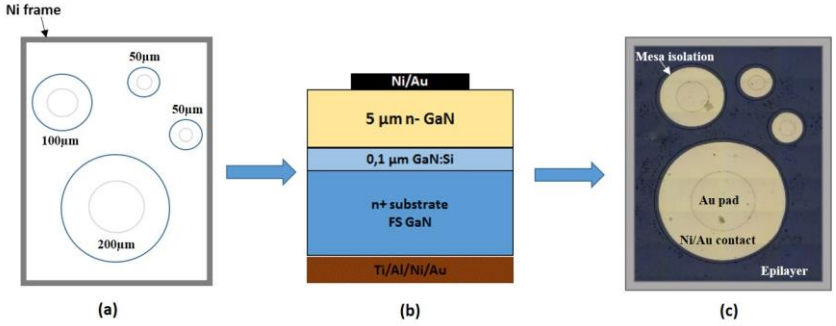

Figure 3.3: (a) Vue de la répartition des diodes dans un champ du masque avant la métallisation. (b) Coupe transversale des diodes Schottky GaN verticales. (c) Image optique des diodes après métallisation. La barre d'échelle de l'image de la figure est de 100µm.

Mesures électriques des diodes par courant-tension I (V) : Le flux de courant à travers un contact Schottky peut être décrit par la théorie bien connue de l'émission thermoïnique (TE). La relation courant-tension I (V) des diodes Schottky est donnée par [26] :

$$I = I_0 \exp\left(\frac{qV}{nkT}\right)[1 - \exp\left(\frac{-qV}{kT}\right)]$$

Avec $I_0 = AA^*T^2\exp(\frac{-q\Phi_B}{kT})$.

La hauteur de barrière Φ_B peut être calculée à partir de I_0 en utilisant : $\Phi_B = \frac{kT}{q}\ln(\frac{AA^*T^2}{I_0})$. Les quantités A, A*, T, k, et q sont respectivement la surface des diodes, la constante de Richardson effective de 26,4 A cm^{-2} K^{-2} pour n-GaN [7,8], la température est donnée en Kelvin, la constante de Boltzman et la charge électrique. Le facteur d'idéalité (n) de l'équation (1) pour (V ≥ 3 kT/q) représente la déviation du mécanisme idéal de transport du courant TE. Il est généralement extrait de la pente de la courbe I (V) :

$$n = \frac{q}{kT}(\frac{dV}{dlnI})$$

En général, la plaquette de GaN contenant les diodes Schottky verticales a été montée sur un circuit imprimé (PCB) avant les mesures électriques pratiques (voir figure 3.5). Ensuite, avec une station sous pointes semi-automatique, le pad Au de la métallisation permet la connexion de l'anode. Comme cathode, l'arrière des diodes est directement collé et relié au PCB par des lignes en Au et nous l'avons câblé avec un câble coaxial.. Avant toute mesure : la table semi-automatique doit être bien réglée avec

Cette thèse est accessible à l'adresse : https://theses.insa-lyon.fr/publication/2023ISAL0011/these.pdf
© [A.J.E. N'Dohi], [2023], INSA Lyon, tous droits réservés

un support (chuck) via un logiciel et une pompe à vide doit être activée pour maintenir la plaquette sur le support et éviter qu'elle ne bouge brusquement pendant la mesure.

Nous avons d'abord mesuré les caractéristiques en direct en réglant la conformité à 10 mA et 1V pour le courant direct et la tension de polarisation respectivement. En ce qui concerne les caractéristiques inverses, nous avons d'abord éteint le système d'éclairage de la station pour minimiser le bruit pendant la mesure en raison de la sensibilité du matériau GaN à la lumière. Ensuite, nous avons réglé la conformité inverse à 100µA et -150V pour le courant et la tension respectivement.

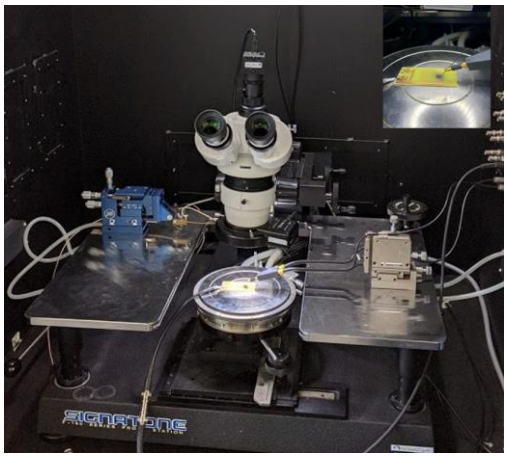

Figure 3.5: Station de sonde I-V semi-automatique

Mesures par la méthode capacité-tension C-V : Les mesures C-V fournissent des informations précises sur les concentrations de dopage des porteurs majoritaires en fonction de la distance (profondeur) de la jonction. Pour les mesures C-V, de nombreuses méthodes de mesure peuvent être utilisées : contacts de sonde au mercure, profilage électrochimique, sonde à pointe classique, mesures de Hall. Cependant, dans le cadre de notre travail, des contacts avec sonde au mercure ont été utilisés pour évaluer la concentration de porteurs dans l'empilement des diodes Schottky GaN verticales. Les mesures ont été effectuées au CRHEA. Voici une vue d'ensemble de la méthode des contacts à sonde de mercure (Figure 3.6).

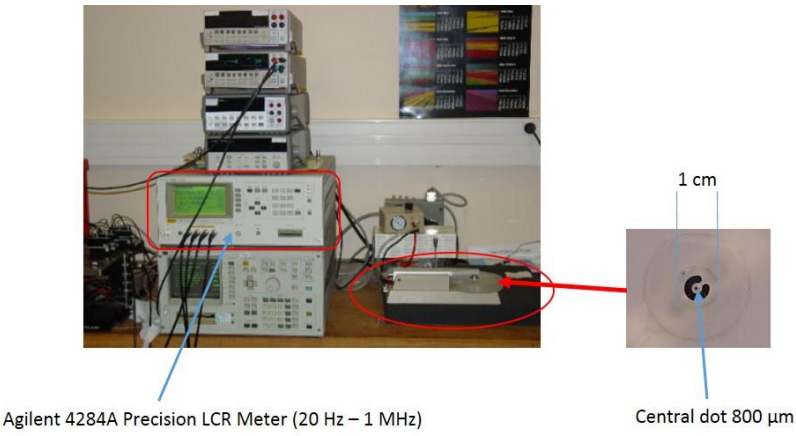

Figure 3.6 : Image de la source de mesure CV de nos échantillons de GaN.

Il s'agit d'un compteur LCR Agilent 4284A Precision MDC de Keysight (20 Hz - 1 MHz), qui peut également mesurer l'impédance à 10 kHz avec l'extraction de paramètres tels que la capacité et la résistance en parallèle. L'image du point central est visible sur le côté droit de l'instrument Agilent.

Cette thèse est accessible à l'adresse : https://theses.insa-lyon.fr/publication/2023ISAL0011/these.pdf
© [A.J.E. N'Dohi], [2023], INSA Lyon, tous droits réservés

CONCLUSION : Dans ce chapitre, nous avons abordé la physique fondamentale dans la caractérisation électrique des diodes. Comme le champ d'application de la thèse était centré sur les diodes Schottky en GaN, nous avons présenté la manière dont elles ont été fabriquées et les différentes méthodes électriques (I(V), C(V)) et instruments que nous avons utilisés pour les caractériser. Les résultats de la caractérisation des diodes seront commentés dans le chapitre 7.

REFERENCES:

[1] Tom Smy, Devices materials and properties, Elec 4705, lecture 13, fall (2009).

[2] Çankaya G, Ucar N. Schottky barrier height dependence on the metal work function for p-type Si Schottky diodes. Zeitschrift für Naturforschung A. 59(11), 795-8 (2004).

[3] N. F. Mott, Proc. Cambridge Philos. Soc. 34, 568 (1938).

[4] Ming-Chang Lee, Integrated Photonic Devices, Introduction to Solid State Physics,

[5] James H.Edgar, Samuel Strite, Isamu Akasaki, Hirushi Amano and Christian Wetzel, "Properties, Processing and Applications of Gallium Nitride and related Semiconductors." INSPEC, London, United Kingdom. (1999).

[6] Ngo TH, Comyn R, Frayssinet E, Chauveau H, Chenot S, Damilano B, Tendille F, Beaumont B, Faurie JP, Nahas N, Cordier Y. Cathodoluminescence and electrical study of vertical GaN-on-GaN Schottky diodes with dislocation clusters. Journal of Crystal Growth. 552,125911, (2020).

[7] M. Drechsler, D.M. Hofmann, B.K. Meyer, T. Detchprohm, H. Amano, I. Akasaki, Japan. J. Appl. Phys. 34, L1178 (1995).

[8] Hui Xu, Fabrication and electrical/optical characterization of bulk GaN based Schottky diodes, Phd thesis, Auburn University, Alabama (2009).

Cette thèse est accessible à l'adresse : https://theses.insa-lyon.fr/publication/2023ISAL0011/these.pdf
© [A.J.E. N'Dohi], [2023], INSA Lyon, tous droits réservés

CHAPITRE 4 : ETUDE PAR MICRO RAMAN DE SUBSTRATS GAN POUR LA TECHNOLOGIE DE COMPOSANTS VERTICAUX

INTRODUCTION : Ici, dans cette étude, nous présentons l'étude micro Raman de la contrainte mécanique résiduelle dans cinq substrats GaN. Les substrats sont dopés avec trois dopants différents : Si, Ge, O_2, avec à peu près la même concentration ($2\times10^{18}cm^{-3}$). En étudiant le mode E_2^h, nous avons évalué le niveau de stress résiduel microscopique qui se produit effectivement pendant le processus de croissance. L'étude de la contrainte résiduelle dans ces substrats de GaN dopés au N permettra de mettre en lumière la qualité des substrats de GaN pour l'efficacité de la technologie des dispositifs verticaux. De plus, ces travaux prouvent que la micro spectroscopie Raman est un outil puissant pour caractériser les substrats GaN.

MÉTHODE EXPÉRIMENTALE : Nous avons étudié cinq substrats GaN de 5 cm de diamètre et de 300µm d'épaisseur fabriqués par la méthode HVPE (épitaxie en phase vapeur d'hydrure) [12] chez Saint-Gobain Lumilog. Deux d'entre eux ont été dopés à l'oxygène (O_2), un a été dopé au germanium (Si) et deux autres ont été dopés au germanium (Ge). La concentration élevée de dopage 2×10^{18} cm^{-3} des substrats était intentionnelle car elle est nécessaire pour de bons contacts ohmiques lors de la fabrication des composants. La spectroscopie micro Raman a été réalisée à température ambiante avec une source laser de 532 nm. Pour les mesures Raman, des cartographies de 150 µm × 150 µm ont été réalisées sur différentes zones de chaque substrat avec une série de plus de 2600 spectres obtenues, traités et fittés par la fonction mixte Lorentz et Gauss.

RÉSULTATS ET DISCUSSIONS :

La figure 4.1 présente les spectres Raman normalisés enregistrés au centre (mesure cartographique) de chaque plaquette de substrat GaN. En considérant généralement les modes E_2^h et A_1 (LO) de ces signaux Raman, nous pouvons conclure que les substrats GaN sont orientés de la symétrie hexagonale qui est la configuration préférée pour la fabrication des composants GaN.

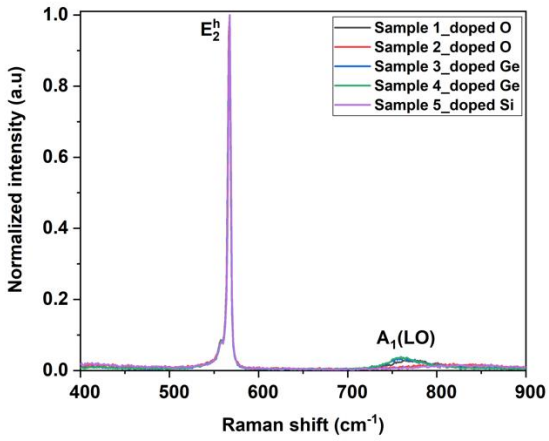

Figure 4.1 : Spectres Raman obtenus à partir du centre des différents substrats.

ETUDE DU MODE RAMAN E_2^h : Le tableau 4.1 est le résumé du résultat de quantification dérivé des cartes de largeur E_2^h. Les substrats ont tous la même valeur moyenne de largeur E_2^h de 3,6 cm^{-1}. Cela

Cette thèse est accessible à l'adresse : https://theses.insa-lyon.fr/publication/2023ISAL0011/these.pdf
© [A.J.E. N'Dohi], [2023], INSA Lyon, tous droits réservés

signifie qu'ils ont la même qualité cristalline. Cette valeur est également une indication d'une bonne qualité cristalline même si le niveau de dopage est d'environ 2×10^{18} cm^{-3} avec différents dopants. Une autre raison de cette bonne cristallinité est que le taux de dislocations (5×10^{6} cm^{-2} - 6×10^{7} cm^{-2}) est raisonnable pour les échantillons de GaN fabriqués par HVPE et n'influence pas la qualité cristalline des substrats. De plus, l'écart-type par rapport à la valeur moyenne de largeur E_2^h montre que l'échantillon dopé à l'O_2 avec moins de dislocations (échantillon 1) est plus homogène (homogénéité cristalline) que l'échantillon dopé au Si avec presque la même densité de dislocation. Cela peut être dû aux propriétés physiques du Si et de l'O en tant que deux principaux dopants donneurs dans le GaN [17].

Tableau 4.1 : Résumé des valeurs de largeur de E_2^h des différents substrats GaN et leur écart-type respectif.

Substrats	dopants	FWHM (valeur moyenne) (cm^{-1})	FWHM (deviation standard) (cm^{-1})	Densité de dislocation moyenne (cm^{-2})
Echantillon 1	O_2	3,6±0,1	0,03	5×10^{6}
Echantillon 2	O_2	3,6±0,1	0.04	10^{7}
Echantillon 3	Ge	3,6±0,1	0.03	10^{7}
Echantillon 4	Ge	3,6±0,1	0.05	10^{7}
Echantillon 5	Si	3,6±0,1	0.05	$< 5\times10^{6}$

Le tableau 4.2 montre les résultats pour le déplacement de la position E_2^h. On observe que le décalage est moindre pour les substrats dopés à l'O_2 (échantillons1 et 2) que pour les substrats dopés au Ge ou Si. Cela indique que la contrainte est plus importante dans les échantillons dopés au Si que dans les échantillons dopés à l'O_2. De plus, nous voyons clairement qu'avec le même ordre de grandeur de concentration de porteur $10^{18}cm^{-3}$, la position E_2^h passe progressivement à haute fréquence des échantillons dopés à O_2 (567,0 ±0,1cm-1) aux échantillons dopés au Si (567,5±0,1 cm^{-1}). Elle révèle que la contrainte est plus compressive dans le cas dopé Si. En outre, nous notons un écart de décalage de 0,5±0,1 cm-1 entre l'échantillon 1 et l'échantillon 5, même s'ils présentent presque le même taux de dislocation. celles-ci ne semblent pas être à l'origine des changements observés, qui pourraient plutôt être dû à l'effet du dopant comme expliqué dans la référence [20]. Nous pouvons conclure qu'un dopage Si crée plus de distorsions de réseau atomique que Ge et O et rend donc le décalage de position E_2^h plus significatif. De plus, nous avons calculé l'écart-type de la position E_2^h pour quantifier la distribution des contraintes dans les échantillons. Nous avons particulièrement constaté que pour le même ordre de taux de dislocation, l'écart-type est de 0,02 pour l'échantillon 1 et de 0,04 pour l'échantillon 5. Cela indique que la variation de la distribution des contraintes est plus significative avec un échantillon dopé au Si qu'avec un échantillon dopé à l'O_2. De plus, dans les cartographies de position E_2^h de chaque échantillon, nous avons observé des taches bleues que nous supposons être des dislocations ou des groupes de dislocations dans les substrats. Plus de détails à ce sujet seront présentés dans les prochains chapitres.

Cette thèse est accessible à l'adresse : https://theses.insa-lyon.fr/publication/2023ISAL0011/these.pdf
© [A.J.E. N'Dohi], [2023], INSA Lyon, tous droits réservés

Tableau 3.2 : Résumé des valeurs de position de E_2^h des différents substrats GaN et leur écart-type respectif.

Substrats	dopants	E_2^h position (moyenne) (cm^{-1})	E_2^h position déviation standard (cm-1)	Densité de dislocation (cm^{-2})
Echantillon1	O_2	567.0±0,1	0,02	5×10^6
Echantillon2	O_2	567.1±0,1	0.03	10^7
Echantillon3	Ge	567.1±0,1	0.04	10^7
Echantillon4	Ge	567.3±0,1	0.02	10^7
Echantillon5	Si	567.5±0,1	0.04	$< 5\times10^6$

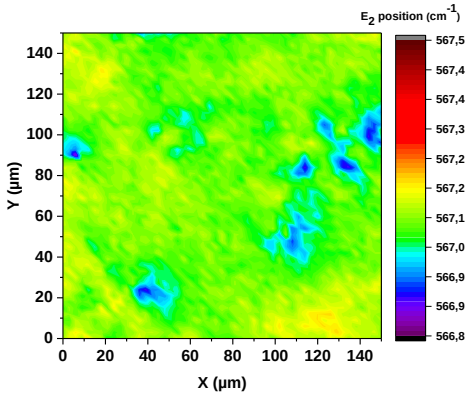

Figure 4.2 : Exemple de cartographie de position du mode E_2^h d'un substrat. Les points bleus peuvent être des dislocations pendant la croissance du substrat.

CONCLUSION : En résumé, nous avons étudié la contrainte et la qualité cristalline de cinq substrats de GaN dopés n^+ en étudiant le mode E_2^h en utilisant la spectroscopie Raman. D'une part, nous avons remarqué que les substrats étudiés ont tous la même qualité cristalline en raison de leur valeur moyenne de largeur E_2^h. De plus, les échantillons 1 et 5 dopés à l'O_2 et au Si n'ont pas la même homogénéité cristalline alors qu'ils contiennent le même ordre de grandeur des dislocations. D'autre part, à partir de l'évaluation du décalage de position E_2^h, nous avons observé que la contrainte est plus compressive et significative dans un échantillon dopé au Si que dans un échantillon dopé à l'O_2 et au Ge, même s'il présente la plus faible densité de dislocations. Le décalage de position E_2^h observé ici et la contrainte associée peuvent provenir de l'effet du dopant, de son incorporation dans les échantillons de GaN et aussi de l'activité de la présence de dislocations dans les échantillons. Cette étude illustre l'efficacité de la spectroscopie micro Raman dans le sondage des propriétés structurelles et mécaniques des substrats GaN pour les applications de dispositifs de puissance.

REFERENCES:

[1] Ban, Vladimir S. "Mass spectrometric and thermodynamics studies of the CVD of some III–V compounds." Journal of Crystal Growth 17, 19-30 (1972).

[2] Van de Walle, Chris G. "Defects and doping in GaN." equilibrium 5, no. 14 15 (1997).

[3] Neugebauer, Jörg, and Chris G. Van de Walle. "Chemical trends for acceptor impurities in GaN." Journal of applied physics 85, no. 5, 3003-3005 (1999).

Cette thèse est accessible à l'adresse : https://theses.insa-lyon.fr/publication/2023ISAL0011/these.pdf
© [A.J.E. N'Dohi], [2023], INSA Lyon, tous droits réservés

CHAPITRE 5 : CARACTÉRISATION MICRO RAMAN DES COUCHES GAN HOMOÉPITAXIALES DOPÉES N POUR LES APPLICATIONS DE COMPOSANTS VERTICAUX

INTRODUCTION : Dans ce travail, nous avons utilisé l'outil micro-Raman pour étudier quantitativement la qualité des échantillons de GaN homo-épitaxial dopés au Si, d'un état $n < 10^{14}$ cm^{-3} non dopé à un état fortement dopé $n > 10^{18}$ cm^{-3}. En suivant la position et la largeur à mi-hauteur FWHM (Full Width Half Maximum) des modes Raman E_2^h et A_1(LO) à mesure que la densité de porteurs augmente, la qualité des échantillons homo-épitaxiaux a été soigneusement sondée. De plus, une calibration de la position A_1(LO) en fonction de la concentration de Si a été effectuée pour quantifier sa sensibilité à des niveaux de dopage faibles et élevés, puis nous avons déduit le mécanisme physique sous-jacent au comportement de A_1(LO) par rapport à la densité de porteurs.

MÉTHODE EXPÉRIMENTALE : Un lot de huit échantillons de GaN homo-épitaxial a été fabriqué par la méthode MOCVD (Metal Organic Chemical Vapor Deposition) [1] sur des substrats GaN de 5 cm de diamètre fournis par Lumilog [2] (voir la section sur la méthode expérimentale pour les substrats GaN). Les couches de GaN ont été développées au CRHEA (Centre de recherche pour l'hétéro épitaxie appliquée). L'ammoniac, le triméthylgallium et le gaz porteur d'hydrogène ont été utilisés pour faire croître les films à 1020 °C avec un taux de croissance de 2 $\mu m \cdot h^{-1}$. Le silane dilué a été ajouté à la phase vapeur afin de doper les couches de GaN. Avant la croissance des couches épaisses faiblement dopées, une fine couche tampon de GaN fortement dopé et de 0,1 μm d'épaisseur était insérée au-dessus du substrat. L'épaisseur des couches a été maintenue à 5 μm (à l'exception de l'échantillon Epi 06 qui était de 10 μm) avec une concentration de porteur de charges de Si allant d'un niveau involontairement dopé $< 10^{14}$ cm^{-3} à un état fortement dopé de $1{,}8\times10^{18}$ cm^{-3}. Avant les mesures Raman, la méthode (C-V) par sonde à mercure a été utilisée pour déterminer le niveau de dopage des couches (mesure Nd-Na) au CRHEA. Les mesures de spectroscopie micro-Raman ont été effectuées à température ambiante avec un laser de 532nm. Au cours des mesures, des cartographies Raman de dimension carrée de 150 μm × 150 μm avec un pas de déplacement de 3 μm ont été effectuées sur différentes zones de chaque échantillon. Une moyenne de plus de 2600 spectres extraits de chaque carte Raman a été obtenue, traité et fitté par la fonction mixte Lorentz et Gauss. Le tableau 1 résume les valeurs extraites du traitement des données. Les erreurs calculées sont les erreurs systématiques basées sur les valeurs moyennes.

Tableau 4.1 : Résumé des valeurs moyennes modes E_2^h et A1 (LO) dérivées de l'ajustement Gauss-Lorentzien.

Echantillons	**Concentration de Si (cm^{-3})**	**A_1(LO) Position (cm^{-1})**	**A_1(LO) FWHM (cm^{-1})**	**E_2(h) Position (cm^{-1})**	**E_2(h) FWHM (cm^{-1})**
Epi 01	**$\leq 10^{14}$**	**733.3 ± 0.1**	**6.3 ± 0.1**	**567.1 ± 0.1**	**3.5 ± 0.1**
Epi 02	**8×10^{15}**	**733.4 ± 0.1**	**6.9 ± 0.1**	**567.1 ± 0.1**	**3.3 ± 0.1**
Epi 03	**1.5×10^{16}**	**733.6 ± 0.1**	**7.0 ± 0.1**	**567.1 ± 0.1**	**3.5 ± 0.1**
Epi 04	**5×10^{16}**	**734.0 ± 0.2**	**7.1 ± 0.1**	**567.1 ± 0.1**	**3.5 ± 0.1**
Epi 05	**7×10^{16}**	**734.2 ± 0.2**	**7.2 ± 0.1**	**567.1 ± 0.1**	**3.5 ± 0.1**
Epi 06	**2.4×10^{17}**	**737.3 ± 0.1**	**10.9 ± 0.3**	**567.1 ± 0.1**	**3.5 ± 0.1**
Epi 07	**4.7×10^{17}**	**743.6 ± 0.2**	**14.9 ± 0.7**	**567.1 ± 0.1**	**3.5 ± 0.1**
Epi 08	**1.8×10^{18}**	**764.2 ± 1.2**	**48 ± 2**	**567.1 ± 0.1**	**3.5 ± 0.1**

Cette thèse est accessible à l'adresse : https://theses.insa-lyon.fr/publication/2023ISAL0011/these.pdf
© [A.J.E. N'Dohi], [2023], INSA Lyon, tous droits réservés

La figure 5.2 montre l'ensemble des spectres Raman enregistrés au centre de chaque échantillon en géométrie de rétrodiffusion. Deux pics principaux peuvent être observés : les pics E_2^h et les pics A_1(LO). Cela confirme la structure cristalline hexagonale des films. Le petit pic à l'épaule du E_2^h peut être attribué au mode E_1 (TO) (558 cm^{-1}) [2].

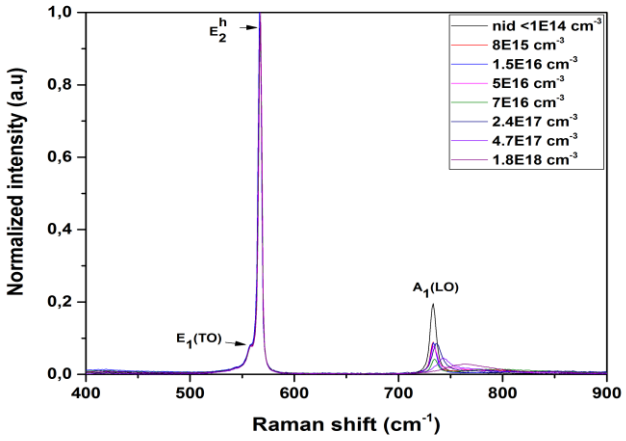

Figure 5.1 : Spectres Raman des couches épitaxiées dopées au Si. La couche nid est la couche non dopée intentionnellement. Les modes A_1(LO) changent clairement avec la concentration de porteur de type-n.

RÉSULTATS ET DISCUSSIONS :

ETUDE DU MODE E_2^h en fonction de LA CONCENTRATION DU DOPANT Si : Le comportement du mode E_2^h (position et largeur) ne change pas à mesure que la densité de porteur augmente (tableau 5.1) avec des valeurs moyennes de 567,1 cm^{-1} et 3,5 cm^{-1} respectivement pour tous les échantillons étudiés. On peut donc conclure qu'il y a aucune influence des impuretés de Si sur la qualité structurale des échantillons. Le niveau de contrainte est aussi le même dans chaque échantillon malgré l'augmentation de la concentration de Si jusqu'à $1{,}8\times10^{18}$ cm^{-3} et l'incorporation des atomes de Si jusqu'au taux de concentration mentionné n'induit pas de contrainte particulière dans les couches par rapport à l'échantillon sans contrainte.

ETUDE DU MODE A_1 (LO) VS CONCENTRATION DU DOPANT Si : le mode A_1(LO) est sensible à la densité de porteurs libres. On observe clairement que lorsque la concentration en Si augmente à des niveaux modérés de 10^{14} cm^{-3} à 7×10^{16} cm^{-3}, la position du pic A_1(LO) se décale légèrement de 0,9 cm^{-1} (déduit du tableau 5.1) ainsi que sa largeur. Ceci révèle que ces changements observés dans le comportement de A_1(LO) ne sont pas dus à la présence de dislocations ou à l'effet de contraintes résiduelles mais plutôt à une variation du niveau de dopage. D'autre part, à des niveaux de dopage plus élevés à partir de $2{,}4\times10^{17}$ à $1{,}8\times10^{18}$ cm^{-3} ; le décalage de la position de A_1(LO) devient important, et la largeur à mi-hauteur s'élargit. De plus, l'intensité maximale diminue lorsque le dopage augmente. Un écart de 30,9 et 41,7 cm^{-1} peuvent être vus en position de A_1(LO) et sa largeur à mi-hauteur respectivement. Ces changements dans le comportement de A_1(LO) en fonction de la concentration en porteurs n sont dus au couplage du mode A_1(LO) avec l'oscillation des porteurs, appelés Plasmons, à travers leur champ électrique macroscopique [3] qui modifie le mode A_1(LO). Lorsque la densité de porteurs augmente, leur couplage de champ électrique avec l'un des modes A_1(LO) devient plus fort, induisant un décalage de fréquence élevé et un élargissement du pic A_1(LO). De plus, le mode A_1(LO) évoluant avec la densité de porteurs libres, nous avons calibré sa position fréquentielle en fonction de la concentration de porteurs. La figure 5.2 montre l'évolution de la position du pic A_1(LO) en fonction de la densité effective de porteurs n (en échelle log). Nous avons découvert que la tendance

Cette thèse est accessible à l'adresse : https://theses.insa-lyon.fr/publication/2023ISAL0011/these.pdf
© [A.J.E. N'Dohi], [2023], INSA Lyon, tous droits réservés

globale de la courbe suit une tendance de croissance sigmoïde, avec un ajustement de Boltzmann comme le meilleur fit. Plus important encore, en zoomant sur la région de dopage léger (Fig. 5.3), nous avons découvert qu'une approximation linéaire pouvait être considérée comme une option d'ajustement, que nous avons exprimée en termes d'équation linéaire comme suit :

$$\boldsymbol{\omega_1 = 1.4 \times 10^{-17}\, n + \omega_0} \quad (1)$$

Où n est la concentration de porteuse n en cm^{-3}, ω_1 (A_1(LO) est le décalage Raman en cm^{-1}) et ω_0 est une valeur de décalage de 733,3 cm^{-1} déduite du graphique. L'approximation linéaire dans la région de faible dopage peut être due à la faible force de couplage entre le champ électrique A_1(LO) et la faible densité de porteurs dans cette région. Cet étalonnage linéaire pour la région de faible dopage est nouvellement rapporté pour les couches minces de GaN homo-épitaxiées sur substrat GaN où le niveau de dopage n < 10^{17} cm^{-3} considéré se situe dans la plage de dopage utilisable des diodes Schottky GaN [4]. Dans le chapitre suivant, nous utiliserons cet étalonnage pour sonder le niveau de dopage et l'homogénéité du dopage des couches épitaxiées de GaN sur GaN pour des diodes Schottky verticales GaN en réalisant des cartographies.

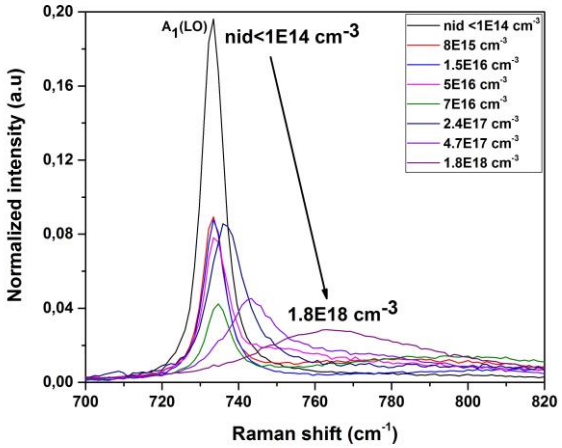

Figure 5.2 : Evolution de la position du pic A_1(LO) en fonction de la densité effective de porteurs n.

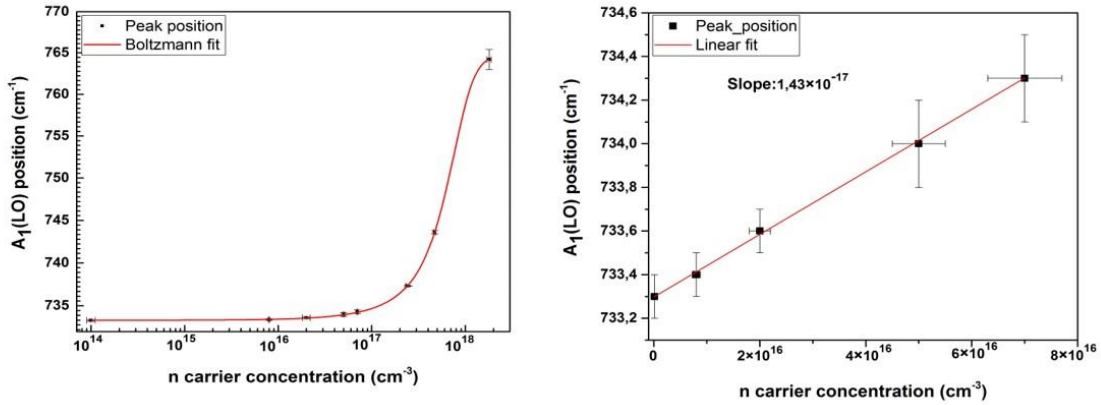

Figure 5.5 : Étalonnage de la position A_1(LO) en fonction de la concentration de dopage n en échelle logarithmique (Gauche). Zoom dans la région de dopage léger n < 10^{17} cm^{-3} avec un ajustement d'approximation linéaire. Les barres d'erreur de la concentration de porteur ont été définies sur la base de 10 % de la concentration initiale de Si pour chaque échantillon (Droite).

Cette thèse est accessible à l'adresse : https://theses.insa-lyon.fr/publication/2023ISAL0011/these.pdf
© [A.J.E. N'Dohi], [2023], INSA Lyon, tous droits réservés

CONCLUSION : Dans cette étude, nous montrons que la spectroscopie Raman peut être utilisée pour sonder les propriétés structurelles et électroniques des couches épitaxiées dopées de type-n développées sur des substrats de GaN par analyse quantitative à la fois de la position et de la FWHM des modes A_1(LO) et E_2^h à mesure que la densité de porteurs de charge augmente. Le comportement de A_1(LO) change radicalement en fonction de la concentration du porteur de charge n ; en particulier à forte concentration, sa position, son intensité et sa largeur changent de manière significative. Pendant ce temps, le E_2^h mode reste inchangé à mesure que la concentration de porteurs augmente. En outre, l'étalonnage de la position A_1(LO) en fonction de la densité du porteur a été effectuée pour sonder sa sensibilité par rapport au niveau de dopage. Plus important encore, nous avions montré qu'une approximation linéaire pouvait être considérée pour relier la position du mode A_1(LO) en fonction de la concentration pour $n < 10^{17}$ cm^{-3}. Dans le chapitre suivant, nous allons examiner l'homogénéité de la concentration de dopage de type n et de la qualité cristalline dans la région de faible dopage pour les applications diodes Schottky verticales à base du GaN.

REFERENCE:

[1] Gomila, G. and Bulashenko, "Effects of the epitaxial layer thickness on the noise properties of Schottky barrier diodes." Journal of applied physics, 86(2), pp.1004-1012 (1999).

[2] Fujito, K., Kubo, S., Nagaoka, H., Mochizuki, T., Namita, H. and Nagao, S., "Bulk GaN crystals grown by HVPE." Journal of Crystal Growth, 311(10), pp.3011-3014 (2009).

[3] Ban, V.S, "Mass spectrometric and thermodynamics studies of the CVD of some III–V compounds." Journal of Crystal Growth, 17, pp.19-30 (1972).

[4] Munir, T., Aziz, A.A. and Abdullah, M.J, "Epilayer Thickness and Doping Density Variation Effects on Current-Voltage (I-V) Characteristics of n-GaN Schottky Diode." In IEEE International Conference on Semiconductor Electronics, pp. 892-895, (2006).

Cette thèse est accessible à l'adresse : https://theses.insa-lyon.fr/publication/2023ISAL0011/these.pdf
© [A.J.E. N'Dohi], [2023], INSA Lyon, tous droits réservés

CHAPITRE 6 : CARACTÉRISATION PHYSIQUE DE DIODES SCHOTTKY VERTICALES A BASE DU GAN

INTRODUCTION : Nous nous concentrons maintenant sur un exemple de dispositif électronique à base de GaN dans ce chapitre. Grâce aux caractérisations physiques, les propriétés physiques des diodes verticales GaN Schottky étudiées sont abordées. Ces propriétés physiques seront utiles pour comprendre les performances électriques de ces diodes Schottky. Par conséquent, le micro-Raman, la cathodoluminescence et le SIMS ont été utilisés de manière concomitante pour faire la lumière sur le comportement physique des diodes Schottky. Dans ce chapitre, nous abordons la présence de défauts structurels et les effets d'homogénéité du dopage efficace sur la qualité des diodes GaN. Pour étudier ces défauts, nous avons principalement utilisé une combinaison de deux techniques physiques non destructives telles que la spectroscopie micro Raman et la Cathodoluminescence (CL). L'association des deux techniques nous aide à étudier les propriétés physiques des diodes. Grâce à la spectroscopie Raman réalisée dans la géométrie de rétrodiffusion, des cartographies 2D ont été réalisées pour observer les défauts structurels [1], leur activité et la distribution de concentration en dopage n [2]. Le décalage et la largeur du pic de E_2^h ont été utilisés pour sonder les défauts structurels et la distribution des contraintes dans les diodes. Le décalage de A_1 (LO) a été suivi pour analyser la distribution des porteurs négatifs dans la couche épitaxiale. Les mesures CL ont permis de mettre en évidence la présence de dislocations en raison de leur activité de recombinaison non radiative. Nous avons également effectué les mesures SIMS sur la couche épi et les résultats montrent la présence d'impuretés de fond telles que le carbone et O. Ainsi, ce chapitre révèle l'efficacité de la spectroscopie Raman dans le sondage des propriétés physiques des dispositifs à base de GaN et être un bon outil de caractérisation corrélative avec d'autres outils de métrologie microélectronique physique.

MÉTHODE EXPÉRIMENTALE : Les diodes Schottky GaN verticales (SBD) de différents diamètres (200 µm, 100 µm et 50 µm) ont été fabriquées par photolithographie standard comme mentionné au chapitre 3. Pour la portée de ce projet ; les échantillons Epi02 (8×10^{15} cm^{-3}) et Epi03 ($\sim 2\times10^{16} cm^{-3}$) (voir chapitre 5) avec une concentration de Si différente ont été choisis pour la fabrication des diodes Schottky en raison de leur faible concentration de porteur effectif ($n<10^{17} cm^{-3}$). Les mesures de spectroscopie Micro-Raman ont été réalisées à température ambiante à l'aide d'un spectromètre confocal (modèle Renishaw Invia). Pour les mesures Raman, des cartographies Raman 2D de taille 500 × 350 µm avec un pas de 5 µm ont été réalisées sur la couche épitaxiée des diodes avant métallisation. Pour les mesures CL, les images ont été enregistrées à température ambiante en utilisant une tension d'accélération de 10 kV et un grossissement de 500× ou 1000×. En inspectant 15 images CL pour chaque échantillon, la densité de dislocations est de $5\sim10 \times 10^6$ cm^{-2} dans des zones de 187 × 500 µm² [3]. On rappelle que les mesures CL ont été aussi réalisée au CHREA sur la couche épitaxiée avant la métallisation. De plus, des mesures SIMS ont été effectuées pour examiner le taux et la présence d'impuretés (de fond) dans la couche de dérive des diodes. Les résultats du SIMS montrent clairement la présence d'impuretés telles que le carbone et l'oxygène dans la couche épitaxiée après croissance et la présence de Si observée à partir du profil SIMS comme dans les rapports de la littérature [4-5].

RÉSULTATS ET DISCUSSIONS :

ETUDE DU COMPORTEMENT DU PIC E_2^h SUR EPI02 ET EPI03 : Ici, en étudiant les cartographies Raman 2D E_2^h obtenues comme décrit précédemment dans la méthode expérimentale sur chaque champ Ni, la contrainte et la qualité cristalline de la couche de dérive des diodes ont été évaluées. Le tableau 6.1 résume les valeurs des positions du mode Raman E_2^h réalisées sur quatre cadres différents

Cette thèse est accessible à l'adresse : https://theses.insa-lyon.fr/publication/2023ISAL0011/these.pdf
© [A.J.E. N'Dohi], [2023], INSA Lyon, tous droits réservés

sur la tranche de GaN d'Epi02 (cadre de la colonne C36). En réalité, la plaquette de l'Epi02 a été découpée en deux lots. Le premier lot contient les champs de la colonne C36 comme mentionné ci-dessus et le second lot étudié contient les trames de la colonne C39. Cependant, comme le deuxième lot de plaquettes Epi02 a été souvent mesuré lors de nombreuses expériences telles que SEM, I(V)T, Raman, il se peut qu'il ait été détérioré après ces opérations. Par conséquent, nous n'examinons que certaines de ses cartographies Raman initiales afin de montrer les dislocations qui y sont présentes et de les corréler avec les données de cathodoluminescence. En dehors de cela, pour plus de commodité, tous les résultats de l'échantillon Epi02 proviennent du premier lot de plaquettes. Les résultats de quantification extraits des cartes de position de E_2^h obtenues montrent un écart de 0,4 cm^{-1} en moyenne qui est relativement quatre fois supérieur à la valeur de résolution spectrale de nos mesures Raman (0,1 cm^{-1}). Cette fluctuation indique que la répartition des contraintes dans Epi02 n'est pas homogène et que, par conséquent, les diodes fabriquées dessus peuvent subir cette inhomogénéité de contrainte. Cela peut être dû à la contribution de certains défauts structurels (dislocations ou impuretés) présents dans Epi02 lors de la fabrication. Cependant, pour confirmer cette observation, davantage d'analyses et de mesures basées sur un outil de caractérisation supplémentaire seraient nécessaires. D'après les ajustements des cartographies de largeur E_2^h, nous observons le même ordre de la valeur moyenne de la largeur de v = 3,6 ± 0,1 cm^{-1} dans tous les cadres que ce soit pour Epi02. Cela révèle que toutes les diodes étudiées dans les cadres Epi02 ont la même qualité cristalline. En se référant à la réf [6], cette valeur de 3,6 cm^{-1} indique une bonne qualité cristalline des couche dopée Si des diodes.

Table 6. 1: E_2^h position and width quantification result for Epi02

Nom cadre	E_2^h position (cm^{-1})	E_2^h largeur (mean value) (cm^{-1})
L45C36	567 ± 0.1	3.6 ± 0.1
L46C36	567.3 ± 0.1	3.6 ± 0.1
L47C36	567.4 ± 0.1	3.6± 0.1
L49C36	567 ± 0.1	3.6± 0.1

Pour Epi03, le comportement du mode E_2^h était différent de celui d'Epi02. Le tableau 6.2 résume les valeurs des positions du mode E_2^h Raman de quatre champs différents sur la tranche de GaN d'Epi03 (cadres de la colonne C38) les résultats de quantification montrent que la position E_2^h est constante pour les quatre champs. Comme interprétation de ce que nous avons observé pour les deux couches, nous voyons que la qualité cristalline de la couche de dérive des diodes n'est pas perturbée bien que la concentration en porteurs n'ait augmenté de l'ordre de 10 (Epi03). Le dopage Si à cette concentration de porteurs n (2 x 10^{16} cm^{-3}) n'affecte pas l'homogénéité du réseau atomique dans la couche de dérive des diodes. Quant à l'état de contrainte, il est approximativement le même dans les deux couches de dérive car la valeur moyenne du décalage de position E_2^h dans Epi03 (567,1 cm^{-1}) est proche de celle d'Epi02 (567,2 cm^{-1}). Cela signifie que le mode E_2^h n'est pas vraiment affecté par le dopage Si car la concentration en porteurs n augmente de l'ordre de 10. Cela confirme ce que nous avons découvert au chapitre 5 concernant le mode E_2^h vs la concentration en porteurs n.

Cette thèse est accessible à l'adresse : https://theses.insa-lyon.fr/publication/2023ISAL0011/these.pdf
© [A.J.E. N'Dohi], [2023], INSA Lyon, tous droits réservés

Table 6. 2: E_2^h position and width quantification result for Epi03

Nom Cadre	E_2^h position (cm^{-1})	E_2^h largeur (cm^{-1})
L50C38	567.1 ± 0.1	3.6 ± 0.1
L52C38	567.1 ± 0.1	3.6 ± 0.1
L54C38	567.1± 0.1	3.7 ± 0.1

LA PRESENCE DE DISLOCATIONS EN EPI02 ET EPI03 : À partir des cartographies Raman de position E_2^h, nous avons identifié la présence des dislocations observées dans l'image de cathodoluminescence pour Epi02 et Epi03. Les dislocations observées dans les images Raman ont été appariées zone par zone conformément aux images cathodoluminescence (figures 6.3 et 4). Elles sont surlignées en bleu et apparaissent dans la zone de faible stress. Ceci révèle que les amas de dislocations peuvent induire une contrainte de traction dans la couche de dérive des diodes étudiées. De plus, il est possible que soit le pas utilisé pour notre cartographie soit trop grand pour observer la contrainte de compression soit que les dislocations observées ici soient des amas de dislocations diminuant localement la contrainte. Néanmoins, davantage d'analyses sont nécessaires pour parvenir efficacement à cette conclusion. Cependant, nous voyons une bonne corrélation entre la spectroscopie Raman et la méthode CL, ce qui confirme l'efficacité de la spectroscopie micro-Raman en tant qu'outil puissant et non destructif pour sonder la présence des dislocations.

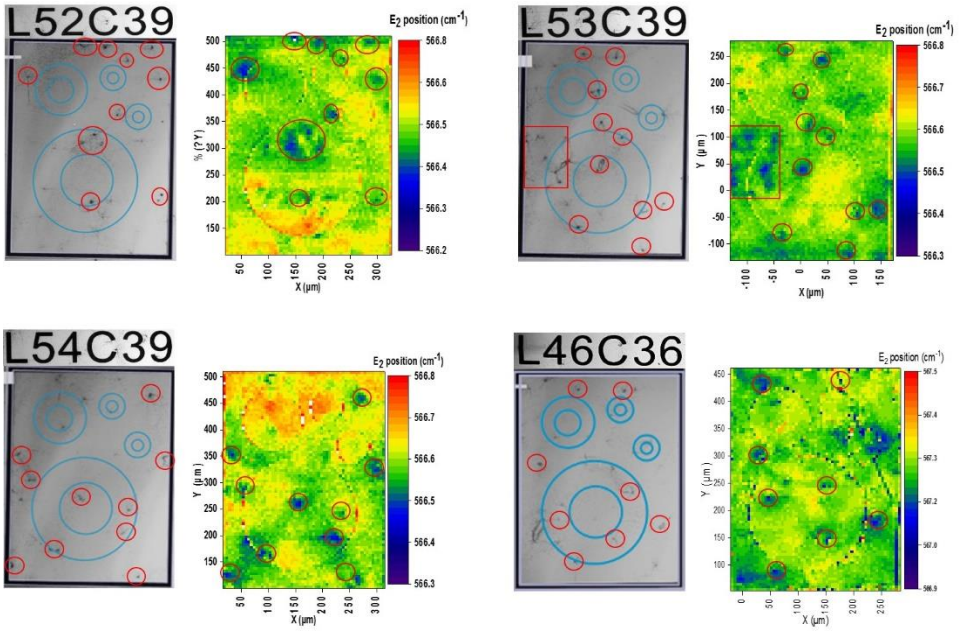

Figure 6.3 : Dislocations (cercle rouges) sur Epi 02.

Cette thèse est accessible à l'adresse : https://theses.insa-lyon.fr/publication/2023ISAL0011/these.pdf
© [A.J.E. N'Dohi], [2023], INSA Lyon, tous droits réservés

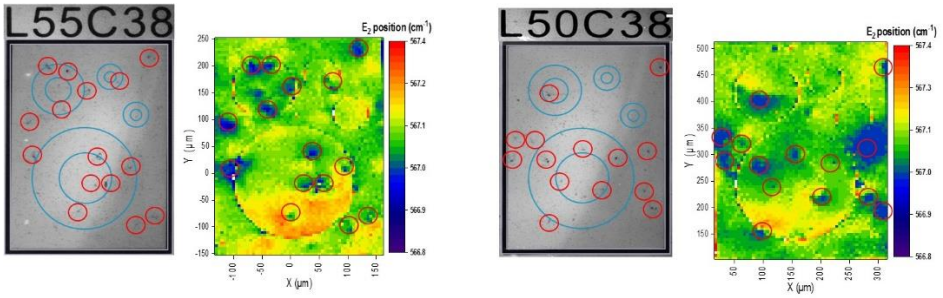

Figure 6.6 : Dislocations (cercles rouges) sur Epi 03.

ETUDE DU COMPORTEMENT DU PIC A1 (LO) SUR EPI02 ET EPI03 : Le décalage de la position A_1 (LO) est connu pour refléter les changements de fréquence plasma et donc nécessaire pour estimer la densité de porteurs libres [7, 8]. À partir des cartographies de position du pic A_1(LO) des images dans Epi02, comme illustré dans les figures 8, nous avons extrait la valeur moyenne du décalage de position A_1(LO) dans chaque image pour Epi02. Le contraste dans les quatre cadres est dominé par les nombreuses zones bleues (733,2 cm^{-1} à 733,4 cm^{-1}) signifiant qu'elles ont de nombreuses régions faiblement dopées. Cette situation peut être due à la présence de défauts structurels particuliers ou d'impuretés (surlignées en bleu) liées au processus de dopage et qui affectent la concentration effective en porteurs de l'Epi02. Selon les résultats du SIMS, il peut s'agir d'impuretés de fond telles que l'oxygène (O) ou le carbone (C) ou une agglomération de celles-ci puisqu'elles existent toutes ensemble dans l'épaisseur de la couche épitaxiée sondée (5 µm). Des analyses complémentaires seraient nécessaires pour déterminer la nature exacte du défaut qui crée ce genre de problème. À partir des cartographies d'intensité du pic A_1(LO), nous avons observé dans Epi02 la présence de taches rouges (type I) qui apparaissent en fait en bleu sur les cartes de position 2D. Ces taches n'apparaissaient pas dans les cartes E_2^h. Par conséquent, ils ne peuvent pas être attribués à des dislocations. Au contraire, ils peuvent représenter des impuretés (telles que le carbone ou l'oxygène) incorporation inhomogène au cours du processus de croissance MOCVD.

Cette thèse est accessible à l'adresse : https://theses.insa-lyon.fr/publication/2023ISAL0011/these.pdf
© [A.J.E. N'Dohi], [2023], INSA Lyon, tous droits réservés

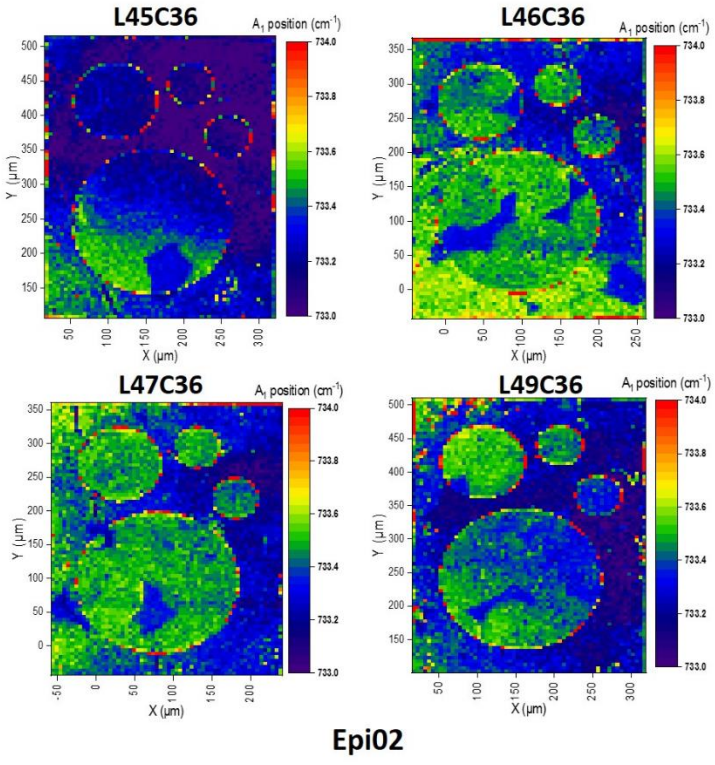

Figure 6.7** : **Cartographies de la position du pic A_1(LO) de Epi02

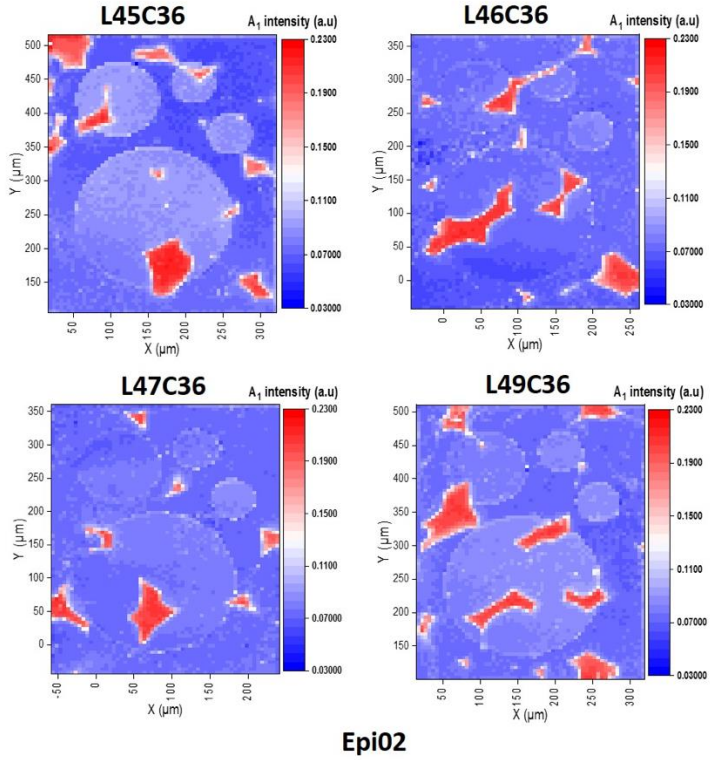

Figure 6.6 : Cartographies de l'intensité du pic A_1(LO) de Epi02.

Pour l'Epi03, la valeur moyenne du décalage de position A_1(LO) est plus élevée que dans Epi02. Généralement, le contraste dans les quatre images montre moins de zone bleue que dans les images Epi02. Au contraire, elles sont relativement couvertes par un contraste vert (733,4 cm^{-1} à 733,6 cm^{-1})

Cette thèse est accessible à l'adresse : https://theses.insa-lyon.fr/publication/2023ISAL0011/these.pdf
© [A.J.E. N'Dohi], [2023], INSA Lyon, tous droits réservés

qui correspond à une zone avec une concentration en porteurs relativement plus élevée (voir figure 11). La présence de zones de couleurs différentes dans ces trames indique que le décalage de position A_1(LO) n'est pas constant sur la zone sondée et donc que le dopage dans la couche de dérive Epi03 n'est pas homogène. Notamment, dans les champs L52C38 et L55C38, nous avons observé des patchs (surlignés en cercle noir) qui font passer la position A_1(LO) vers une fréquence plus élevée c'est-à-dire une zone de concentration plus élevée. Cette tache rouge peut être due à un défaut lié au processus de dopage. Les cartes d'intensité A_1 (LO) des quatre champs montrent les mêmes taches rouges observées dans Epi02 (voir figure 12). Ces taches rouges sont dispersées de manière aléatoire sur les champ. Le champ L54C38 semble en avoir moins sur sa surface tandis que les autres ont leurs diodes presque recouvertes par les patchs rouges. Cela peut indiquer l'activité de ces patchs sur les diodes lorsqu'ils se propagent à travers les cadres. En outre, ils apparaissent principalement dans la zone d'intensité plus élevée comme dans le cas Epi02. Cela implique qu'ils diminuent la concentration de porteurs de type n dans les champs.

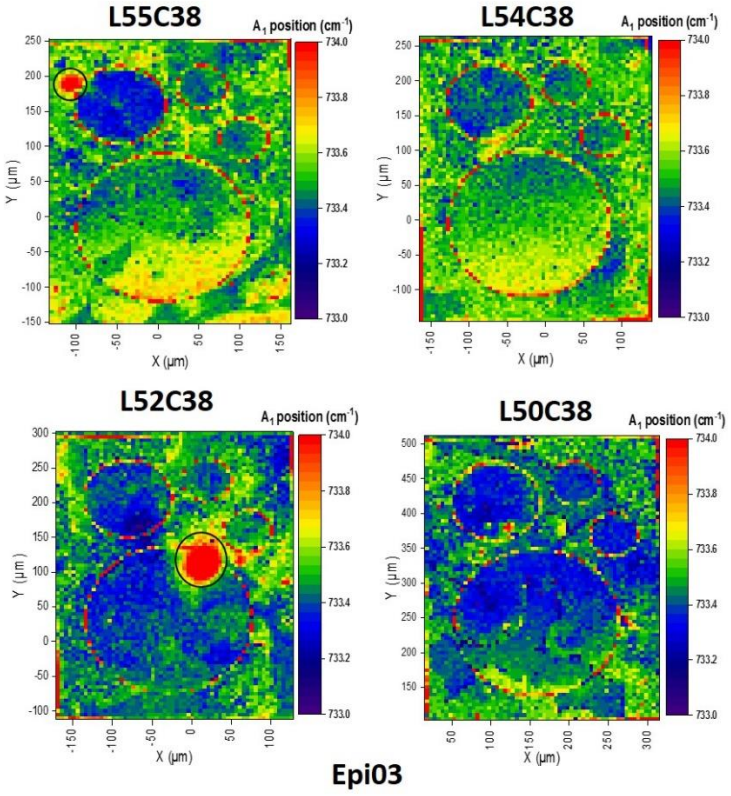

Figure 8.7 : Cartographies de la position du pic A_1(LO) de Epi03

Cette thèse est accessible à l'adresse : https://theses.insa-lyon.fr/publication/2023ISAL0011/these.pdf
© [A.J.E. N'Dohi], [2023], INSA Lyon, tous droits réservés

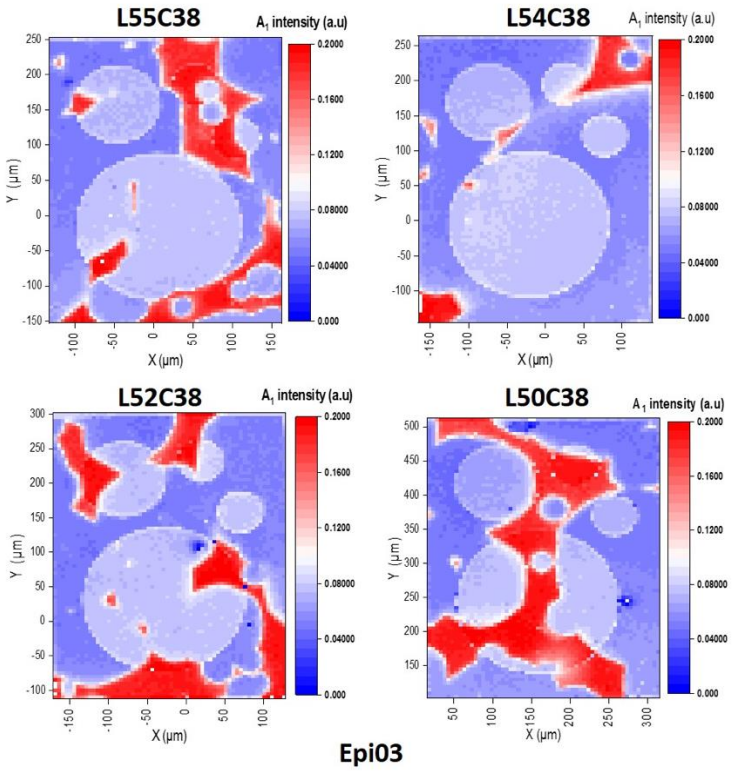

Figure 6.8 : Cartographies de l'intensité du pic A_1(LO) de Epi03

Enfin, la concentration de porteurs de charge n estimée dans Epi02 et Epi03 sur la base de l'équation de calibration dans le chapitre 5 montre une bonne corrélation entre la méthode de spectroscopie Raman et les méthodes avec sonde de mercure C-V dans la détermination de la concentration de porteurs de charge.

CONCLUSION : Ce chapitre montre l'efficacité de la spectroscopie micro-Raman en tant qu'outil pour sonder les propriétés structurelles et électroniques des dispositifs à base de GaN. À partir des cartographies de position E_2^h nous avons observé des dislocations qui correspondent bien aux résultats de cathodoluminescence des couches Epi02 et Epi03 GaN avec différentes concentrations de Si. De plus, des cartographies de position 2D de A1 (LO) des Epi02 et Epi03 ont été utilisées respectivement pour estimer la concentration de porteurs dans la couche de dérive des diodes en corrélation avec la sonde de mercure CV. De plus, à partir des cartographies d'intensité de A_1 (LO), nous avons observé des taches particulières devenant plus épaisses et étendues dans Epi03 que dans Epi02. Cela signifie que lorsque la concentration en porteurs de type-n augmente (Epi03), la morphologie de ces taches change également. Ainsi, comme ceux-ci sont liés aux cartographie de A_1 (LO) (intensité, position), ils peuvent être attribués aux impuretés résiduelles venant du processus de dopage. D'après les résultats SIMS, il peut s'agir d'impuretés de fond de C ou O qui peuvent affecter l'homogénéité locale du dopage. Dans le prochain et dernier chapitre, nous examinerons les performances électriques des diodes en présence des amas de dislocations observés et des impuretés de fond.

REFERENCES:

[1] M. Amilusik, D. Wlodarczyk, A. Suchocki, M. Bockowski. Japanese Journal of Applied Physics, 58, SCCB32, (2019).

[2] T. Kozawa, T. Kachi, H. Kano, Y. Taga, M. Hashimoto, N. Koide, K. Manabe, Journal of Applied Physics, 75(2), 1098 (1994).

Cette thèse est accessible à l'adresse : https://theses.insa-lyon.fr/publication/2023ISAL0011/these.pdf
© [A.J.E. N'Dohi], [2023], INSA Lyon, tous droits réservés

[3] T. H. Ngo, R. Comyn, E. Frayssinet, H. Chauveau, S. Chenot, B. Damilano, F. Tendille, Y. Cordier, Journal of Crystal Growth, 552, 125911, (2020).

[4] M.A Reshchikov, M. Vorobiov, O Andrieiev, K Ding, N Izyumskaya, V. Avrutin, A. Usikov, Helava H, Y Makarov. Determination of the concentration of impurities in GaN from photoluminescence and secondary-ion mass spectrometry. Sci Rep 10:.1-7. 2020.

[5] Jr JA Freitas, WJ Moore, BV Shanabrook, GC Braga, SK Lee, SS Park, JY Han, DD Koleske. Donors in hydride-vapor-phase epitaxial GaN. J Cryst Growth, 246: 307-14, 2002.

[6] C. Nenstiel, M. Bügler, G. Callsen, F. Nippert, T. Kure, S. Fritze, A. Dadgar, Physica status solidi (RRL)–Rapid Research Letters 9, 12, 716-721, (2015).

[7] K.M. Chen, Y.H. Yeh, Y. H. Wu, C. H. Chiang, D. R. Yang, Z.S. Gao, C.L. Chao, Japanese Journal of Applied Physics, 49, 091001, (2010).

[8] C. Nenstiel, M. Bügler, G. Callsen, F. Nippert, T. Kure, S. Fritze, A. Dadgar, Physica status solidi (RRL)–Rapid Research Letters 9,12, 716-721, (2015).

Cette thèse est accessible à l'adresse : https://theses.insa-lyon.fr/publication/2023ISAL0011/these.pdf
© [A.J.E. N'Dohi], [2023], INSA Lyon, tous droits réservés

CHAPITRE 7 : CARACTERISATION ELECTRIQUE DES DIODES SCHOTTKY GAN VERTICALES

INTRODUCTION : Ce chapitre traite des caractéristiques électriques des diodes Schottky étudiées au chapitre 6. Ces diodes ont été fabriquées sur la couche de dérive Epi02 et Epi03. Une des raisons du choix de ces deux couches épitaxiées de GaN est que leur niveau de dopage nominal n est adapté aux performances électriques des diodes Schottky. Les paramètres électriques des caractéristiques directes et inverses I (V) seront abordés. À travers cela, une explication provisoire et une conclusion sur la qualité et les performances des diodes seront tirées. Auparavant, nous avons étudié les propriétés physiques de deux couches (Epi02 et Epi03) sur lesquelles les diodes GaN Schottky ont été conçues et fabriquées. Lorsque la concentration en porteurs n augmente d'un facteur 10 dans le cas Epi03 ($1 \sim 2 \times 10^{16}$ cm^{-3}), les propriétés physiques étaient différentes de celles de l'Epi02 (8×10^{15} cm^{-3}). Ici, en analysant les caractéristiques I(V) des diodes verticales sur Epi02 et Epi03 avec l'augmentation du niveau de dopage n, plus d'informations sur les performances des diodes et leur qualité ont été données en plus de leurs propriétés physiques. Des paramètres électriques tels que le facteur d'idéalité, la tension seuil, la hauteur de la barrière et le courant de fuite inverse ont été calculés et une évaluation éventuelle a été faite sur les performances des diodes sur les couches épitaxiées Epi02 et Epi03. Cependant, pour établir une corrélation efficace entre les propriétés électriques et physiques des diodes, des techniques de caractérisation supplémentaires et des mesures sur plus de composants seraient nécessaires.

MÉTHODE EXPÉRIMENTALE : Les mesures I (V) ont été effectuées à l'aide de l'alimentation SMU (voir chapitre 3). Des paramètres de courant limite (faible valeur) ont été définis pour éviter le claquage prématurée des diodes. Ces courants de sécurité sont appelés courant de compliance, c'est à dire le courant maximum que l'alimentation délivre quelle que soit la tension directe ou inverse appliquée. Le courant de compliance était de 1 mA pour la mesure directe et de 100 µA pour le courant inverse. La tension maximale inverse a été fixée à -120V pour protéger les diodes. Comme la pointe, que nous avons utilisée pour les mesures sur la station sous pointes, a un grand rayon de courbure, nous n'avons mesuré que les diodes 200µm et 100µm des couches de dérive Epi02 et Epi03. Pour réduire le signal de bruit lors des mesures de polarisation inverse des diodes, nous avons éteint la lumière de la station I(V) et nous avons effectué toutes les mesures (directes et inverses) à température ambiante.

RÉSULTATS ET DISCUSSIONS : Les résultats obtenus à partir des mesures I (V) pour les diodes Epi02 ($8\times10^{15}cm^{-3}$) et Epi03 ($1\sim2\times10^{16}cm^{-3}$) (100µm, 200µm) en polarisation directe et inverse seront exposés ici. Pour évaluer les performances électriques des diodes étudiées structurellement au chapitre 6, nous avons analysé exactement les mêmes champs avec des mesures I(V).

Mesures électriques sur les diodes Epi02 : À partir de l'échelle linéaire, nous voyons que toutes les diodes présentent un comportement de diode Schottky avec une tension d'activation d'au moins 0,5 V. Avec l'échelle semi-logarithmique, on remarque que les diodes ont toutes la même tendance en dessous et au-delà de la tension moyenne d'amorçage (0.5V). Cela implique que la densité de courant direct est indépendante de la taille de la diode. Cela montre également que les diodes sont dominés par le même mécanisme de conduction du courant direct.

$$J_{TE} = J_s \exp\left(\frac{q(V - IR_s)}{nkT} - 1\right) (1)$$

Cette thèse est accessible à l'adresse : https://theses.insa-lyon.fr/publication/2023ISAL0011/these.pdf
© [A.J.E. N'Dohi], [2023], INSA Lyon, tous droits réservés

$$J_s = A^* T^2 \exp\left(-\frac{q\Phi_B}{kT}\right) \quad (2)$$

Où Js est la densité de courant de saturation, q est la charge élémentaire, V est la tension de polarisation appliquée, I est le courant résultant, R_s est la résistance série, k est la constante de Boltzmann, T est la température, A* est la constante de Richardson pour le GaN (26,9 A/cm^{2}K^2 [1]), n est le facteur d'idéalité, Φ_B est la hauteur de barrière Schottky (SBH). Dans la référence [2], il a été rapporté que les paramètres SBD (n, Φ_B et R_s) extraits avec la méthode de Cheung sont également cohérents avec l'évaluation du modèle TE de la courbe I (V) :

$$\frac{\partial V}{\partial \ln(J)} = JA^* R_S + \frac{nkT}{q}$$

La pente de la courbe donne la résistance spécifique. A partir de l'ordonnée à l'origine de la courbe, nous déduisons le facteur d'idéalité et calculons donc la hauteur de la barrière $\frac{\partial V}{\partial \ln(J)}$.

Les diodes 100µm ont leur densité de courant de fuite inverse entre 8.8×10^{-5}A/cm^2 et 1.1×10^{-4} A/cm^2. Les diodes 200µm affichent une plus petite densité de courant inverse de 8.7×10^{-6}A/cm^2 à 1.05×10^{-4} A/cm^2. Nous observons également que même à l'intérieur de chaque champ, la densité de courant inverse n'est pas la même entre les diodes 100µm et 200µm du cadre L46C36 (diodes 100µm, 200µm). Le L45C36_100µm, L46C36_100µm, L49C36_100µm, les diodes L45C36_200µm montrent une densité de courant de fuite plus élevée tandis que les L47C36_200µm, L49C36_200µm ont une densité de courant de fuite plus faible. Par conséquent, nous soupçonnons que cet écart peut être dû à l'inhomogénéité de la distribution des défauts, tels que les dislocations vis et/ou la présence d'impuretés modifiant localement le dopage comme observé au chapitre 6, dans la couche de dérive Epi02. Pour conclure efficacement, nous suggérons d'autres méthodes de caractérisation supplémentaires pour compléter ces observations. La valeur des paramètres en direct et inverse extraits pour les diodes dans chaque champ de l'échantillon Epi02 peut être vue dans le tableau 7.1.

Tableau 7.1 : Valeurs des paramètres en direct et inverse des diodes Epi02

Diodes colonne C36	**Rs [mΩ.cm^2]**	**n**	**Φ_B[eV]**	**Densité de courant de fuite [A . cm^{-2}] à -120V**
L45C36_100µm	**0.61**	**1.04**	**0.48**	**1.40×10^{-4}**
L46 C36_100µm	**0.68**	**1.63**	**0.52**	**1.26×10^{-4}**
L47 C36_100µm	**0.42**	**1.76**	**0.51**	**8.8×10^{-5}**
L49 C36_100µm	**0.23**	**1.26**	**0.52**	**1.1×10^{-4}**
L45 C36_200µm	**0.05**	**1.10**	**0.53**	**9.62×10^{-5}**
L46 C36_200µm	**0.87**	**1.14**	**0.53**	**1.05×10^{-4}**
L47 C36_200µm	**1.17**	**1.07**	**0.53**	**7.70×10^{-6}**
L49 C36_200µm	**1.86**	**1.08**	**0.53**	**8.70×10^{-6}**

Cette thèse est accessible à l'adresse : https://theses.insa-lyon.fr/publication/2023ISAL0011/these.pdf
© [A.J.E. N'Dohi], [2023], INSA Lyon, tous droits réservés

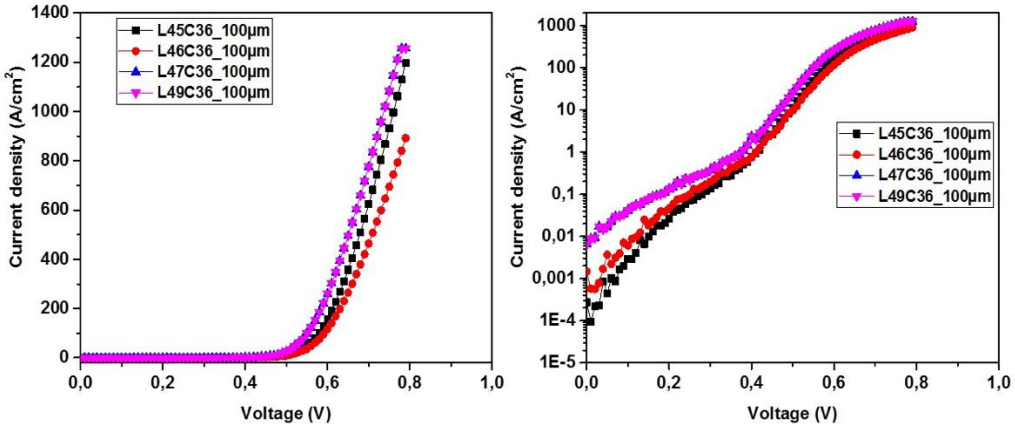

Figure.9. 1 : Tracés I(V) des diodes Epi02 (100µm) en direct linéaire (gauche) et semi log (droite).

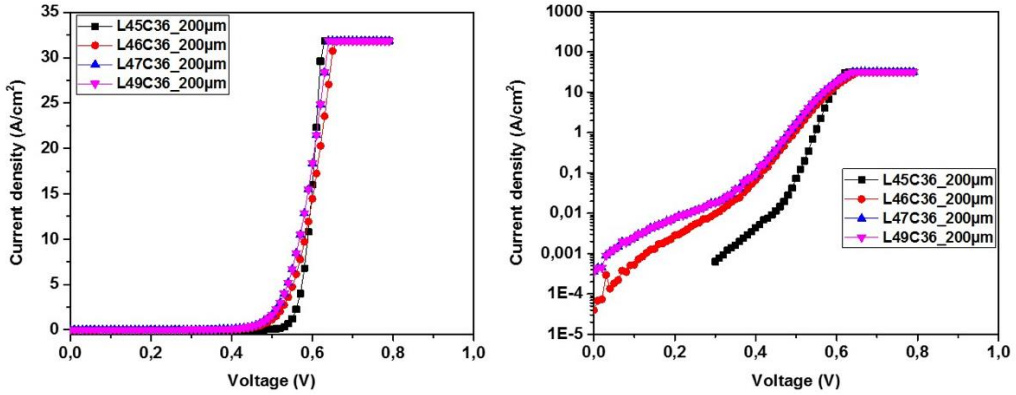

Figure** Erreur ! Il n'y a pas de texte répondant à ce style dans ce document.**2 : Tracés I(V) des diodes Epi02 (200µm) en direct linéaire (gauche) et semi log (droite).

Mesures électriques sur les diodes Epi03 : Nous avons effectué de la même manière les mesures I (V) sur les diodes Epi03 comme dans le cas Epi02. D'après le tracé à l'échelle linéaire, les diodes de 100 µm montrent le comportement de redressement avec une tension d'activation généralement autour de 0,6 V. Le diagramme semi-logarithmique montre qu'ils ont tous la même propriété de rectification. Comme dans le cas précédent, ce comportement de redressement est également dominé par le mécanisme d'émission thermoïnique. Pour les diodes 200µm, seules les diodes de (L50C38, L54C38, L55C38) ont le comportement de redressement avec une tension d'amorçage comprise entre 0,5V et 0,6V. Les diodes L52C38_200µm ne montrent cependant pas le comportement de redressement. Son comportement à partir des tracés linéaires et semi-log révèle un énorme écart par rapport à une diode Schottky normale. Il a plutôt tendance à suivre un comportement quasi-ohmique. Dans la région de polarisation inverse (0V, les diodes de 100µm (figure 6_côté droit) affichent une densité de courant de fuite assez élevée variant entre 10^{-2}A/cm^2 ~ 12A/cm^2 ordre de variation $-120V$. Parmi eux, le L50C38_100µm et le L52C38_100µm présentent la densité de courant de fuite la plus élevée. Cela peut être dû à la présence de défauts structurels (dislocations ou impuretés) qui créent plus de chemins de fuite dans les diodes. Le tableau 7.2 présente les paramètres Schottky calculés sur la base de la méthode de Cheung comme dans le cas Epi02. Nous voyons que la résistance spécifique à l'état passant est faible pour 100 µm et 200 µm en dehors de la diode L52C38_200 µm. Il est généralement compris entre 0,04 et 0,24 mΩ., ce qui est encore plus faible que l'échantillon Epi02. Cela signifie que pendant le

Cette thèse est accessible à l'adresse : https://theses.insa-lyon.fr/publication/2023ISAL0011/these.pdf
© [A.J.E. N'Dohi], [2023], INSA Lyon, tous droits réservés

fonctionnement, les pertes seront plus faibles dans ces diodes. La valeur de hauteur de barrière (0,39 0,52 eV) est également inférieure pour la plupart des diodes par rapport au cas Epi02. Il y a une légère dispersion dans la valeur de barrière pour les diodes dans le même champ ou hors champ pour les diodes 100 µm et 200 µm. Cela indique une distribution inhomogène de la hauteur de la barrière Schottky en raison de l'oxyde interfacial ou des états d'interface, à l'interface métal-semi-conducteur à mesure que le facteur d'idéalité augmente [3].

Tableau 7.2 : Valeurs des paramètres en direct et inverse des diodes Epi03

Diodes colonne C38	**Rs [mΩ.cm^2]**	**n**	**Φ_B[eV]**	**Densité de courant de fuite [A . cm^{-2}] à -120V**
L50C38_100µm	**0.07**	**2,11**	**0,48**	**12,84**
L52C38_100µm	**0.06**	**1,70**	**0.48**	**5,92**
L54C38_100µm	**0.07**	**1,64**	**0,49**	**2×10^{-2}**
L55C38_100µm	**0.04**	**1,37**	**0,50**	**$5{,}3\times 10^{-2}$**
L50C38_200µm	**0.25**	**1,66**	**0,39**	**$3{,}4 \times 10^{-1}$**
L52C38_200µm	**NO**	**NO**	**NO**	**$3{,}3 \times 10^{-1}$**
L54C38_200µm	**0.05**	**1,16**	**0,51**	**$3{,}2 \times 10^{-1}$**
L55C38_200µm	**0.24**	**1,19**	**0,52**	**$4{,}9 \times 10^{-3}$**

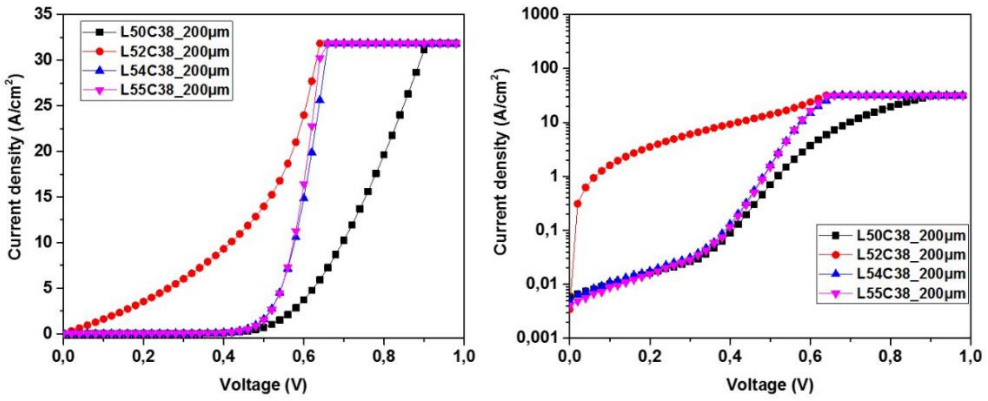

Figure 7.3 : Tracés I(V) des diodes Epi03 (100µm) en direct linéaire (gauche) et semi log (droite).

Cette thèse est accessible à l'adresse : https://theses.insa-lyon.fr/publication/2023ISAL0011/these.pdf
© [A.J.E. N'Dohi], [2023], INSA Lyon, tous droits réservés

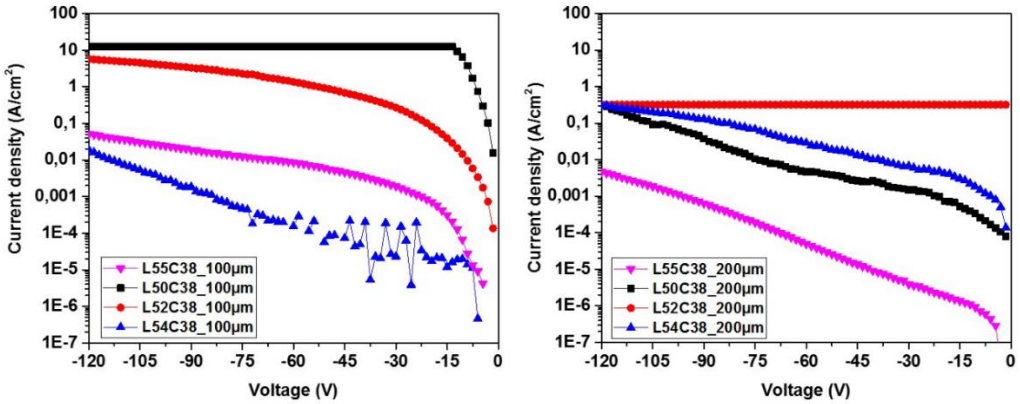

Figure 7.4 : Tracés I(V) des diodes Epi02 (200µm) en direct linéaire (gauche) et semi log (droite).

Comportement électrique et variation de la concentration de dopage : L'impact de la concentration de dopage peut être vu de manière impressionnante dans le comportement I–V, en particulier pour la réduction des courants de fuite inverses. De plus, les performances de la diode dans le sens direct changent avec le dopage [4]. Ici, nous sondons l'effet de la concentration de dopage sur les diodes Schottky (100µm, 200µm) lorsque la concentration de porteurs de charge n augmente de 8×10^{15} cm^{-3} (Epi02) à $1{\sim}2{\times}10^{16}cm^{-3}$ (Epi03). Le tableau 3 est l'évaluation des paramètres de Schottky en direct et en inverse de courant de fuite inverse pour les diodes 100µm lorsque la concentration en porteurs n augmente d'un facteur 10. Nous observons clairement que les caractéristiques directes sont influencées par la concentration en porteurs. Nous remarquons une augmentation du facteur d'idéalité à mesure que la concentration en porteurs augmente. Cela affecte la qualité du contact Schottky en induisant des défauts liés au dopage ou des impuretés qui affecteront les performances du contact Schottky. De plus, la hauteur de la barrière diminue légèrement avec l'augmentation de la concentration en porteurs. Cela indique qu'un niveau de dopage plus élevé créera des inhomogénéités ou des défauts liés au dopage (défauts de type II mentionnés au chapitre 6) dans la distribution de la hauteur de la barrière et affectera donc les performances du dispositif. En inverse, nous observons clairement que lorsque la concentration de porteurs augmente, la densité de courant inverse augmente. La figure 7.6 est le tracé semi-logarithmique de la densité de courant inverse lorsque la concentration de porteurs augmente. Il confirme l'effet de la concentration de dopage sur les performances électriques des diodes.

Cette thèse est accessible à l'adresse : https://theses.insa-lyon.fr/publication/2023ISAL0011/these.pdf
© [A.J.E. N'Dohi], [2023], INSA Lyon, tous droits réservés

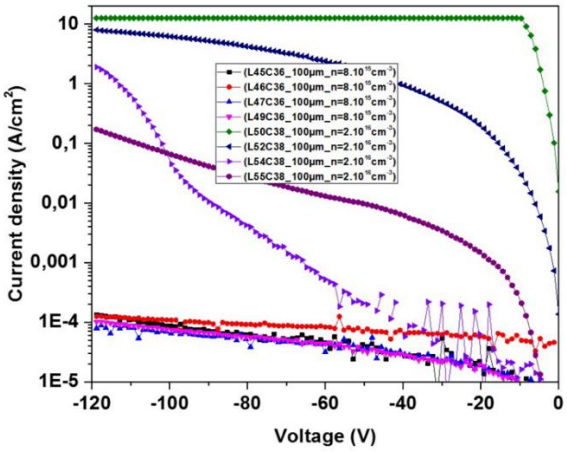

Figure 7.5 : tracé semi-logarithmique de la densité de courant inverse des diodes(100µm) lorsque la concentration de porteurs augmente.

Pour les diodes 200 µm, l'augmentation de la concentration en porteurs affecte également les caractéristiques directes et inverses (figure 7.7). En direct, nous voyons que la résistance spécifique est beaucoup plus faible à 2×10^{16} cm^{-3}, le facteur d'idéalité augmente également tandis que la hauteur de la barrière diminue. Cette tendance a également été observée dans la référence [4], où avec une concentration de dopage plus élevée, le facteur d'idéalité augmente et en même temps la hauteur de la barrière diminue. Il a été mentionné dans cette référence qu'un dopage plus élevé conduit normalement à des contributions plus importantes des courants tunnel et également à l'abaissement de la barrière de force d'image en raison du décalage du niveau de Fermi, qui est en fait l'une des raisons qui crée la tendance observée. De plus, la densité de courant de fuite inverse est également affectée par la concentration de porteurs. Cela indique que davantage de chemins de fuite sont créés dans les diodes en raison de l'augmentation de la concentration de dopage. Au chapitre 6, nous avons trouvé à partir des cartographies Raman A_1 (LO) que des défauts liés au processus de dopage apparaissent dans la couche de dérive des diodes et s'étendent sur toute la surface active des diodes. Par exemple, les diodes des champs L50C38 et L52C38 sont plus intéressants. Les défauts de type II (surlignés en cercles noirs) apparaissent dans la couche de dérive en plus des défauts de type I (taches rouges étendues dans les cartes d'intensité) lorsque l'on considère leurs cartographies Raman A_1 (LO) (chapitre). Nous soupçonnons que l'un des chemins de fuite peut être lié au processus de dopage. Ces types de défauts peuvent créer davantage de chemins de fuite du fait du dopage inhomogène des diodes dans les champs qui les contiennent. De plus, la présence des dislocations de filetage trouvées au chapitre 6 n'est pas négligeable car elles peuvent également être considérées comme des chemins de fuite qui influencent les performances de la diode. Pour l'instant, d'après ce que nous avons découvert, nous nous attendons à ce que les dislocations et les impuretés de fond (défauts de type I et II) liées au processus de dopage puissent être les chemins de fuite dans la couche épitaxiées des diodes et leur influence est plus visible lorsque la concentration en porteurs n augmente, notamment pour ceux liés au processus de dopage.

Cette thèse est accessible à l'adresse : https://theses.insa-lyon.fr/publication/2023ISAL0011/these.pdf
© [A.J.E. N'Dohi], [2023], INSA Lyon, tous droits réservés

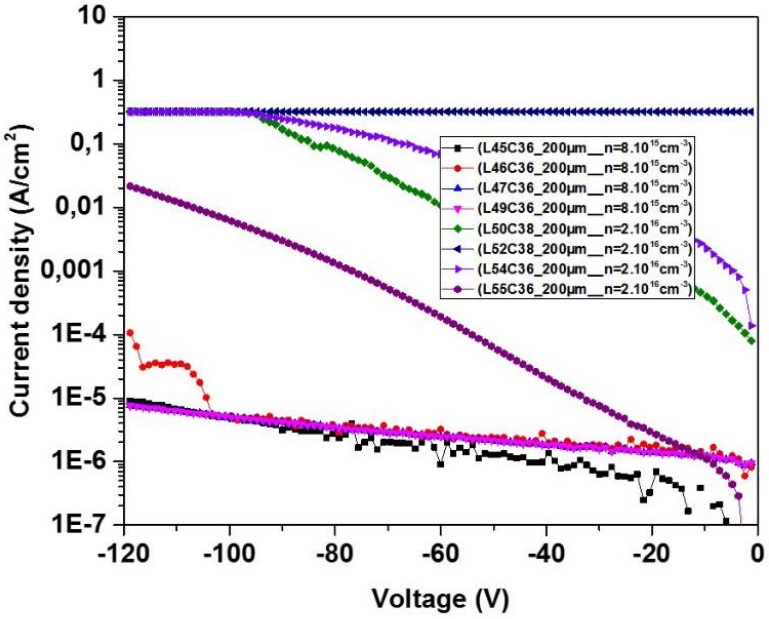

Figure 7.6 : tracé semi-logarithmique de la densité de courant inverse des diodes (200µm) lorsque la concentration de porteurs augmente.

CONCLUSION : Nous avons sondé les caractéristiques électriques des diodes GaN Schottky de 100 µm et 200 µm en utilisant des mesures I (V) classiques dans les régions de polarisation directe et inverse. Nous avons remarqué que la concentration en porteurs n joue un rôle important sur les deux caractéristiques. En régime direct, nous voyons que la résistance spécifique diminue, le facteur d'idéalité augmente lorsque la hauteur de la barrière diminue avec le dopage. Dans la polarisation inverse, l'augmentation de la concentration de dopant n crée une augmentation de la densité de courant de fuite inverse. Nous en déduisons que les défauts structuraux (dislocations) -trouvés dans le chapitre 6 précédent peuvent en être responsables. De plus, comme l'augmentation de la densité de courant inverse suit l'augmentation de la concentration de dopage, nous soupçonnons que des défauts tels que la présence d'impuretés trouvées dans les cartographies Raman du pic A_1 (LO) et qui sont liés au processus de dopage peuvent en être responsables en créant des chemins de fuite dans les diodes. Dans le but de corréler les propriétés physiques des diodes du chapitre 6 aux propriétés électriques des mêmes diodes dans ce chapitre, nous suggérons que des caractérisations plus électriques et physiques telles que l'OBIC (Optical Beam Induced Current = courant induit par faisceau optique), spectroscopie Raman 3D, IVT et la DLTS seront nécessaire pour conclure efficacement sur ces observations.

REFERENCES :

[1] Ngo, Thi Huong, Rémi Comyn, Eric Frayssinet, Hyonju Chauveau, Sébastien Chenot, Benjamin Damilano, Florian Tendille et al. "Cathodoluminescence and electrical study of vertical GaN-on-GaN Schottky diodes with dislocation clusters." Journal of Crystal Growth 552, 125911. (2020).

[2] Ha, Sieu D., R. Jaramillo, D. M. Silevitch, Frank Schoofs, Kian Kerman, John D. Baniecki, and Shriram Ramanathan. "Hall effect measurements on epitaxial SmNiO 3 thin films and implications for antiferromagnetism." Physical Review B 87, no. 12, 125150. (2013).

[3] Tung, R. T. "Electron transport at metal-semiconductor interfaces: General theory." Physical Review B 45, no. 23 13509. (1992).

Cette thèse est accessible à l'adresse : https://theses.insa-lyon.fr/publication/2023ISAL0011/these.pdf
© [A.J.E. N'Dohi], [2023], INSA Lyon, tous droits réservés

[4] Contacts, Metal-Semiconductor. "E.H Rhoderick and R.H. Williams." Clarendon, Oxford 1-70. (1988).

Cette thèse est accessible à l'adresse : https://theses.insa-lyon.fr/publication/2023ISAL0011/these.pdf
© [A.J.E. N'Dohi], [2023], INSA Lyon, tous droits réservés

CONCLUSION : Dans cette thèse, nous avons confronté les propriétés physiques et électriques des matériaux et dispositifs GaN à travers une approche de caractérisations multiphysiques. En partant du contexte théorique sur le GaN et de l'état de l'art sur les dispositifs GaN au chapitre 1, nous sommes entrés dans les détails des aspects fondamentaux des méthodes de caractérisation physique et des mesures électriques que nous avons utilisées au cours de ce projet dans les chapitres 2 et 3 respectivement. Au chapitre 4, nous avons étudié certains substrats GaN dopés n avec Si, Ge et O_2 en utilisant la spectroscopie Raman, car avoir de bonnes performances des dispositifs nécessite un substrat natif fortement dopé et de bonne qualité cristalline. Nous avons mis en lumière l'effet possible des dopants sur les propriétés microstructurales des substrats. Cette étude a également confirmé l'efficacité de l'outil micro Raman pour l'analyse microstructurale quantitative des matériaux GaN. Puis, dans le chapitre 5, nous avons continué de sonder des échantillons de GaN avec des epitxaies homo-épitaxiales dopées n avec une concentration en n comprise entre $10^{14}cm^{-3}$ et $10^{18}cm^{-3}$. Nous avons trouvé une réponse linéaire due à une faible force d'interaction entre le champ électrique du phonon A_1 (LO) et le champ électrique à faible densité de porteurs. À partir de cette étude, nous avons réussi à montrer que le micro-Raman est un outil efficace pour examiner l'effet de la concentration de dopage sur la qualité cristalline dans le matériau GaN. De plus, au chapitre 6, nous avons étudié les propriétés physiques des diodes Schottky GaN verticales basées sur la combinaison de la spectroscopie micro-Raman et de la méthode de cathodoluminescence (CL) principalement. Nous avons découvert une bonne corrélation entre la spectroscopie Raman et la méthode CL dans l'identification des dislocations de filetage dans les échantillons de GaN. Cela montre également l'efficacité de la spectroscopie micro-Raman en tant qu'outil puissant et non destructif pour sonder la présence des dislocations et évaluer la concentration de porteurs n dans les matériaux et dispositifs GaN. Les cartographies d'intensité et de positions du pic A_1 (LO), nous ont permis d'observer des patchs particuliers qui ont tendance à affecter la concentration effective de porteurs n dans les couches épitaxiées des diodes. Nous soupçonnons que ces patchs soient liés au processus de dopage, en tant qu'impuretés atomiques, car des mesures SIMS sur ces mêmes couches ont révélé la présence d'impuretés telles que O et C. Enfin, au chapitre 7, le comportement électrique des diodes Schottky GaN verticales (100µm, 200µm) a été analysé avec deux concentrations de dopage $8\times10^{15}cm^{-3}$ et $1\text{-}2\times10^{16}cm^{-3}$. Grâce aux mesures I(V) à température ambiante, nous avons étudié les effets des défauts structurels trouvés au chapitre 6 sur les performances des diodes. Cependant, pour corréler efficacement les propriétés physiques avec le comportement électrique, nous suggérons que des caractérisations électriques complémentaires (telles que des mesures OBIC, DLTS ou encore I(V)T) et physiques sur de nombreuses diodes seraient nécessaires pour tirer une conclusion finale à ce sujet. Cela pourrait être fait comme un travail futur pour étendre ce projet de thèse.

Cette thèse est accessible à l'adresse : https://theses.insa-lyon.fr/publication/2023ISAL0011/these.pdf
© [A.J.E. N'Dohi], [2023], INSA Lyon, tous droits réservés

FOLIO ADMINISTRATIF

THESE DE L'INSA LYON, MEMBRE DE L'UNIVERSITE DE LYON

NOM : N'DOHI DATE de SOUTENANCE : 03/03/2023

Prenames: ATSE JULIEN ERIC

TITRE: Multiphysics characterization of GaN and devices for power electronics

NATURE : Doctorat Numéro d'ordre : 2023ISAL0011

Ecole doctorale : Electronique Electrotechnique Automatique

Spécialité : Microélectronique optique et laser

RESUME :
Malgré ses avantages technologiques, Le silicium présente des limites en raison de son incapacité à opérer sous haute tension à température et pression élevée. Ainsi, le besoin de recourir aux matériaux ayant des propriétés supérieures à celles du silicium est de plus en plus grandissant. Les semi-conducteurs à grande bande d'énergie interdite comme le Carbure de silicium (SiC), le nitrure de gallium (GaN) et le diamant montrent les potentialités à travailler sous haute tension à cause de leur propriété physique respective. L'industrie des semi-conducteurs les considère comme de potentiels candidats pour l'électronique de puissance. En réalité, ces matériaux à grand gap peuvent être utiliser comme onduleurs, redresseurs de courant et même convertisseurs pour une distribution efficace et effective de l'énergie. Cependant, le chemin pour atteindre une série de production effective avec une maturité technologique et industrielle est encore longue parce que les récentes recherches ont montré que leur performance en tant que composants de puissance est épinglée par quelques phénomènes physiques comme l'apparition de défauts, les effets de contraintes mécaniques, le control du dopage de la couche ou la région active, les fuites et perte d'énergie. Ainsi, une analyse profonde de ces problèmes fondamentaux est requise pour permettre de trouver les solutions adéquates en vue d'optimiser leur performance. Dans cette thèse, nous avons confronté les propriétés physiques et électriques des matériaux et dispositifs GaN à travers une approche de caractérisations multi physiques et électrique tels que le micro Raman la cathodoluminescence et les mesures classiques de courant-tension I(V). L'objectif est de sonder la performance physique de ces matériaux de puissance, surtout ceux conçu à base du GaN parce que la mobilité des porteurs de charges dans le GaN et son énergie de bande interdite permettent aux composants de puissances fabriqués à base du GaN d'opérer dans les commutations de fréquences et radio fréquence élevée que ceux du SiC. Ainsi, le couplage de ces méthodes de caractérisation nous permettra d'avoir une vue profonde des mécanismes physiques qui régissent la performance du GaN sous haute tension et à saisir la contradiction existant entre les paramètres théoriques physiques établis par les simulations d'éléments finies et la réalité expérimentale.

MOTS-CLÉS : Nitrure de gallium, Micro Raman, cathodoluminescence, courant-tension I(V).

Laboratoire (s) de recherche : Laboratoire Ampère

Directeur de thèse: Dominique Planson

Président de jury : Nathalie Malbert

Composition du jury : MALBERT Nathalie, BOUDART Bertrand, KUBALL Martin, JUILLAGUET Sandrine, SONNEVILLE Camille, PLANSON Dominique.

Cette thèse est accessible à l'adresse : https://theses.insa-lyon.fr/publication/2023ISAL0011/these.pdf
© [A.J.E. N'Dohi], [2023], INSA Lyon, tous droits réservés

INSTITUT NATIONAL DES SCIENCES APPLIQUÉES LYON

Département de la Formation par la Recherche et des Études Doctorales (**FEDORA**)

Bâtiment INSA direction, 1er étage
37, av. J. Capelle
69621 Villeurbanne Cédex
fedora@insa-lyon.fr

Référence : TH0947_NDOHI

L'INSA Lyon a mis en place une procédure de contrôle systématique via un outil de détection de similitudes (logiciel Compilatio). Après le dépôt du manuscrit de thèse, celui-ci est analysé par l'outil. Pour tout taux de similarité supérieur à 10%, le manuscrit est vérifié par l'équipe de FEDORA. Il s'agit notamment d'exclure les auto-citations, à condition qu'elles soient correctement référencées avec citation expresse dans le manuscrit.

Par ce document, il est attesté que ce manuscrit, dans la forme communiquée par la personne doctorante à l'INSA Lyon, satisfait aux exigences de l'Etablissement concernant le taux maximal de similitude admissible.

INSA LYON
Campus LyonTech La Doua
20, avenue Albert Einstein - 69621 Villeurbanne cedex - France
Tél. +33 (0)4 72 43 83 83 - Fax +33 (0)4 72 43 85 00
www.insa-lyon.fr

membre de UNIVERSITÉ DE LYON

Cette thèse est accessible à l'adresse : https://theses.insa-lyon.fr/publication/2023ISAL0011/these.pdf
© [A.J.E. N'Dohi], [2023], INSA Lyon, tous droits réservés